National and Kapodistrian University of Athens

School of Science – Department of Geology and Geoenvironment

Laboratory of Climatology and Atmospheric Environment

Doctoral Dissertation

Solar radiation/energy forecasting and measurement applications: the role of clouds and aerosols

Papachristopoulou Kyriakoula
Physicist
MSc. Environmental Physics

Athens 2023

Εθνικό και Καποδιστριακό Πανεπιστήμιο Αθηνών

Σχολή Θετικών Επιστημών – Τμήμα Γεωλογίας και Γεωπεριβάλλοντος

Εργαστήριο Κλιματολογίας και Ατμοσφαιρικού Περιβάλλοντος

Διδακτορική Διατριβή

Εφαρμογές μετρήσεων και πρόγνωσης της ηλιακής ακτινοβολίας και ενέργειας με έμφαση στο ρόλο των αερολυμάτων και των νεφών

Παπαχριστοπούλου Κυριακούλα
Φυσικός
MSc. Φυσική Περιβάλλοντος

Αθήνα 2023

Σχολή Θετικών Επιστημών – Τμήμα Γεωλογίας και Γεωπεριβάλλοντος

Εργαστήριο Κλιματολογίας και Ατμοσφαιρικού Περιβάλλοντος

Διδακτορικό Δίπλωμα

Τίτλος: «Εφαρμογές μετρήσεων και πρόγνωσης της ηλιακής ακτινοβολίας και ενέργειας με έμφαση στο ρόλο των αερολυμάτων και των νεφών»

Title: “Solar radiation/energy forecasting and measurement applications: the role of clouds and aerosols”

Συγγραφέας: Κυριακούλα Παπαχριστοπούλου

Αριθμός Μητρώου: 290

Τριμελής Επιτροπή:

Μαρία Χατζάκη, Επίκουρη Καθηγήτρια (Επιβλέπουσα)

Στυλιανός Καζαντζής, Κύριος Ερευνητής

Παναγιώτης Νάστος, Καθηγητής

Supervising Committee

Hatzaki Maria, Assistant Professor, National and Kapodistrian University of Athens (Supervisor)

Kazadzis Stelios, Senior scientist, Physikalisch-Meteorologisches Observatorium Davos, World Radiation Center, Switzerland

Nastos Panagiotis, Professor, National and Kapodistrian University of Athens

Examination Committee

Alkiviadis Bais, Professor, Aristotle University of Thessaloniki

Philippe Blanc, Professor, MINES ParisTech / PSL Research University

Konstantinos Eleftheratos, Associate Professor, National and Kapodistrian University of Athens

Sotiropoulou Georgia, Assistant Professor, National and Kapodistrian University of Athens

This thesis was defended in public on September 18, 2023

Στους γονείς μου

Preface – Acknowledgments

I would like to express my sincere gratitude towards my supervisors Asst. Prof. Maria Hatzaki and Dr. Stelios Kazadzis, Senior Scientist for trusting and supporting me; their continuous advising and encouragement throughout the entire journey of this doctoral thesis were pivotal. I would, especially, like to thank Dr. Stelios Kazadzis for his motivation and invaluable guidance, his insightful comments and our scientific discussions and the opportunity to conduct research at the Physikalisch Meteorologisches Observatorium Davos/World Radiation Center (PMOD/WRC) in Switzerland, during my Swiss scholarship fellowship. I would also like to acknowledge Prof. Panagiotis Nastos, member of my advisory committee, for his scientific guidance and advice – from my first years as a postgraduate student, until today.

I am also indebted to the members of my doctoral examination committee, Prof. Alkiviadis Bais, Prof. Philippe Blanc, Assoc. Prof. Konstantinos Eleftheratos and Asst. Prof. Sotiropoulou Georgia, for their insightful feedback, which has significantly enriched this work.

I would also like to thank all whom I collaborated with and who helped me throughout the PhD period. I would expressly like to thank Dr. Ilias Fountoulakis for the excellent collaboration, help and guidance both in the scientific and the technical parts of this effort. Additionally, his contribution to the ARIS HPC project was invaluable. I would like to thank Dr. Panos Raptis for his advice and support from the beginning of my PhD, for all the discussions that we had and notably for his contribution to the megacities project. Finally, I would like to thank Dr. Antonis Gkikas not only for the close interaction during the entire PhD period, but also, more notably, for kindly providing the MIDAS dataset and his constant support.

Programs that funded my work should be acknowledged, including the European Commission projects EuroGEO e-shape (grant agreement No. 820852), the European Commission project 'EXCELSIOR': ERATOSTHENES: Excellence Research Centre for Earth Surveillance and Space-Based Monitoring of the Environment (grant no. 857510) and the PANGEA4CalVal project (Grant Agreement 101079201), funded by the European Union. Furthermore, I could not go on without acknowledging the support for the research I conducted, within the realm of my doctorate, by the Swiss Government Excellence Scholarship, offered by the Swiss Government via the Federal Commission for Scholarships for Foreign Student, FCS, which gave me the ability to conduct research at ETH Zurich, Department of Physics, as an FCS visiting student. What is more, during that period, I had the opportunity to conduct research and work at the PMOD/WRC and I would like to acknowledge the Instrument Data quality Evaluation and Assessment Service – Quality Assurance for Earth Observation (IDEAS-QA4EO) project (contract no. QA4EO/SER/SUB/09; TPZ PO no. 600006842-PMOD/WRC). Finally, part of this thesis was conducted during a Short-Term Scientific

Mission (STSM) grant “D4DS” (Dust impact on the 4D Solar spectral radiation field and related interdisciplinary effects) funded by COST (European Cooperation in Science and Technology) Action: InDust (CA16202).

I would like to acknowledge Prof. Alkiviadis Bais for providing pyranometer data from the Thessaloniki station; Dr. Basil E. Psiloglou for providing pyranometer data from the Athens station (ASNOA: the NOA’s Actinometric Station); the principal investigators and co-investigators and their staff for establishing and maintaining the 37 AERONET sites used in this thesis; and the eight site instrument operators and technical staff of the BSRN network stations, who made the ground-based measurements feasible. I would also like to acknowledge Prof. Andreas Kazantzidis and PhD candidate Nikolaos Papadimitriou for their contribution to the cloud function approach; Dr. Akriti Masoom for the analysis of the ground-based data for the megacities study; Dr. Vassilis Amiridis, Dr. Emmanouil Proestakis and Dr. Eleni Marinou for the kind provision of the LIVAS database and products used for the thesis – especially Dr. Emmanouil Proestakis for his guidance and support on the dataset. I would like to acknowledge Prof. Bernhard Mayer and Asst. Professor Claudia Emde and their team for the provision and development of the library for radiative transfer – libRadtran, which is freely available under the GNU General Public License, a tool that was an essential part of the implementation of this PhD thesis. I would like to acknowledge the EUMETSAT NWC SAF services, as well as the OMI team, for providing all the necessary data used for this thesis; the free use of the GOME-2 surface LER database, provided through the AC SAF of EUMETSAT – the GOME-2 surface LER database was created by the Royal Netherlands Meteorological Institute (KNMI). Finally, this work was supported by computational time, granted by the National Infrastructures for Research and Technology S.A. (GRNET) at the National HPC facility - ARIS - under project ID pa210301- SO-LISIS.

I am acknowledging the COST Action HARMONIA, CA21119, supported by COST (European Cooperation in Science and Technology); this is a COST Action that is chaired by Dr. Stelios Kazadzis and I am pleased to be part of the Action’s Core Group member as WG5 Co-Leader.

Taking this opportunity, I would like to express my appreciation to my parents for their unwavering love and their endless encouragement and support, which all contribute to who I am today and to my achievements. I would like to thank my little sister Eftychia for supporting my choices, during a difficult period for my family.

I would like to thank all my friends who are always there for me; which has also been the case during my doctoral studies. Special thanks to my friends Dr. Marilia Mavropoulou, PhD candidates Iliana Polychroni and Aristotelis Dimou for their help in the technical aspects of this effort and the

constructive discussions we had. A special mention to my friends Filomila Kafe and Dr. Kostas Seintis, during my stay in Switzerland for their help and support.

Last, but not least, I would like to thank my husband Thanos for his love, patience and understanding; his continuous support and valuable advice; for always supporting my dreams and decisions and for believing in me.

Kyriakoula Papachristopoulou

Abstract

Aerosols and clouds play a dominant role for solar radiation attenuation with great implication in climate and energy related applications. The scope of this dissertation is to investigate the role of aerosols and clouds to this attenuation, aiming to improve surface solar radiation forecasting and related applications. In addition, atmospheric aerosols, being also of particular concern for human health, have both natural and anthropogenic origin, and it is more than necessary to understand and analyze their variability at different spatial scales.

Cities are one of the major sources of anthropogenic aerosols. The increased urbanization (70% of world's population by 2050) raises several environmental challenges, including air quality degradation. The spatial and temporal variability of urban aerosol state of 81 cities with a population over 5 million was investigated, relying on daily satellite-based aerosol optical depth (AOD) retrievals of fine spatial resolution, over an 18-year period (2003 to 2020). The population changes of those cities were also examined. According to the results the European and American cities have lower aerosol loads compared to African and Asian cities. For European, North American, and East Asian cities, aerosols are decreasing over time while their population is increasing. Especially for Chinese cities the greatest reduction in aerosols was found, despite their population growth, in response to the rigorous environmental measure implemented the last decade. For the rest of Asian, African, and South American cities, an increase in their aerosol load was found along with an increase of their population. For Indian cities the greatest increase in aerosol loads was found, a change that was correlated with the population growth. The agreement of the satellite-derived AOD trends against those obtained from ground-based AERONET measurements was also examined. Most of the trends agreed in sign for ground-based stations within the geographical limits of the contiguous urban area of the examined cities. This study highlights the vital and essential contribution of spaceborne products to monitor aerosol burden over megacities.

To analyze both anthropogenic and nature aerosols, including their direct radiative effects, focus was put on the regional scale and especially to the broader Mediterranean basin. The natural aerosol component that has significant contribution to the aerosol mixture over Mediterranean is dust. The continuous satellite monitoring of atmospheric aerosols provides long term satellite datasets of AOD, dust optical depth (DOD) and their vertical distribution in the atmosphere which contribute to understanding their direct radiative effects. The quantification of total and dust aerosols direct effects on global horizontal irradiance (GHI; important for photovoltaic installations) and direct normal irradiance (DNI; important for concentrating solar power systems) was attained for the broader Mediterranean basin, over the period 2003-2017, using the satellite based ModIs Dust AeroSol

(MIDAS) AOD/DOD datasets and radiative transfer modeling (RTM), under clear-sky conditions. The Mediterranean basin is a region of high interest for such a research effort since it combines high solar energy potential with an increasing capacity in solar energy installations. Aerosol attenuation of annual GHI and DNI were 1–13% and 5–47%, respectively. Over North Africa and the Middle East, attenuation by dust was found to contribute 45–90% to the overall attenuation by aerosols. After 2008, attenuation of surface solar radiation by aerosols became weaker mainly because of changes in the amount of dust. Sensitivity analysis using different AOD/DOD inputs from Copernicus Atmosphere Monitoring Service (CAMS) reanalysis dataset revealed that using CAMS products leads to underestimation of the aerosol and dust radiative effects compared to MIDAS, mainly because the former underestimates DOD. The results of this analysis are important for understanding of the role of aerosols and especially of dust on GHI and DNI over the Mediterranean Basin and planning of future solar installations.

As solar energy nowcasting and short-term forecasting are essential for the optimization of solar renewable energy use in the energy mix, accurate clouds and aerosol datasets are the key factors to achieve optimum results. SENSE2 is the upgraded version of an existing solar energy nowcasting system that produces real-time estimates of surface GHI based on earth observation data (satellite and model based) at high spatial and temporal resolution (~5 km, 15 min) for a domain including Europe and the Middle East–North Africa (MENA). The improvements that have been introduced to SENSE2 are a new model configuration and the upgrade of cloud and aerosol inputs. The improved SENSE2 has been validated for 1 year (2017) using ground-based measurements from 10 stations. The limitations of evaluating such a model were investigated using surface-based sensors due to cloud effects. Results for instantaneous (every 15 min) comparisons show that the GHI estimates are within ±50 W m^{-2} (or ±10%) of the measured GHI for 61% of the cases after the implementation of the new model configuration and a proposed bias correction. The bias ranges from -12 to 23 W m^{-2} (or from -2 to 6.1%) with a mean value 11.3 W m^{-2} (2.3%). It was demonstrated that the main overestimation of the SENSE2 GHI is linked with the uncertainties of the cloud-related information within the satellite pixel, while relatively low underestimation, linked with AOD forecasts (derived from CAMS), is reported for cloudless-sky GHI. The highest deviations for instantaneous comparisons are associated with cloudy atmospheric conditions when clouds obscure the sun over the ground-based station. Thus, they are much more closely linked with satellite vs. ground-based comparison limitations than the actual model performance. The NextSENSE2 short term forecasting system (up to 3 h ahead) based on a cloud motion vector technique, was also validated. It was found that it outperforms the persistence forecasting method, which assumes the same cloud conditions for the future time steps, especially for periods with increased cloudiness and changes in cloudiness.

Keywords: solar radiation, aerosol, clouds, solar radiation forecasting, radiative transfer modeling

Περίληψη

Η εξασθένηση που προκαλούν τα σύννεφα και τα ατμοσφαιρικά αιωρούμενα σωματίδια στην ηλιακή ακτινοβολία που φτάνει στην επιφάνεια της γης έχει σημαντικές επιπτώσεις στο κλίμα της γης αλλά και σε εφαρμογές που σχετίζονται με την παραγωγή ηλιακής ενέργειας. Το αντικείμενο μελέτης της παρούσας διατριβής είναι η διερεύνηση του ρόλου των αερολυμάτων και των νεφών σε αυτή την εξασθένηση, με στόχο τη βελτίωση των συστημάτων πρόγνωσης της ηλιακής ακτινοβολίας που φτάνει στο έδαφος και άλλων σχετικών με την εκμετάλλευση της ηλιακής ενέργειας εφαρμογών. Επιπλέον, τα αιωρούμενα σωματίδια , τα οποία έχουν επίσης σημαντικές επιπτώσεις στην υγεία του ανθρώπου, κατατάσσονται σε φυσικής και ανθρωπογενούς προέλευσης, και είναι κάτι παραπάνω από απαραίτητο να κατανοήσουμε και να αναλύσουμε τις μεταβολές τους σε διάφορες χωρικές κλίμακες.

Οι πόλεις αποτελούν την κύρια πηγή ανθρωπογενών αερολυμάτων. Ο παγκόσμιος ρυθμός αστικοποίησης συνεχίζει να αυξάνεται (το 70% του παγκόσμιου πληθυσμού μέχρι το 2050) το οποίο συνδέεται με πληθώρα περιβαλλοντικών επιπτώσεων όπως η υποβάθμιση της ποιότητας του ατμοσφαιρικού αέρα. Στην παρούσα διατριβή μελετήθηκε η χωρική και χρονική μεταβλητότητα των αστικών αερολυμάτων 81 πόλεων με πληθυσμό πάνω από 5 εκατομμύρια, χρησιμοποιώντας ένα υψηλής χωρικής ανάλυσης δορυφορικό προϊόν του οπτικού βάθους των αερολυμάτων (AOD), για ένα χρονικό διάστημα 18 χρόνων (2003 με 2020). Μελετήθηκαν επίσης οι μεταβολές στον πληθυσμό των πόλεων αυτών για το ίδιο χρονικό διάστημα. Σύμφωνα με τα αποτελέσματα οι πόλεις της Ευρώπης και της Αμερικής έχουν λιγότερα αιωρούμενα σωματίδια σε σχέση τις πόλεις της Αφρικής και της Ασίας. Μείωση των αιωρούμενων σωματιδίων βρέθηκε για τις πόλεις της Ευρώπης, Βόρειας Αμερικής και της Ανατολικής Ασίας, ενώ βρέθηκε αύξηση του πληθυσμού τους για το ίδιο διάστημα. Η μεγαλύτερη μείωση των αιωρούμενων σωματιδίων βρέθηκε για τις πόλεις της Κίνας, παρόλη την αύξηση του πληθυσμού τους, η οποία οφείλεται στα αυστηρά περιβαλλοντικά μέτρα που πάρθηκαν στη χώρα την τελευταία δεκαετία. Αύξηση των αιωρούμενων σωματιδίων βρέθηκε για τις υπόλοιπες πόλεις της Ασίας, τις πόλεις της Αφρικής και της Νότιας Αμερικής, σε συνδυασμό με την αύξηση στον πληθυσμό τους. Η μεγαλύτερη αύξηση βρέθηκε για τις πόλεις της Ινδίας, η οποία βρέθηκε να συσχετίζεται με την αύξηση στον πληθυσμό τους. Εξετάστηκε επίσης κατά πόσο οι τάσεις των τιμών του AOD που υπολογίστηκαν από τα δορυφορικά δεδομένα συμφωνούν με τις αντίστοιχες τιμές από μετρήσεις εδάφους του δικτύου AERONET. Οι τιμές των τάσεων που υπολογίστηκαν από τις προαναφερθείσες δυο πηγές είχαν το ίδιο πρόσημο όταν ο επίγειος σταθμός ήταν εντός της γεωγραφικής περιοχής που καλύπτεται από τον αστικό ιστό της υπό μελέτη πόλεως. Τα αποτελέσματα της παρούσα μελέτης δίνουν έμφαση στη σημαντική συνεισφορά των δορυφορικών παρατηρήσεων στην καταγραφή των αιωρούμενων σωματιδίων σε μεγαλουπόλεις.

Η ανάλυση των αερολυμάτων τόσο ανθρωπογενούς όσο και φυσικής προέλευσης, συμπεριλαμβανομένου της άμεσης επίδρασης τους στην ηλιακή ακτινοβολία έγινε σε περιοχική κλίμακα και συγκεκριμένα στην ευρύτερη περιοχή της Μεσογείου. Η ερημική σκόνη αποτελεί μια βασική συνιστώσα των αερολυμάτων φυσικής προέλευσης στη Μεσόγειο. Η συνεχής παρατήρηση των αιωρούμενων σωματιδίων από δορυφόρους παρέχει μακροχρόνιες μετρήσεις του AOD, του οπτικού βάθους της σκόνης (DOD) αλλά και της κατακόρυφης δομής τους μέσα στην ατμόσφαιρα, δεδομένα πολύτιμα στην κατανόηση της άμεσης αλληλεπίδρασης των αερολυμάτων με την ακτινοβολία. Χρησιμοποιώντας δεδομένα του AOD και DOD που βασίζονται σε δορυφορικές παρατηρήσεις του ραδιόμετρου MODIS (βάση δεδομένων MIDAS – ModIs Dust AeroSol) και μοντέλο διάδοσης ακτινοβολίας ποσοτικοποιήθηκε η άμεση επίδραση του συνόλου των αερολυμάτων και χωριστά μόνο της σκόνης στην ολική ηλιακή ακτινοβολία σε οριζόντιο επίπεδο (GHI; η οποία είναι σημαντική για τα φωτοβολταϊκά συστήματα) και στην άμεση ηλιακή ακτινοβολία κάθετα προς τη διεύθυνση διάδοσης (DNI; η οποία είναι σημαντική για τα συγκεντρωτικά ηλιακά συστήματα) υπό ανέφελο ουρανό, για την ευρύτερη περιοχή της Μεσογείου, για την περίοδο 2003 – 2017. Η περιοχή αυτή είναι ιδιαίτερου ενδιαφέροντος καθώς είναι μια περιοχή με υψηλό ηλιακό δυναμικό και αύξηση των εγκαταστάσεων εκμετάλλευσης της ηλιακής ενέργειας. Η μέση ετήσια εξασθένηση της GHI και της DNI που οφείλεται στο σύνολο των αερολυμάτων βρέθηκε μεταξύ 1% με 13% και μεταξύ 5% με 47%, αντίστοιχα. Για την περιοχή της Βόρειας Αφρικής και της Μέσης Ανατολής, το 45 με 90% της εξασθένησης και των δύο συνιστωσών της ηλιακής ακτινοβολίας από το σύνολο των αερολυμάτων βρέθηκε να οφείλεται στη συνιστώσα της ερημική σκόνης. Μετά το 2008 βρέθηκε μείωση της εξασθένησης της ηλιακής ακτινοβολίας που φτάνει στην επιφάνεια της γης από το σύνολο των αερολυμάτων, το οποίο αποδόθηκε κυρίως στις μεταβολές της συνιστώσας της ερημικής σκόνης. Τέλος, πραγματοποιήθηκε ανάλυση ευαισθησίας των αποτελεσμάτων χρησιμοποιώντας διαφορετικά δεδομένα AOD και DOD, και συγκεκριμένα από το μοντέλο Copernicus Atmosphere Monitoring Service (CAMS reanalysis dataset). Σύμφωνα με τα αποτελέσματα υποεκτιμάται η άμεση επίδραση του συνόλου των αερολυμάτων και χωριστά μόνο της σκόνης στην ηλιακή ακτινοβολία όταν χρησιμοποιούνται δεδομένα AOD και DOD από το μοντέλο του CAMS σε σχέση με τις αντίστοιχες τιμές όταν χρησιμοποιήθηκε η βάση δεδομένων MIDAS, κυρίως γιατί το μοντέλο του CAMS υποεκτιμά το DOD. Τα αποτελέσματα της ανάλυσης αυτής είναι σημαντικά τόσο για την κατανόηση του ρόλου των αερολυμάτων και ειδικά της ερημικής σκόνης στην GHI και DNI στην ευρύτερη περιοχή της Μεσογείου, καθώς και στη φάση σχεδιασμού νέων εγκαταστάσεων εκμετάλλευσης ηλιακής ενέργειας.

Η εκτίμηση των επιπέδων της ηλιακής ενέργειας που φτάνει στην επιφάνεια της γης σε πραγματικό χρόνο (nowcasting), και η βραχυπρόθεσμη πρόγνωσή της (short-term forecasting) είναι σημαντικά εργαλεία για την βέλτιστη ένταξη των συστημάτων εκμετάλλευσης ηλιακής ενέργειας στην αγορά

ενέργειας. Η ακρίβεια των αποτελεσμάτων των εργαλείων αυτών εξαρτάται σε μεγάλο βαθμό από την ακρίβεια των δεδομένων νεφοκάλυψης και των αιωρούμενων σωματιδίων, τα οποία αποτελούν τα κύρια δεδομένα εισόδου τους. Το σύστημα SENSE2 είναι η βελτιωμένη έκδοση ενός προϋπάρχοντος συστήματος nowcasting των επιπέδων της ηλιακής ενέργειας που φτάνει στην επιφάνεια της γης, το οποίο παράγει σε πραγματικό χρόνο εκτιμήσεις της GHI στην επιφάνεια χρησιμοποιώντας δεδομένα από δορυφόρους και μοντέλα, σε υψηλή χωρική και χρονική ανάλυση (~5 km, 15 min) με περιοχή κάλυψης την Ευρώπη, τη Βόρεια Αφρική και τη Μέση Ανατολή. Οι βελτιώσεις που έγιναν στο σύστημα SENSE2 στα πλαίσια της παρούσας διατριβής αφορά στον τρόπο υπολογισμού της GHI και το πως λαμβάνει υπόψιν το μοντέλο τα σύννεφα και τα αιωρούμενα σωματίδια. Έγινε αξιολόγηση του βελτιωμένου συστήματος SENSE2 χρησιμοποιώντας επίγειες μετρήσεις από 10 σταθμούς για 1 χρόνο (2017). Διερευνήθηκαν επίσης τα μειονεκτήματα και οι περιορισμοί στην αξιολόγηση τέτοιων μοντέλων με επίγειες μετρήσεις λόγω της επίδρασης των νεφών. Σύμφωνα με τα αποτελέσματα των συγκρίσεων στιγμιαίων τιμών (χρονική κλίμακα 15 min) οι διαφορές των εκτιμώμενων τιμών της GHI σε σχέση με τις επίγειες μετρήσεις είναι εντός του ±50 W m^{-2} (ή ±10%) για το 61% των περιπτώσεων, αφού εφαρμόστηκαν οι βελτιώσεις στο νέο μοντέλο και μια προτεινόμενη διόρθωση συστηματικών σφαλμάτων. Το μέσο σφάλμα της εκτιμώμενης GHI βρέθηκε μεταξύ -12 με 23 W m^{-2} (ή από -2% με 6.1%) για τους 10 σταθμούς, με μέση τιμή 11.3 W m^{-2} (2.3%) για όλους του σταθμούς. Δείχθηκε ότι ο κύριος λόγος υπερεκτίμησης της GHI από το SENSE2 οφείλεται σε αβεβαιότητες που σχετίζονται τη νεφοκάλυψη εντός του εικονοστοιχείου (pixel) του δορυφόρου, ενώ η σχετικά μικρή υποεκτίμηση της GHI υπό ανέφελο ουρανό οφείλεται στις προγνώσεις των τιμών του AOD (από το μοντέλο του CAMS). Στις συγκρίσεις στιγμιαίων τιμών, οι μεγαλύτερες αποκλίσεις βρέθηκαν όταν υπήρχαν νέφη και όταν αυτά έκρυβαν τον ήλιο σε σχέση με τον επίγειο σταθμό, δείχνοντας ότι οι αποκλίσεις που βρέθηκαν για το μοντέλο συνδέονται περισσότερο με τους περιορισμούς που εισάγονται όταν συγκρίνονται επίγειες μετρήσεις με δορυφορικά προϊόντα, παρά με την καθαυτή επίδοση του μοντέλου. Αξιολογήθηκε επίσης το σύστημα βραχυπρόθεσμης πρόγνωσης (με ορίζοντα πρόγνωσης 3 h) των επιπέδων της ηλιακής ενέργειας NextSENSE2 το οποίο βασίζεται στη μέθοδο υπολογισμού διανυσμάτων της κίνησης των νεφών (cloud motion vector technique). Για μια πιο αντικειμενική αξιολόγηση του μοντέλου, συγκρίθηκε επίσης με τη μέθοδο πρόγνωσης «persistence», στην οποία οι συνθήκες νεφοκάλυψης θεωρούνται ίδιες για όλες τις μελλοντικές χρονικές στιγμές του ορίζοντα πρόγνωσης, και βρέθηκε ότι το NextSENSE2 υπερτερεί ειδικά σε περιόδους με αυξημένη νεφοκάλυψη και εναλλαγές στη νεφοκάλυψη.

Λέξεις κλειδιά: ηλιακή ακτινοβολία, αερολύματα, σύννεφα, πρόγνωση ηλιακής ακτινοβολίας, μοντέλο διάδοσης ακτινοβολίας

List of Abbreviations

AE	**A**ngstrom **E**xponent
AERONET	**AE**rosol **R**obotic **NET**work
AOD	**A**erosol **O**ptical **D**epth
BOA	**b**ottom **o**f the **a**tmosphere
BSRN	**B**aseline **S**urface **R**adiation **N**etwork
CALIPSO	**C**loud-**A**erosol **L**idar and **I**nfrared **P**athfinder **S**atellite
CAMS	**C**opernicus **A**tmospheric **M**onitoring **S**ervice
CMF	**C**loud **M**odification **F**actor
CMV	**C**loud **M**otion **V**ector
COT	**C**loud **O**ptical **T**hickness
CSPs	**C**oncentrating **S**olar **P**ower systems
DB	**D**ata**b**ase
DI	**D**irect **I**rradiance
DNI	**D**irect **N**ormal **I**rradiance or Irradiation
DOD	**D**ust **O**ptical **D**epth
DREs	**D**irect **R**adiative **E**ffects
DSSI	**D**ownwelling **S**urface **S**olar **I**rradiance
DU SSA	**D**ust **S**ingle **S**cattering **A**lbedo
ECMWF	**E**uropean **C**entre for **M**edium-Range **W**eather **F**orecasts
EO	**E**arth **O**bservation
IR	**I**nfra**r**ed
GI	**G**lobal **I**rradiance
GHI	**G**lobal **H**orizontal **I**rradiance or Irradiation
LibRadtran	**Lib**rary of **Rad**iative **tran**sfer
LUT	**l**ook **u**p **t**able
MACv2	**M**ax-Planck **A**erosol **C**limatology **v**ersion **2**
MIDAS	**M**od**I**s **D**ust **A**ero**S**ol
MMA	**M**ajor **M**etropolitan **A**rea
MODIS	**MOD**erate resolution **I**maging **S**pectroradiometer
MSG	**M**eteosat **S**econd **G**eneration
NIR	**N**ear **I**nf**r**ared
NWC SAF	**S**atellite **A**pplication **F**acilities of **N**o**wc**asting and Very Short-Range Forecasting
OMI	**O**zone **M**onitoring **I**nstrument
PM	**P**articulate **M**atter
PV	**P**hoto**v**oltaic
RTM	**R**adiative **t**ransfer **m**odel
SZA	**S**olar **Z**enith **A**ngle
SSA	**S**ingle **S**cattering **A**lbedo
SW	**S**hort**w**ave
TCWV	**T**otal **C**olumn **W**ater **V**apor
TOA	**T**op **O**f the **A**tmosphere
TOC	**T**otal **O**zone **C**olumn
TOMS	**T**otal **O**zone **M**apping **S**pectrometer
UN	**U**nited **N**ations
UV	**U**ltra**V**iolet
UVA	**U**ltra**V**iolet-A
UVB	**U**ltra**V**iolet-B
VIS	**Vis**ible

Contents

1 Introduction

Aerosols and clouds are the key atmospheric factors that determine the solar radiation field inside the earth – atmosphere system, with great implications in earth's climate and the solar energy sector of renewables. Aerosols have both natural and anthropogenic origin with several open scientific questions regarding their trends for assessing aerosol sources' changes over time. Their presence in the lower part of the atmosphere is harmful for human health. Cities are main sources of anthropogenic aerosols, making imperative the need for emissions regulations to minimize their health's effect. However, the earth's population tends to be concentrated in large urban centers, which increases the energy demand with great environmental implications, with renewables being the sustainable way for their mitigation. The interaction between solar radiation with clouds and aerosol particles has not yet been fully understood and much scientific research has been focused on this area. According to Fifth Assessment Report of IPCC (Boucher et al., 2013), the largest uncertainty to estimates and interpretations of Earth's changing energy budget is contributed by clouds and aerosols. Aerosol optical properties control the sign of the Earth's radiative budget by cooling or heating the atmosphere. Continuous monitoring of aerosol properties from ground and space, and studies of aerosols radiative effects aim to reduce those uncertainties. The continuously growing solar renewable energy sector needs accurate solar resource for optimal planning and deployment. Accurate cloud and aerosol datasets and their interactions with solar radiation are essential for estimating solar energy on earth's surface. In addition, solar radiation/energy forecasting techniques depend on the level of accuracy of predicting cloud motion on various spatial resolutions.

Since 2018, about 55% of the world's population has been living in urban areas and the current projections suggest that this percentage will rise to 60% by 2030 and to 70% by 2050 (UN, 2019b). Consequently, the population growth will impose difficulties in implementing the United Nations (UN) Agenda for Sustainable Development Goals (SDGs), including SDG 11 related to "making cities and human settlements inclusive, safe, resilient and sustainable". Megacities are defined as cities with more than 10 million inhabitants. According to UN (2018a), there are 33 megacities worldwide and this number is expected to increase to 43 in 2030. Even though ~ 7% of the global population in 2018 resides in those megacities (UN, 2018a), their continuous increase both in size and number bring them in the spotlight, as they will accommodate an increased share of the world's population (projected to ~ 10% by 2030). This population growth of cities, and especially those with more than 5 million inhabitants, raises urgent and critical environmental issues, like air quality (WHO, 2021). The worst pollutant affecting megacities is suspended particulate matter or aerosols. This is of particular concern, as high levels of aerosols are known to be related to increased morbidity and mortality rates, and in many of the megacities in developing countries healthcare for acute cases is less proficient than in

developed countries. Particularly, in 2019, cities' air pollution constituted the 4th leading risk factor for early death at a global scale (HEI, 2020).

Many countries worldwide have enforced policies in recent decades to reduce anthropogenic aerosol emissions in urban areas towards mitigating the aerosol adverse health effects. These policies include the transition of thermal engines technologies to hybrid and pure electric technologies, pollution fees on big industries and schemes for air quality control. The exact policies and the level of implementation largely differ between countries, but it is the main cause of decrease in aerosol concentration in some megacities. WHA69 (WHO, 2016) set a global roadmap and targets for reduction of air pollution related deaths, urban air quality and clean energy. In the United States (US), the first regulations were legislated in 1970, and Environmental Protection Agency (EPA) reported a drop of ~40% in aerosol related air pollution in major US cities in the last half century (DeMocker, 2003). In the European Union (EU) countries, a decrease of ~29% in aerosols has been reported since 1970 as a result of policy measures and technological improvements (Turnock et al., 2016). In South and Central American countries, a poor emission control has been reported, resulting in 150 million people living in urban areas with poor air quality (UNEP, 2016). Jin et al. (2016) summarized the policies and their implementation over the last three decades for China, and consequently China's anthropogenic emissions markedly declined in the last decade (Zheng et al., 2018). In 2019, India launched the National Clean Air Programme, with the objective to reduce in 2024 the particulate air pollution by 20% to 30% with respect to 2017 levels, in 122 cities (Ganguly et al., 2020). The regulations for air pollution for many African cities are weak or non-existent (Abera et al., 2020), which will be challenging for their future air quality, since many African cities have an unprecedented population growth. So, it is of vital importance to understand the trends of aerosol loads and their spatial variability over those great population agglomerations, this way assessing the effectiveness of air pollution emission regulations. Additionally, quantifying aerosol regime over cities is important for the solar renewable systems, of large or rooftop scale. In Chapter 4 the aerosol spatial and temporal variability over the greatest cities of the world is investigated using spaceborne data and possible links of the latter with changes in cities' population.

Aerosols are among the main climate change drivers and estimates of changes in their radiative effects are highly significant for climate-change-related policy making as they are linked to changes in surface temperature (IPCC, 2013). Nevertheless, estimates of the total anthropogenic radiative forcing are still highly uncertain (Chen, 2021). Several reasons contribute to these not yet well-constrained estimates, such as the heterogeneity of the processes governing aerosols' production and removal, which in turn regulate optical and microphysical properties, both determining the associated aerosol–radiation interactions. Focusing on Earth's surface, apart from the importance of aerosols on climate, studies quantifying the impact of total aerosols (natural and anthropogenic) on incoming solar

irradiance are also essential for other societal benefit areas such as the energy sector (e.g., Dumka et al., 2021; Juliano et al., 2022; Kosmopoulos et al., 2018). Towards the reduction of greenhouse gas emissions and climate change mitigation, the deployment of renewable energy technologies is one of the main pillars (Edenhofer et al., 2011; IPCC, 2022), while at the same time renewable energy technologies provide energy in a sustainable manner. Diverse renewable-energy technologies are being investigated worldwide, and their deployment has been increasing, with solar energy markets growing rapidly, such that they could become the major source of energy supplies in the coming decades (Arvizu et al., 2011; IEA, 2022). For electricity production, the systems in use are the photovoltaic (PV) cells and the concentrating solar power (CSP) plants, which harness different components of the solar irradiance: the global horizontal irradiance and the direct normal irradiance, respectively (Kato, 2016; Sengupta et al., 2021). Within the North Africa, Middle East, and Europe (NAMEE) domain, International Energy Agency (IEA) projections up to 2025 indicate a continuous growth in solar PV capacity, while some countries (e.g., Morocco) are increasing their CSP capacity (IEA, 2020).

The Mediterranean Basin, located at the crossroads of air masses from all over the globe (Lelieveld et al., 2002), experiences high aerosol concentrations of both natural and anthropogenic origin, and the aerosol spatiotemporal variability over the area has been investigated in several studies (e.g., Basart et al., 2012; Hatzianastassiou et al., 2009; Nabat et al., 2013; Papadimas et al., 2008). In addition, due to its proximity to the Earth's most active dust sources located across the Sahara Desert and Middle East deserts, the Mediterranean Basin often experiences high dust aerosol loads (dust intrusions). Several studies have investigated the Saharan dust transport towards the Mediterranean Basin by exploiting, either solely or combined, in situ measurements, remote sensing (ground-based or satellite) retrievals and atmospheric dust numerical products (e.g., Engelstaedter et al., 2006; Nastos, 2012). Across the Mediterranean Sea, dust concentrations fade down from south to north because of the removal of mineral particles from the atmosphere, either due to dry or wet deposition (Moulin et al., 1998). It should be noted that long-range transport of Saharan mineral particles has also been recorded over northern Europe (Bégue et al., 2012; Papayannis et al., 2008). Additionally, there is a distinct seasonal cycle of the longitudinal spatial distribution of dust with higher concentrations in spring at the eastern and central Mediterranean and in summer at the western Mediterranean (Georgoulias et al., 2016; Gkikas et al., 2013; Moulin et al., 1998). The seasonal patterns are related to the seasonality of the prevailing meteorological conditions over the area (Gkikas et al., 2015; Moulin et al., 1998). This intricate aerosol regime along with the increased capacity of solar energy systems in the surrounding countries, makes the Mediterranean Basin one of the most interesting areas for investigating the aerosol and dust radiative effects.

Over most of the globe, the availability of downwelling surface solar irradiance depends mainly on attenuation by clouds, but the role of aerosols is also significant and under certain conditions can be dominant (e.g., Fountoulakis et al., 2021; Neher et al., 2019). The countries around the Mediterranean Basin, apart from their prolonged sunshine durations, also experience high levels of aerosol loads, mainly composed of mineral particles. For the southern part of the domain, due to the rare cloudy conditions, aerosols and specifically desert dust constitute the most common source of DSSI attenuation, as was demonstrated in a study for Egypt by Kosmopoulos et al. (2018). It must be pointed out here that even for southern Europe, dust can substantially reduce surface solar radiation during dust intrusions (Kosmopoulos et al., 2017). Thus, studying the radiative effects of dust is of great interest for the broader Mediterranean Basin. Existing studies are limited to specific locations or dust event days (e.g., Fountoulakis et al., 2021; Kosmopoulos et al., 2017, 2018). An extensive analysis of the total aerosol and dust radiative effects for the broader Mediterranean basin over a 15-year period was conducted, using both spaceborne and reanalysis model aerosol data and additional climatological datasets and the results are presented in Chapter 5.

Since solar energy resources are strongly affected by atmospheric conditions, they are highly variable spatially and temporally. From rooftop installations to large solar power plants, reliable information about solar resources is needed. Ground-based measurements of surface solar radiation are only available for a few locations (due to the operation's cost and maintenance), with possible gaps in time. Hence modeled data are necessary throughout all the various stages of a project development, while due to the routine operations and management forecast data are also needed (Sengupta et al., 2021). Existing climatological datasets are needed for solar energy potential assessments for planning of future solar installations which is important for financial investors. Estimates of solar radiation in real time are important for power plant installations successful deployment and management. Short term solar energy forecasting of up to 6 h ahead concerns utility companies and energy suppliers, since it supports integration of produced energy into the grid and solar energy trading. Therefore, there is a need for operational nowcasting and short-term solar forecasting for real-time energy production, to better integrate solar energy exploitation technologies with national and international power systems. Under all skies, the availability of solar resources is primarily affected by clouds (e.g., Fountoulakis et al., 2021); for clear-sky conditions, it depends on the atmospheric composition, with the most important variables being aerosols (e.g., Fountoulakis et al., 2021) and water vapor (e.g., Yu et al., 2021). Among those variables, clouds and aerosols are characterized by large temporal and spatial variability, making them key variables for solar energy applications. Hence, to increase the accuracy of nowcasting and forecasting tools, it is imperative to understand spatiotemporal variability of cloud and aerosol properties when implementing the tools.

Continuously improved earth observation (EO) data (satellite-based and atmospheric models) are exploited to produce accurate estimates of spectral surface solar radiation in real time (nowcasting), which has numerous applications in different fields aside from the solar energy sector (e.g., Kosmopoulos et al., 2018; Qu et al., 2014; Thomas et al., 2016), like human health (e.g., P. G. Kosmopoulos et al., 2021; Schenzinger et al., 2023). Due to their large area coverage and high temporal resolution, geostationary satellite data are used to produce estimates of surface solar radiation both in real time as an operational service and to generate historical archives based on long-term satellite measurements. Several methods exist for obtaining satellite estimates of surface solar irradiance (an overview in Sengupta et al. (2021)). The continued developments and improvements in satellite estimates of surface solar radiation made since the 1980s resulted in accurate real-time as well as climatological datasets (Habte et al., 2017; Pfeifroth et al., 2023b; Qu et al., 2014, 2017; Schroedter-Homscheidt et al., 2022; Sengupta et al., 2018; Urraca et al., 2017), although certain sources of biases and common factors that increase the uncertainty have been reported: an increase in the distance from the subsatellite point and more frequent occurrences of clouds (especially fragmented cloud cover), complex terrain, and bright surfaces (snow, desert). In addition, it is a challenge per se and increases the evaluation uncertainties when any model is validated at an instantaneous timescale. Gridded satellite estimates with ground-based point measurements of surface solar radiation differ not only due to model uncertainties but also due to the different spatiotemporal scales involved (satellite pixels represent a large area and large time intervals of a few minutes; ground-based measurements represent the area exactly over the station for smaller time intervals).

Motivated by the recent advances in satellite-based retrievals of surface solar radiation and building upon the knowledge of already-existing and well-established methodologies, an upgrade has been performed to an existing service that provides satellite estimates of surface solar radiation in real time. The aim is for the improved nowcasting system to be the basis of the new forecasting system. The Solar Energy Nowcasting System (SENSE) was developed under the EU project Geo Cradle by the Beyond Centre of EO Research and Satellite Remote Sensing at the National Observatory of Athens, Greece, in collaboration with the Physical and Meteorological Observatory at Davos of the World Radiation Center, Switzerland (Kosmopoulos et al., 2018). It is a combination of geophysical input parameters from satellite-based and model data sources and a neural network (NN) technique trained on precalculated surface solar radiation simulations (look-up table – LUT) using a radiative transfer model (RTM). It uses the cloud optical thickness (COT) retrievals produced by the Application Facilities Support to Nowcasting and Very Short Range Forecasting (NWC-SAF) algorithm based on Meteosat Second Generation (MSG) satellite data and aerosol optical depth (AOD) forecasts from the Copernicus Atmospheric Monitoring Service (CAMS) as inputs to the NN to derive the surface solar radiation in real time. More details about the previous version of the SENSE service can be found in

Kosmopoulos et al. (2018). In the same publication, the validation of this method showed good agreement on daily and monthly levels; however, various sources of uncertainties have been identified mainly concerning the use of the NN (especially under high irradiance values), the COT input, and the structure and density of atmospheric parameters in the LUTs. At Chapter 6 of the thesis the development of the new version of the model, called SENSE2, is presented and validated against ground-based measurements, investigating the role of clouds and aerosols in the nowcasting. The reason for the development of the new version of the model was to minimize the identified uncertainties of the previous version of the model, before using this model for the new forecasting system. For the new version, it was decided that the fully physical approach of the model, which benefits from cloud optical property monitoring by the MSG satellites and recent advances in EO, would be retained, while the scheme that replaces the direct radiative transfer calculations was improved.

In operational solar energy forecasting several different methods are used (Sengupta et al., 2021; Yang et al., 2022), which are categorized with the forecasting time horizon (few seconds to few days) and the exogenous data i.e., sky cameras, satellite data and numerical weather predictions. The cloud motion vector (CMV) technique is commonly used on satellite data for solar forecasting a few hours (up to 6 h) ahead. The CMVs are calculated using consecutive satellite images and, assuming a constant cloud speed, the future cloud positions are derived by applying the CMV field to the latest cloud image. The use of CMVs for short-term forecasting of surface solar radiation based on satellite data started almost 20 years ago (Hammer et al., 1999, 2003; Lorenz et al., 2004). In the last decade, interest in using optical flow techniques from the computer vision community in satellite images for cloud motion estimation in the context of solar forecasting has increased. One of the first works was by (Urbich et al., 2018), who used two optical flow methods for the European domain and compared them when they were used to forecast MSG-satellite-derived effective cloud albedo. When combined with SPECMAGIC NOW, those forecasted values of effective cloud albedo deliver short-term forecasts of surface solar irradiance (SESORA – seamless solar radiation; Urbich et al., 2019). Kallio-Myers et al. (2020) used an optical flow method on SEVIRI-based images of effective cloud albedo to forecast global horizontal irradiance up to 4 h ahead with 15 min time resolution for southern Finland by applying the Heliosat method to the forecasted effective cloud albedo maps in combination with the Pvlib Solis clear-sky model (the Solis–Heliosat forecasting model). In the same study, they also found that their forecasting model mostly outperforms persistence, especially under changes in cloudiness. It is a common practice to benchmark forecasts of surface solar radiation with the persistence approach (e.g., Garniwa et al., 2023; Kallio-Myers et al., 2020), a method that assumes constant cloudy conditions for future time steps.

The NextSENSE system was first introduced in a study by Kosmopoulos et al. (2020) as a novel short-term solar energy forecasting system (3 h ahead; every 15 min) based on forecasts of satellite-derived COT using a CMV technique, with solar irradiance estimated by the SENSE model. The NextSENSE system was developed as a continuation of SENSE during the EU project e-shape and by the same research groups previously mentioned. The CMV technique that is employed is based on state-of-the-art image-processing technologies (dense optical flow). The evaluation of the CMV forecasts was performed by Kosmopoulos et al. (2020) for selected test days with different cloud movement patterns against the real MSG COT and in terms of irradiance estimates using both forecasted and real COT. They found that the deviations of forecasted irradiances compared with nowcasting outputs ranged from 18% to 34% under changing cloudy conditions, outperforming the persistence method for certain conditions. In the last chapter (Chapter 6) of the thesis the validation of the NextSENSE model for 1 full year of irradiance forecasts with ground-based measurements is presented, to obtain more robust conclusions. Additionally, as NextSENSE is based on the same hierarchy of SENSE with only the CMV analysis added, all improvements to SENSE2 are inherited by the new NextSENSE2 system too.

2 Theory

2.1 Solar radiation

The definition of basic radiometric quantities precedes, necessary for the proper description of the radiation, whether solar or another. These radiometric quantities can be defined at any wavelength λ (spectral quantities) or can be used for the whole spectrum (total quantities).

The monochromatic intensity I(λ) (or radiance in W m^{-2} sr^{-1} nm^{-1}) is defined as:

$$I(\lambda) = \frac{dE(\lambda)}{\cos\theta \, d\Omega \, d\lambda \, dt \, dA} \qquad (2.1)$$

where dE(λ) is the differential amount of radiant energy, in a time interval dt and in specific wavelength interval λ to λ+dλ, which crosses which crosses an element of area dA, in directions confined in a differential solid angle dΩ, which is oriented at an angle θ to the normal of dA (Fig. 2.1).

The monochromatic irradiance F(λ) (in W m^{-2} nm^{-1}) is defined by integrating the normal component of I(λ) over the entire hemispheric solid angle:

$$F(\lambda) = \int_0^{2\pi} \int_0^{\pi/2} I(\lambda, \theta, \varphi) \cos\theta \sin\theta \, d\theta \, d\varphi \qquad (2.2)$$

The total irradiance F (in W m^{-2}) is the monochromatic irradiance integrated over the whole spectrum of the solar radiation. The irradiation H is the energy received per unit area during a time interval expressed in J m^{-2}, and it can be calculated by integrating the total irradiance F for a given duration Δt.

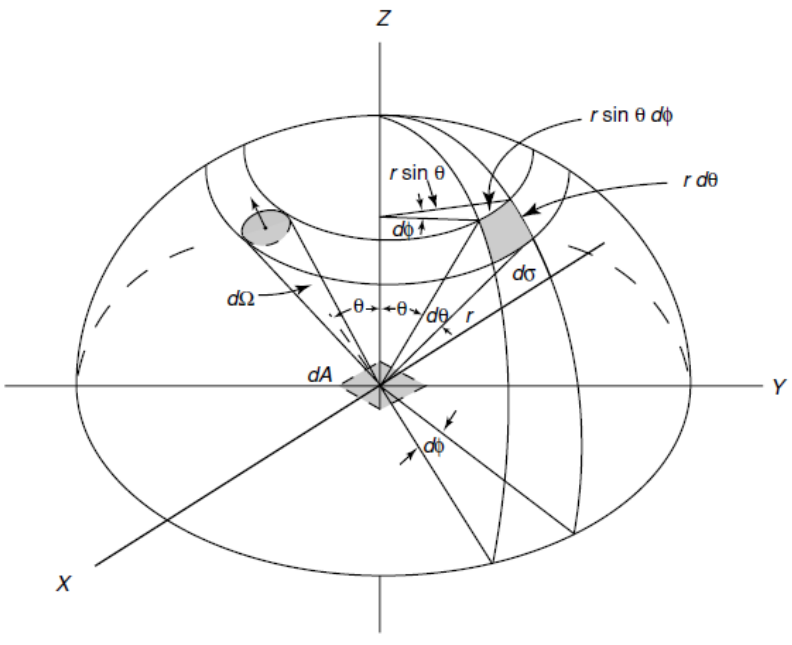

Figure 2.1 Differential solid angle dΩ and its representation in polar coordinates (Liou, 2002).

The primary natural source of energy on Earth is the sun, which radiates energy in the form of electromagnetic radiation. The spectral distribution solar radiation emitted by the sun and received by a surface at the top of the Earth's atmosphere is depicted in Fig. 2.2, known as the extraterrestrial radiation. The dotted line is the theoretical emission of a blackbody with sun's temperature (surface temperature around 5800K) according to Planck's law. Sun radiates over a spectral range between 200nm and 4000nm and exhibits a marked peak around 500nm. Almost 50% of the emitted power lies in the visible spectrum, ~8% in the ultraviolet (UV) and the rest in the near and middle infrared. The amount of solar radiation at the top of the atmosphere (TOA) varies mainly due to changes in the position of the Earth relative to the sun (and variations in the solar activity to a lesser extent).

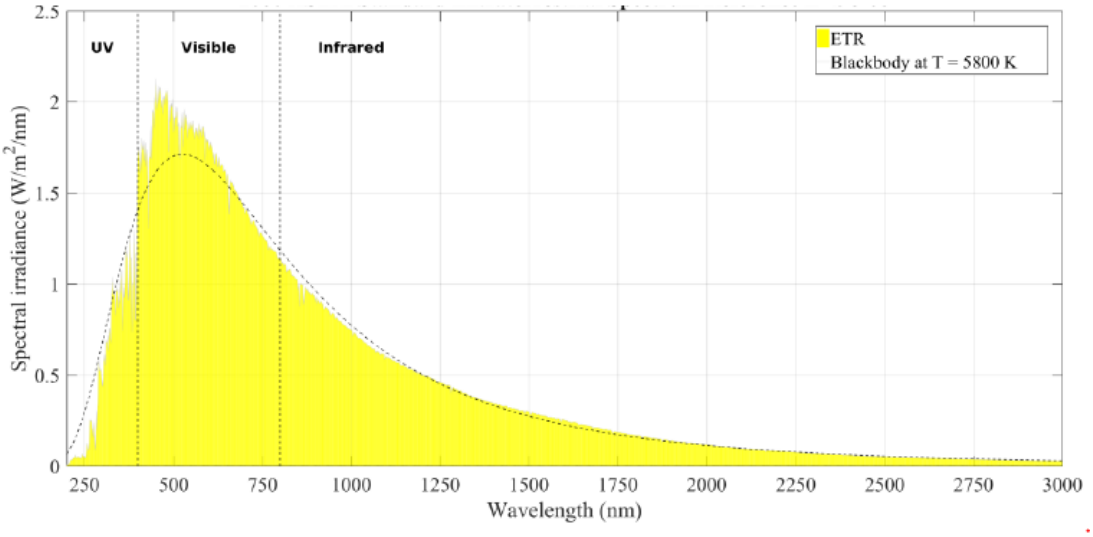

Figure 2.2 Reference extraterrestrial spectrum (ETS) by ASTM Standard E490-19 (yellow area) and spectral distribution the emission of a blackbody with T=5800 K using Planck's law (Figure from Sengupta et al. (2021), given by Philippe Blanc, MINES ParisTech/ARMINE).

Only a part of the extraterrestrial radiation reaches the Earth's surface, about 70-80% in case of a cloudless sky (or clear sky) and this proportion decreases in the presence of clouds. This proportion also decreases with increasing concentrations of aerosols, water vapor and other trace gases. The rest is attenuated (mainly absorbed or backscattered to space) and modified by the atmospheric constituents in its downward path to the ground. Radiative transfer theory describes the interactions between radiation and the medium it passes through. Radiative transfer in the atmosphere has to do with the interactions between solar radiation and the constituents of the atmosphere, where absorption and scattering are the main optical phenomena that are taking place. Both scattering and absorption remove energy from a beam of light, which is attenuated, and this attenuation is called extinction.

Absorption is the physical phenomenon that takes place in the atmosphere, where the radiant energy absorbed by the atmospheric constituents is converted into another form of energy. Inside the earth's atmosphere attenuation by absorption happens due to atmospheric gases and aerosols. Figure 2.3 reflects the absorption by gases at different wavelengths of the solar spectrum, by depicting the

fraction of the flux transmitted to the ground for a moderately dry and clean atmosphere without aerosols. At wavelengths less than 280 nm solar radiation is absorbed by the ozone (O_3) layer in the stratosphere, as well as by tropospheric ozone resulted by human activities. In the lower stratosphere and in troposphere other gases absorb solar radiation such as dioxygen (O_2), nitrogen oxides (NOx), water vapor (H_2O), carbon dioxide (CO_2), methane (CH_4) and other gases. The water vapor strongly absorbs radiation resulting in wide and deep absorption lines.

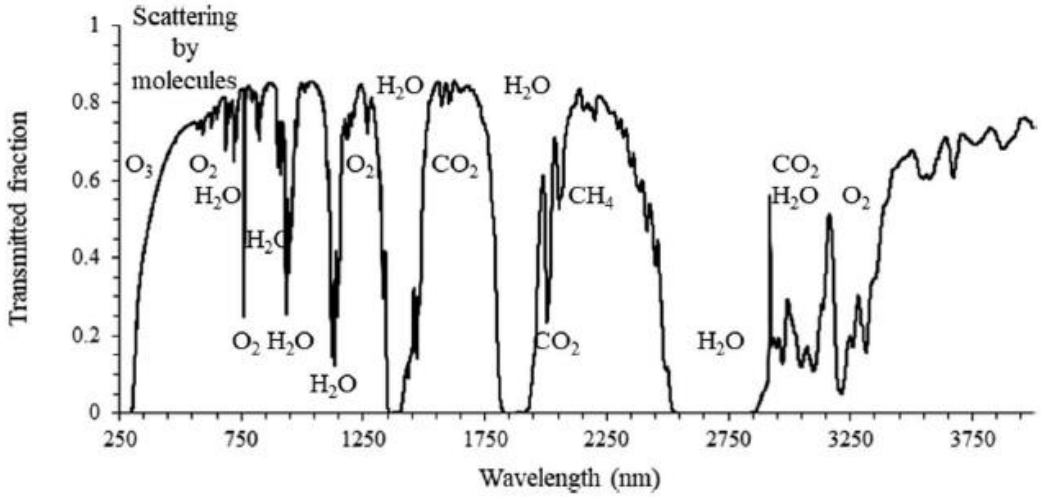

Figure 2.3 Spectral distribution of the ratio between the fluxes received on the ground and at the top of the atmosphere (fraction of solar flux transmitted by the atmosphere), from 250 to 4000 nm, for a moderately dry and clean atmosphere without aerosols (Wald, 2021).

Scattering is a fundamental physical phenomenon associated with radiation and its interaction with matter. It occurs at all wavelengths with varying intensity. The blue color of the sky, the white clouds, rainbows are a few of the optical phenomena of scattering in the atmosphere. Scattering is the process by which a particle continuously abstracts energy from the incident electromagnetic wave and radiates that energy in all directions (Fig. 2.4). In the atmosphere, the particles responsible for scattering range in size from gas molecules (~10^{-4} μm) to aerosols (~1 μm), water droplets (~10 μm), ice crystals (~100 μm), and large raindrops and hail particles (~1 cm). Size parameter χ is a physical term to infer the effect of particle size on scattering. For a spherical particle, it is defined as the ratio of the particle circumference to the incident wavelength, λ:

$$\chi = \frac{2\pi r}{\lambda} \qquad (2.3)$$

If $\chi << 1$, the scattering is called Rayleigh scattering. A small particle tends to scatter light equally in the forward and backward directions. (Fig. 2.4 (a)). This is the case for molecules in the atmosphere, for wavelengths less than about 700 nm (Fig. 2.3). The blue color of the sky and sky polarization are explained by the scattering of visible light (0.4–0.7 μm) by atmospheric molecules, where blue photons are more scattered than those with longer wavelengths.

When the particle becomes larger, the scattered energy becomes increasingly concentrated in the forward direction with increasingly complex scattering features (Fig. 2.4 (c)). For particles whose sizes are comparable to or larger than the wavelength, $\chi \gtrsim 1$, the scattering is referred as Lorenz–Mie scattering.

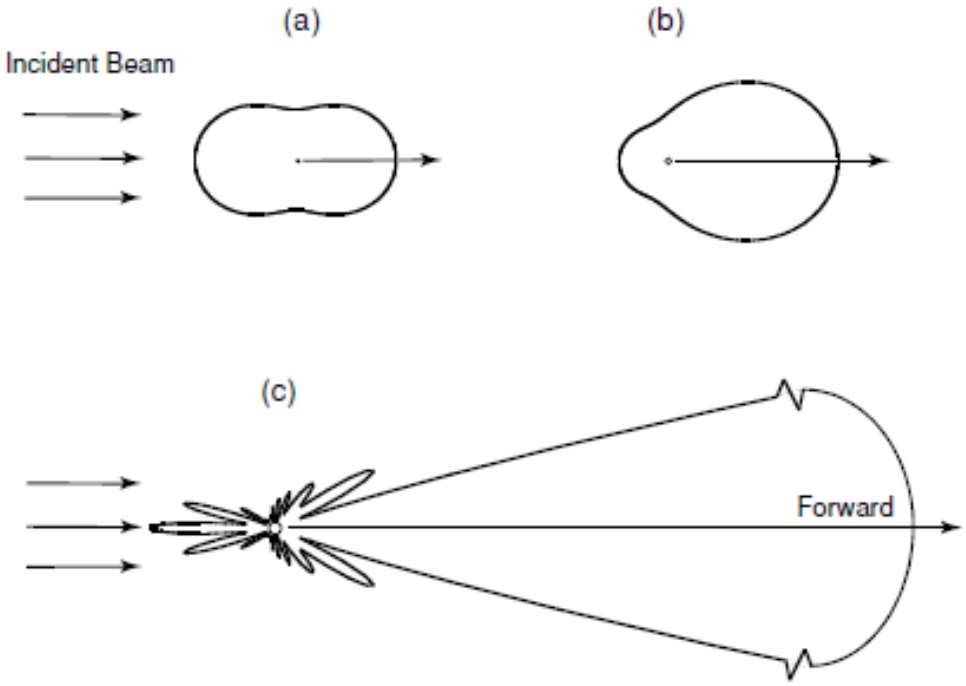

Figure 2.4 The angular distribution of the scattered intensity from spherical aerosols of three sizes illuminated by the visible light of 500 nm: **(a)** 10^{-4} μm, **(b)** 0.1 μm, and **(c)** 1 μm. The forward scattering for the 1μm aerosol is extremely large and is scaled for presentation purposes (Liou, 2002).

The phase function describes the way that a body scatters energy to different directions, namely the scattering pattern. It gives the probability that the energy is scattered in each direction. In the case of isotropic scattering, the energy is scattered equally in all directions. The scattering pattern (and hence the phase function) depends on the nature of the scatterer, its shape, size, and surface properties and on the wavelength.

Aerosols absorb but especially scatter solar radiation, with a strong dependence on the wavelength and aerosol type, for more details see Section 2.2. Clouds mainly scatter solar radiation, with negligible wavelength dependence. They are the main attenuators of the solar radiation reaching the earth's surface, with optical thick clouds backscatter most of the solar radiation back to space, resulting in significant attenuation of the radiation field at the ground. More details about clouds and their radiative effects in Sections 2.3.

The solar radiation intensity I(λ) traversing the atmosphere is attenuated by its interaction with the atmospheric components (Fig. 2.5), hence:

$$dI(\lambda) = -k(\lambda)\rho\, I(\lambda)\, ds \qquad (2.4)$$

where ds is the thickness of the medium in the direction of propagation, ρ is the density of the material and k(λ) is the mass extinction cross section ($cm^2\ g^{-1}$) for radiation at wavelength λ, due to absorption and scattering by the material. If $I_0(\lambda)$ is the incident intensity at s=0, by integration the emergent intensity at distance s (Fig. 2.5) can be obtained by the following formula assuming that k(λ) is independent of the distance s (homogeneous medium):

$$I_{s_1}(\lambda) = I_0(\lambda) \exp(-k(\lambda)\, u) \qquad (2.5)$$

where $u = \int_0^{s_1} \rho\, ds$ is defined as the path length. Equation 2.5 is known as Beer's law, or Bouguer's law or Lambert's law (sometimes referred as Beer-Bouguer-Lambert law (Liou, 2002)).

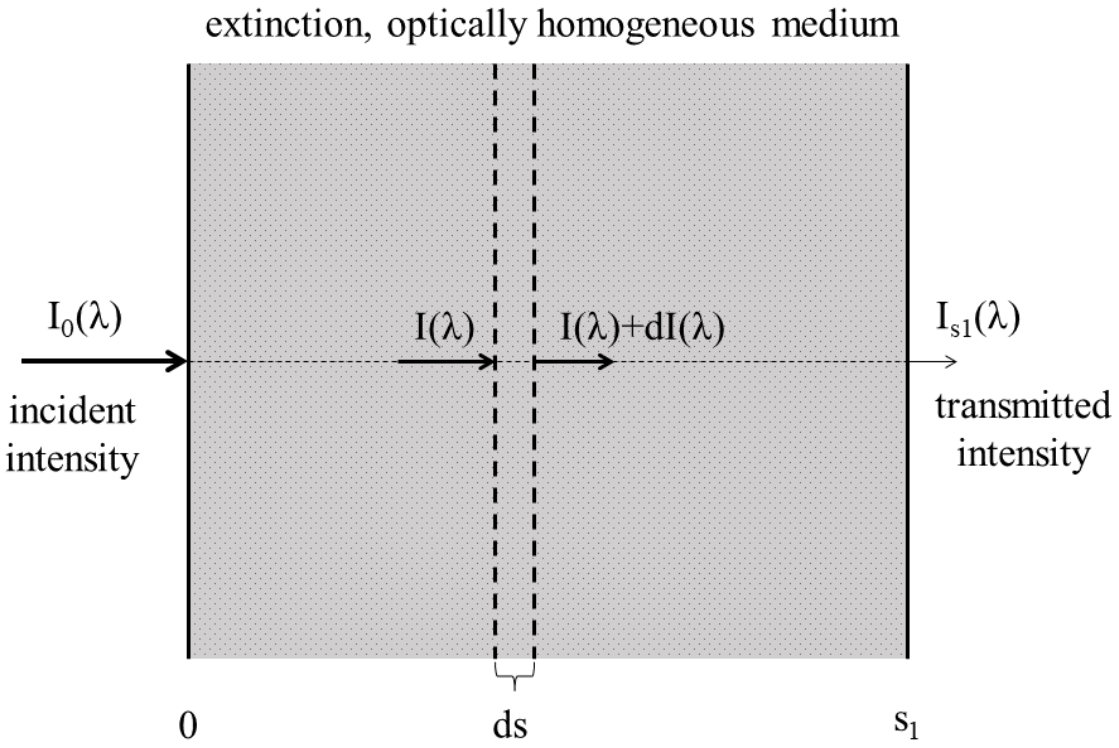

Figure 2.5 Depletion of the intensity through an extinction medium (Adopted by Liou (2002)).

A part of the solar radiation that finally will reach the ground is reflected by the Earth's surface, part of which is backscattered toward the ground and so on. The reflection by the ground depends on the surface properties, the wavelength of incident radiation as well as the angle of incidence. Surface albedo is the quantity that describes how the sun rays are reflected by the ground, which spectrally varies.

The solar irradiance (total or spectral) received on the ground by a horizontal surface has two components, a direct and a diffuse (Fig. 2.6). Global horizontal irradiance (GHI) is the sum of these

components. The direct component is the radiation directly emitted by the sun, while the diffuse component comes from every direction and is the result of interaction of solar radiation with the atmospheric constituents. If the horizontal plane is surrounded in certain directions by reliefs, the reflected component by the ground should also be considered to the sum. Finally, the direct component at normal incidence is called direct normal irradiance (DNI) calculated by the following formula:

$$\mathrm{DNI} = \frac{\mathrm{Direct}}{\cos(SZA)} \qquad (2.6)$$

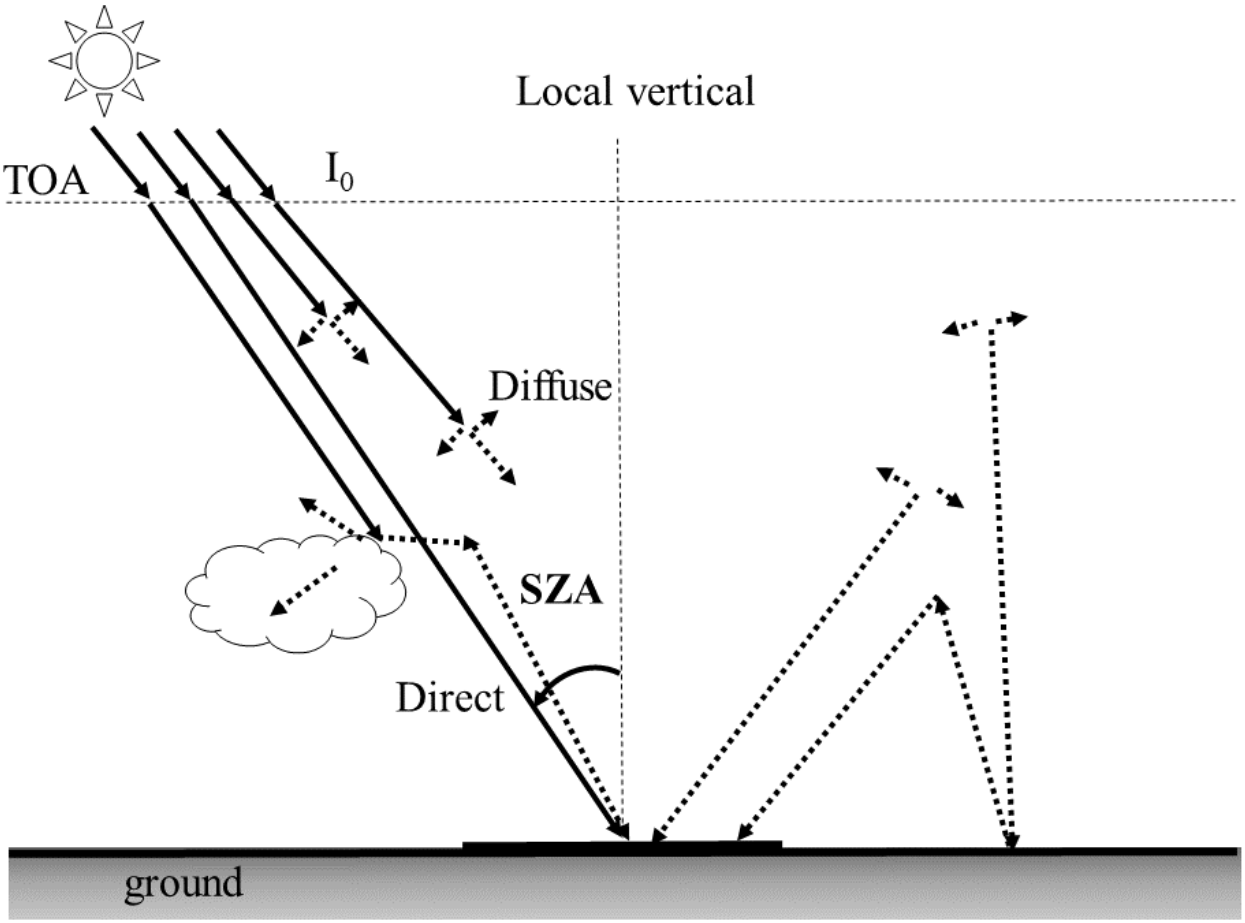

Figure 2.6 Schematic representation of the direct and diffuse components of the solar irradiance received on a horizontal surface. SZA is solar zenith angle.

The relative geometry between the direction of the sun and an observer on the ground plays a major role in determining the amount of solar radiation at the earth's surface. The apparent position of the sun varies with the time and the geographic location, and it can be determined by the solar zenith angle (SZA) and solar azimuth (Fig. 2.7). SZA is the angle formed by the direction of the sun and the local vertical. The solar azimuth is the angle formed by the projection of the direction of the sun on the horizontal plane and the north and it increases clockwise.

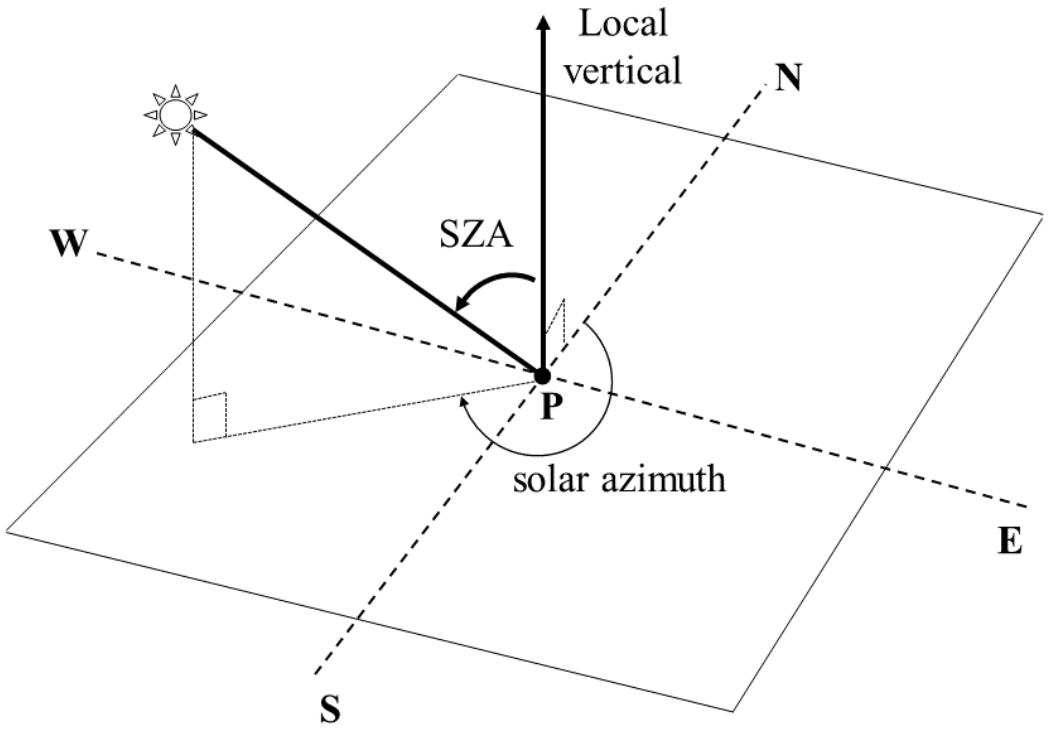

Figure 2.7 Solar angles (solar zenith angle -SZA and solar azimuth) describing the apparent course of the sun in the sky for an observer located at P in the northern hemisphere.

2.1.1 Measuring solar radiation at the ground

Different instruments measure different solar radiation components, at a given location at a given time. The total global, direct, and diffuse solar irradiance is measured by pyranometers, pyrheliometers and pyranometers with a shadow ring or shadow ball, respectively. Radiation at specific spectral bands (e.g., ultraviolet) can be measured using spectral filters or specific detectors.

The pyranometers are commonly used by meteorological stations and others for measuring total global irradiance. The same principles apply for all pyranometers despite the type of the detector or the measurement spectral window. The detector is at the end of a short tube, which opening is protected by a double dome. The spectral transmission of the domes is the same for all wavelengths and sun positions. The pyranometer receives solar radiation from the upper hemisphere (with a field of view – FOV 360° or 2π steradians), hence providing measurements of global irradiance. This type of radiometer is mounted horizontally to measure GHI, ideally in a location free of natural or artificial obstacles on the horizon. The uncertainties in measuring radiation depend on the instrument. GHI measurement uncertainties for pyranometers in the field range from 3-5% for SZAs between 30° and 60°, assuming regular and high-quality maintenance (Sengupta et al., 2021).

2.2 Aerosols

Particulate Matter (PM) or aerosols are tiny particles suspended in the atmosphere, either in solid phase or liquid phase or both. They have natural or anthropogenic origin, and they arise directly from emissions (primary aerosol) or from the conversion of certain gases to atmospheric aerosols (secondary aerosol) (Seinfeld & Pandis, 2006). Aerosols from natural sources are windborne dust, marine, volcanic, pollen, etc. Anthropogenic aerosols are a significant fraction of tropospheric aerosols, containing sulfate, nitrate, carbonaceous material (black/elemental and organic carbon), etc. Anthropogenic activities that produce atmospheric aerosols are the combustion of fuels, predominantly emitting black carbon (or soot), industrial and agricultural activities, biomass burning, etc. Their size differs from a few nanometers (nm) to tens of micrometers (μm) (Fig. 2.8). Particles are categorized in fine and coarse according to their size (diameter less and greater than 2.5 μm).

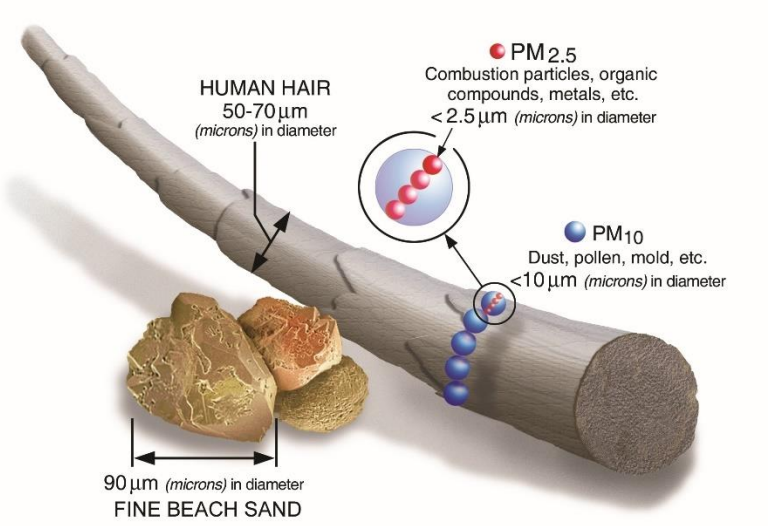

Figure 2.8 Size comparisons for PM particles (Source: https://www.epa.gov/pm-pollution/particulate-matter-pm-basics#PM).

Aerosols absorb and mainly scatter solar radiation, but this is not the same for types of aerosols. For example, soot strongly absorbs compared to surfaces which are more scattering aerosols. The attenuation of solar radiation by aerosols is highly variable and depends on their concentrations and their microphysical properties (size, shape, and chemical composition), all with significant variations in space and time.

One way to quantify aerosol loads inside the atmosphere is through optical terms by using the total column parameter of Aerosol Optical Depth (AOD) which can be derived using remote sensing techniques (see Section 2.4). The AOD(λ) (or $\tau_{aer}(\lambda)$ see Section 2.4) is a total atmospheric column optical property, and it can be expressed in terms of extinction coefficient (β_{ext}) as:

$$\mathrm{AOD}(\lambda) = \int_0^{z_\infty} \beta_{\mathrm{ext}}(\lambda, z)\mathrm{d}z \qquad (2.7)$$

AOD is dimensionless and ranges from 0 (no aerosols) to about 5 (turbid atmosphere). AOD is strongly dependent on the aerosol mass concentration.

The spectral dependence of AOD can be quantified by the Angstrom Exponent (AE) α. An empirical expression has been given by Ångström (1929):

$$\mathrm{AOD}(\lambda) = \beta\,\lambda^{-\alpha} \qquad (2.8)$$

where λ is the wavelength in μm of the corresponding AOD(λ) and β is Angstrom's turbidity coefficient, which describes the general haziness of the atmosphere. Angstrom exponent can be computed by spectral values of AOD:

$$\alpha = -\frac{\mathrm{dln}\mathrm{AOD}(\lambda)}{\mathrm{dln}\lambda} = -\frac{\ln\left(\frac{\mathrm{AOD}(\lambda_2)}{\mathrm{AOD}(\lambda_1)}\right)}{\ln\left(\frac{\lambda_2}{\lambda_1}\right)} \qquad (2.9)$$

The Angstrom exponent α is used as an indicator of the aerosol type (e.g., Eck et al., 1999) and it provides information about the aerosol size. Fine mode particles are associated with large α values (>2.0), and coarse particles have α values close to zero. Assuming that α is known, Equation 2.9 can be used to calculate AOD at any wavelength.

The fraction of the light extinction that is scattered is given by the ratio of scattering to total extinction and it is called single-scattering albedo (SSA), ω.

$$\omega(\lambda) = \frac{\beta_{\mathrm{scat}}(\lambda)}{\beta_{\mathrm{ext}}(\lambda)} = \frac{\beta_{\mathrm{scat}}(\lambda)}{\beta_{\mathrm{scat}}(\lambda) + \beta_{\mathrm{abs}}(\lambda)} \qquad (2.10)$$

Thus, the fraction of the light absorbed is 1-ω. The ω is wavelength dependent and it depends also on the aerosol size distribution and chemical composition. SSA values range from 0 to 1, with high values indicating more scattering aerosols.

Aerosols modulate the radiation field of Earth's atmospheric system with several implications for life on earth. The physical mechanisms through which they influence the radiation budget are manifold. Aerosols interact directly (direct effects) with the shortwave (SW) and longwave (LW) radiation through scattering and absorption. Moreover, through their interactions with clouds, they have semidirect and indirect effects by altering the atmospheric conditions related to cloud formation/dissipation due to absorbing aerosols and by acting as cloud condensation and ice nuclei (altering the microphysical and hence the optical properties of clouds) (e.g., Lohmann & Feichter (2005)). The direct radiative effects of aerosols refer to changes in radiative fluxes due to the direct aerosol-radiation interaction (radiative effects due to aerosol-radiation interactions (REari), as renamed in the IPCC AR5 (Boucher et al., 2013). Cloud-free aerosol direct radiative effects depend on

aerosol optical properties such as the spectrally resolved aerosol extinction coefficient or the integrated AOD, the SSA, the scattering phase function or the integrated asymmetry parameter and other environmental parameters such as surface reflectance and the concentration of atmospheric trace gases (Landi et al., 2021; Loeb et al., 2021; Yu et al., 2006). Their magnitude corresponds to the perturbation of the radiation fields induced by aerosols, within the Earth's atmospheric system, with respect to an atmospheric state without their presence.

Dust particles constitute a major component of atmospheric aerosol load (Textor et al., 2006; Wang et al., 2021). Their emission is primarily wind-driven over the arid or semi-arid regions of the planet. The Sahara Desert in North Africa, the Arabian and the Asian deserts are the major dust sources on Earth, with the highest contribution to global dust load (more than 50%) being emitted from North Africa (Ginoux et al., 2012; Prospero et al., 2002; Tegen & Schepanski, 2009). Even though the dust sources are localized, the spatial distribution of dust over the globe is extensive due to dust mobilization under favorable meteorological conditions. Dust can be transported over long distances with significant implications for the climate of the affected areas and the global climate (Kallos et al., 2006; Prospero, 1996; Varga et al., 2021). In addition to its significant radiative effects, dust also plays a key role in other processes such as the productivity of oceanic waters and terrestrial ecosystems (Jickells et al., 2005) and affects human health (Fussell & Kelly, 2021; Querol et al., 2019; Soleimani et al., 2020). The diameter of dust particles is of the order of 0.5–50 μm and, thus, the Ångström exponent of dust aerosols is smaller than 1 (Shin et al., 2019). Dust particles generally scatter and redistribute rather than absorb solar radiation (SSA > 0.9 at visible wavelengths), although dust absorbs solar radiation at short (i.e., ultraviolet) and long (i.e., infrared) wavelengths more effectively (Di Biagio et al., 2019; Otto et al., 2009; Sicard et al., 2014).

2.3 Clouds

Clouds are large visible masses suspended in the atmosphere, mostly in the troposphere, consisting of water droplets or ice crystals or both. Clouds constitute one of the main attenuators of solar radiation reaching the Earth's surface.

Cloud coverage, their characteristics and optical properties are highly variable with time and geographical location. Cirrus clouds allow a significant amount of radiation to pass through, hence they are optically thin. Optically thick clouds (like cumulonimbus) scatter and reflect radiation strongly in all directions, resulting in noticeable radiation attenuation.

The absorption by clouds is small, but they strongly scatter solar radiation. The attenuation of solar radiation by clouds is described by the optical property of cloud optical thickness (COT). COT can vary from zero to more than 100. COT values depend on the vertical extent of the cloud, its phase and

the size of the water droplets and ices crystals. The size of the cloud scatterers is large compared to solar radiation wavelengths, and under these conditions the scattering is non-selective, which means that the scattering is uniform at all wavelengths, except for those in the infrared. This explains the white or gray color of clouds for an observer on the ground, because all the visible wavelengths are scattered in the same manner.

Another way to quantify the attenuation of solar radiation by clouds is through cloud modification factor (CMF). It is the normalization of the solar radiation received on the surface by the one that would be received without clouds. CMF is dimensionless and it takes values from zero, meaning overcast conditions to 1 which signifies clear sky conditions.

The diffuse component of solar radiation received by a horizontal surface can be increased in the presence of clouds, because clouds backscatter downwards the ground reflected radiation. A special case is the sparse cloudiness with sun visible by an observer on the ground. In this case it is possible to measure on a horizontal surface on the ground irradiance greater than the extraterrestrial one, called cloud enhancement. This is explained by the fact that the direct component of solar radiation is this of the clear sky, but the diffuse component is greater than that of the clear sky due to the multiple scattering by the nearby clouds on the ground receiver.

2.4 Remote Sensing

Remote sensing is the science of inferring information about an object from a distance. There are two techniques of remote sensing. Passive remote sensing exploits the electromagnetic radiation emitted by the sun and the earth itself, after its interaction with earth's atmosphere. In active remote sensing, an artificial source of radiation is used instead, and the backscattered radiation is detected.

The passive remote sensing of aerosols (and other atmospheric constituents) from ground-based radiometers uses the direct component of solar radiation (see geometry in Fig. 2.9), under cloudless conditions following the Beer–Bouguer–Lambert law:

$$I(\lambda) = \left(\frac{r_0}{r}\right)^2 I_0(\lambda) \exp\left(-\tau(\lambda) m(SZA)\right) \qquad (2.11)$$

where $I(\lambda)$ is the solar intensity of a given wavelength measured at the ground at a given time, r and r_0 are the actual and the mean earth-sun distances, $I_0(\lambda)$ is the solar intensity at TOA corresponding to r_0 and $m(SZA)=1/\cos(SZA)$ is the air mass factor. The total optical depth $\tau(\lambda)$ is the sum of the individual values contributed from aerosols (aer), Rayleigh molecules (R), ozone (O3) and nitrogen dioxide (NO2):

$$\tau(\lambda) = \tau_{aer}(\lambda) + \tau_R(\lambda) + \tau_{O3}(\lambda) + \tau_{NO2}(\lambda) \qquad (2.12)$$

The $\tau_{aer}(\lambda)$ can be retrieved using the previous equations and direct solar intensity measurements at specific wavelengths to minimize the effects of water vapor and ozone absorption.

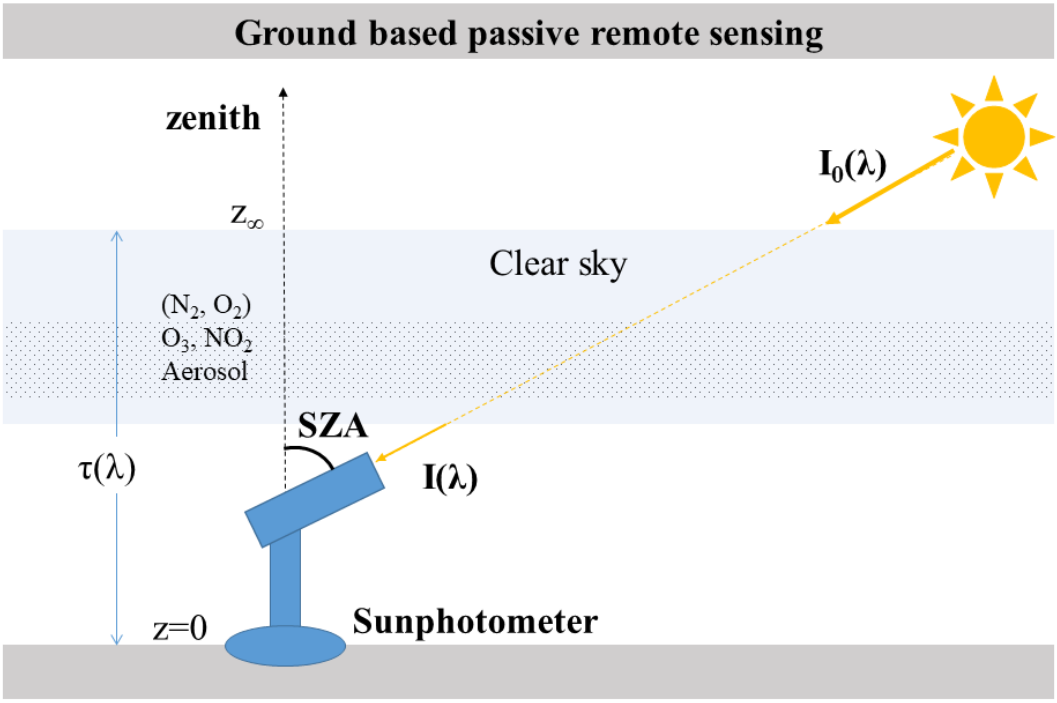

Figure 2.9 Ground based remote sensing geometry. The ground-based radiometer measures the direct solar beam intensity at the ground ($I(\lambda)$), $I_0(\lambda)$ is the solar intensity at the top of the atmosphere, $\tau(\lambda)$ is the optical depth and SZA the solar zenith angle.

Remote sensing using ground-based instruments is not available everywhere, with satellite remote sensing (Fig. 2.10 (a)) filling that spatial observational gap, providing data at high spatial and temporal resolution. The orbit of satellites carrying the instrument determines its observation capabilities. Geostationary satellites constantly monitor the same disc of earth, with high temporal resolution (observe diurnal variations). Polar orbit satellites allow for the whole earth to be monitored, with sun-synchronous satellites covering the whole earth every day or within a few days. In the last three decades there has been an advancement in satellite remote sensing of tropospheric composition (Burrows et al., 2011).

MODerate resolution Imaging Spectroradiometer (MODIS) is a key instrument on board polar-orbiting NASA satellites (Fig. 2.10 (b)) continuously monitoring earth for more than 20 years. The orbit is sun-synchronous, which means that the satellite passes over the same spot of the Earth at about the same local time every day. It acquires data in 36 spectral bands providing valuable products concerning land, oceans, and the lower atmosphere. Its atmospheric products for clouds, water vapor and aerosols are the results of retrieval algorithms concerning, providing a long-term data record for those essential geophysical parameters.

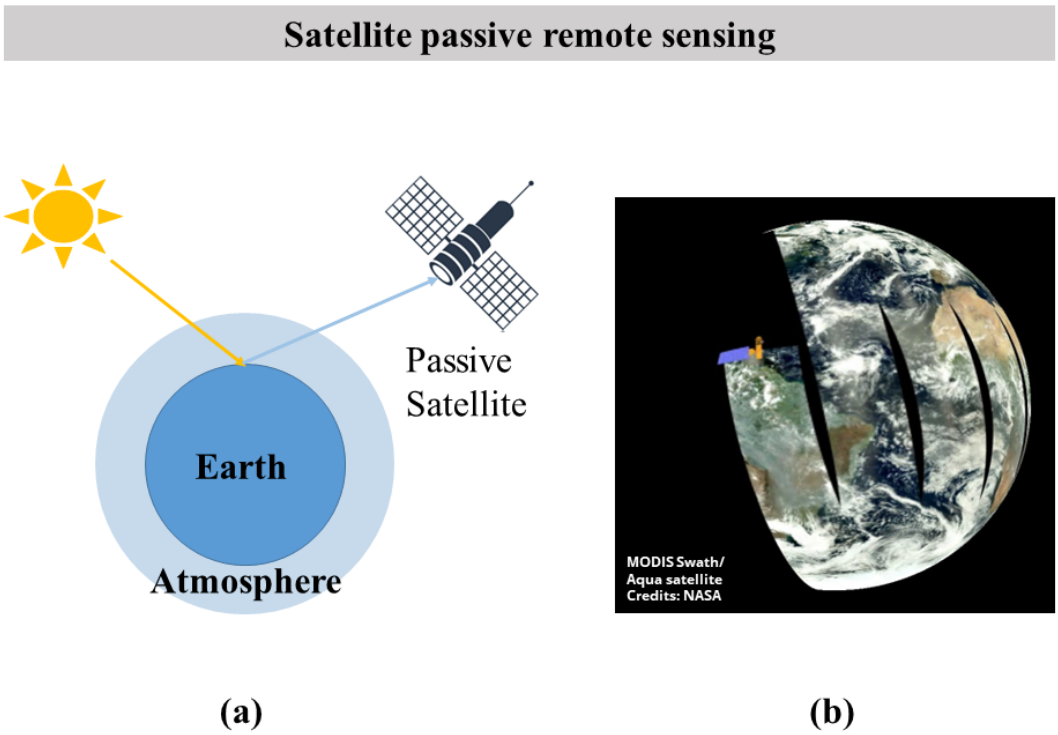

Figure 2.10 (a) Satellite passive remote sensing. **(b)** Moderate Resolution Imaging Spectroradiometer (MODIS) onboard NASA Earth Observing System Aqua (Credits for the image: NASA).

2.5 Surface solar radiation estimates

Solar resources assessment at a particular location is important for planning and management of solar energy technologies. The necessary GHI and DNI measurements for this are available only in a few places and this gap is filled by modeled values. Long term estimates of surface solar radiation can be generated at specific locations by using ground-based measurements of relevant meteorological parameters (cloud coverage, visibility, water vapor etc.) as input to radiative transfer models or at empirical relations. Of particular importance are gridded long-term estimates of surface GHI and DNI with high spatial and temporal resolution and a wide coverage (up to the global scale) provided by two different sources:

1. from satellite information
2. numerical weather prediction (NWP) models.

Due to their large area coverage and high temporal resolution, geostationary satellite data are used to produce estimates of surface solar radiation both in real time as an operational service and to generate historical archives of GHI and DNI based on long-term satellite measurements. Gridded long-term GHI data can also be obtained by NWP models either by their actual operational weather forecast or by running them in reanalysis mode. An overview of those techniques is provided in Sengupta et al. (2021).

2.5.1 Satellite -based surface solar radiation estimates

Several methods exist for obtaining satellite estimates of surface solar irradiance. A well-established method considers cloud extinction through the cloud coverage index (Cano et al., 1986) or cloud index, calculated from normalized satellite reflectances. Using the cloud index, the transmission factor or the clear-sky index (also called the cloud modification factor; "CMF" hereafter) is calculated, which is finally multiplied by the results of a clear-sky model to retrieve the solar irradiance at the earth's surface (Hammer et al., 2003). This is the general idea behind the HELIOSAT method (Cano et al., 1986; Hammer et al., 2003) widely used in various European research projects and applications. The derivative Heliosat-2 method (Rigollier et al., 2004) is launched in real time by the SoDa service and produces the HelioClim-3 database (Qu et al., 2014), a real-time solar radiation database dating from February 2004 onwards. A more recent version of the HelioClim-3 database (Thomas et al., 2016) – version 5 (HC3v5) – combines the McClear clear-sky model (Gschwind et al., 2019; Lefèvre et al., 2013) with cloud index values extracted from Meteosat Second Generation (MSG) satellite images. The Satellite Application Facility on Climate Monitoring (CM SAF) provides satellite-based estimates of surface solar radiation using data from Meteosat geostationary satellites. Currently, the third edition of the Surface Solar Radiation Data Set – Heliosat (SARAH-3, Pfeifroth et al., 2023a) – covers the period 1983–2020 as a climate data record (CDR) and is operationally extended into the present with a delay of a few days (Interim Climate Data Record (ICDR)). The retrieval algorithm MAGICSOL (Müller et al., 2015; Pfeifroth & Trentmann, 2023) is a combination of a modified Heliosat method to derive the effective cloud albedo (CAL) and the SPECMAGIC clear-sky model (Mueller et al., 2012). More available open-access satellite-based surface solar radiation climatological datasets based on the cloud index method can be found in Müller & Pfeifroth (2022).

There are also fully physical models that directly estimate surface solar radiation using radiative transfer models (RTMs) and geophysical parameters – including clouds (cloud and aerosol optical properties and total column values for water vapor and ozone content) and surface conditions – as inputs for a given atmospheric state. The combination of multi-channel information from geostationary satellites with cloud retrieval schemes provides cloud optical properties that can be explicitly used in RTMs to account for cloud extinction and finally to calculate the surface solar radiation. Parameterizations or look-up tables based on RTM simulations are used instead of direct radiative transfer calculations to optimize the computational time for operational use of the models. This is the case for the Heliosat-4 method (Qu et al., 2017), which is used in Copernicus Radiation Service (CAMS Radiation Service) estimates of surface solar irradiance. Their Heliosat-4 method is composed 5 of two models that independently consider clear-sky and cloudy conditions. Specifically, the McClear model (Lefèvre et al., 2013; Gschwind et al., 2019) is used for calculations of cloud-free irradiances and the McCloud model for calculating the extinction of irradiance by clouds (through the

clear-sky index), both of which are based on look-up tables (LUTs) to speed up calculations. The input cloud properties of the current CAMS Radiation Service v4 are retrieved by the adapted APOLLO Next Generation scheme from the MSG/SEVIRI (Spinning Enhanced Visible and Infrared Imager) satellite images (Schroedter-Homscheidt et al., 2022). The most recent version of the US National Renewable Energy Laboratory's (NREL's) gridded National Solar Radiation Database (NSRDB; 1998–2016; Sengupta et al., 2018) is also based on a fully physical model. This is the Physical Solar Model (PSM), which was developed by NREL and produces gridded surface solar irradiance estimates using satellite retrievals for clouds and other atmospheric properties from GOES data as input to the radiative transfer model.

2.6 Surface solar radiation forecasting

Forecasting solar radiation is essential for optimal operation and planning of solar power systems. An overview of all important aspects regarding solar forecasting is given by Yang et al. (2022) and Sengupta et al. (2021). The operational solar energy forecasting time horizon spans from a few seconds to a few days, to fill the different needs of power system control and operations. The day ahead forecasts are necessary to predict the net load of the next day and the intraday forecasts are needed in real-time markets to update the previous day schedules with the latest information.

The solar forecasting methods are categorized according to the forecast horizon and the datasets used (Fig. 2.11). A review of solar forecasting methods and their classification was presented in Inman et al. (2013) (Fig. 2.11 (a)), however due to technological and scientific advances in datasets, significant changes arise in this classification, almost ten years after (Fig. 2.11 (b), (Yang et al., 2022)). NWP traditionally has been used for day-ahead forecasting, but now there are available hourly updated NWP models for solar forecasting (Zhang et al., 2022). Currently, satellite images are used for a few minutes to a few hours ahead forecasting. Methods that are based on sky camera images and ground-based data are almost at the same timescale from few seconds to few minutes ahead. There are many statistical and machine learning methods that have been extensively used for solar radiation forecasting (e.g., El Alani et al., 2023; Hou et al., 2022). It is noteworthy that the statistical learning is limited now only as a post processing tool of the NWP outputs, instead of a stand-alone category.

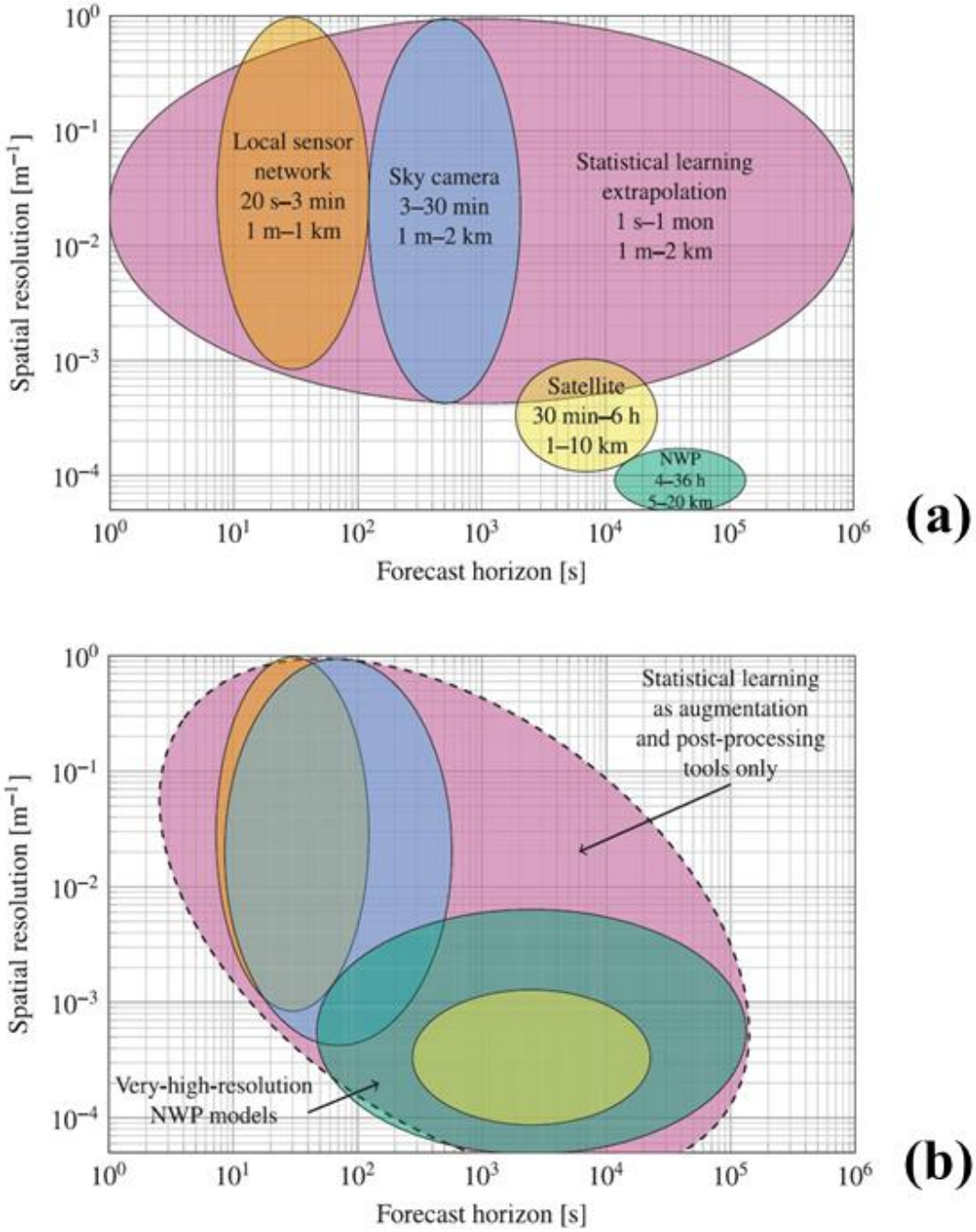

Figure 2.11 Figure adapted by Yang et al. (2022) about the association among forecast horizon, spatial resolution, and solar forecasting approaches **(a)** as first proposed by Inman et al. (2013) and **(b)** the current perception after new facts and knowledge considered by Yang et al., (2022).

3 Data and methods

3.1 Aerosol optical properties datasets

3.1.1 Ground – based measurements from the AERONET network

The AErosol Robotic NETwork (AERONET) (Holben et al., 1998) is a federation of ground-based aerosol remote sensing networks. It provides long-term, continuous, and easy to access data of aerosol optical, microphysical, and radiative properties for more than 25 years. The network provided global observations of AOD at various wavelengths, inversion products and precipitable water. Currently, Version 3 (Giles et al., 2019) AOD data are available at three quality levels. The AERONET observations can be used for aerosol research and characterization, for validation of satellite retrievals, for synergistic studies etc. and they can be easily downloaded from the AERONET data base https://aeronet.gsfc.nasa.gov/. The various AERONET datasets utilized for this thesis are described in the corresponding sections (Section 4 and 6).

3.1.2 Spaceborne AOD and DOD - ModIs Dust AeroSol (MIDAS) dataset

Daily retrievals of AOD at 550 nm from the MODerate resolution Imaging Spectroradiometer onboard the Aqua satellite (MODIS-Aqua) were used for this thesis. Specifically, quality assured Collection 6.1 MODIS – Aqua Level 2 AOD retrievals (Levy et al., 2013; Wei et al., 2019b) from the Dark Target (DT) and Deep Blue (DB) retrieval algorithms were merged according to Sayer et al. (2014) into one dataset and presented by Gkikas et al., (2021). AOD values from DT retrieval algorithm above ocean and land and DB above land were selected based on quality assurance (QA) of the retrievals. Then, the AOD values from both retrieval algorithms were merged by applying additional quality filtering criteria (see Sect. 2.1 in Gkikas et al., 2021) and stored in a scientific dataset. Based on this MODIS AOD combined product and on MERRA-2 (Gelaro et al., 2017; Randles et al., 2017) reanalysis data of dust optical depth (DOD) to AOD ratio, the MIDAS (ModIs Dust AeroSol; Gkikas et al., 2021, 2022) dataset was developed providing columnar mid-visible (550 nm) DOD and the corresponding AOD, on a daily basis, at fine spatial resolution (0.1° x 0.1°) and at global scale over the period 2003–2020. Regarding the DOD uncertainties, there were assessed in Gkikas et al. (2021) by considering the AOD and Merra-2 dust fraction uncertainties, as they were calculated using AERONET retrievals (Giles et al., 2019) and LIVAS database (Amiridis et al., 2015) as references, respectively. The MIDAS dataset (Gkikas et al., 2021, 2022) is available online at https://doi.org/10.5281/zenodo.4244106 (Gkikas et al., 2020). Considering its global coverage at fine spatial and temporal resolution, over a long period (2003–2020), this dataset is suitable for dust climatological studies (e.g., Fountoulakis et al., 2021; Gkikas et al., 2022; Logothetis et al., 2021).

3.1.3 Spaceborne profiles of aerosols (LIVAS/CALIPSO)

LIVAS is a three-dimensional (3-D) multi-wavelength global aerosol and cloud optical database, which provides averaged profiles of aerosol optical properties at 355, 532, 1064, 1570 and 2050 nm and cloud optical properties at the wavelength of 532 nm (Amiridis et al., 2015). Established based on the Cloud-Aerosol Lidar and Infrared Pathfinder Satellite (CALIPSO) (Winker et al., 2010), LIVAS data have been used in various studies for 3D aerosol climatology (e.g., Gkikas et al., 2021; Proestakis et al., 2018). To produce Level 2 (L2) Version 4 (V4) profiles of aerosol and cloud optical properties and layer classification information (Kim et al., 2018), LIVAS applies a series of quality-assurance procedures (Tackett et al., 2018) prior averaging to generate the Level 3 (L3) aerosol profile products, including, among others, vertical profiles of total-aerosol extinction coefficient and AOD at 532 nm. The original LIVAS database is established on a uniform grid of 1° x 1° spatial resolution, with the CALIPSO original vertical resolution, while with respect to the temporal resolution, the aerosol optical properties are provided (1) at the CALIPSO per-orbit level, (2) on monthly means, and (3) on long-term averaged profiles (6/2006–12/2020). However, for the scientific objectives of the present study, the LIVAS total-aerosol extinction coefficient profiles and AODs at 532 nm were generated in a 5° x 5° spatial resolution, providing time-averaged profiles of the CALIPSO total-aerosol extinction coefficient at 532 nm for the domains of northwest Africa and central-eastern Europe (more information is provided in Sections 3.7.2).

3.1.4 Model based AOD and DOD - Copernicus Atmospheric Monitoring Service (CAMS) reanalysis dataset

The CAMS reanalysis, available from 2003 onwards, is the global reanalysis dataset of atmospheric composition of the European Centre for Medium-Range Weather Forecasts (ECMWF), consisting of three-dimensional time-consistent atmospheric composition fields, including aerosols and chemical species (Inness et al., 2019). It is based on ECMWF's Integrated Forecast System (IFS), including an aerosol module described in Morcrette et al. (2009). Five species of tropospheric aerosols are included in the CAMS aerosol model, including dust. For dust sources, the parameterization of Ginoux et al. (2001) is implemented. The satellite-derived aerosol products that were assimilated in the CAMS reanalysis were the MODIS-Aqua and MODIS-Terra AOD retrievals (Benedetti et al., 2009) and, in addition, the retrievals from the Advanced Along-Track Scanning Radiometer (AATSR) onboard Envisat from 2003 to March 2012. More details regarding the updates in the meteorological part of IFS and in the aerosol and chemical modules, the data assimilation process and the emission datasets are given in Inness et al. (2019) and the references therein. CAMS reanalysis products are available from the Copernicus Atmosphere Data Store (ADS, https://ads.atmosphere.copernicus.eu/#!/home) on

a 3-hourly basis. AOD and DOD at 550 nm were obtained programmatically for the period 2003–2017 on a 0.4° x 0.4° lat/lon grid.

3.1.5 Climatological SSA and AE dataset

For the UV–visible–near-IR additional optical properties for all aerosols and dust, climatological values from the second version of the Max-Planck Aerosol Climatology (MACv2) (Kinne, 2019) were utilized, which are available at a global scale with a 1° x 1° spatial resolution. The interannual variability of total aerosol optical properties is provided over the period 2001–2016 in terms of monthly means for every year. Long-term monthly means for the whole period are provided for five different aerosol species, including dust. In the current thesis, SSA at 550 nm was used for total aerosols and dust (DU SSA). AODs at 470 nm and 850 nm, for total aerosols, were obtained from MACv2 and were used to calculate the Ångström exponent (AE) (AE 470–850 nm). For dust, a fixed climatological value of 0.4 for AE 440–675 nm was used as proposed by Taylor et al., (2015) for the Mediterranean domain.

3.2 Cloud optical properties - EUMETSAT NWC SAF

The Satellite Application Facilities of Nowcasting and Very Short-Range Forecasting, NWC SAF of EUMETSAT (Derrien & Le Gléau, 2005; Meteo France, 2016) provides a comprehensive system that supports operational and research activities related with nowcasting. It provides a software package that it can be combined with the data from geostationary satellites to generate a set of meteorological products in real time.

Data from the channels of geostationary Meteosat Second Generation (MSG) satellites are broadcasted operationally at the National Observatory of Athens. The software package of NWC SAF uses as input those data for the near real time generation of a set of meteorological products. The product of interest in this thesis is Cloud Microphysics (CMIC), which contains the information of Cloud optical Thickness (COT). The operational outputs of COT for a complete year (2017) were used for the needs of this thesis (see Section 6).

3.3 Datasets of other atmospheric variables

3.3.1 Model based Total Column Water Vapor (TCWV) - CAMS Reanalysis dataset

In the same manner with CAMS AOD and DOD, TCWV was obtained from CAMS reanalysis dataset (Inness et al., 2019) for the period 2003–2017 on a 0.4° x 0.4° lat/lon grid, on a 3-hourly basis.

3.3.2 Satellite based Total Ozone Column (TOC) dataset

To obtain TOC data for the period 2003-2017, a new dataset was constructed by combining data from Ozone Monitoring Instrument (OMI) onboard NASA's Aura satellite from 1 October 2004 until 31 December 2017 and from Total Ozone Mapping Spectrometer (TOMS) onboard the Earth Probe (EP) satellite from 1 January 2003 to 30 September 2004. The satellite-based TOC retrievals were collected from the daily global OMI TOMS-Like TOC Level 3 (OMTO3d) gridded on a 1° x 1° grid product (Bhartia, 2012) and from the EP TOMS Level 3 (TOMSEPL3) version 8 product, which provides daily data on a global grid of 1° x 1.25°. The OMI and TOMS satellite retrievals of TOC were downloaded from https://disc.gsfc.nasa.gov/datasets/.

3.4 Ground-based irradiance measurements

To validate the modeled GHI (Section 6.2), ground-based measurements from pyranometers were utilized. The ground-based 1 min GHI measurements were collected from stations of the Baseline Surface Radiation Network (BSRN; Driemel et al., 2018), which are within the study area and have data for all of 2017, and from two additional stations at Athens (ASNOA: the NOA's Actinometric Station) and Thessaloniki. Table 3.1 summarizes information on all 10 stations utilized, and Fig. 3.1 depicts their geographical locations.

Table 3.1 Detailed information about the ground-based sations used to validate the modeled GHI (Section 6.2).

	Ground-based pyranometer				AERONET station
Name	**Network**	**Lat. (°N)**	**Lon. (°E)**	**Location**	
ATH - Athens	-	37.9	23.7	Greece (Europe)	Co-located
CAB – Cabauw	BSRN	51.9711	4.9267	Amsterdam (Europe)	Co-located
CAM – Camborne	BSRN	50.2167	-5.3167	London (Europe)	Co-located
CAR – Carpentras	BSRN	44.083	5.059	Paris (Europe)	Co-located
CNR – Cener	BSRN	42.816	-1.601	Madrid (Europe)	Co-located
LER – Lerwick	BSRN	60.1389	-1.1847	London (Europe)	Co-located
LIN – Lindenberg	BSRN	52.21	14.122	Berlin (Europe)	Co-located (metObs LIN)
PAL – Palaiseau, SIRTA Obser	BSRN	48.713	2.208	Paris (Europe)	Co-located
TAM – Tamanrasset	BSRN	22.7903	5.5292	Algiers (Africa)	Co-located
THE -Thessaloniki	-	40.63	22.96	Greece (Europe)	Co-located

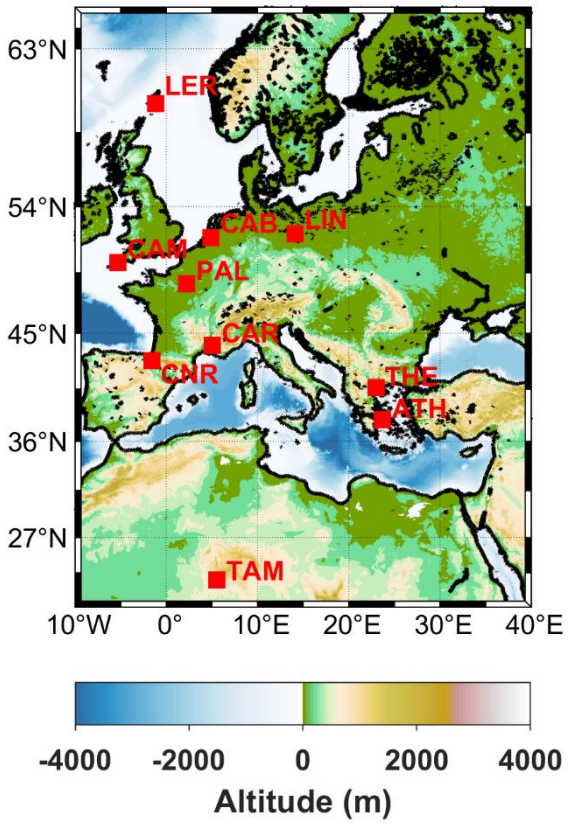

Figure 3.1 Locations of the ground-based stations measuring global horizontal irradiance (GHI) that are used to validate the modeled GHI (Section 6.2). These are eight BSRN stations plus Athens and Thessaloniki in Greece.

BSRN station-to-archive files were accessed and manipulated using the SolarData v1.1 R package (Yang, 2019). The function that reads the data from the station-to-archive files also computes several auxiliary variables, such as solar zenith angle, clear sky irradiances using the Ineichen-Perez clear-sky model (Ineichen & Perez, 2002), and extraterrestrial GHI. Using the same methodology, the Ineichen-Perez clear sky model values were also computed for the non BSRN station data by adjusting the functions of the Solar-Data v1.1 R package for the non-BSRN stations.

The BSRN recommended Quality Check (QC) tests (Long & Dutton, 2010) were applied to the collected measurements to ensure that they were of the best quality. Measurements that did not pass the above QC tests were flagged and labeled as missing values. The GHI records that are available at the two Greek stations (1951–present in Athens; 1993–present in Thessaloniki) are among the longest continuous high-quality GHI records in the eastern Mediterranean Basin, an area where BSRN data are not available for the period of this study. The pyranometers in Athens and Thessaloniki are calibrated regularly, and the GHI measurements were subjected to quality control before being used in the study. More information on the GHI datasets for the Thessaloniki and Athens stations can be found in Bais et al. (2013) and Kazadzis et al. (2018), respectively.

3.5 Megacities information and population datasets from United Nations

Megacities are defined as cities with a population of more than 10 million, but in our analysis, we include cities with populations between 5 and 10 million as well, due to their potential to become megacities in the coming decades, as estimated by UN projections (UN, 2018a). Table 3.2 summarizes the number of cities according to their population by 2018 and future projections. According to UN projections, 10 cities with populations between 5 and 10 million are expected to become megacities soon. In this thesis, we focus on 81 cities, with more than 5 million inhabitants as reported in 2018, which are listed in Table A1 (UN, 2018a, 2019a) and their geographical location is depicted in Figure 3.2.

It should be mentioned that the UN data correspond mostly (65%) to urban agglomerations, for which the city's boundaries are defined as the extent of the contiguous urban area (or built-up area). A small part refers to the metropolitan areas (25%) and even smaller (10%) to the city proper. For a major metropolitan area (MMA), more than one city is close together, and in most cases with no distinct limits. For example, in the Kinki MMA, Osaka is the city with the highest population and the Los Angeles metropolitan area includes the Long Beach and Santa Ana population. There are five MMAs included in this study, and they are shown in bold in Table A1. One last remark concerning population data is about Guangzhou, Shenzhen, Hong Kong, Dongguan, and Foshan (shown in italics in Table A1). They are all located in the Guangdong–Hong Kong–Macau Greater Bay Area. This area, which is confined in a domain narrower than 1° x 1°, also includes five other cities with population more than 1 million, forming a megalopolis, which is the largest urban agglomeration on the planet. The cities in this region and the MMAs will be exempted from the spatial gradient analysis.

Table 3.2 Number of cities according to their population (adopted by UN (2018a)).

	By 2018	**Projection to 2030**
Megacities (≥ 10 million)	33	43
5-10 million	48 (10 of those -20% - are projected to become megacities by 2030)	66
Total ≥ 5 million	**81**	109
1-5 million	467	597
≥ 1 million	548 28 of those -5% - are projected to cross the 5 million mark)	706
500,000 -1 million	598	710

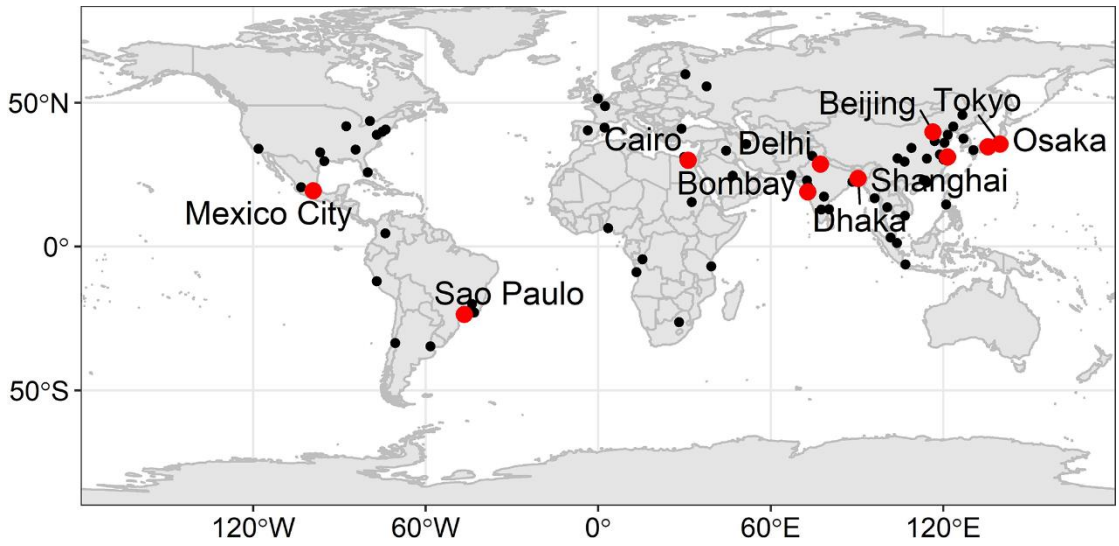

Figure 3.2 Map of the location of the 81 cities with population greater than 5 million (black circles). Red circles denote the 10 megacities with the highest population.

To calculate the population changes every city's population estimates in thousands of inhabitants in an annual base for the period 2003-2020 utilized from the UN's collection of datasets (UN, 2018b).

3.6 Radiative transfer modeling (RTM)

3.6.1 Library of Radiative transfer (LibRadtran)

Library of Radiative transfer (LibRadtran) package (Emde et al., 2016; Mayer & Kylling, 2005) is a collection of routines and functions for radiative transfer calculations under different atmospheric conditions. The main program of the libRadtran package is uvspec. This program contains a selection of different radiative transfer equation solvers to calculate the radiation field in the Earth's atmosphere for a variety of input parameters. The model input parameters are specified with a plain text file. This file must contain specific commands to determine the atmospheric parameters such as:

1) Rayleigh scattering

2) Molecular absorption

3) Aerosols

4) Water and ice clouds

5) Surface albedo

3.6.2 Shortwave (SW) Clear sky look up table (LUT)

To minimize the computational time of directly simulating irradiances using RTM, clear-sky global horizontal irradiance (GHI) and direct normal irradiance (DNI) estimations were based on a detailed LUT of ~16 million combinations for a wide range of the state of the earth-atmosphere system and sun

position. It was generated using the National Infrastructures for Research and Technology (GRNET) High Performance Computing Services and the computational resources of ARIS GRNET infrastructure. The RTM simulations were performed using the libRadtran package (Emde et al., 2016; Mayer & Kylling, 2005). Table 3.3 summarizes the input variables and their resolution. The number of variables and their resolution resulted in a total of ~16 million runs.

Table 3.3 Input parameters for radiative transfer simulations performed on the ARIS GRNET supercomputer resulted to the 7D GHI/DNI LUT.

Parameter	Range	Resolution
Solar zenith angle (SZA; in degrees)	1 to 89	1
Aerosol optical depth at 550nm (AOD)	0 to 2, 2.5,3.0	0.05
Single scattering albedo (SSA)	0.6 to 1	0.1
Ångström exponent (AE)	0 to 2	0.4
Total ozone column (TOC; in DU)	200 to 500	100
Water vapor (WV; in cm)	0.5 to 3	0.5
Surface albedo	0.05 to 0.8	0.15

RTM simulations were performed spectrally from 280 to 3000 nm, with 1 nm spectral resolution using the DISORT radiative transfer solver in pseudo-spherical mode (Buras et al., 2011). The molecular absorption parameterization of representative wavelength approach (REPTRAN; Gasteiger et al., 2014) was used to account for the absorption of atmospheric gases for the whole solar spectrum. The Kurucz 1.0nm (Kurucz, 1994) extraterrestrial solar spectrum and the US Standard Atmosphere (Anderson et al., 1986) were used as inputs. The default aerosol model of Shettle (1989) was used as the basis, and the aerosol optical properties of AOD, single scattering albedo (SSA), and Ångström exponent (AE) were modified varying according to Table 3.3. The spectral global irradiances were integrated over the spectral range of the simulations to derive the GHI and DNI.

3.7 Sensitivity analysis for the effect of aerosol vertical distribution on surface solar radiation

An RTM sensitivity analysis has been performed by using different and more realistic profiles of aerosols than the default of libRadtran (Shettle, 1989) to investigate how changes in the vertical distribution of aerosol optical properties affect the simulated solar radiation that reaches the Earth's surface. We simulated the total shortwave (SW, 280–3000 nm integral) global irradiance (GI) and direct irradiance (DI) with different aerosol extinction profiles and for different aerosols and atmospheric conditions. For better insight, different spectral regions are discussed separately,

ultraviolet-B (UVB, 280–315 nm integral), ultraviolet-A (UVA, 315–400 nm integral), visible (VIS, 400–700 nm integral), near infrared (NIR, 700–3000 nm integral).

- As a first step, the sensitivity of the solar radiation profile to the altitude of a hypothetical aerosol layer was investigated using artificial aerosol extinction coefficient profiles.
- As a second step, radiative transfer (RT) simulations were performed using aerosol extinction coefficient profiles from the LIVAS (see Section 3.1.3), and the results were compared with the results of simulations with the default libRadtran profile (Shettle, 1989) which assumed an exponential decrease in the aerosol extinction coefficient with altitude in the troposphere.

The simulations were performed using the uvspec model of the libRadtran package (Emde et al., 2016; Mayer & Kylling, 2005). Several input parameters were explicitly defined for each of the simulations: TCWV, TOC, surface albedo, columnar aerosol optical properties (AOD, SSA and AE), and the vertical profile of the extinction coefficient at 532 nm. The latter was then scaled to the value of the AOD at each wavelength. In all cases, the profiles of parameters other than AOD aerosol optical properties (e.g., SSA, AE) were assumed to be constant throughout the atmosphere. The standard atmospheric profile (standard US atmosphere (Anderson et al., 1986)) was used for all simulations. Thus, the default libRadtran profiles of TOC, TCWV, etc. were scaled to defined columnar values. Spectral simulations in the range of 280–3000 nm were performed with a step of 1 nm. The extraterrestrial solar spectrum suggested by Kurucz (1994) and the sdisort (Buras et al., 2011) solver were used for the simulations. Simulations were performed separately for the four spectral regions: UVB, UVA, VIS, NIR. For the simulations in the NIR region, absorption was parametrized using the correlated-k KATO2 distribution (Kato et al., 1999; Wandji Nyamsi et al., 2015). Although the latter parameterization introduced some additional uncertainty into the simulations compared to more detailed parameterizations, the additional uncertainty was negligible for the NIR integral (Mayer & Kylling, 2005). The produced spectra were integrated to calculate and analyze the total irradiance in the four spectral bands (UVB, UVA, VIS, NIR) and the total SW global and direct irradiances.

3.7.1 Sensitivity Study Using Artificial Extinction Profiles

The first step of the study was to perform simulations for five different artificial homogeneous layers of aerosols, with layer bases at 0, 1, 2, 3, and 4 km (hereafter referred as L0 to L4, respectively) from the surface (assuming that the surface is at mean sea level). Three of the five layers are shown in Figure 3.3. The width of each layer was 1.5 km. The aerosol extinction coefficient above and below each layer was considered zero. Simulations were performed for combinations of different atmospheric and surface parameters, as well as different aerosol optical properties (see Table 3.4). For

the simulations in each spectral band, the AOD was independent from wavelength (i.e., AE was set to zero).

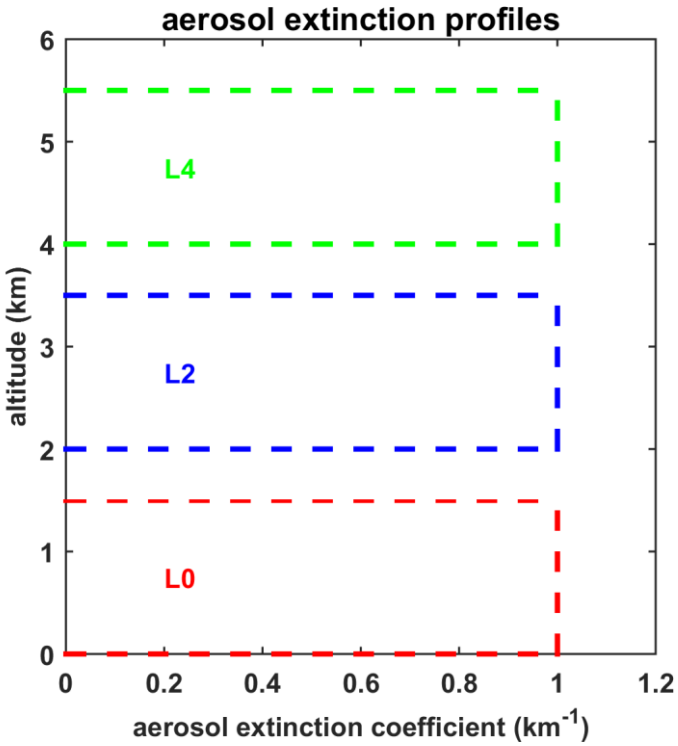

Figure 3.3 Three of the five artificial aerosol profiles that were used for the simulations (here for AOD = 1.5).

Table 3.4 UVSPEC model input parameters for the simulations with the artificial aerosol profiles.

Property	**values**
SZA	20°, 40°, 60°, 80°
AOD (all wavelengths)	0.2, 0.5, 1.0
SSA (all wavelengths)	0.75, 0.95
AE	0
TOC	350 DU
TCWV	10, 30 mm
Surface albedo	0.1, 0.4, 0.8

For the same sets of parameters and different extinction coefficient profiles, comparisons between the surface values of the GI and DI were performed. In all cases, the results for elevated aerosol layers were compared with the results for L0. This way, it was possible to investigate the effect of different aerosol layer altitudes and understand the physical mechanisms that are responsible for the differences in surface GI and DI.

3.7.2 Effect of extinction coefficient profile for typical aerosol conditions - LIVAS Profiles

Aerosol extinction profiles at 532 nm from the LIVAS climatology were averaged for two 5° x 5° regions with centers in northwestern Saharan desert, Africa (32.5° N, 7.5° E), and central-eastern Europe (47.5° N, 17.5° E) for the period 6/2006–12/2020. In the following, the two regions are

referred to as NW Africa and CE Europe, respectively. From the daily LIVAS profiles, monthly averaged profiles were calculated and subsequently averaged again to calculate seasonal profiles for winter (December, January, February; DJF), spring (March, April, May; MAM), summer (June, July, August; JJA), and autumn (September, October, November; SON). Seasonal profiles were used to perform RT simulations. RT simulations were also performed using the libRadtran default profile (Shettle, 1989). RT simulations for each season were performed for both profiles assuming climatological seasonal averages for TCWV, TOC, aerosol optical properties (AOD, SSA, AE), and surface albedo.

Climatological seasonal TCWV from the CAMS (Section 3.3.1), TOC from the OMI (Section 3.3.2), and AOD retrievals at 550 nm from the MODIS (Section 3.1.2) were averaged for the same areas and seasons and used for the simulations. Seasonal climatological averages for the period 2006–2020 were calculated from monthly averaged surface albedo from the Modern-Era Retrospective Analysis for Research and Applications, Version 2 (MERRA-2) climatology (GMAO, 2015) and was used for the simulations in VIS and IR. Surface albedo in UV differs significantly from surface albedo in VIS for land-surface types such as deserts. Thus, typical values were used (Feister & Grewe, 1995; Varotsos et al., 2014) since large-scale climatological data are not available. Seasonally averaged SSA and AE were calculated from monthly averages, which were derived from the MACv2 climatology (Kinne, 2019) and used for the RT simulations. The above parameters are listed in Tables 3.5-3.7.

Table 3.5 AOD at 550 nm, TCWV, TOC, and surface albedo used in the simulations for NW Africa and CE Europe.

	winter	spring	summer	autumn
		550 nm AOD		
NW Africa	0.19	0.35	0.35	0.26
CE Europe	0.07	0.18	0.22	0.13
		TCWV (mm)		
NW Africa	11.4	14.6	22.3	20.4
CE Europe	9.6	14.4	25.7	17.4
		Total ozone (DU)		
NW Africa	299.4	318.3	298.4	282.2
CE Europe	333.3	358.6	320.2	287.8
		Surface albedo		
NW Africa VIS/IR	0.42	0.40	0.41	0.41
NW Africa UVB/UVA	0.10	0.10	0.10	0.10
CE Europe VIS/IR	0.15	0.15	0.15	0.15
CE Europe UVB/UVA	0.05	0.05	0.05	0.05

Table 3.6 SSA used in the simulations for NW Africa and CE Europe. For each spectral band, independent from wavelength SSA was assumed.

		winter	spring	summer	autumn
NW Africa	UVB	0.84	0.77	0.81	0.80
	UVA	0.85	0.78	0.82	0.81
	VIS	0.93	0.93	0.94	0.93
	IR	0.94	0.96	0.96	0.96
CE Europe	UVB	0.80	0.86	0.87	0.83
	UVA	0.81	0.87	0.88	0.85
	VIS	0.87	0.91	0.92	0.90
	IR	0.86	0.91	0.91	0.89

Table 3.7 AE used in the simulations for NW Africa and CE Europe.

		winter	spring	summer	autumn
NW Africa	UVB	1.32	0.74	1.04	0.89
	UVA	1.32	0.74	1.04	0.89
	VIS	1.32	0.74	1.04	0.89
	IR	0.65	0.20	0.31	0.30
CE Europe	UVB	1.32	1.52	1.66	1.41
	UVA	1.32	1.52	1.66	1.41
	VIS	1.32	1.52	1.66	1.41
	IR	1.32	1.30	1.40	1.27

3.8 Methodology to derive aerosol/dust shortwave (SW) Direct Radiative Effects (DREs) on surface

For quantifying the impact of total aerosols and dust on the downwelling surface solar irradiance (DSSI) components GHI and DNI, their levels were estimated by performing RTM simulations following the LUT approach (see Section 3.6.2) using as inputs the satellite (MIDAS) retrievals and reanalysis (CAMS) products of AOD and DOD, complemented by additional aerosol optical properties and atmospheric parameters acquired from the MACv2 climatology, spaceborne observations (OMI, TOMS) and reanalysis products (CAMS), which are described in detail in Sections 3.1 and 3.3 and are summarized here in Table 3.8.

Table 3.8 Datasets of total aerosol and dust optical properties and key atmospheric parameters for radiative transfer model (RTM) simulations (based on LUT approach) of downwelling surface solar irradiance (DSSI).

Parameter	Description (Spatial–Temporal Resolution)	Source	Reference
Aerosol optical properties	Satellite-retrieved aerosol optical depth (AOD) (0.1° × 0.1°, 1 day)	ModIs Dust Aerosol (MIDAS)	Gkikas et al., 2021
	Modeled AOD (0.4° × 0.4°, 3 h)	Copernicus Atmospheric Monitoring Service (CAMS) reanalysis	Inness et al., 2019

	Single scattering albedo (SSA) (1° × 1°, 1 month)	Max-Planck Aerosol Climatology (MACv2)	Kinne, 2019
	Ångström exponent (AE) (1° × 1°, 1 month)	MACv2	Kinne, 2019
Dust optical properties	Satellite-based dust optical depth (DOD) (0.1° × 0.1°, 1 day)	MIDAS	Gkikas et al., 2021
	Modeled DOD (0.4° × 0.4°, 3 h)	CAMS reanalysis	Inness et al., 2019
	Dust SSA (DU SSA) (1° × 1°, 12 monthly means)	MACv2	Kinne, 2019
Water vapor	Modeled total column water vapor (TCWV) (0.4° × 0.4°, 3 h)	CAMS reanalysis	Inness et al., 2019
Ozone	Satellite-retrieved total ozone column (TOC) (1° × 1° / 1° × 1.25°, 1 day)	Ozone Monitoring Instrument (OMI) TOMS-Like Level 3 product/Earth Probe (EP) Total Ozone Mapping Spectrometer (TOMS) Level 3 version 8 product	Bhartia, 2012 TOMS Science Team

The analysis was performed for the domain that is confined between 27°N–50°N and 15°W–40°E, which includes the countries around the Mediterranean Sea, as well as part of Central Europe and the Middle East. Analysis was performed with a spatial resolution of 0.4° x 0.4° and for the period 2003–2017.

3.8.1 Database (DB) for Radiative Properties - Dealing with different spatial and temporal scales among datasets

The original datasets differ in spatial and temporal resolution. Initially, the spatial and temporal homogenization of datasets with missing values was performed, which was then followed by the geolocation and synchronization among all datasets in order to generate a complete database (DB) of all the input parameters needed for the RTM simulations (SZA, AOD or DOD, SSA, AE, TCWV, TOC) on a 0.4° x 0.4° lon/lat grid, on an hourly basis, which was selected to be the frequency of RTM simulations in order to account for the sun elevation. Figure 3.4 provides a schematic overview of this process.

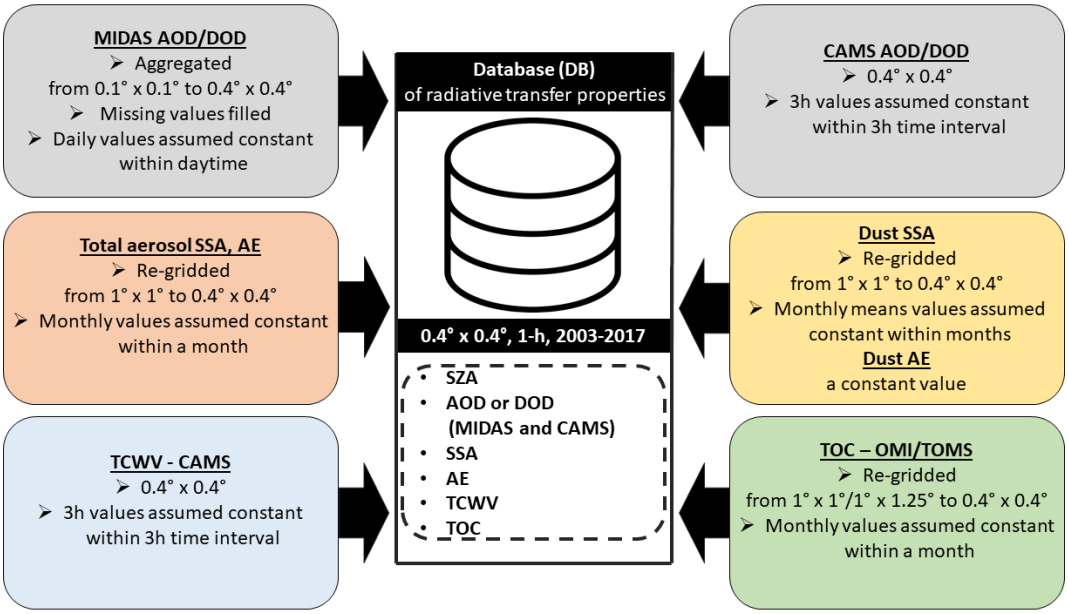

Figure 3.4 Schematic overview of the database (DB) created for the RTM simulations, on a 0.4° × 0.4° lon/lat grid and 1 h temporal resolution.

The MIDAS dataset was aggregated to the coarser spatial resolution of 0.4° x 0.4° to achieve a small number of missing values. The median value was selected as the aggregation method, as a nonparametric measure of central tendency, based on the findings of Sayer & Knobelspiesse (2019). To homogenize MIDAS dataset in time and space, the missing values were filled by monthly means. Seasonal means were utilized when the monthly data availability was low (<20% or less than 6 days in a month). In cases with low seasonal availability, the spatial gaps were filled using bilinear interpolation. For the 1 h RTM simulations, daily MIDAS values were used and the AOD and DOD were assumed invariant in the day.

The diurnal variability of CAMS datasets (AOD, DOD and TCWV) was taken into account and the 3 h values were assumed invariant within each 3-h time interval. For TOC, a temporal fitting was performed to fill the days missing with monthly mean values, and a spatial bilinear fit was performed to fill the gaps in space. Both OMI and TOMS datasets were bilinearly interpolated to a 0.4° x 0.4° grid. Again, TOC was assumed invariant in the day. The 1° x 1° fields of MACv2 were also bilinearly interpolated to the 0.4° x 0.4° grid and the monthly values of SSA and AE were used, assuming that they remain constant during each month.

3.8.2 Direct Radiative Effects (DREs)

The hourly values of clear-sky DSSI in terms of global and direct components were obtained relying on the precalculated LUTs (Section 3.6.2), to achieve realistic computational times, as similarly done in Kosmopoulos et al. (2018a). Using the DB described in Section 3.8.1 as inputs and linear interpolation to the LUTs, instantaneous values of total irradiances (global and direct) every 1 h

during daytime were extracted for each grid cell (0.4° x 0.4°) for 2003–2017. This procedure was repeated five times, as different experiments, described in Table 3.9, to quantify the total aerosol as well as the dust effect on different DSSI components, for the two different datasets (MIDAS, CAMS).

Table 3.9 The different experiments for which DSSI values were extracted from the LUTs.

Atmospheric conditions	Dataset
Aerosol included	MIDAS AOD
	CAMS AOD
Dust included	MIDAS DOD
	CAMS DOD
Aerosol-free	AOD = 0

By integrating the 1 h instantaneous values of total irradiances over sunlight hours, the daily global horizontal irradiation (GHI) and direct normal irradiation (DNI) components (in MJ/m^2) were calculated, and those values were post-corrected for the Earth–Sun distance, and for the surface elevation following the methodology described in Fountoulakis et al. (2021). Using LUT instead of simulating DSSI for the exact conditions of each time step induced some additional uncertainty in the results, which however is small. By comparing the daily integrals using both approaches for particular grid points, it was estimated that the additional (2-fold) uncertainty in the daily integrals is ~0.2 kW m^{-2}, which for the domain of study corresponds to less than 1% of the simulated DSSI in spring, summer and autumn and to less than 10% at the northernmost latitudes of the domain in winter. The corresponding uncertainty in the monthly integrals is much smaller, less than 1% in all cases.

Using the simulated daily irradiations, mean annual and seasonal integrals (INTs) of GHI and DNI, for cloudless conditions, were calculated for the five different experiments described in Table 3.9 using the following formula:

$$\frac{\mathrm{INT_{i\_on}} - \mathrm{INT_{aer\_free}}}{\mathrm{INT_{aer\_free}}} \times 100\% \qquad (3.1)$$

where i stands for aerosols and dust. The relative change (expressed in %) in DSSI due to aerosols and dust presence was calculated with respect to an aerosol-free atmosphere. Using the same formula, the daily relative changes were calculated as well.

3.8.3 DREs of extreme dust events

The broader Mediterranean Basin is an area frequently affected by dust outbreaks (Gkikas et al., 2016, 2022), resulting in extremely high concentrations of mineral particles and maximized DODs. Thus, we aimed to quantify the impact of those extreme DOD values on GHI and DNI. To this end, the

methodology proposed by Gkikas et al. (2012) and the objective and dynamic algorithm of Gkikas et al. (2009) was applied to MIDAS DOD values to define the extreme dust episode days (eDEDs). First, for every pixel, the mean DOD ($\overline{\mathrm{DOD}}$) and the associated standard deviation (σ_{DOD}) values were calculated, using the daily values of DOD over the period 2003–2017. An extreme dust episode occurs on a specific day and at a specific location (pixel) when DOD values are higher than a critical value (threshold):

$$\mathrm{DOD} \geq \overline{\mathrm{DOD}} + 4\sigma_{\mathrm{DOD}} \qquad (3.2)$$

This algorithm is characterized as dynamic since the DOD threshold values are not constant for each pixel. Finally, to characterize a day as an eDED, at least 300 pixels should undergo an extreme dust episode, providing that the data availability for this day is more than 50%. From our analysis, 67 eDEDs were found for the whole study period 2003–2017, or on average 4.5 eDEDs year^{-1}.

3.9 The cloud motion vector (CMV) method of the Solar Energy Forecasting system – NextSENSE2

NextSENSE2 is the operational system that provides forecasts of GHI up to 3 h ahead with a 15 min time step by applying a cloud motion vector (CMV) technique to the MSG COT product. It uses CMVs to predict the motions of the clouds and project their future positions. The CMVs in NextSENSE2 are calculated by applying a state-of-the-art optical flow algorithm from the computer vision community. Optical flow is the apparent motion of objects between consecutive frames, which is caused by the relative movement between the object and a camera. The Farnebäck (2003) two-frame motion estimation technique is applied to images of the COT product (Kosmopoulos et al., 2020). Several other optical flow algorithms, like TV-L1, are available as free software (OpenCV) and are used for cloud motion estimation in solar energy short-term forecasting systems (Urbich et al., 2019). In this study, we used the Farnebäck technique based on the results of a previous study by Kosmopoulos et al. (2020). The optical flow displacement vectors are calculated by applying the algorithm to two consecutive images of satellite-derived COT. This CMV field is applied to the later COT image (real) to get the next COT image (forecasted COT). This procedure is performed 12 times, resulting in the 3h forecasting horizon. The main assumptions are brightness constancy and that the cloud's displacements are only two-dimensional (i.e., in the image plane). More details regarding the CMV model and forecasted COT can be found in Kosmopoulos et al. (2020).

3.10 Persistence forecast

It is not easy to evaluate the quality of different forecasting methods of surface solar radiation using only statistical metrics, since the study period, the geographical area, and other factors affect their

forecasting accuracies. That is why it is a typical evaluation practice to benchmark the different forecasts against some simple forecast methods (Pelland et al., 2013). We used the persistence forecast to benchmark the CMV-forecasted GHI of the NextSENSE2 system, which is a commonly used reference in solar forecasting (e.g., Kosmopoulos et al., 2020; Kallio-Myers et al., 2020). This method assumes that the state of the clouds remains constant for future time steps, while all other variables, like SZA, dynamically change. Hence, it uses the same COT values from the later satellite information as input to the next time steps in order to forecast the GHI up to 3 h ahead.

3.11 Evaluation metrics

Common statistical metrics were adopted for the validation of the SENSE2- or NextSENSE2-derived GHI values against ground-based measurements (Section 6.2). Given that the error is defined as the difference between the modeled values (x_{m_i}) and the observed values (x_{o_i}), we have three common metrics: the mean bias error (MBE), root mean square error (RMSE), and Pearson correlation coefficient (R).

$$\mathrm{MBE} = \frac{1}{N}\sum_{i=1}^{N}(x_{m_i} - x_{o_i}) \qquad (3.3)$$

$$\mathrm{RMSE} = \sqrt{\frac{1}{N}\sum_{i=1}^{N}(x_{m_i} - x_{o_i})^2} \qquad (3.4)$$

The relative values of the latter two metrics, rMBE and rRMSE, were obtained with respect to the mean of the observed values of GHI.

An additional metric, the forecast skill (FS), was used to assess the performance of CMV-forecasted GHI using the persistence model as a benchmark model:

$$\mathrm{FS} = 1 - \frac{\mathrm{rRMSE}_{\mathrm{CMV}}}{\mathrm{rRMSE}_{\mathrm{pers.}}} \qquad (3.5)$$

where $\mathrm{rRMSE}_{\mathrm{CMV}}$ and $\mathrm{rRMSE}_{\mathrm{pers}}$ are the relative RMSEs of the CMV and persistence forecasting models, respectively.

4 Aerosol state and trends in megacities

This chapter is based on the publication: ***Papachristopoulou, K.****, Raptis, I.-P., Gkikas, A., Fountoulakis, I., Masoom, A., and Kazadzis, S.: Aerosol optical depth regime over megacities of the world, Atmos. Chem. Phys., 22, 15703–15727, https://doi.org/10.5194/acp-22-15703-2022, 2022.*

Analyzing the aerosol spatiotemporal variability over megacities is of great importance for air quality and human health. Additionally, since aerosols attenuate the solar radiation reaching the earth surface, this analysis is also valuable in terms of solar energy rooftop applications, which consists one of the most promising ways of green energy production at urban environments.

Aerosol-related air pollution can be quantified, in optical terms, through aerosol optical depth (AOD). Apart from AERONET (Section 3.1.1) during the last 20–25 years long-term AOD measurements from ground-based sun photometers have been deployed from additional established global/regional networks such as GAW-PFR (Kazadzis et al., 2018b) and SKYNET (Nakajima et al., 2020). Although the most precise method for monitoring AOD is provided by surface sun photometers, these measurements are scarce, lacking full spatial and temporal coverage. On the contrary, satellite remote sensing is a powerful tool for monitoring AOD around the globe (Kaufman et al., 2002) at considerable accuracy, almost on a daily basis and at relatively fine spatial resolution. Even though the quality of spaceborne AOD over urban surfaces depends strongly on the limitations of the retrieval algorithms (Gupta et al., 2016), it is an aerosol parameter available worldwide at high spatial and temporal resolution.

There are many studies dealing with AOD trends at local (e.g., Raptis et al., 2020; Vohra et al., 2021), regional (e.g., Che et al., 2019; Cherian & Quaas, 2020; Zhao et al., 2017) and global scale (e.g., Buchholz et al., 2021; Gupta et al., 2022; Logothetis et al., 2021; Wei et al., 2019a). AOD trends (either from spaceborne or from ground-based observations) in the last two decades indicate robust regional patterns, with decreasing aerosol loads over Europe and US since 2000 and reversed to decreasing since 2010 for East Asia and continuously increasing over South Asia, which is also supported by in situ particulate concentration measurements (Gulev et al., 2021 and references therein). Nevertheless, limited studies have focused on aerosol regime over megacities, which are the major anthropogenic aerosol sources worldwide and, hence, studies specific for megacities provide the direct link between aerosol load and emissions variability. To conduct such studies, it is necessary to have a dense surface-based network or to take advantage of the satellite remote sensing coverage capabilities. Alpert et al. (2012), relying on spaceborne aerosol measurements (MODIS and MISR), investigated the AOD tendencies over the 189 largest cities worldwide for the 8-year period 2002–2010. They found increasing AOD trends for the largest cities in the Indian subcontinent, the Middle

East, and North China, whereas opposite trends were evident in European, northeast US and southeast Asian megacities. In this chapter up-to-date and state-of-the art spaceborne aerosol retrievals (AOD) and dust optical depth (DOD) were used to study local and transported aerosols that can affect air quality in large cities around the globe. Based on the idea of Alpert et al. (2012), we used a finer spatial resolution (0.1°) aerosol product able to reveal aerosol air pollution disparities within megacities and will allow for a more detailed AOD spatial analysis at urban scale and for a period from 2003 to 2020, to have more robust trends.

In order to investigate the aerosol regime of megacities the following scientific questions were addressed in this chapter:

– What is the spatial variability of AOD in megacities at different geographical locations?

– What is temporal variability?

– Are ground-based AOD measuring stations adequate for reflecting the spatiotemporal changes of AOD in megacity scales?

– Are AOD trends related to cities' population changes?

4.1 Methodology

4.1.1 Spatial features

Initially, the geographical distribution of long-term (2003–2020) mean annual and seasonal AOD was derived for a square area spanning of ±1° around the city center (as defined by the UN (2018b) database). The goal of this analysis was to investigate the AOD variability inside the urban areas, as retrieved by spaceborne data. In addition, visual inspection of aerosol distributions over 1°x1° areas and the identified patterns were used for the first qualitative classification of megacities (Section 4.2.1). The main advantage of the MIDAS AOD dataset is the high spatial resolution (of 0.1°) and the daily data availability. However, there were challenges during averaging regarding the data availability, and for this reason temporal availability criteria were applied. Every seasonal mean value was calculated when at least 9 days were available (1st threshold applied), whereas the annual means were computed when at least three seasonal means were calculated (2nd threshold applied). The choice of the 9 days was made after conducting sensitivity analysis on data availability limitations for calculating AOD trends. Based on the filtered year-by-year seasonal and annual means, their respective long-term averages were calculated. In Fig. 4.1, the geographical distributions of the annual (Fig. 4.1b) and seasonal (Fig. 4.1d) long-term averages are illustrated for the megacity of Tokyo. Comparing the AOD field ±1° around the city's center (black circle) with the corresponding Google Earth satellite map (Fig. 4.1a), higher values of mean AOD can been seen over the urban

agglomeration of Tokyo, with respect to the surrounding area, throughout the year (Fig. 4.1 b, d). The blank boxes are pixels that do not fulfill the applied criteria for data availability or data are not available. This example case demonstrates the applied methodology as it will be explained in the following sections.

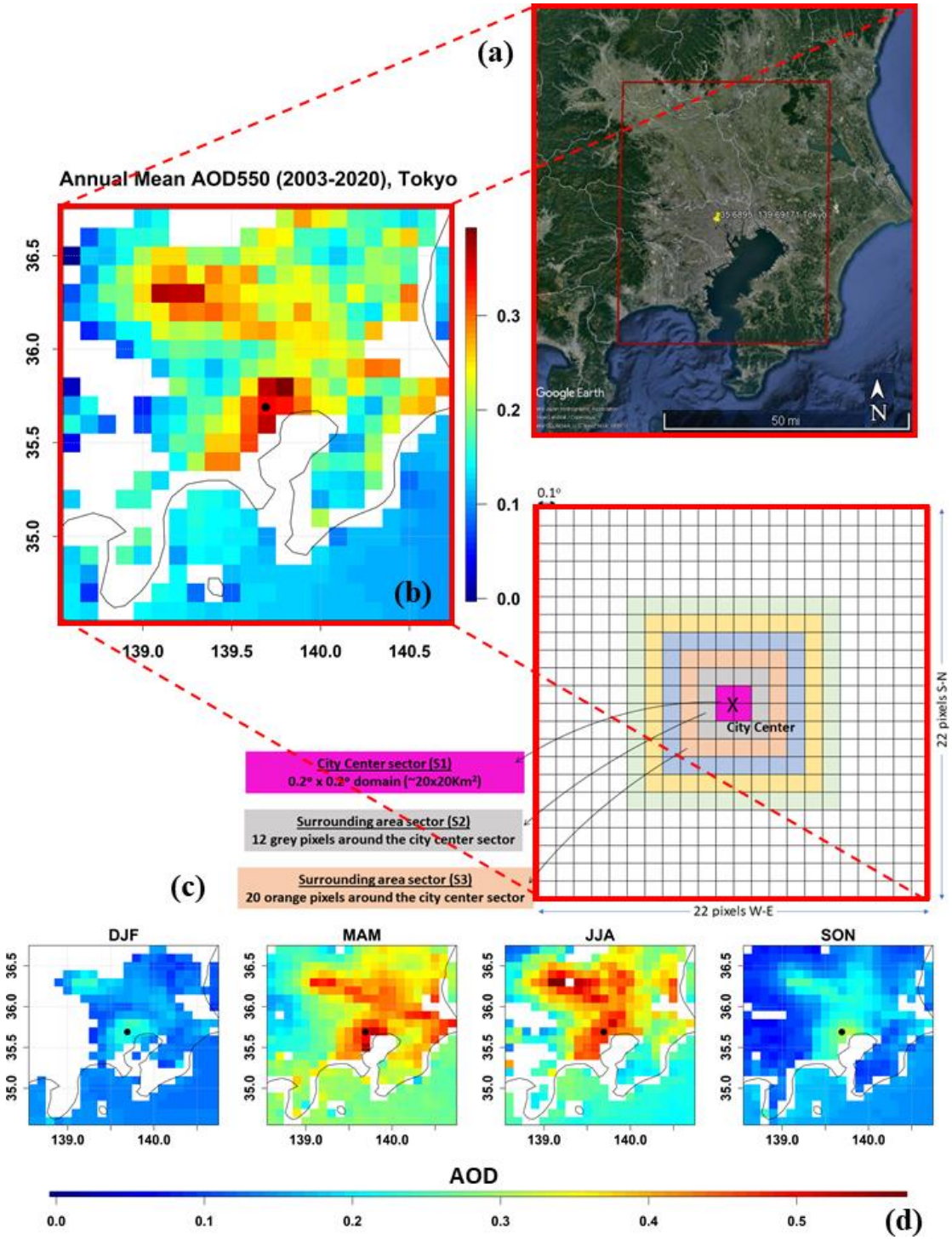

Figure 4.1 (a) Geographical limits of the study area for the megacity of Tokyo on © Google Earth maps, © Google Maps. **(b)** Geographical distribution of the long-term (2003–2020) annually averaged AOD for the broader area of Tokyo megacity. **(c)** Spatial representation equal lat/long grid of AOD data and the sectors under investigation with different colors. **(d)** Geographical distribution of the seasonally averaged AOD for the broader area of Tokyo megacity. Blank pixels do not fulfil the data availability criteria. The black circle denotes the pixel of the megacity center.

To investigate further the spatial AOD variability, we quantified the AOD gradients between the city's center and the surrounding areas. The square area of each city was divided into six different sectors (Fig. 4.1c). Sector 1 (or S1) is the 4-pixel area that encompasses the city center. The daily AOD time series has been constructed by calculating the AOD median for each sector under investigation. Median was selected rather than mean for AOD aggregation, as a non-parametric statistic of central tendency, accounting for the not normally distributed AOD data at those spatial and temporal scales (Sayer & Knobelspiesse, 2019). This aggregation process increased the data availability compared to the single pixel approach. Following the previous procedure with filtered seasonal and annual means, the long-term average AOD for every sector was derived. An example for Tokyo is given in Fig. 4.2. For this megacity, a mean AOD value ~ 0.35 was found over the city's center and decreasing mean AOD values moving towards the outer sections. Although a uniform approach like this ignores the effect of topography (mainly mountains and sea) that breaks the symmetry around many cities, it could be considered an indicator of the spatial distribution of AOD. It should also be highlighted that the "city center" area could have different characteristics and be wider than the area assumed in this approach. These assumptions are used only to make the results comparable, and studies focusing on a small number of cities should make a specific division for each case. To give a single number that will describe the spatial gradient of AOD field from megacities center to the surrounding area, linear regression was performed to the sectoral annual AOD averages in order to calculate the AOD changes per 0.1° along with their statistical significance. The results then were expressed in Δ(AOD) per 1° and finally were converted in Δ(AOD) per 100 km (see next paragraph) and were used for a categorization of the megacities.

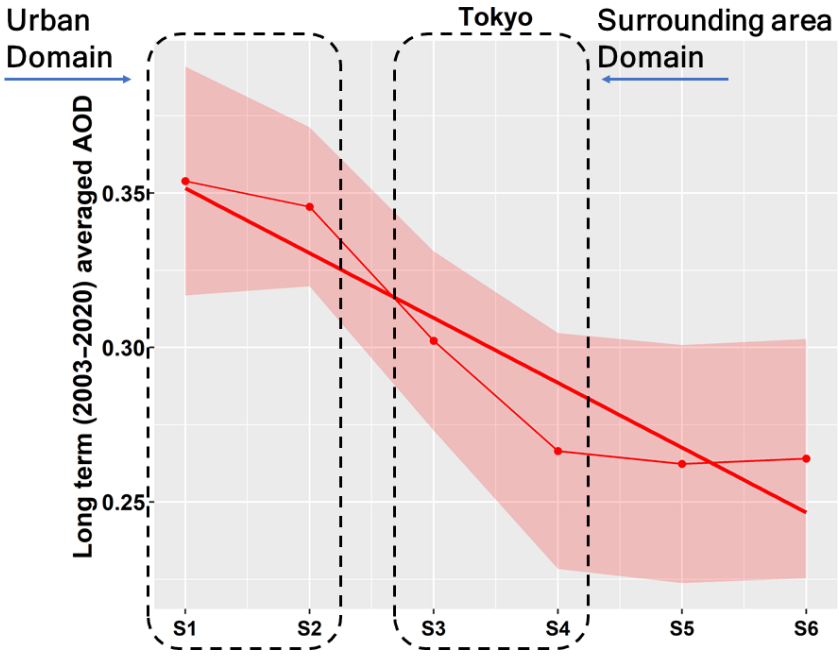

Figure 4.2 The long-term average of AOD (red points) for Tokyo megacity for the six different sectors considered around every megacity center. The shaded area denotes 1σ. The solid red line is the regression line resulted from the six points.

Another source of uncertainty for the unified pixel-based approach that was followed for all cities would be the east-west (E-W) direction size of the pixel. While the pixel size in the north-south (N-S) direction is the same (~ 110 km for 10 pixels = 1°), this is not the case in the E-W direction. More than 50% of the cities are located at absolute latitudes 15–45° (Fig. 4.3a) with a median size of 10 pixels (= 1°) in E–W direction of 95 km (Fig. 4.3b) and with the majority of the cities (over 75%) within the ±10 km limit. Even for the high latitude cities (~ 60°), the E–W size of the 10 pixels (= 1°) is ~ 65 km (~ 2/3 of the median). This difference for the high latitudes cities has been considered in the subsequent two-domain analysis (see Sect. 4.1.2), by including additional pixels in the analysis. For the six-sector analysis, we expressed the single measure of the AOD gradients in terms of distance to account for the difference in the east–west direction. We derived the equivalent distance of the 1° for every city by taking the mean of 110 km size in the N–S direction and the distance in E–W direction (Fig. 4.3b) and subsequently we converted the single measure of the AOD gradients from Δ(AOD) per 1° in terms of distance in Δ(AOD) per 100 km. Finally, Fig. 4.3c shows the distribution of cities elevation, a parameter that has also been considered in the interpretation of the results.

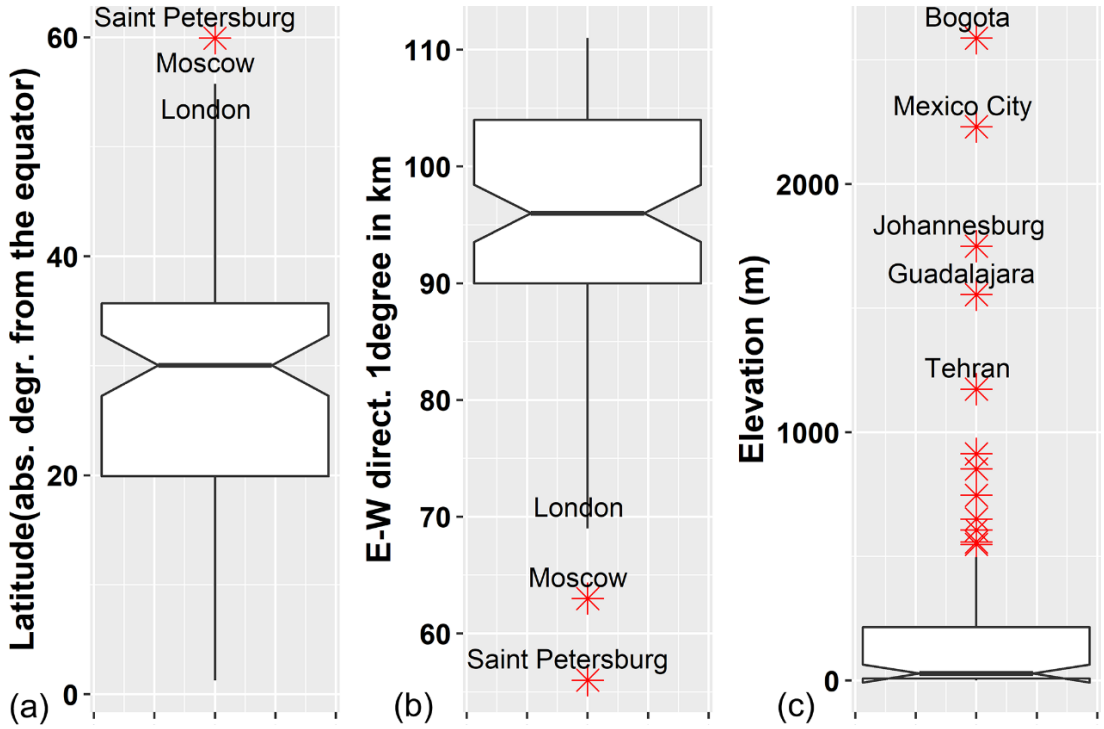

Figure 4.3 The distribution of the absolute values of megacities latitude **(a)**. The distribution of the equivalent length of 1° east–west (E–W) direction in km **(b)**. The distribution of megacities elevation in m **(c)**.

4.1.2 Temporal variability and long-term averages

To investigate the temporal variability of AOD and derive the long-term mean values, an area of 0.4° x 0.4° (4 x 4 pixels, S1 and S2 combined) was considered as representative of the urban agglomerations, denoted as urban domain hereafter (Fig. 4.4). In the same manner as in six-sector analysis (Section 4.1.1), the daily AOD time series has been constructed for the urban domain by

calculating the AOD median. Filtered (the same temporal criteria as in Section 4.1.1) annual mean AOD values were calculated and based on them, the long-term (2003–2020) annual mean values were calculated for the urban domain. The AOD interannual variability and decadal trends for the urban domain were derived, and the methodological details are described in the following subsection. A 4 x 6 pixels area (instead of 4 x 4) was considered for high latitude cities (London, Moscow, and Saint Petersburg) to have comparable areas for all cities. The differences in annual mean AOD were 1–5% compared to the same results without making this correction. Despite the small increase in data availability (~ 10%) when this correction was applied, the trend calculations remained stable. In general, the uncertainties introduced due to the pixel size are minor compared to those associated with the data availability.

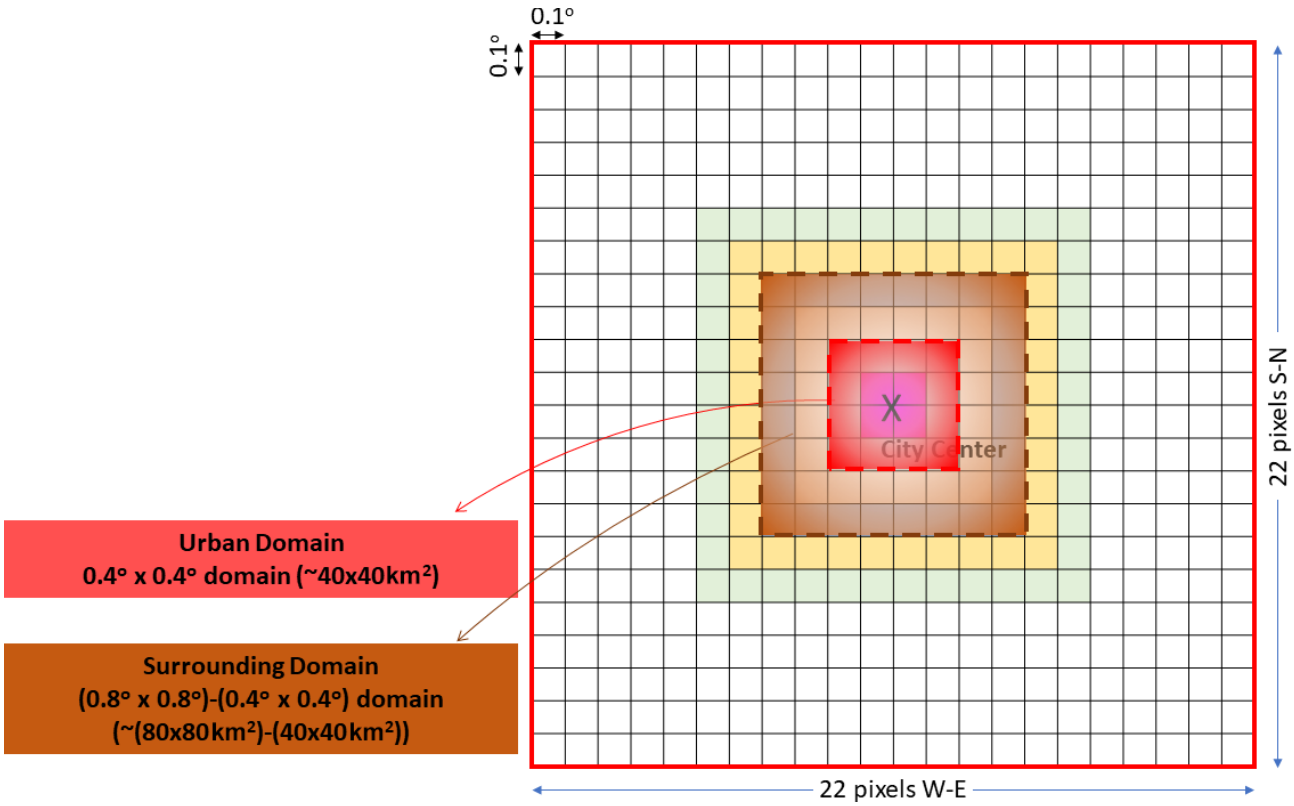

Figure 4.4 Spatial representation of equal lat/long grid of the AOD data and the urban domain (red) and surrounding area domain (brown) under investigation.

4.1.3 AOD interannual variability and trends

The linear trends were calculated by using simple linear regression for the filtered annual mean values when at least 10 years (out of 18) were available. The statistical significance of the trends was assessed by performing the t -test. In Fig. 4.5, we are presenting an example for Tokyo. The red and brown curves correspond to the annual means for the urban and surrounding domains, respectively, the shaded areas represent the standard deviation, and the same-colored lines denote the calculated linear trends. For this interannual time series, declining AOD trends are evident both for the urban and the surrounding domains of the Tokyo megacity.

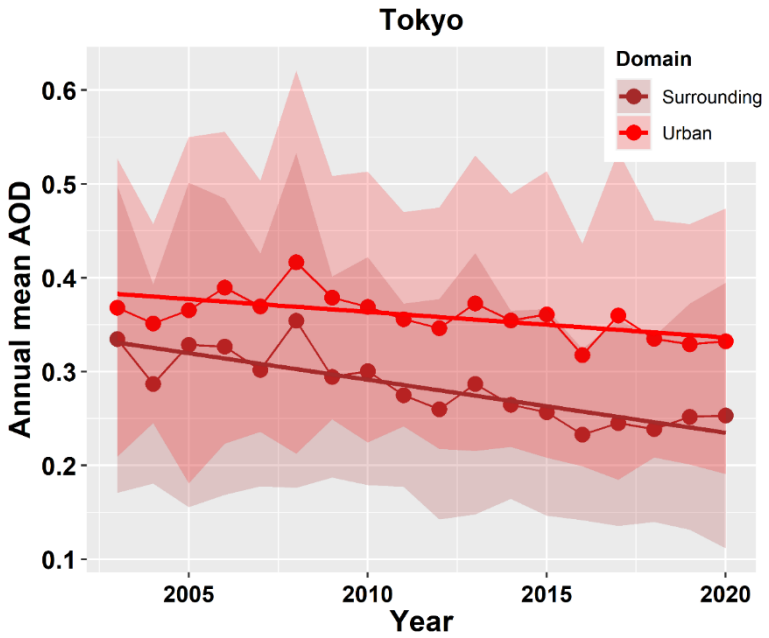

Figure 4.5 Annual mean AOD values for the Tokyo megacity (red points) and the surrounding area (brown points) and the corresponding standard deviations (shaded areas). The linear trends are depicted with the straight lines.

4.1.4 AOD intra-annual variability

Monthly mean AOD values were calculated when 3 days were available. From those filtered monthly AODs, the long-term monthly mean AOD values were derived, to assess the intra-annual variability of aerosol loads for every city's urban domain. As an example, the intra-annual variability for the megacity of Tokyo is given in Fig. 4.6. To give a single measure of AOD intra-annual variability, the temporal coefficient of variation (CV) was derived. The mean and the standard deviation (SD) were calculated for cities with at least nine monthly values, and then the temporal CV was calculated using the following formula:

$$\mathrm{CV} = \frac{\mathrm{SD}}{\mathrm{mean}} 100\% \qquad (4.1)$$

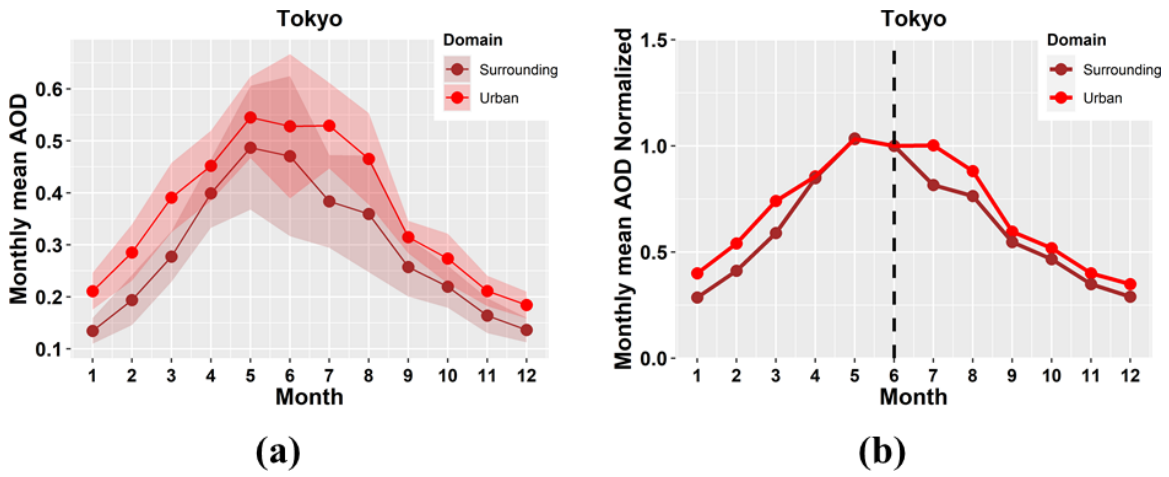

Figure 4.6 (a) AOD intraannual variability for Tokyo megacity (red line) and the surrounding area (brown line). **(b)** Normalized monthly mean AOD values with respect to June mean AOD value.

4.1.5 Spatiotemporal variability

To investigate the spatiotemporal AOD variability, the long-term mean AOD values and the linear trends were also derived for a second domain corresponding to the surrounding area of the urban agglomerations (brownish cells in Fig. 4.4). This domain (surrounding domain hereafter, Fig. 4.4) is the remainder from a broader 8 x 8 pixel domain around the city's center after eliminating the urban domain (4 x 4 pixels). Again, for high latitude cities, extra pixels were considered (12 x 8 pixels) adjusting for different pixel area, but even smaller differences were observed (1–4%), with respect to those found for the urban domain considering this change.

4.1.6 Megacities' population interannual variability and trends

To identify possible links between cities demographic temporal changes and AOD temporal changes for the last two decades the annual UN population data (Section 3.5) were analyzed in conjunction with satellite derived annual mean AOD values representative for every city.

The filtered annual mean AOD values (see Section 4.1.1) and their standard deviation for Kolkata city are presented in Fig. 4.7 (red points and red shaded area, respectively) along with AOD linear trend and its statistical significance. An example of the 18-year population counts time series is given with black points in Fig. 4.7 and the calculated linear trend (dotted black lines). The aim of this analysis was to identify cities with significant population changes and if those changes are related with corresponding AOD changes.

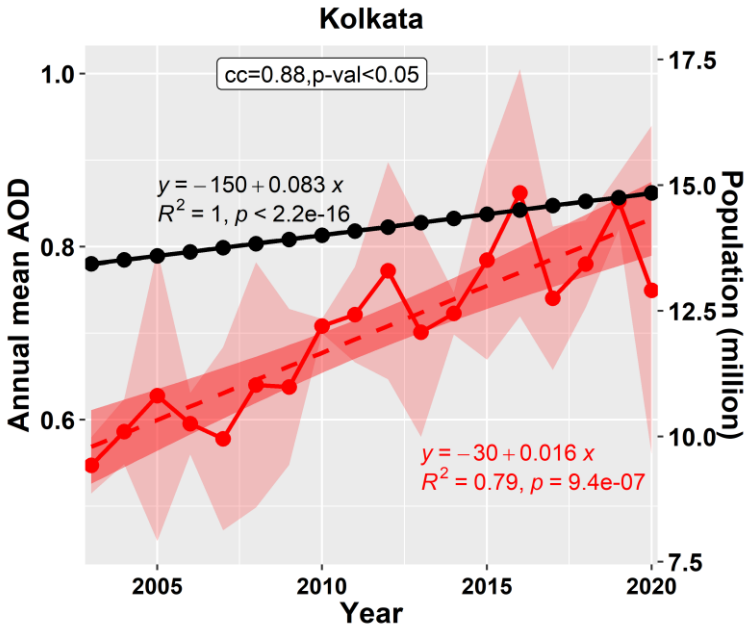

Figure 4.7 Time series of annual UN population estimates (black points) for Kolkata, India. Linear regression line (dotted black lines) is depicted for the study period 2003-2020. Annual mean AOD values (red points) between 2003-2020 for the urban domain of Kolkata and their standard deviation (red shaded area) are provided along with linear regression line (dotted red line). The annotation box provides the Pearson correlation coefficient (cc) and its statistical significance between annual population and mean AOD values.

4.2 Megacities' spatial AOD characteristics

In this section, megacities' AOD spatial variability has been investigated and used as a proxy for cities' classification.

4.2.1 Geographical distribution

As already mentioned in Section 4.1.1, the aim of deriving the geographical distribution of the 18-year period mean annual and seasonal AOD at the original spatial resolution (0.1°) of satellite retrievals over 1° x 1° area around every city's center, was to investigate the AOD variability inside and around cities by the visual inspection of those geographical distributions. An example of the analysis performed is given for Tokyo megacity in Section 4.1.1. The same approach was followed for all the examined cities. The first important result of this analysis was that the comparison of the AOD fields (±1° around cities' centers) with the corresponding Google Earth maps confirms that the selection of the 4 x 4 urban domain is representative of cities' urban agglomerations and the remainder up to 8 x 8 pixels area is representative of cities' surroundings. Additionally, by examining the spatial AOD heterogeneities between the urban and surrounding domains for all megacities, interesting features were found, which led to their first qualitative classification.

Out of the 81 cities, 53% are coastal and 47% are inland. This classification is important, as coastal cities are related with low data availability –due to satellite retrieval algorithm restrictions– and most cities that are not present in the following results are costal. One group consists of high-elevated (> 2000 m) cities such as Mexico City and Bogotá. Those cities are characterized by low data availability and for the available pixels, the AOD values are very low, which is not consistent with the GB measurements (see Section 4.5), thus, they were excluded from the spatial gradient analysis. Another group contains inland cities adjacent to large deserts where dust regularly dominates the aerosol mixture (Cairo, Tehran, Riyadh, Baghdad, and Khartoum).

Cities with few blank pixels (< 50%) within the defined limits are clustered in three distinct groups. There are cities where the AOD field decreases from the central sector towards the surrounding areas (~ 60% for coastal and ~ 35% for inland). This is always the case for the MMA group of megacities. For several cities (~ 40% for coastal and for inland), an opposite gradient is found, attributed to the higher anthropogenic activities (e.g., industrial zones) in the outer domain. Finally, in the third category only inland cities (~ 25%) are grouped, where a uniform distribution of AOD exhibits a weak spatial variation. This is a qualitative classification, based on the data at the original spatial resolution at 0.1°. To give a quantitative measure of this spatial variability and to reduce uncertainty compared to the singe pixel approach, the six-sector and two-domain analysis was performed (see Section 4.2.2).

4.2.2 Long-term means and spatial variability

One of the objectives of this analysis was to take advantage of the high spatial resolution (0.1°) of MODIS AOD product to assess disparities in aerosol air pollution exposure levels within those high-risk communities. The aggregation of the AOD for the different sectors and domains that has been applied (see Sect. 4.1.1 and 4.1.2), increases confidence in these results relative to the single pixel approach. It must be pointed out here that the combination of the local topography and the location of the anthropogenic activity outside the examined cities (industrial zones, nearby smaller cities) distorts the spatial AOD distribution, highlighting the possible inhomogeneity of the city sectors or domains of the surrounding area we have used.

Spatial (six-sector) analysis

To give a single measure of the AOD gradients (i.e., sharp, or smooth) in the vicinity of the megacities, a linear fit was applied to the six sectoral 18-year mean AOD values. The slopes are expressed as Δ(AOD) per 100 km and along with their statistical significance are presented in Fig. 4.8. Negative values indicate that greater values of AOD were found in the city center and are denoted with blue color. Positive values are related to higher AOD values moving away from cities' center and are denoted with red color. Due to low data availability, 24 cities were discarded from the analysis. The MMAs and cities with high elevation (> 2000 m) were also excluded from this spatial gradient analysis. In Appendix A for every city, the mean AOD values for six sectors are given, normalized with the 18-year mean value of S1 (Fig. A1).

For most megacities (~ 65%), lower mean AOD values resulted for the surrounding areas with respect to the city's center (i.e., negative Δ(AOD)). This percentage is raised to ~ 75% when only the statistically significant results are considered. The largest values of negative AOD gradients were found for Xian (China), Alexandria (Egypt) and Santiago (Chile), attributed to complex topography (high mountains and coastal areas). On the other hand, only 19 (~ 35%) cities have larger mean AOD values in the surrounding sectors (i.e., positive Δ(AOD)) and most of them are in China and India. The reason that higher AODs were recorded in the surrounding sectors for most of those cities is that they are enclosing smaller-scale cities (MMAs have been already excluded from the analysis), which, however, host significant sources of anthropogenic aerosols. For example, Shanghai is the Chinese city with the largest positive AOD gradient attributed to the influence from the nearby megacity Suzhou at the west and the Pacific Ocean at the east part of the city.

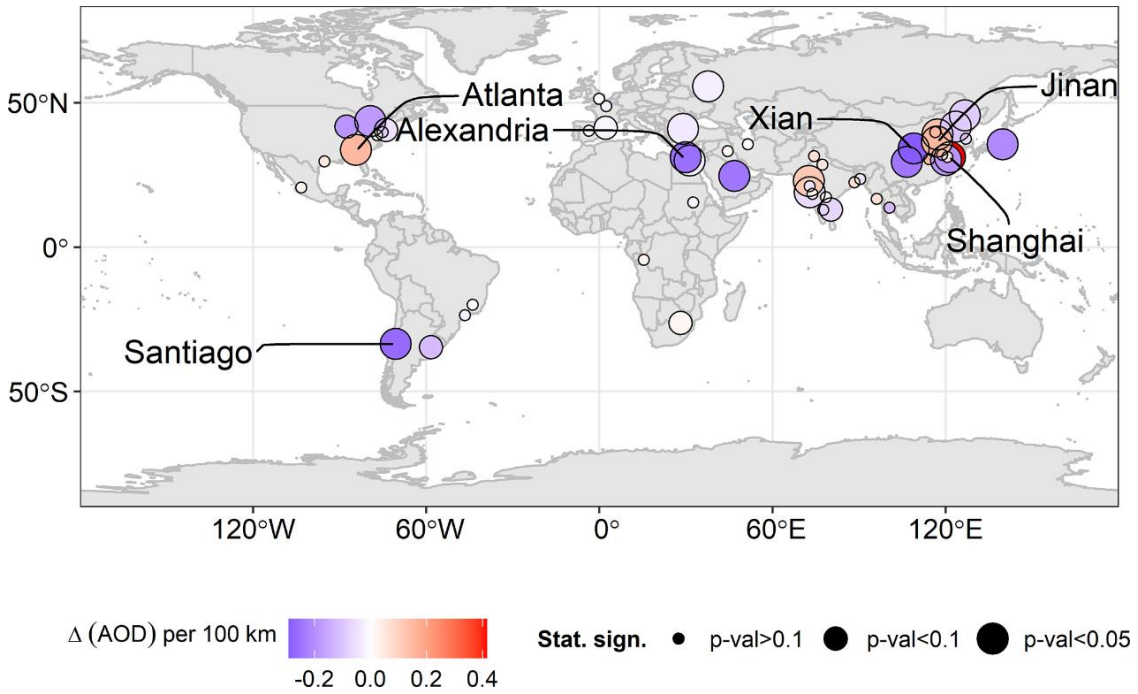

Figure 4.8 Spatial AOD gradients per 100 km (1(AOD) per 100 km) from city center to surroundings. The circle radius is proportional to the statistical significance of the trends. The three cities with the greatest negative AOD gradient are Xian, Alexandria, and Santiago and the three cities with greatest positive AOD gradient are Shanghai, Jinan, and Atlanta.

Two-domain spatial analysis

The geographical distribution analysis (Section 4.1.1) revealed that the 4 x 4 pixels area is a domain well fitted to the cities' urban agglomeration (urban domain). The remainder between the urban domain and an area up to 8 x 8 pixels (surrounding domain) was found also to be representative for the surrounding area of all cities. The results for this two-domain analysis are presented in this section.

The geographical distribution of the long-term mean AOD values for the urban domain is presented in Fig. 4.9. Four cities (BOGO, HCMC, KUAL, SING) are not included due to low data availability. Low mean AOD values were found for European and American cities in contrast to Asian and African cities. Specifically, the larger mean AOD values (> 0.5) were recorded for Chinese cities, with Indian cities following, since both areas are densely populated and with high industrial activity. Many megacities (mostly Asian) lying in the proximity of great deserts are also influenced by natural aerosols of desert dust (Gkikas et al., 2022; Proestakis et al., 2018). To investigate further this feature and quantify this influence, the long-term mean DOD, and the DOD to AOD ratio – as a metric of dust contribution in the aerosol mixture – were derived using the MIDAS DOD and AOD products and the obtained results are presented in Fig. 4.10. Significant dust contribution (~ 20–40%) was found for the western Chinese cities, with mean DOD values ranging from 0.1 to 0.2, that were influenced by the nearby arid and semi-arid regions (namely the great Gobi Desert and the Taklamakan Desert). For Indian and Pakistan cities around the Thar Desert (India–Pakistan borders), even bigger dust contribution was found ~ 40–50% and mean DOD values ranging from 0.15 to 0.35. The greatest dust

contribution (up to 60%) with significant mean DOD values up to ~ 0.4 was found for the African cities of Khartoum and Cairo and for all Middle East cities (Riyadh, Baghdad, and Tehran) that are influenced by the great deserts of North Africa and Middle East.

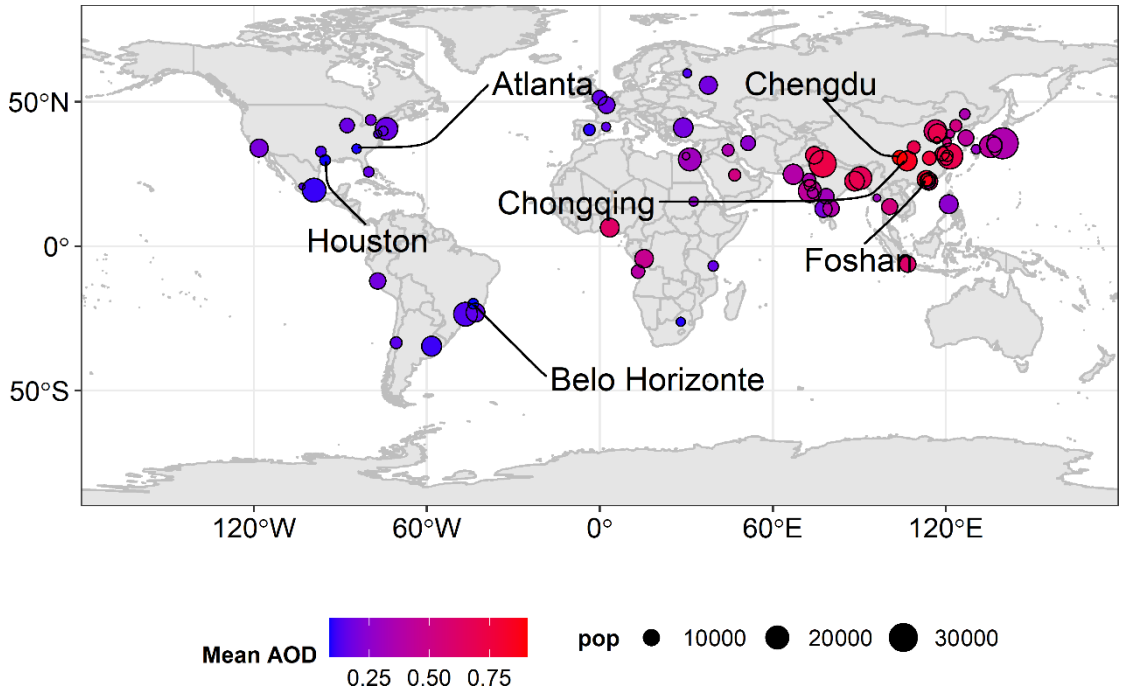

Figure 4.9 Long-term (2003–2020) mean AOD for megacities urban domain (~ 40 km x 40 km around cities center). The circle radius is in proportion to cities' population. Three cities with greatest mean AOD are those of Chengdu, Foshan, and Chongqing and the three cities with lowest mean AOD values are those of Atlanta, Houston, and Belo Horizonte.

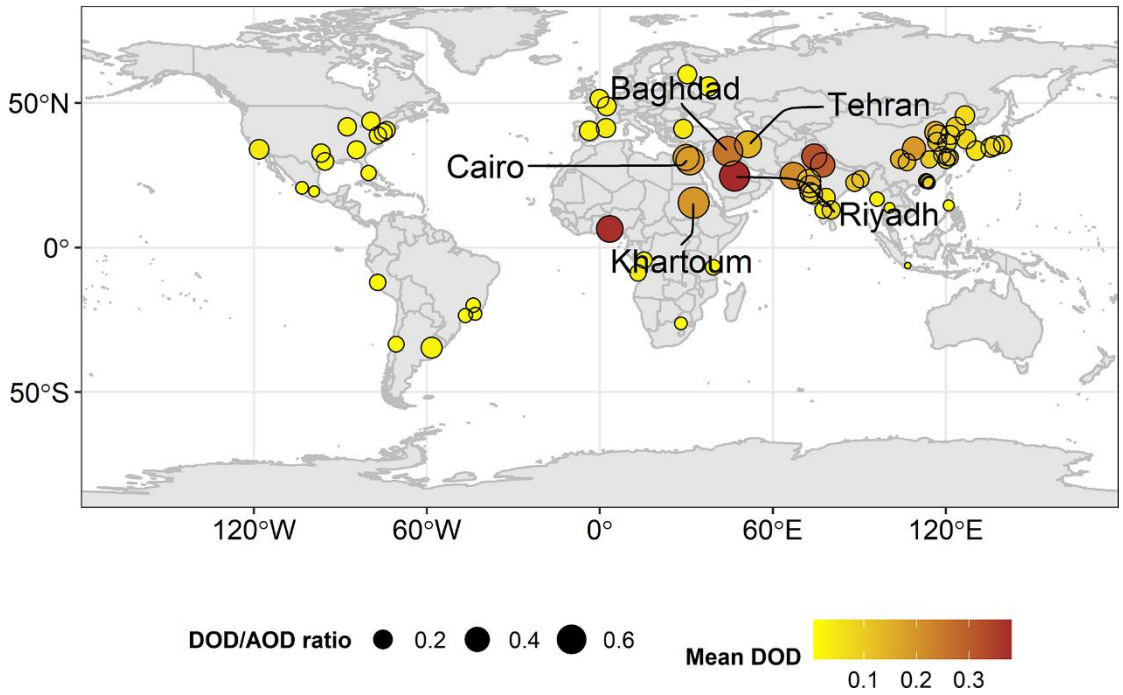

Figure 4.10 Long-term (2003–2020) mean DOD for megacities urban domain (~40 km x 40 km around cities center). The circle radius is in proportion to the DOD to AOD ratio. Five cities with the greatest dust contribution (mean DOD/AOD ratio) are Khartoum, Riyadh, Baghdad, Cairo, and Tehran.

To contrast the mean AODs for the urban domain against those of the surrounding area, we have reproduced a global scatterplot with their matchups, presenting also ancillary information (i.e., continent, population, coastal/inland) (Fig. 4.11). Points residing on top of the one-by-one line indicate cities with homogeneous spatial AOD distributions (inside and surrounding area), whereas above/below the equality line, AODs are higher in the surrounding and urban domain, respectively.

Almost 60% of the cities have greater mean AOD values over the urban domain and 40% have greater values over the surrounding domain. There are more cities with differences exceeding 10% when higher values of AOD are recorded over the urban domain compared to the opposite case. In general, the obtained results are in line with those of spatial gradients (sectoral analysis, Fig. 4.8), while almost all cities (apart from four) are included here due to the greater data availability for the two-domain approach. Shenzhen, Osaka, and Jakarta show the biggest decrease of 0.15–0.25 (~ 25–35 %) in a range of few kilometers from their center. On the other hand, Chinese cities (Shanghai, Suzhou, and Qingdao) and Atlanta have greater mean AOD values in the area surrounding the center.

Additionally, the classification of the cities according to their geographical location (in line with Fig. 4.9) came up, according to the obtained results for both domains. All European and American cities yield mean AODs ranging from 0.08 to 0.20, in contrast to African and Asian cities in which the corresponding levels range from 0.25 to 0.9 (apart from Bangalore (0.2), Dar es Salaam (0.17) and Johannesburg (0.09)).

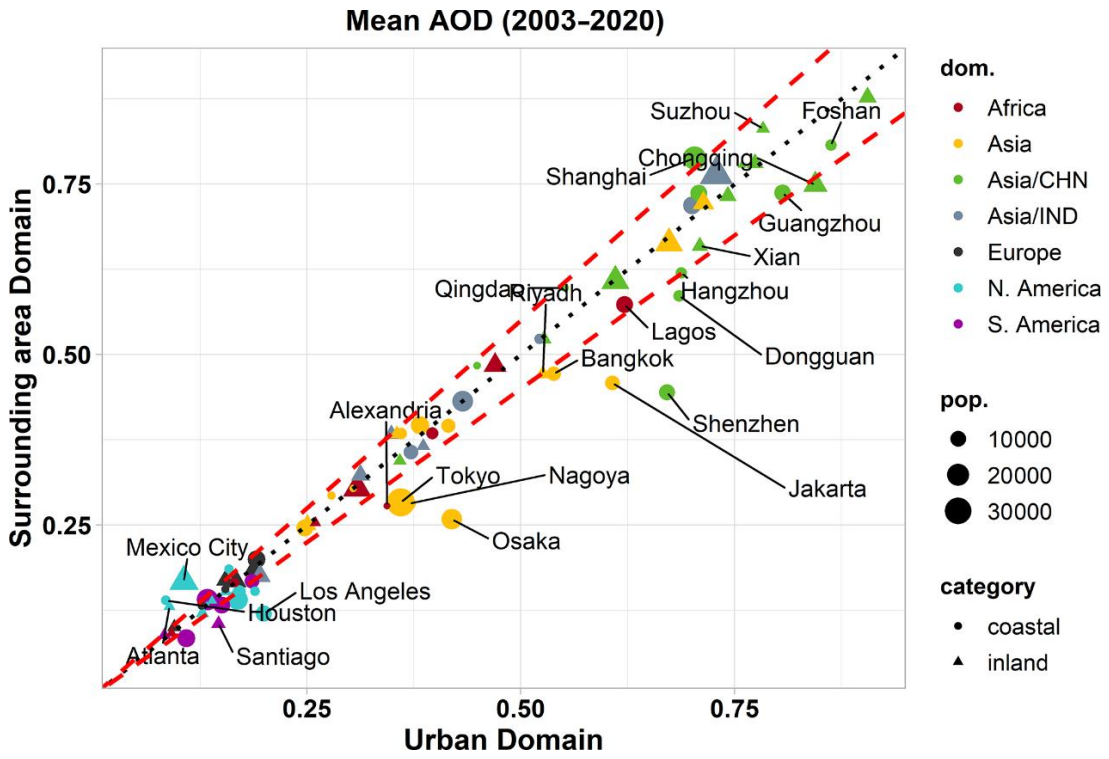

Figure 4.11 Long-term (2003–2020) mean AOD for megacities' urban domain (~ 40 km x 40 km around cities' centers) versus the surrounding area domain. The name of the cities with difference in mean AOD greater than ±0.04 between the two domains is depicted. The dotted black line is the identity line, and the dashed red lines denote ±10% difference in mean AOD between the two domains.

4.3 Temporal variability

4.3.1 AOD trends

The geographical distribution of the AOD changes per decade (Fig. 4.12, after excluding 11 cities which did not fulfill the temporal criteria) revealed pronounced regional features. The resulted AOD trends for the megacities are reflecting the changes in the anthropogenic emissions, associated with the air quality regulations implemented throughout the years, in the same manner that previous studies have shown the connection of the satellite-observed AOD trends with the implemented mitigation policies in regional scales (Gupta et al., 2022; Zhao et al., 2017).

For all European and US/Canadian cities, decreasing AOD values were found (up to ~0.03 and ~0.07 per decade, respectively), in accordance with the AOD decrease in western Europe and eastern North America that has already been reported in the literature, and was associated with a series of air quality control measures that have been implemented (Gupta et al., 2022; Zhao et al., 2017). While negative trends have been found in this study for Los Angeles, other recent studies report small positive trends for the western United States of America that are associated with reduced precipitation and increased fire activity over the area (Cherian & Quaas, 2020; Gupta et al., 2022). However, the latter studies refer to much wider areas and not to the city of Los Angeles, which indicates that the trends in the city may be related to different mechanisms (i.e., reduction of anthropogenic emissions dominates over the increase due to increasing dust and smoke events), relative to the trends over the wider region of the western US. Statistically significant negative AOD trends were found for the eastern Asian megacities, with the highest values (in absolute terms) up to ~-0.3 per decade being evident for the Chinese megacities. This result (net negative AOD trend for the whole study period for Chinese cities) is in agreement with recent studies that reported AOD decrease for eastern China (Gupta et al., 2022), which was associated with the implemented emission control policies. Specifically, for China, while up to 2010 AOD was increasing (e.g., Hsu et al., 2012) due to the rapid economic and industrial development of the country, after 2011 declining AOD trends have been recorded for the central and eastern sectors of the country, related with the reduction in anthropogenic aerosol emissions due to the implementation of emission control measures (Sogacheva et al., 2018; Zhao et al., 2017). According to Sogacheva et al., (2018), the gradual AOD decline after 2011 is more prominent for the highly populated and industrialized southeast China regions, being in agreement with our results.

On the contrary, strong positive AOD trends (ranging from 0.07 up to 0.16 per decade) were found for all megacities in the Indian subcontinent, reflecting the increased industrial and financial development during this period, and is in agreement with previous studies (e.g., Buchholz et al., 2021). In their recent study, Samset et al., (2019), showed that the climate implications of this dipole pattern of

positive AOD trends over southern Asia and strong negative values over eastern Asia observed since 2010 might be strong not only on a regional scale but also for areas away from the sources.

Positive AOD trends were also found for the Middle East megacities, ranging from 0.03 to 0.1 per decade. This finding is in line with the AOD trends that resulted from the analyses of retrievals from different satellite sensors (Che et al., 2019), although negative trends have been reported in the study of Gupta et al. (2022) who analyzed AOD from CALIOP. For the Latin American megacities, the highest AOD trends are positive (~0.03 per decade for Buenos Aires and Lima), reflecting the poor emission control measures over this geographical domain. In recent studies (Buchholz et al., 2021; Gupta et al., 2022), a reduction in AOD was reported for South America, attributed to the decline in forest fires, which might explain the negative AOD trends for the rest of Latin American cities. Sub-Saharan Africa is an area for which AOD decrease has been reported in previous studies, which is opposite to our findings (+0.06 per decade for Luanda and +0.03 per decade for Dar es Salaam). For this area, an increase in AOD was also found by the recent study of Gupta et al. (2022), which was associated with the increase in biomass burning of agricultural activity in the dry season over the area. However, since our study is focused on megacities, our findings may reflect the increasing urbanization in combination with the limited air quality regulations over the area, but further investigation is needed.

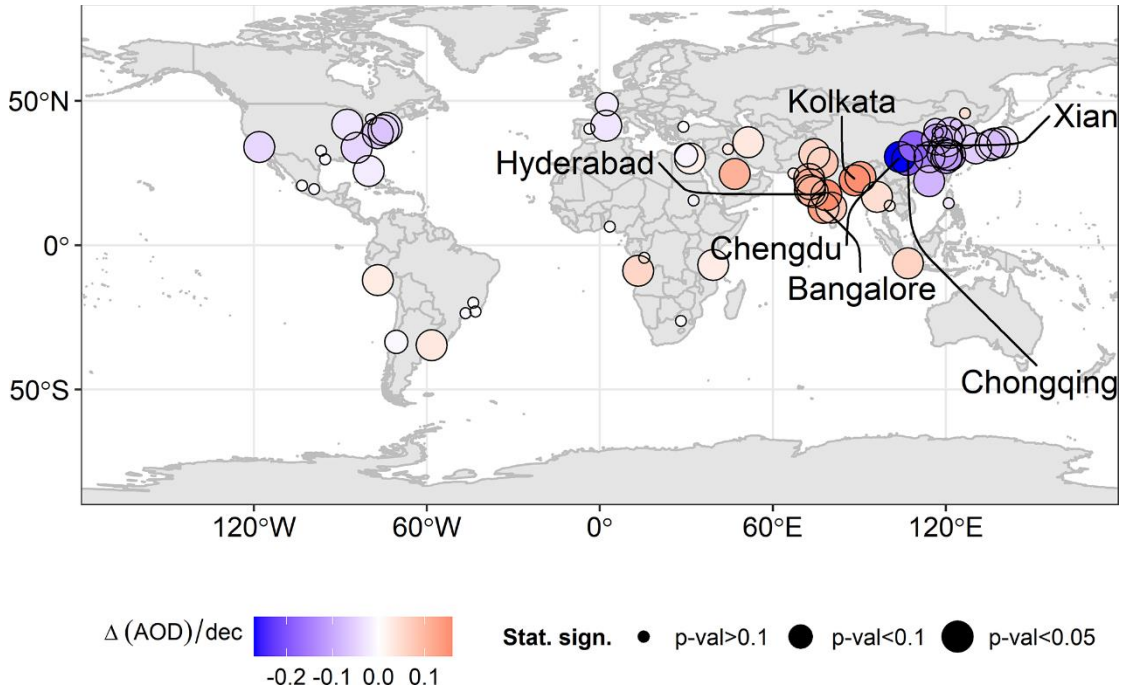

Figure 4.12 Linear trend of AOD per decade for urban domain (~ 40 km x 40 km around cities' centers). The circle radius is in proportion to the statistical significance of the trends. Three cities with greatest increase of AOD are Hyderabad, Kolkata, and Bangalore and the three cities with greatest decrease of AOD are Chengdu, Chongqing, and Xian.

The comparison of the AOD trends against the long-term mean AOD of the urban domain revealed an interesting clustering of cities, according to their geographical location (Fig. 4.13). It has to be pointed

out here that only the statistically significant trends were included in Fig. 4.13, thus ensuring robust and meaningful results.

In all European and North American cities, low AOD climatological values and decreasing trends were found. Note that in some US cities like Atlanta,Washington, Philadelphia and New York, apart from their relatively low mean AOD values (<0.17), considerable negative trends (ranging from -53 to -28%) were recorded.

All Indian cities have positive AOD trends regardless of their mean AOD levels, which span from low to high values. Among them, Kolkata is the city where extremely high mean AODs (0.70) and large positive trends (+22% per decade and the higher in absolute values +0.16 per decade) were revealed. Of particular interest is Bangalore, which has relatively low mean AOD value (0.20), but the maximum positive AOD trend is almost +69% per decade. Bangalore's population increased from 6 million to 12 million during the last two decades, which is one of the biggest population increases for cities at this scale and, thus, it can explain to a large degree the extreme increase of AOD. Meanwhile, financial development in the area is linked more with new technologies and not heavy industry, which partially answers the relatively low mean AOD.

All Chinese cities are subjected to AOD decrease (up to ~ 30%), while at the same time they have the highest mean AOD values ranging from 0.45 to 0.91. Chengdu is the city with the biggest mean AOD value along with the highest AOD decrease of ~ 30% per decade (or ~ 0.3 per decade).

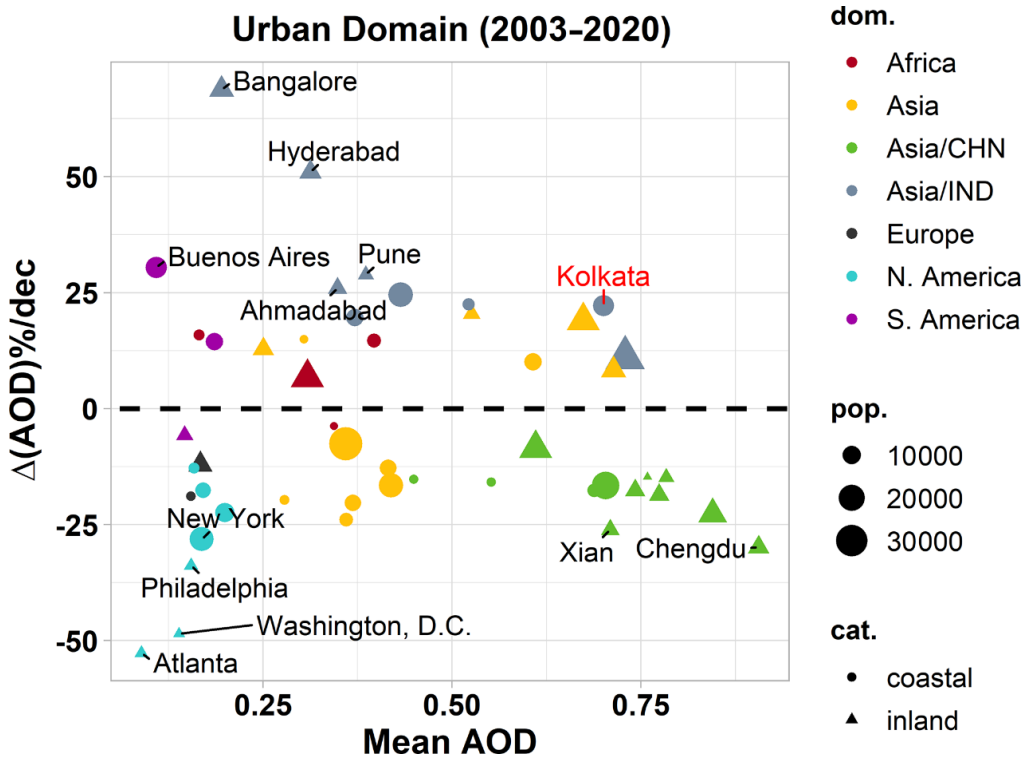

Figure 4.13 AOD decadal changes expressed in percentages (Δ(AOD)%per decade) versus the long-term mean AOD for the urban domain. Only statistically significant AOD trends are presented (P < 0.1). Cities with absolute values of Δ(AOD)% per decade greater than 25% are denoted in the figure.

4.3.2 Intra-annual variability

AOD exhibits strong intra-annual variability (Zhao et al., 2018), which is quite important to be analyzed at megacities' scales to improve our understanding regarding the aerosol-related health effects. The normalized (using the mean AOD of June as reference) monthly mean values for all cities are provided in Appendix A, Fig. A2, classified for the different geographical domains. To investigate the intra-annual variability of AOD at city level, the temporal CV (Sect. 4.1.4) was calculated. The geographical distribution of temporal CV is illustrated in Fig. 4.14, only for cities complying with the defined temporal criteria (four cities were omitted). Low CV values (< 20%) were found for eastern India, most of the Chinese cities and the eastem Mediterranean. The highest CV values (>70%) were recorded for three US cities. To further investigate those results, the relationship between temporal CV and the long-term mean AOD values for the urban domain was examined (Fig. 4.15).

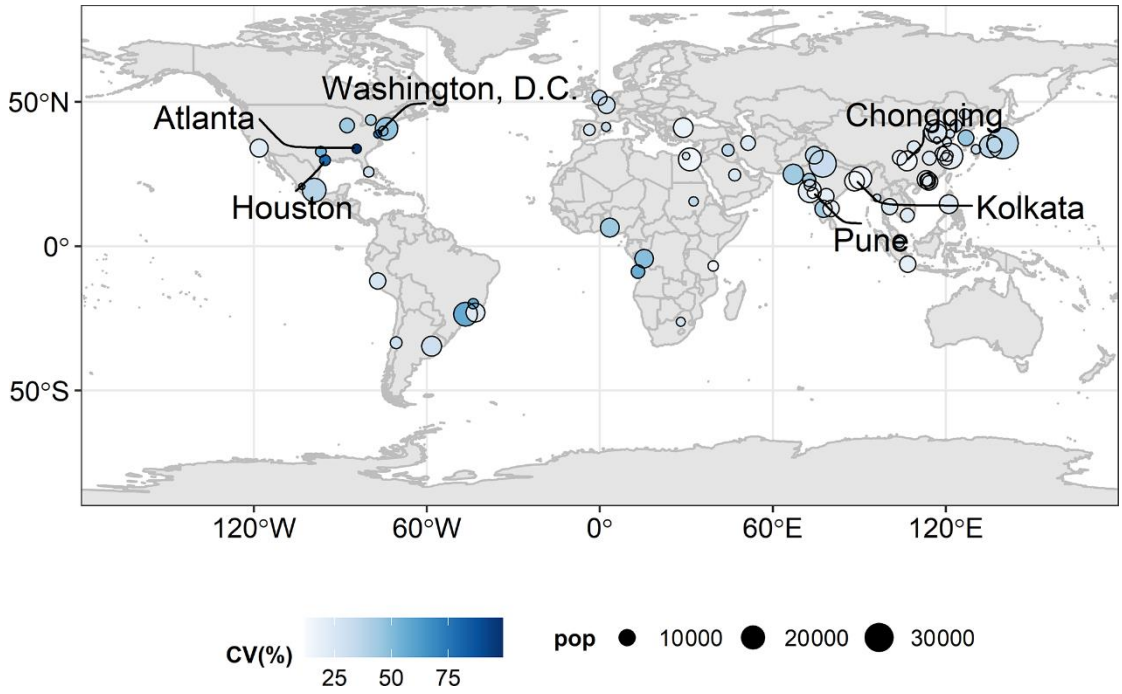

Figure 4.14 Temporal coefficient of variation (CV) of monthly mean AOD (intraannual variability) expressed in percentages for megacities' urban domains (~ 40 km x 40 km around cities' center). The circle radius is proportional to the cities' population. Three cities with the highest temporal CV are Atlanta, Houston and Washington, DC and the three cities with lowest values are Kolkata, Chongqing, and Pune.

A non-linear relationship was found, with the gradual decrease of the mean AOD to be related with increasing CV levels (Fig. 4.15). The greater values of CV (> 50%) were found only in the group of cities with low mean AOD values (< 0.25, with only exception being Luanda) and almost all are US cities on the East Coast. For North American cities, the monthly mean AOD values during the boreal winter are decreasing close to zero and maximized during summer, this resulted in this high intra-annual variability (Fig. A2b) especially for southeastern US cities. These high values of intra-annual variability for southeastern US cities, and most notably Atlanta, are explained by the high AOD values over the area during summer due to secondary aerosol formation by biogenic volatile organic

compound (BVOC) oxidation (Goldstein et al., 2009). For most southern American cities, rather stable values were found throughout the year (Fig. A2c). For moderate AOD levels (0.25–0.50), a limit of 50% was found for the CV values. For the cities with high aerosol loads (> 0.50), which are mostly Chinese cities, the CV values are confined to the limit 10–40 %.

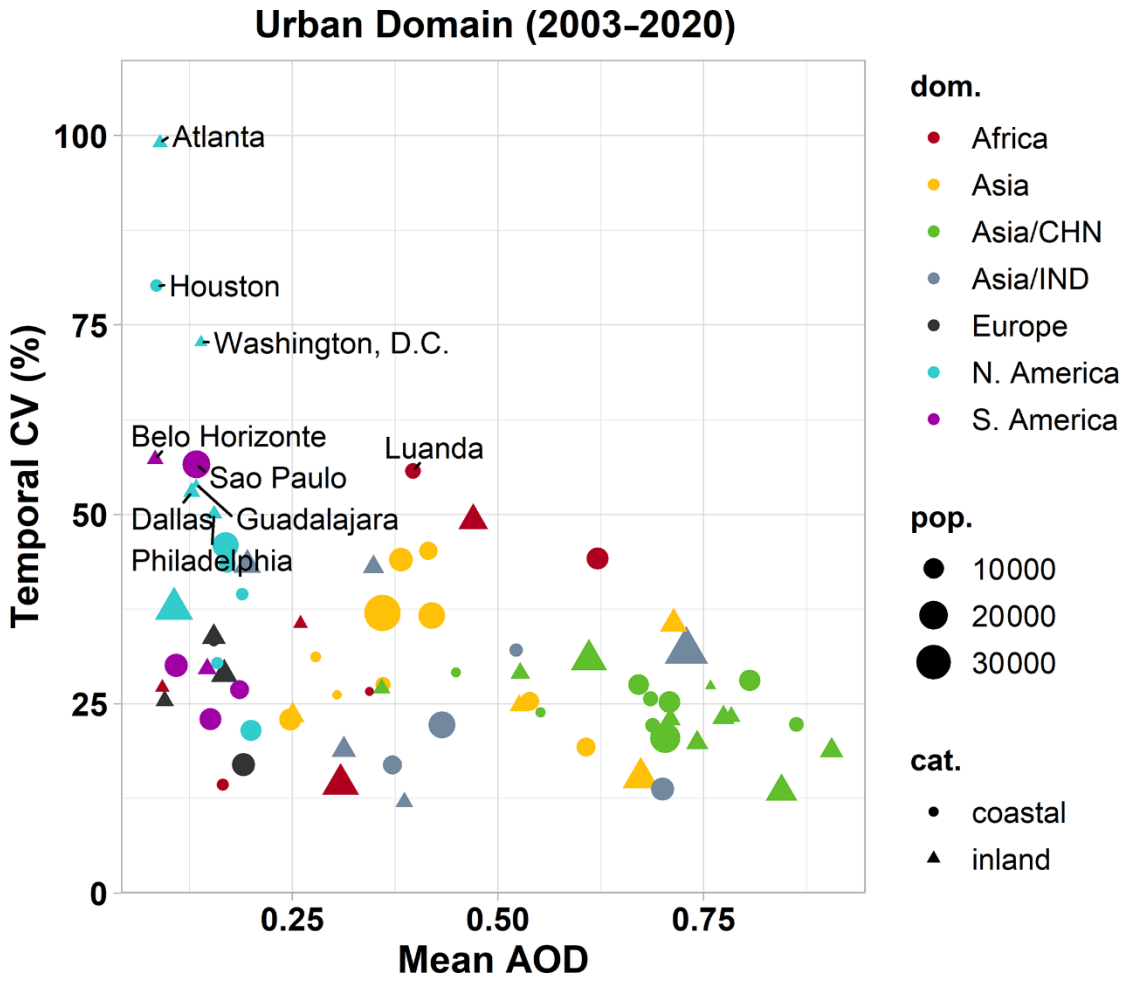

Figure 4.15 Temporal coefficient of variation expressed in percentages (CV %) against the long-term mean AOD for the urban domain. The size and the color of the points denote cities' population and geographical domain, respectively. The shape of the points denotes costal or inland cities.

4.4 Spatiotemporal variability

Towards assessing the AOD spatiotemporal variability, the decadal AOD linear trends for the urban and the surrounding domains were compared (Fig. 4.16). We are presenting only the points in the scatterplot when the AOD trends are statistically significant ($p < 0.1$), both for the surrounding and urban domains (43 pairs). Points residing above/below the identity line correspond to AOD trend (negative or positive) that is higher in the surrounding/urban domain, respectively.

All cities in India exhibit an increase of AOD both in the urban and surrounding domains. The largest difference was found in Hyderabad where AOD trend is 10% larger for the urban domain, indicating an increase of anthropogenic activity within the boundaries of the urban agglomeration. For cities where AOD decreases were found, two groups are shaped. The first one, that has greater AOD

decrease for the urban domain, consists mostly of East Asian cities. Chongqing is the Chinese megacity with the largest difference (~ 20%), reflecting the adaptation of effective measures towards reducing city's aerosols air pollution (Gao et al., 2021). The second group, which consists mostly of the North American cities, has greater AOD decrease for the surrounding domain.

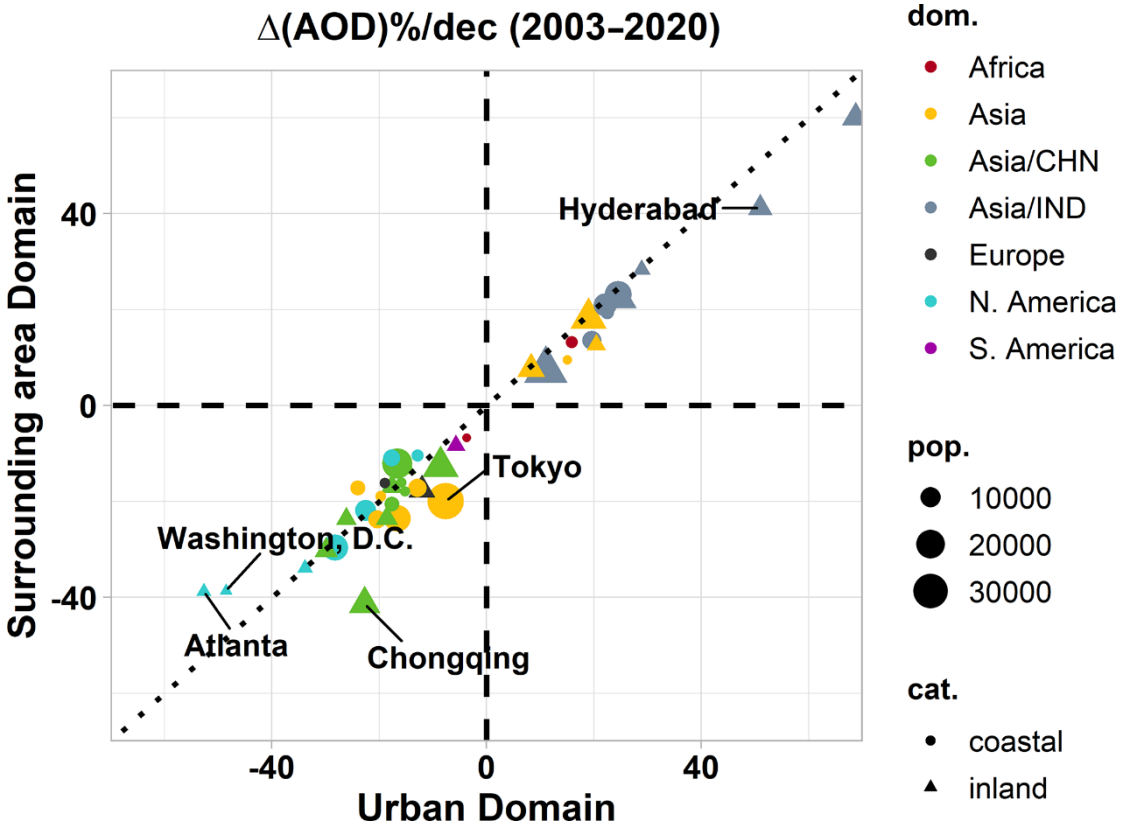

Figure 4.16 AOD decadal changes expressed in percentages (Δ(AOD)% per decade) for the surrounding domain versus the urban domain. Only statistically significant AOD trends are presented ($P < 0.1$). The dotted line is the identity line. Cities with absolute differences of Δ(AOD)% per decade greater than 10% between the two domains are denoted in the figure.

4.5 Evaluation with ground- based (GB) measurements (AERONET)

For cities with available long-term time series of AOD in the 2003–2020 period from GB stations of the AERONET network, an evaluation of the satellite AOD averages and trends was performed. The level 2, version 3 (Giles et al., 2019) daily mean product of AOD at 500 nm was collected for stations with at least 8 years of data within the study period. Using the Ångström exponent, 440–870 nm, the AOD values were interpolated at 550 nm. Table A2 summarizes the information of the 27 AERONET stations utilized. Statistics and trends of ground-based measurements were calculated with the same methodology and data availability criteria applied to the satellite data (see Sections 4.1.2 and 4.1.3). This comparison is separated by the GB stations located within the 4x4 pixel area of the urban domain and those residing in the surrounding domain of a city. The daily averaged AOD product was used from the AERONET stations to derive long-term mean AOD and linear trends, using the same approach as followed with the satellite data. The diurnal AOD variability of the AERONET data was

not considered and this may slightly affect the long-term mean AOD (Smirnov et al., 2002), but it plays a minor role for the calculation of trends.

Regarding the long-term mean AOD (Fig. 4.17), for the urban domain there is a good agreement between the satellite derived and the GB values (correlation coefficient R ~ 0.93). The largest deviations (expressed as percentages) between spaceborne and ground-based AODs are recorded in general for weak-load cities, and those deviations are maximized in the high-altitude city of Mexico (> 2000 m) and in Osaka due to low satellite data availability. There are only few GB stations in the surrounding domain, so the R is not representative. The satellite derived mean AOD is overestimated, but in those cases, the area that was selected for getting the satellite data is considerably large and it is unlikely that the in-situ measurement statistics would coincide with satellite observations statistics.

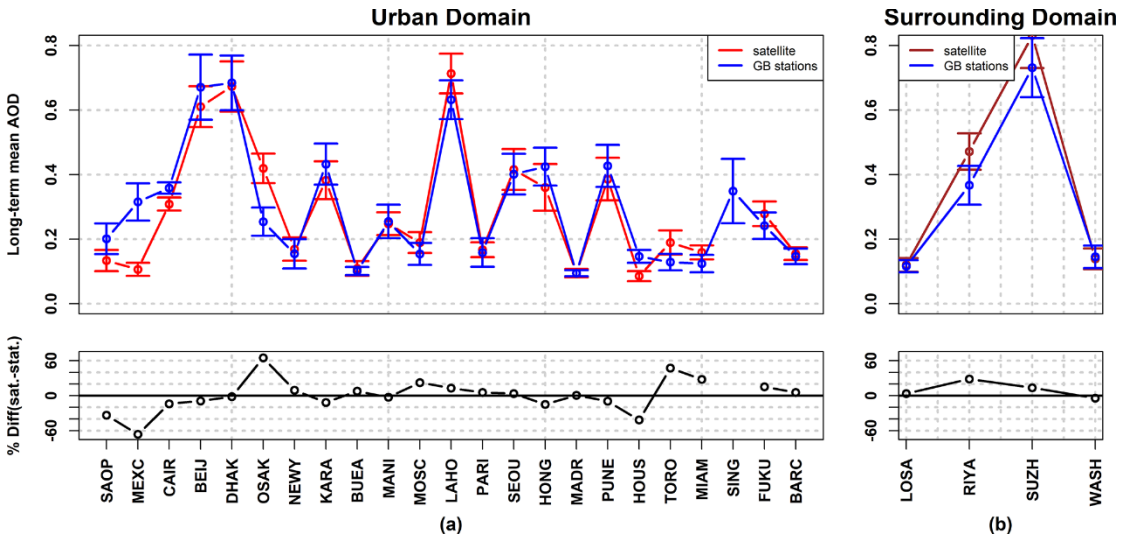

Figure 4.17 (a) Satellite-derived (red line) and GB (blue line) long-term mean AODs and their relative difference expressed in percentage (black line) for the urban domain of cities. **(b)** The same for the surrounding domain (brown line for the satellite-derived values).

A relatively good agreement was also found for the decadal linear trends (Fig. 4.18), with R ~ 0.79 for the urban domain. For 75% of cases, GB and satellite-derived trends have the same sign for both domains. In Fig. 4.18, the results are presented only when both spaceborne and ground-based AOD trends are statistically significant. For the urban domain, all the statistically significant trends have the same sign. For the surrounding domain, the trends' signs differ only for LOSA. This difference can be attributed to the shorter period of measurements at the LOSA AERONET station (8 years). Additionally, in a recent study (Wei et al., 2019c), western North America was found to be the area with fewer sites with the same signs between MODIS- and AERONET-derived AOD trends. Nevertheless, our analysis does not focus on a validation of satellite AOD against AERONET, thus, an exact colocation of the AERONET stations with satellite pixels was not attained. To further investigate the obtained differences, the spatial CV was calculated for the urban and surrounding domain, as the ratio of standard deviation and mean values of the pixel long-term mean AODs derived in

geographical domain analysis. The results are presented in the lower panel of Fig. 4.18 along with the percentage of the available pixels inside the domain under investigation. For LOSA, the greatest value of spatial CV was found (> 50%), which was anticipated, since the spatial extent of Los Angeles metropolitan area is high (including Long Beach and Santa Ana), highlighting the importance of the selection of the GB location.

An additional interesting feature is that the absolute values of all satellite-derived statistically significant trends (Fig. 4.18) have lower magnitude compared to the GB results. This difference in magnitude could be attributed to the domain aggregated satellite values compared to point-derived results of the GB stations, which may smooth out the AOD fields. In a recent study by Logothetis et al. (2021), a sensitivity analysis was performed between coarse (1°) and fine (0.1°) spatial resolution of spaceborne AOD retrievals which revealed AOD trends of lower magnitude for the coarse spatial resolution data. Moreover, the daily satellite value, corresponding to satellite overpass, contains less information compared to the continuous monitoring during daytime of cloudless days of the ground-based photometers.

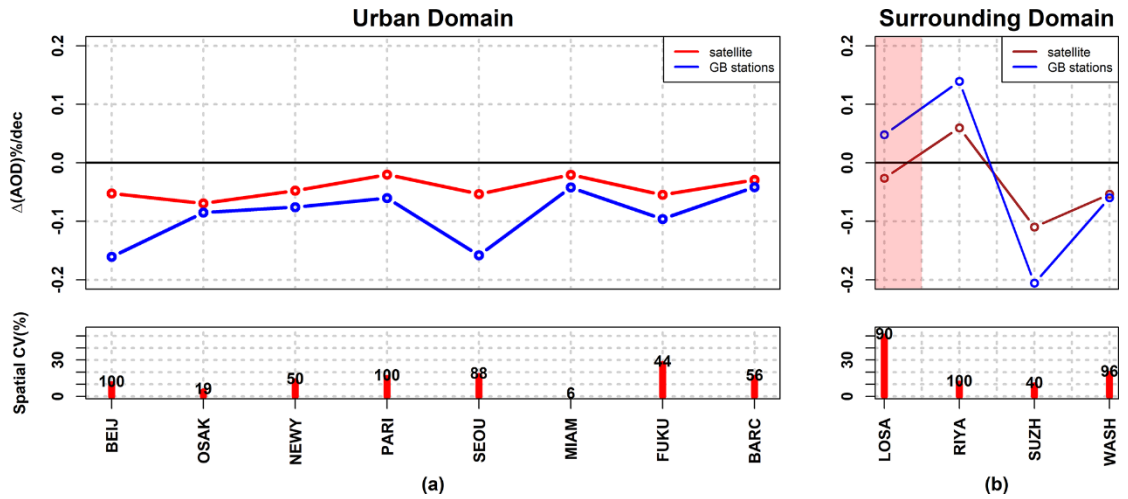

Figure 4.18 (a) Satellite-derived (red line) and GB (blue line) statistically significant (P < 0.1) AOD linear trends for the urban domain and the corresponding spatial CV (red bars) for every city; the numbers on top of the bars declare the pixel availability for the domain. **(b)** The same for the surrounding domain (brown line for the satellite-derived values).

Hence, GB stations are representing the close area around their location and the representativeness of AERONET stations to characterize aerosol load/trends in megacities should be considered individually in each case, according to local conditions.

4.6 Population changes and relation to AOD trends

For all cities but one (Fukuoka), the population for the period 2003-2020 has increased (Fig. 4.19), and those results were found to be statistically significant. Delhi has the greatest increase, almost 7.5 million inhabitants per decade. Thirteen Asian and African megacities (with population >11 million)

are experiencing the greater values of population increase (>3 million per decade) and Luanda (Angola, Africa) is the only one non megacity (population ~8 million) that is experiencing the same population increase, which means that it is anticipated to exceed the limit of 10 million and become a megacity soon. Seoul exhibits the lowest population increase (~0.1 million per decade). Fukuoka is the only city where a population decrease was found (approximately 0.01 million per decade), but this change wasn't found to be statistically significant.

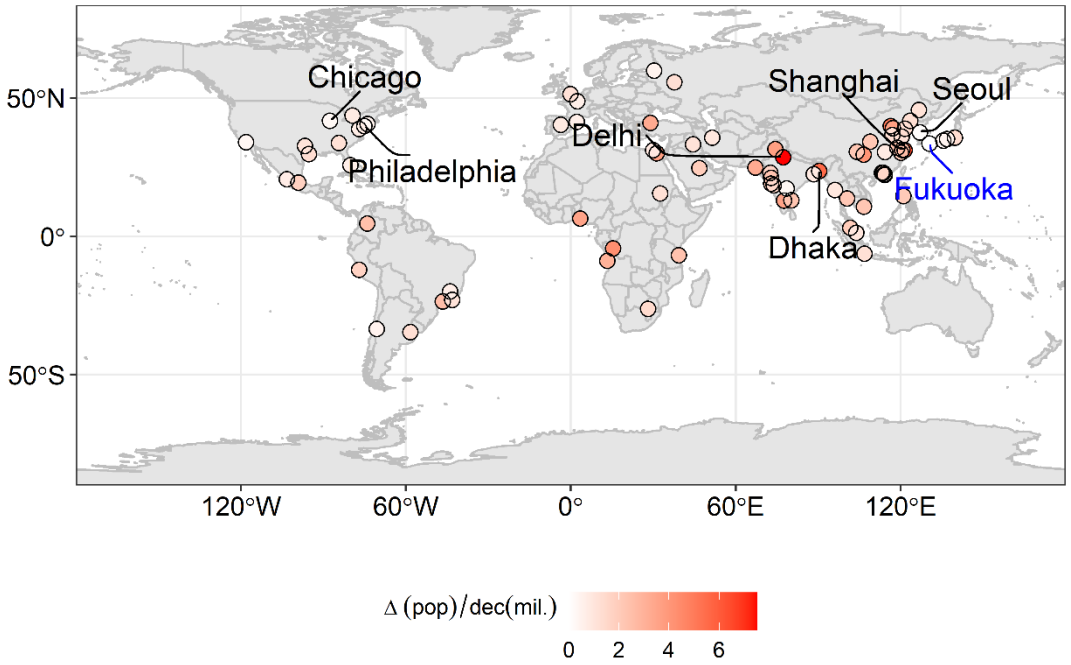

Figure 4.19 Linear trend of population for period 2003-2020 based on UN population counts. All results are statistically significant (P<0.05) but Fukuoka. Three cities with greatest increase of population (>5.5 mil. per decade) are Delhi, Shanghai, and Dhaka and the three cities with lowest increase of population (<0.3 mil. per decade) are Philadelphia, Chicago, and Seoul. Fukuoka was found to be the only city with population decrease (< -0.01 mil. per decade) but this result is not statistically significant.

The relative population changes per decade are compared against corresponding relative AOD changes in Fig. 4.20 (only statistically significant trends, P<0.1, are presented). For all European, North American, and eastern Asian cities (e.g., all Japanese) AOD decrease was derived, while they are associated with small population increase. In contrast for all Indian, most African and South American, and some Asian cities, their population increase is accompanied by positive AOD decadal trends. The population increase of Indian cities is correlated with their increase in AOD. Bangalore is the Indian city with the greatest AOD and population increase, simultaneously. An interesting cluster of cities are Chinese, which almost all had a considerable population increase, however, the measures applied for air pollution resulted in AOD decrease for all. Xian is the Chinese city with the greatest population increase and AOD decrease at the same time. While the AOD increase in relative terms for Africa cities is small, their population is considerably increased (Dar es Salaam is the African city with the greatest positive population trend).

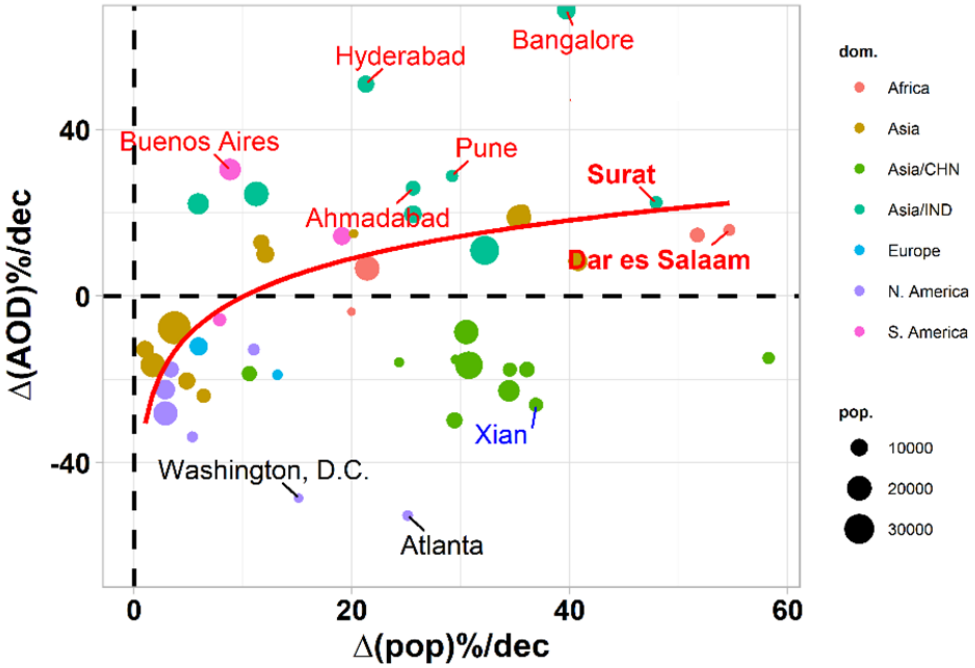

Figure 4.20 AOD versus population decadal changes expressed as percentages. Only statistically significant trends are presented (P<0.1).

4.7 Summary and conclusions

Motivated by the environmental challenges caused by increasing urbanization and to maximize the use of spaceborne aerosol products, in this chapter the aerosol regime over the megacities of the world using satellite aerosol retrievals was investigated. We took advantage of the global coverage, the high sampling frequency (daily values) and the relatively fine spatial resolution (0.1° x 0.1° grid) of the 18 years MODIS-based AOD and DOD at 550 nm products, in order to examine the spatiotemporal variability of aerosol loads for the largest 81 cities of the world.

For all European and American cities, mean AOD ranges mainly from 0.08 to 0.20. For all African and Asian cities but three (Bangalore (0.2), Dar es Salaam (0.17) and Johannesburg (0.09)), mean AOD ranges from 0.25 up to almost 0.90. There are cities which lie in the proximity of deserts or in the path of transported mineral dust particles, which were found to have considerable dust contribution (up to 70%) and the associated mean DOD values (up to 0.4) can be considered as a constant background aerosol source for those megacities. Results of this contribution can be used by policymakers for defining the legislations on air quality urban thresholds.

Most cities (~ 60%) have greater mean AOD values over their urban agglomeration domain. Mostly Chinese and Indian megacities tend to have higher AOD in the surrounding areas of the city center. Shanghai is the city with the largest difference (13% greater mean AOD values for the surrounding domain), but in general for the cities grouped in this category, the declinations between the two

domains are lower compared to the first category, because of the high mean AOD values of the urban domain. Finding disparities in the exposure at urban scales using satellite remote sensing may be a useful tool for air pollution assessment and finally taking diverse reduction measures at community level. As AOD differences are also observed for different months/seasons during the year, AOD intra-annual variability at megacities' scale have been quantified. Low intra-annual variability (temporal CV 10–40 %) was found for Chinese, eastern Indian and eastern Mediterranean megacities, while high values (> 50%) of temporal CV was recorded for eastern American megacities.

Although Chinese cities were found with the highest mean AOD values (up to ~0.90), they also exhibit the highest AOD decrease in absolute values up to ~0.3 per decade (or 30% per decade), in response to the rigorous emission control measures implemented in the country, especially after 2010, despite their considerable population growth. The effectiveness of those measures also reflects the fact that, for Chinese cities, the AOD decrease was found to be higher for the urban domain (up to ~20%). Decreasing AOD values were also derived for US/Canadian and European megacities (up to ~ 0.07 and ~ 0.03 per decade) due to a series of air pollution control policies in the last decades. Small population growth was found for those cities. The maximum worldwide negative AOD trends in relative terms, ~30–55%, per decade were derived for most US cities, which simultaneously have low mean AOD values (less than ~ 0.15). The highest AOD increase worldwide in absolute (up to ~ 0.16 per decade for Kolkata) and relative terms (~ +70% per decade for Bangalore) was found for Indian megacities, correlated with their population growth. Statistically significant positive AOD trends were found for all Indian cities, reflecting the increasing urbanization and industrialization of the country. The AOD increase for Indian megacities was found to be greater (up to ~ 10%) for the urban domain. Statistically significant AOD increase was also found for Middle East, South African and some Latin America megacities (up to ~ 0.1, 0.06 and 0.03, respectively), along with an increase in their population. According to our results population growth and environmental measures to reduce aerosol loads in megacities are competing factors for their air quality.

For cities where long-term ground-based AERONET measurements of AOD were available, the extent at which those measurements can capture the spatial and temporal AOD variability was investigated with respect to the spatial and temporal variability that were derived from satellite data. For GB stations within the urban agglomerations, a good agreement of the long-term mean AOD was found (R ~ 0.93) and with coincident signs on AOD trends in 75% of the selected stations. The resulted discrepancies are attributed, apart from the satellite retrievals-related limitations (one overpass per day, high elevated pixels, low data availability, etc.) and the GB retrieval limitations (large temporal gaps due to instrument issues/calibration, shorter operating time periods, etc.), to the point (GB) versus area-averaged (satellite) comparison. It was found that for areas with non-homogeneous aerosol fields (great spatial CV, e.g., LOSA in our analysis), great differences (opposite signs) were

recorded between satellite and GB trends. Those findings highlight the importance of the GB station location selection for future planning of aerosol measuring sites, to achieve representative AOD measurements for a specific city.

We acknowledge that the total column optical property of AOD analyzed in this study to describe aerosol load variability, is not always proportional to the surface particulate matter (PM) concentrations, which is a parameter better describing the cities' air quality, monitored, regulated by the cities' authorities, and related directly to health effects. However, PM concentrations are derived by in situ measurements and a dense network of those measurements is needed to describe the PM spatial distribution for a city. Even though these ground air quality monitoring stations are valuable, there are relatively few and unevenly distributed within cities around the world, especially in developing countries. One way to provide consistent PM data worldwide is by combining available PM measurements with satellite AOD observations and chemical transport models (e.g., HEI, 2020). Therefore, the use of satellite AOD is a very fitting source of information to have global coverage and high spatiotemporal resolution of aerosol loads over urban areas, keeping in mind that the agreement between satellite columnar AOD and ground-based PM concentrations is determined at a large degree by the vertical structure of aerosol layers (e.g., Gkikas et al., 2016).

According to the findings in this chapter, long-term high-resolution spaceborne AOD retrievals can be utilized for detecting spatial and temporal aerosol variability at an urban scale, helping towards the current and future assessments of aerosol related impacts in megacities. The link of the AOD changes with population and emission trends revealed that the AOD increases for cities with population growth and poor emission regulations.

5 Aerosol direct effects on solar radiation

This chapter is primarily based on the publication: Papachristopoulou, K.; Fountoulakis, I.; Gkikas, A.; Kosmopoulos, P.G.; Nastos, P.T.; Hatzaki, M.; Kazadzis, S. 15-Year Analysis of Direct Effects of Total and Dust Aerosols in Solar Radiation/Energy over the Mediterranean Basin. Remote Sens. 2022, 14, 1535. https://doi.org/10.3390/rs14071535

According to the results of the previous chapter, aerosol loads increase in the absence of emission regulation measures in the greatest cities of the world. The quantification of changes in the aerosol direct radiative effect that is induced by such changes in aerosol loads is of great importance for solar energy applications. In this chapter, the aerosol and especially dust effects on DSSI in terms of GHI (important for PV installations) and DNI (important for CSPs) were investigated on a regional scale, specifically for the broader Mediterranean Basin using earth observation data and radiative transfer modeling. The selection of the study area was based on its high solar energy potential, especial for the southern parts of the domain, the complexity of the aerosol state over the area (both anthropogenic and natural aerosols, including dust) and the increased installation of solar energy exploitation systems in the surrounding countries, as it was discussed in the Introduction.

The earth observation data which were explored consist of two different aerosol optical depth (AOD) and dust optical depth (DOD) datasets, the newly developed satellite-based MIDAS (Section 3.1.2) and the model derived CAMS reanalysis datasets (Section 3.1.4), to investigating the advantages and limitations of existing model and satellite-based aerosol time series for solar-energy-related applications. The most accurate estimates of those optical properties are provided from ground-based remote sensing instruments (sun photometers), which are however sparse, and their geographical distribution is spatially inhomogeneous. This observational gap is complemented by satellite remote sensing along with the related retrieval algorithms, providing considerably accurate measurements with global coverage and high spatial and temporal resolution. Although they are still not as accurate as ground-based estimates of the aerosol optical properties, the accuracy of satellite-based aerosol products has been improved substantially in recent years (Sayer et al., 2013, 2020). A significant disadvantage of satellite products is that they are representative of relatively wide areas rather than specific locations, and thus they can be highly uncertain when they are used to study aerosols over complex environments (Kazadzis et al., 2009; Wei et al., 2020). For reanalysis datasets, compared to satellite products, their spatial resolution is relatively low, and regardless of the assimilation process of aerosol observations, the performance of their outputs depends on modeling aspects (e.g., the balance between the different aerosol components constituting the aerosol column at any given location and time) (Gueymard & Yang, 2020).

Since the results of the analysis presented in this chapter are based on radiative transfer model (RTM) simulations, as a first step a sensitivity analysis was conducted investigating the effect of changes in the aerosol profiles on simulated irradiances in the earth's surface (methodology at Section 3.7) and the results are presented in Section 5.1. The quantification of the long-term effects of total aerosols and dust on different DSSI components (GHI and DNI) with respect to aerosol-free conditions were derived, using both AOD and DOD datasets as inputs to RTM simulations using the LUT approach. For the simulations, additional aerosol optical properties and atmospheric parameters were used as inputs as well. Furthermore, the advantages and limitations of existing model and satellite-based aerosol time series for solar-energy-related applications were investigated. Details of the methodology are provided in Section 3.8 and the results are presented in Sections 5.2-5.5. In Section 5.6 the 15-year climatology of clear sky GHI and DNI in the Mediterranean Basin is presented. Finally, the same methodology was applied for a smaller area inside the Mediterranean domain, in order to extend the analysis to all-skies conditions, namely, to consider also clouds and compared both aerosol and cloud radiative effects in a Mediterranean environment and the results are presented in Section 5.7.

5.1 Sensitivity analysis for the effect of the aerosol vertical distribution on surface solar radiation

In most climatic studies, default aerosol profiles are used which commonly assume an exponential decrease in aerosol extinction (with aerosols concentrated in the first 1–2 km from the surface). In many cases, this assumption does not affect the modeled irradiance at the bottom of the atmosphere (BOA) and the top of the atmosphere (TOA) significantly (e.g., Petržala (2022)). The scientific question to be answered here is how deviations of the actual vertical distribution of aerosol optical properties from the default profile affect the solar radiation that reaches the Earth's surface.

5.1.1 Sensitivity Study Using Artificial Extinction Profiles

As described in Section 3.7.1, the magnitude of the differences in spectral surface solar radiation when the altitude of the aerosol layer changes was investigated using artificial aerosol extinction profiles. Relative differences (%) were calculated between simulations for which all parameters were the same, except the aerosol extinction coefficient profile. The radiation profiles for elevated aerosol layers (L1 to L4) were compared with the radiation profiles for L0. L0 was used as reference because it is closer to commonly used climatological profiles, as most of the radiation extinction by aerosols takes place near the surface. Sensitivity of the results to different TCWV was found to be very small even in the NIR. Thus, only results for TCWV = 1 g cm^{-2} are presented. Moreover, the sensitivity analysis performed prior to the simulations revealed that the effect of changes in TOC (within the realistic limits of 200-400 DU) on the results was also negligible. Therefore, all simulations were performed

for TOC = 350 DU. In this section, the effect of the altitude of the aerosol layer on global irradiance (GI) at the surface is discussed for AOD = 1.

Differences (in %) in the GI for the four spectral bands, as it was simulated for aerosols at higher altitudes (L1 to L4) and aerosols at L0, are presented in Fig. 5.1. Below SZA = 60° and for low surface albedo, the altitude of the aerosol layer had a small impact on the GI that reached the surface, since differences were in all cases below 5%. For SZA = 80°, the differences were larger, up to 15%, mainly for UVA and NIR. For UVA, increasing the altitude of the layer led to increased absorption by absorbing (SSA = 0.75) aerosols. For L4, the reduction was nearly 8% with respect to the UVA at the BOA for L0. A possible explanation is that the direct beam that enters L0 is significantly weaker than the direct beam that enters L4. At such a large SZA, the optical path inside the layer is longer for photons of the direct beam relative to scattered photons. Thus, when the aerosol layer is higher, absorption of UVA irradiance by aerosols is stronger. For UVB, the corresponding reduction is smaller because at high SZA (above 60°) the contribution of the direct component is already weak relative to the contribution of the scattered component of GI at 5.5 km. In the VIS and NIR regions, although the direct component is stronger than in UV, the photons are scattered less effectively in the atmosphere. Thus, in aerosol-free skies, the direct component of VIS and NIR GI was similar at 1.5 km and 5.5 km. In NIR, the GI at the BOA at SZA = 80° increased with increasing altitude of the aerosol layer (by 12–14% for L4), for both absorbing and reflective aerosols. This is possibly because scattering of the NIR at higher altitude at such large SZA results in a reduced optical path for a significant fraction of the scattered photons as they propagate “more vertically” below the aerosol layer, moving towards the surface, and are thus absorbed less effectively by atmospheric molecules (mainly by water vapor).

The altitude of the aerosol layer plays a more significant role over highly reflective surfaces, especially when Rayleigh scattering is strong (i.e., in the UVB and UVA regions). The global irradiance at BOA increases with increasing aerosol layer altitude, by up to 15% in the UVB for L4 and small SZA. When the layer of aerosols is inside a denser atmosphere (i.e., near the surface) the photons follow longer paths in the layer (due to multiple Rayleigh scattering) with respect to elevated aerosol layers. This phenomenon is intensified over reflective surfaces due to multiple interactions of the photons with the surface, the dense atmosphere, and the aerosol particles. If the layer constitutes absorbing aerosols, then increased absorption leads to even larger differences between GI at the BOA for elevated aerosol layers and L0, and up to 15% for L4. Longer wavelengths are scattered less effectively in the atmosphere, which is the reason for the very small (below 3%) differences between Fig. 5.1 e, f (for reflective and absorbing aerosols). Rayleigh scattering in the NIR is negligible; thus, the corresponding differences between panels 5.1g and 5.1h are nearly zero.

Changes in total irradiance (panels 5.1i and 5.1j) due to different altitude of the aerosol layer are determined by changes in the VIS and the IR. For increasing altitude of the aerosol layers, the total GI at BOA increases. The increase was smaller than 5% for SZAs below 60° and larger for SZA = 80°. The increase was similar for L2, L3, and L4, at 7–8%. Changing the surface albedo has negligible impact on total GI at the BOA. It must be mentioned that in realistic conditions, the AE is larger than 0, and subsequently, the effect of aerosols is larger at shorter wavelengths, which means that the contribution of changes in the NIR to the changes in the total GI would be less significant than the contribution of NIR in the results presented in panels 5.1i and 5.1j.

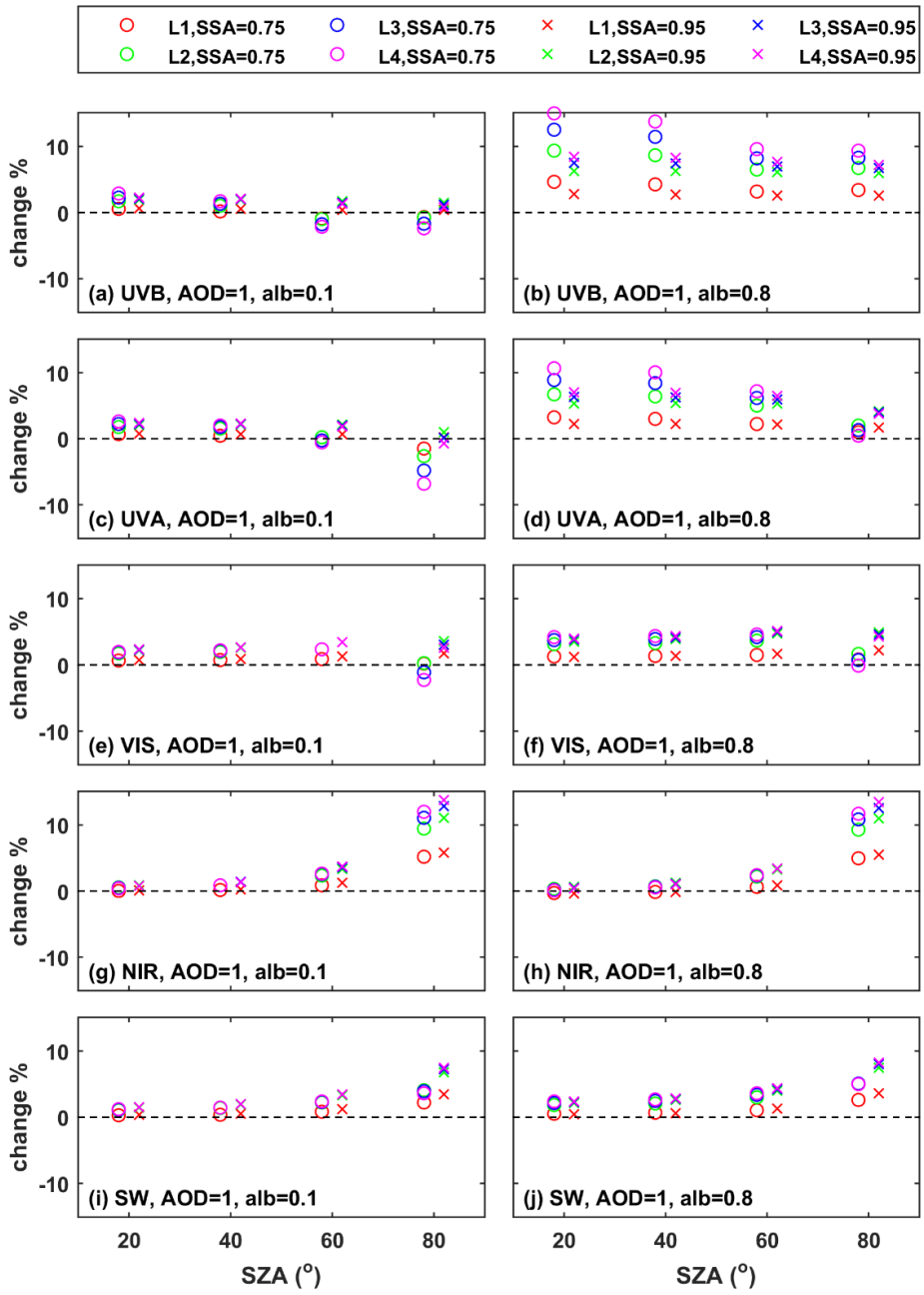

Figure 5.1 Relative differences in GI at the BOA for different altitudes of the elevated aerosol layer, SSA and surface albedo with respect to the corresponding conditions when aerosols are at L0 (elevated layer - L0). The presented results are for AOD = 1 and TCWV = 1 g/cm^2. Different rows represent different spectral regions (UVB, UVA, VIS, NIR). Different columns represent different surface albedo (left: 0.1, right: 0.8).

5.1.2 Effect of extinction coefficient profile for typical aerosol conditions - LIVAS Profiles

The methodology used in this section has been described in Section 3.7.2. The differences between the seasonal total-aerosol extinction coefficient (at 532 nm) profiles from LIVAS and the libRadtran default profile (Shettle, 1989) (both scaled to the seasonally averaged AOD at 550 nm) for the two regions are presented in Fig. 5.2. The profiles used to calculate the differences are shown in Appendix B (Fig. B21).

The different characteristics of aerosols over the two regions lead to quite different patterns in the extinction coefficient profile differences. Over CE Europe, continental aerosols constitute a significant fraction of the aerosol mixture, while over NW Africa, dust plays a very significant role. In winter, for both areas, aerosol extinction was underestimated below ~1.5 km and overestimated above the same altitude when the default profile was used for the simulations.

For CE Europe, the pattern of differences between the default and measured vertical profiles of aerosol extinction coefficient were as follows. Negative differences (i.e., overestimation by the default profile) appear above an altitude that ranges from ~2 km in winter to ~4 km in spring. Then, the differences become positive. In spring and summer, the differences approach zero near the surface.

For NW Africa, there is a stronger seasonal dependence on the extinction coefficient differences relative to CE Europe. In spring and autumn, the differences are negative above 5–6 km, and positive below, approaching zero at about 2 km. In summer, differences in the extinction coefficient are again negative above ~6 km and positive below. Then, the differences become negative again below 2 km.

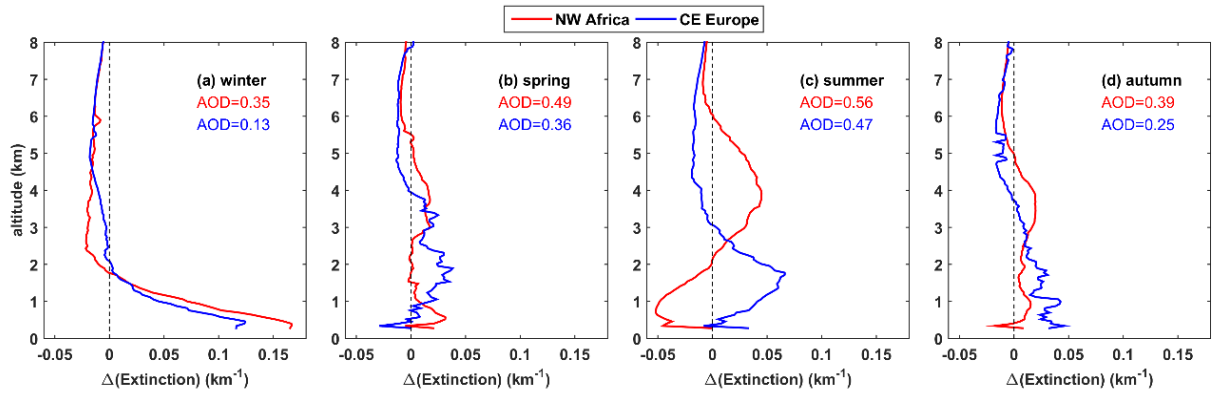

Figure 5.2 Differences between the LIVAS and the libRadtran default extinction coefficient profiles for the AOD at 350 nm. The results are shown for CE Europe (blue line) and NW Africa (red line) for the four seasons of the year. The 350 nm AOD for each is also shown in the panels with the corresponding colors.

In Fig. 5.3, the differences in the GI at the BOA are presented for each region and each season of the year. In all cases, the differences were below 3%, and especially for VIS and NIR, they were in many cases below 0.5%. Given that more than 85% of total SW irradiance is in the VIS and NIR regions, changes in SW GI were also close to zero. These results confirm that for typical aerosol conditions,

using a more realistic profile instead of the default is not necessary for the study of the GI at the Earth's surface.

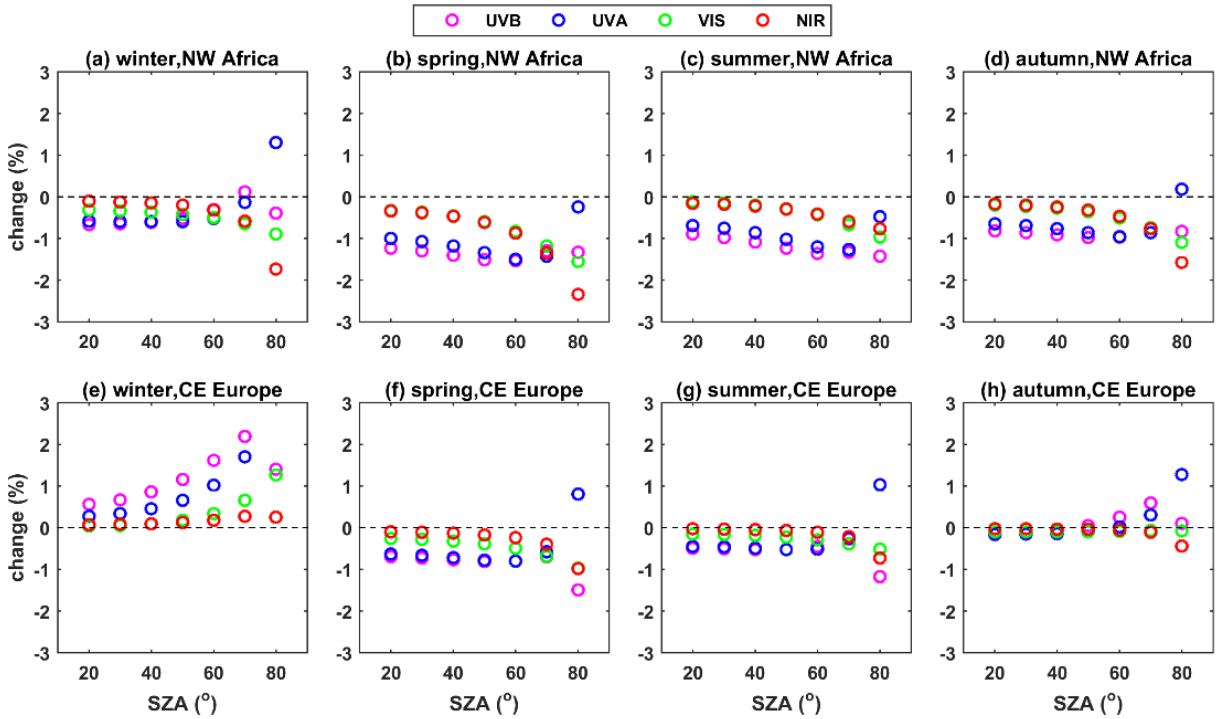

Figure 5.3 Change (in %) in the simulated GI reaching the surface due to the use of the LIVAS profiles instead of the default libRadtran profile.

5.2 Satellite-Derived and Modeled AODs and DODs—Climatology and Intercomparison

One of the aims of this study is to investigate the benefits and the drawbacks of choosing between satellite- and model-derived AOD and DOD datasets for estimating their radiative effects. To this end, MIDAS and CAMS datasets were explored. For the MIDAS–CAMS comparison, the aggregated MIDAS datasets were used, before filling in the missing values (see Section 3.8.1). CAMS datasets, which have a diurnal variation (3 h temporal resolution), were synchronized with MIDAS datasets (MODIS-Aqua overpass time) to achieve an exact collocation. In Fig. 5.4, the MIDAS cloudless sky data availability (expressed in percentage) is illustrated. Three regions can be distinguished. North Africa, which, due to its scarce cloudiness, has the highest data availability, with more than 70% of daily satellite retrievals with respect to the whole period. Over the Mediterranean Sea, data availability decreases down to 60%. Over Europe, the MIDAS data amount further decreases and is minimized (~20%) in mountainous regions (i.e., Alps). For the temporal aggregation, only grid points with at least 20% data availability on annual and seasonal bases were used, to ensure the representativeness of the results.

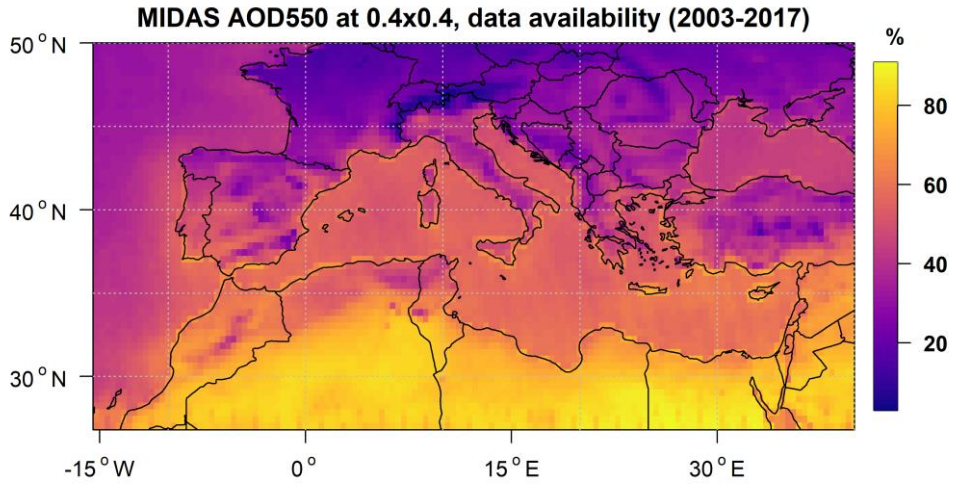

Figure 5.4 MIDAS dataset data availability.

The geographical distribution of the long-term annual averaged values of AOD (Fig. 5.5 a and b) and DOD (Fig. 5.6 a and b) were derived for both datasets. The corresponding seasonal results are given in Appendix B (Fig. B1-4). Our analysis expands further CAMS DOD product evaluation (Bennouna et al., 2020) in terms of its spatial and temporal variability performance. The frequency histogram of the CAMS–MODIS biases and their mean annual geographical distribution are presented in panels c and d, respectively, for AOD (Fig. 5.5) and DOD (Fig. 5.6). By performing t-tests for the differences shown in Fig. 5.5 d and 5.6 d, most differences were found to be statistically significant (not shown in the figures for clarity) on a 95% confidence level (p-value<0.05).

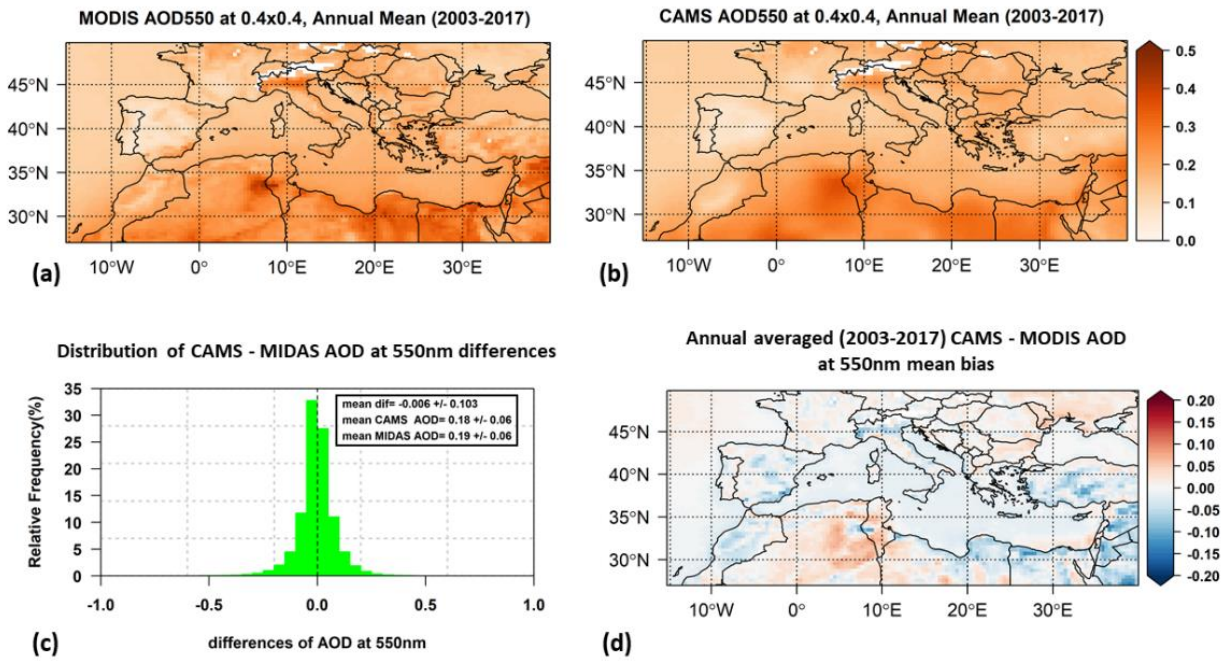

Figure 5.5 Geographical distribution of long-term average of annual mean AOD at 550 nm from MODIS **(a)** and CAMS **(b)**. Frequency distribution of CAMS–MODIS AOD biases with their mean value **(c)** and geographical distribution of annual mean biases **(d)**. Blank grid points are those that did not fulfill the criterion of at least 20% data availability on an annual basis.

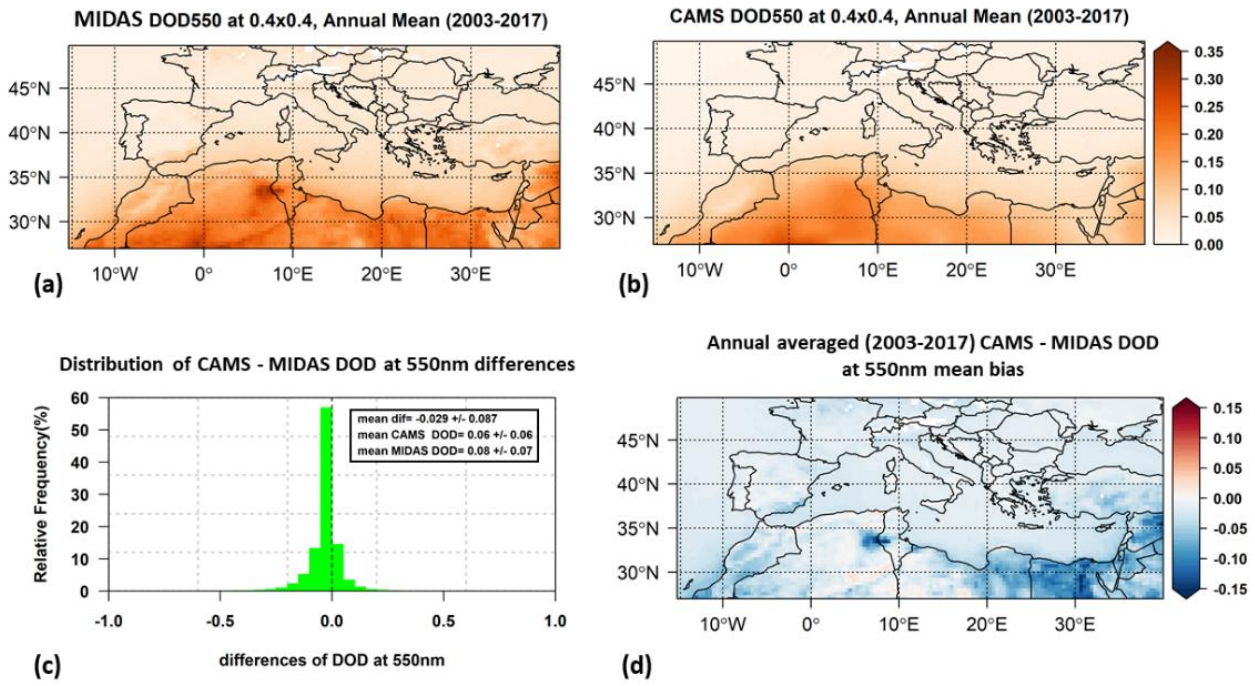

Figure 5.6 Geographical distribution of long-term average of annual mean DOD at 550 nm from MIDAS **(a)** and CAMS **(b)**. Frequency distribution of CAMS–MIDAS DOD biases with their mean value **(c)** and geographical distribution of annual mean biases **(d)**. Blank grid points are those that did not fulfill the criterion of at least 20% data availability on an annual basis.

5.2.1 Aerosol optical depth

In general, the AOD spatial features are similarly reproduced for both datasets (Fig. 5.5 a, b), and the regional averages are almost equal (0.19 ± 0.06 for MODIS and 0.18 ± 0.06 for CAMS, Table 5.1). Our findings are also in good agreement with those of previous studies focusing on the same region (Floutsi et al., 2016; Nabat et al., 2013; Papadimas et al., 2008). Between the two datasets, differences were found in the magnitude of the maximum AOD levels. The annual mean AOD values for each individual pixel range from 0.05 to 0.48 for MIDAS and from 0.05 to 0.37 for CAMS. For both datasets, the maximum and minimum AOD values were found over the same areas. Over North Africa and parts of the Middle East, maximum AOD values were derived that were mainly attributed to desert dust. Large AOD values related to anthropogenic activity (Crosier et al., 2007; El-Metwally et al., 2008) were found over the megacity of Cairo, Egypt, and the Po Valley, Italy. Low AOD values (0.05–0.15) were found over most of the Iberian Peninsula and southern France, which agrees with Obregón et al. (2020), who attributed the low AOD to the clean air masses that were transferred over these areas from the Atlantic Ocean due to the westerly air flow (Obregón et al., 2020) and the references therein).

Table 5.1 Regional averages of mean annual and seasonal AOD and DOD at 550 nm from MIDAS and CAMS and CAMS–MIDAS bias. The maximum of seasonal values is denoted as bold, emphasizing the peak of the seasonal cycle.

	AOD			DOD		
	CAMS	**MIDAS**	**mean bias (CAMS–MIDAS)**	**CAMS**	**MIDAS**	**mean bias (CAMS–MIDAS)**
			Annual			
	0.18±0.06	0.19±0.06	-0.005±0.025	0.06±0.06	0.08±0.07	-0.026±0.021
			Seasonal			
winter	0.11±0.05	0.13±0.06	-0.019±0.021	0.03±0.03	0.06±0.05	-0.030±0.025
spring	0.21±0.07	0.21±0.07	-0.003±0.027	**0.07±0.07**	**0.11±0.08**	-0.037±0.024
summer	**0.23±0.08**	**0.23±0.07**	0.003±0.038	**0.08±0.08**	**0.10±0.08**	-0.019±0.027
autumn	0.15±0.06	0.16±0.07	-0.007±0.028	0.05±0.05	0.07±0.06	-0.023±0.022

Overall, the CAMS-simulated AODs are slightly underestimated (mean bias -0.006) with respect to MIDAS AOD (Fig. 5.5c), which was found to be statistically significant on the 95% confidence level (p-value < 0.05, t-test for the differences). This agrees with the results of previous studies (Bennouna et al., 2020), where lower CAMS AODs relative to MODIS were reported over the NAMEE domain. The geographical distribution of the annual mean bias (Fig. 5.5d) revealed areas with annual mean bias that differed a lot from the average value for the whole region. The most significant negative differences were found over an extensive area of Northeast Africa and parts of the Middle East (with annual mean bias up to -0.14), which can be explained by the AOD overestimation of MODIS Dark Target and Deep Blue combined product over these areas (Wei et al., 2019b). There are also areas with much higher CAMS AOD values relative to MIDAS. Maximum positive differences (up to 0.1) were found over Northwest Africa, which can be explained by the CAMS model overestimation of the organic matter over that area (Bennouna et al., 2020). This CAMS AOD overestimation is more pronounced in summer (Fig. B5c).

There is a clear seasonal cycle (Fig. B1 and B2) of the AOD over the Mediterranean Basin. CAMS AOD reproduces the regional patterns of the MODIS AOD seasonal variability quite well, but again there were differences in the magnitude of maximum seasonally averaged AODs between the two datasets. In summer, AODs are maximized (0.66 for MODIS and not exceeding 0.56 for CAMS) over North Africa, particularly in its western parts. Large AOD values were also found over southeast Europe in spring and summer, which are mainly due to emissions of anthropogenic aerosols such as sulfates (Nabat et al., 2013), with a peak in spring over Po Valley with mean values of 0.37 for MODIS and 0.28 for CAMS. In Table 5.1, the regionally averaged seasonal mean AOD values are summarized. A distinct seasonal cycle was revealed in both datasets with maximum values during summer and minimum values during winter, which is the same as the seasonal cycle reported by Papadimas et al. (2008). The seasonal variations of AOD are linked to the atmospheric circulation and

the meteorological conditions over the study area that are affecting the aerosol emission, removal, and transport processes (Diémoz et al., 2019; Gkikas et al., 2012).

5.2.2 Dust optical depth

There is a clear latitudinal gradient of DOD (Fig. 5.6 a, b). For both datasets, the largest DOD values were found over North Africa and parts of the Middle East, where major dust sources (Sahara and Arabian Peninsula deserts) are located (Ginoux et al., 2012; Prospero et al., 2002). For the annually averaged MIDAS DOD, a maximum of 0.35 was found over a persistently dust-active region of salt lakes (local "chotts") and dry lakes in the borders of Tunisia and northeast Algeria. Large values (0.32) were also found over the desert of central Algeria. Over the eastern Libyan Desert and Egypt, for most pixels, DOD ranges from 0.12 to 0.25. The same range of values was found over the dust sources of Mesopotamia and the Jordan River Basin in the Middle East. A CAMS DOD deficiency is reflected in the systematically lower corresponding values over the aforementioned sources (0.2, 0.26 and 0.05 to 0.15 respectively). Regarding the regional averages (Table 5.1), there is a small difference between MIDAS and CAMS (0.08 ± 0.07 and 0.06 ± 0.06 respectively) in absolute values.

A relatively high, statistically significant at the 95% confidence level, underestimation (mean bias almost -0.03) of CAMS DODs against MIDAS (Fig. 5.6 c) was found. Average CAMS DOD is almost 40% lower compared to MIDAS DOD, which agrees with the underestimation of CAMS DOD (up to 46%) with respect to AERONET observations reported by Bennouna et al. (2020) over the same area. According to the latter study, the higher CAMS DOD underestimation was found during wintertime, which was attributed to overestimations in biomass-burning organic matter (OM). In summer, the DOD underestimation was attributed to the overestimation of secondary organics over heavily populated areas. The geographical distribution of annual mean bias (Fig. 5.6d) revealed that MIDAS DOD is larger than CAMS DOD almost everywhere. The largest values of CAMS DOD underestimation (up to -0.15) were found over the dust sources of the Saharan and Middle East deserts, not only for the annually averaged DOD but also for the seasonal DOD (Fig. B6).

The geographical distribution of DOD over the Mediterranean Basin was found to follow a seasonal cycle (Fig. B3 and B4) with maxima in spring and summer, in agreement with the findings of previous studies (Gkikas et al., 2013; Moulin et al., 1998; Nabat et al., 2013). In winter, high DOD levels are confined mainly over northeastern Africa, with DODs up to 0.25 and 0.13 for MIDAS and CAMS, respectively. Dust activity is enhanced in spring, with elevated DOD values (maximum values up to 0.42 for MIDAS and 0.27 for CAMS) over an extended area covering the central and eastern parts of North Africa and the part of the Middle East. In summer, elevated dust levels were found mainly over northwestern Africa, while the highest mean seasonal DOD values were found for this season. In summer, the smallest differences between the two datasets were found (DOD equal to 0.45 for

MIDAS and 0.44 for CAMS). This seasonal cycle of dust activity and transport over the Mediterranean agrees with previous studies, which also investigated the atmospheric circulation patterns favoring this cycle (Gkikas et al., 2015).

The differences that were found between the two different datasets (MIDAS, CAMS), especially regarding the maximum AOD/DOD levels, were investigated further. It was found that a great portion of MIDAS high AOD and DOD values are missing from the CAMS dataset. Table 5.2 summarizes the amount of data that are higher than 1, 1.5, 2 and 3 in terms of AOD and DOD for both datasets. It also shows the percentage of the missing high values from CAMS datasets compared to MIDAS. For the MIDAS AOD dataset, 0.05% of the values exceed 2, while the corresponding percentage for CAMS is only 0.0015%. For DOD, over 90% of the missing high values have a lower threshold of DOD 1.5, due to strong CAMS DOD underestimation. For very high aerosol burdens there are significant differences between the explored datasets, especially when considering the dust component.

Finally, based on the MIDAS dataset, we estimated that the long-term dust contribution to total aerosols in optical terms ranges from 40% to 90% over North Africa and the Middle East, making dust the most important aerosol component over these areas.

Table 5.2 Summary statistics of AOD and DOD (from both MIDAS and CAMS datasets) values greater than specific threshold values 1, 1.5, 2 and 3.

	AOD			DOD		
	CAMS	**MIDAS**	**Missing from CAMS compared to MIDAS**	**CAMS**	**MIDAS**	**Missing from CAMS compared to MIDAS**
>1	0.19%	0.46%	57%	0.08%	0.31%	75%
>1.5	0.02%	0.13%	85%	0.007%	0.09%	92%
>2	0.0015%	0.05%	97%	0.0008%	0.04%	98%
>3	0.000009%	0.014%	~100%	0	0.01%	100%

5.3 Aerosol and dust direct effects on DSSI

In this section, the quantification of total aerosol and dust radiative effects on GHI and DNI over the Mediterranean Basin is presented. Moreover, the effects on DSSI when different datasets (MIDAS or CAMS) of AOD/DOD are used were investigated. For this purpose, in total ~23 million data points were compared. The average number of data points (days) compared for each of the ~8000 pixels of the Mediterranean Basin was ~3000 per pixel or ~200 per pixel per year.

The change in the mean annual integral of GHI due to the presence of total aerosols and dust is presented in Fig. 5.7 and 5.8, respectively, estimated using MIDAS (panel a) and CAMS (panel b) datasets. The corresponding results for DNI are shown in Fig. 5.9 and 5.10. The corresponding seasonal results are given in the Appendix (Fig. B 7 – B 14). In all cases, the patterns of GHI and DNI changes are consistent with those of AOD and DOD. The higher the AOD and DOD values are, the higher their radiative effect. Due to the interactions of the incoming solar radiation with the overlying

aerosol (dust) layers, the GHI and DNI reaching the surface are reduced with respect to an aerosol-free atmosphere, thus explaining the existence of negative values throughout the domain. The day-to-day variations of these effects are presented in Fig. 5.11. AOD GHI attenuation stands for the GHI reduction by total aerosols and DOD GHI attenuation means the GHI reduction by the dust component. The same nomenclature is used for the DNI component.

5.3.1 Aerosol direct effects on GHI

There is a qualitative agreement in the geographical distribution of the annual AOD GHI attenuation between the two datasets (Fig. 5.7), and their regional averages using the MIDAS dataset (5.2%, Table 5.3) are almost the same as those with CAMS (5.1%). The differences in the magnitude of annual mean AODs and especially for the maximum values were also inherited to their radiative effects. The long-term GHI reduction due to aerosols was found to range from 1% to 13% for MIDAS and from 2% to 10% for CAMS.

In general, three subdomains (D) are highlighted for the annual AOD GHI attenuation, based on aerosol load spatial patterns. The highest effects were found over North Africa and the Middle East (D1), where the annual AOD GHI attenuation varies from 4% to 13% based on the MIDAS dataset (4% to 10% for CAMS). Lower values were found for central and southeastern Europe and the Anatolian Peninsula (D2), ranging from 3% to 8% (3% to 7%), with the largest values over the Po Valley. Over the Iberian Peninsula and southern France (D3), the lowest annual AOD GHI attenuation was found, ranging from 1% to 6% (2% to 5%), except for southeastern Spain (attenuation reaches 8% only for MIDAS dataset). The same low values of the total aerosol direct effect on the downwelling surface fluxes of the global solar radiation were also found in previous studies (Obregón et al., 2020; Papadimas et al., 2012) over the same area.

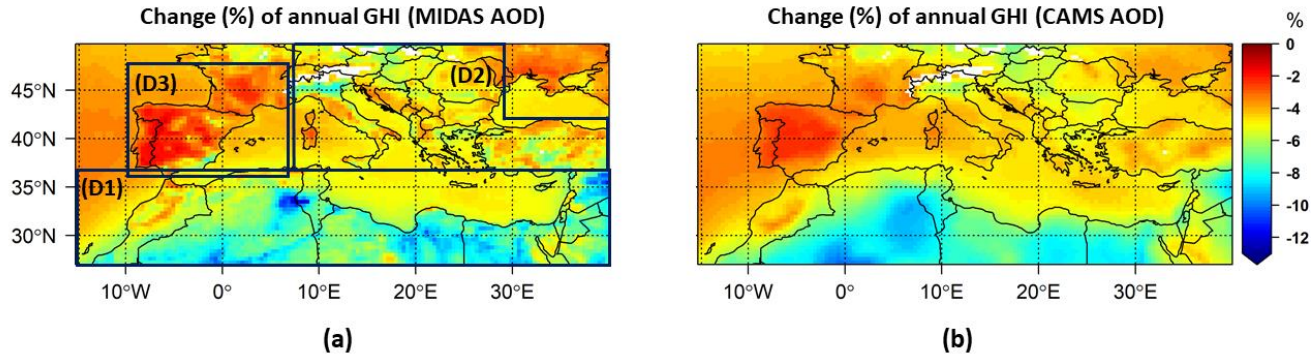

Figure 5.7 Change (in %) of the mean annual integral of GHI due to the presence of aerosols under **(a)** MIDAS AOD and **(b)** CAMS AOD. Blank grid points are those that did not fulfill the criterion of at least 20% data availability on an annual basis.

Table 5.3 Change (in %) of the regional averaged mean annual and seasonal integrals of GHI due to total aerosols (AOD) and dust (DOD) from both datasets of MIDAS and CAMS. The maximum of seasonal values is denoted as bold, emphasizing the peak of the seasonal cycle.

	AOD		DOD	
	CAMS	**MIDAS**	**CAMS**	**MIDAS**
		Annual		
	-5.1 (±1.5)	-5.2 (±1.6)	- 1.7(± 1.7)	-2.4 (±1.8)
		Seasonal		
winter	-4.9 (±1.5)	**-5.5 (±1.7)**	- 1.2(± 1.2)	-2.3 (±1.7)
spring	**-5.3 (±1.7)**	-5.3 (±1.8)	**- 1.9(± 1.9)**	**- 2.9 (±2.0)**
summer	-5.2 (±1.9)	-5.0 (±1.7)	**- 1.9(± 2.1)**	**- 2.3(±2.0)**
autumn	-5.0 (±1.5)	-5.1 (±1.6)	- 1.5(± 1.5)	- 2.2(±1.8)

There are pronounced seasonal variations (Fig. B7 and B8) of the AOD GHI attenuation geographical distribution. The maximum MIDAS AOD GHI attenuation up to 14% (10% for CAMS) was found in spring over North Africa. For CAMS, the maximum reduction was found for summer over northwestern Africa and was 13%, which was similar to the corresponding attenuation for the MODIS dataset. In Table 5.3, the regional averages of the seasonal AOD GHI attenuation are summarized. The seasonal cycle of AOD GHI attenuation for both datasets differs from the seasonal cycle of the corresponding AOD values. The most notable difference is that the peak of AOD GHI attenuation was derived in winter for the MIDAS dataset instead of summer when the peak of MIDAS AOD was found. The unexpected peak of the GHI attenuation in winter was mainly due to significant attenuation of the GHI over Egypt and eastern Libya, which was subsequently attributed to minimum seasonal SSA values in winter over the area (Fig. B15a). For the CAMS AOD dataset, a small shift of maximum GHI attenuation to spring instead of summer was found.

5.3.2 Dust direct effects on GHI

Under the absence of non-dust aerosol species, the spatial patterns of GHI attenuation, based on MIDAS and CAMS DODs (Fig. 5.8, B9, and B10), show a clear south-north gradient regulated by the reduction in dust load amount from sources to distant downwind regions. The CAMS DOD underestimation is also depicted in the GHI attenuation which is lower than the MIDAS GHI attenuation. Maximum values of the annual DOD GHI attenuation were found over North Africa and parts of the Middle East, ranging from 2% to 10% for MIDAS and from 2% to 8% for CAMS. This attenuation of GHI by dust accounts for ~45-90% of the overall attenuation by aerosols over this area on an annual basis. Dust contribution becomes more significant (up to 95%) on a seasonal basis over the same areas. In summer, the seasonal mean reached 11% for MIDAS and 10.5% for CAMS, over north-western Africa. Except for summer, the CAMS DOD GHI attenuation is significantly lower than the MIDAS DOD GHI attenuation for the rest of the year.

Regarding the regionally averaged values (Table 5.3), the annual GHI attenuation due to MIDAS DOD (2.4%) is almost 30% larger than the attenuation estimated for CAMS DOD (1.7%). The seasonal cycle of GHI attenuation attributed to dust is the same as the seasonal cycle of DOD with maxima in spring and summer, with the spring peak being higher by 21% than the summer peak (for MIDAS), which could not be explained solely by the corresponding DOD differences between the two seasons (9%). The sharp MIDAS peak in spring can also be explained by the lower DU SSA values over North Africa and parts of the Middle East during spring (Fig. B16b).

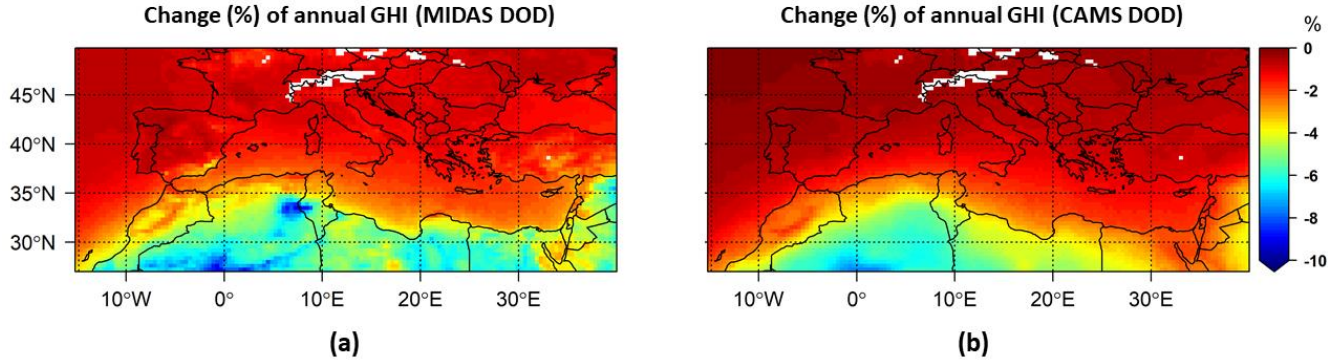

Figure 5.8 Change (in %) of the mean annual integral of GHI due to the presence of dust under **(a)** MIDAS DOD and **(b)** CAMS DOD. Blank grid points are those that did not fulfill the criterion of at least 20% data availability on an annual basis.

5.3.3 Aerosol direct effects on DNI

The average of AOD DNI attenuation (Fig. 5.9) ranged from 5% to 47% for MIDAS and from 10% to 39% for CAMS. The AOD differences between the CAMS and MIDAS datasets were amplified in terms of DNI attenuation. The maximum DNI attenuation was found for D1 for both datasets, with values ranging from 15% to 47% for MIDAS and to 39% for CAMS. In D1, areas such as Morocco, North Algeria, North Tunisia, and the areas around the Red Sea, annual DNI attenuations were less than 20%, which makes these areas favorable for CSP (DNI-related) installations. For D2, an average DNI reduction between 15% and 25% was derived, similar for both datasets, except for Po Valley where CAMS DNI attenuation (26%) was 6% lower than the MIDAS DNI attenuation (32%). The lowest values were found for D3 ranging from 5% to 25% (except for southeastern Spain where it was 35%) for MIDAS and from 10% to 20% for CAMS. The seasonal AOD DNI attenuation values (Fig. B11 and B12) reached higher values up to 53% for MIDAS and 49% for CAMS, which were found over Northwest Africa in summer. The seasonal cycle (Table 5.4) of DNI AOD attenuation followed the corresponding seasonal cycle of the AOD, for both datasets, with maximum in summer and minimum in winter.

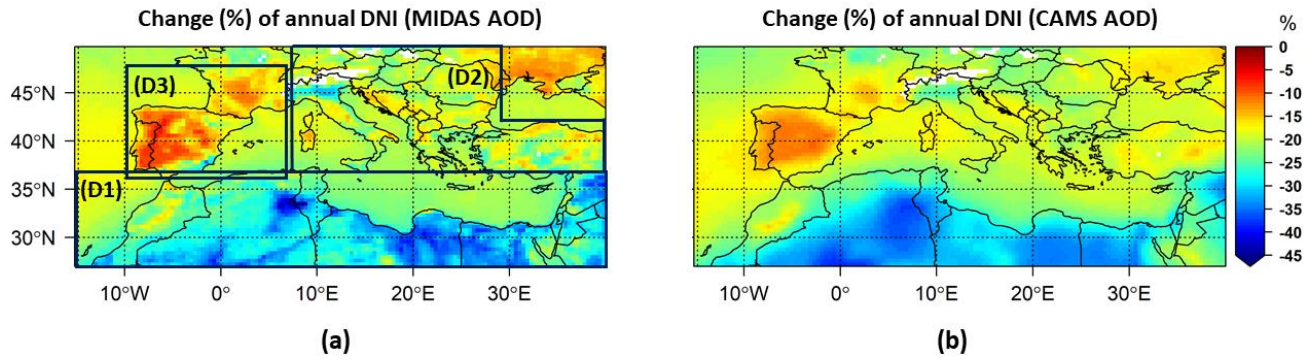

Figure 5.9 Change (in %) of the mean annual integral of DNI due to the presence of aerosols under **(a)** MIDAS AOD and **(b)** CAMS AOD. Blank grid points are those that did not fulfill the criterion of at least 20% data availability on an annual basis.

Table 5.4 Change (in %) of the regional averaged mean annual and seasonal integrals of DNI due to total aerosols (AOD) and dust (DOD) from both datasets of MIDAS and CAMS. The maximum seasonal value is denoted as bold, emphasizing the peak of the seasonal cycle.

	AOD		DOD	
	CAMS	**MIDAS**	**CAMS**	**MIDAS**
		Annual		
	-22.2 (±5.6)	- 22.1(±5.6)	-7.5 (±6.7)	-10.7(±7.2)
		Seasonal		
winter	-17.9 (±5.5)	- 19.6 (±6.0)	-4.9 (±4.7)	-9.0(±7.3)
spring	-23.6 (±6.2)	- 23.2 (±6.7)	**-8.5 (±7.6)**	**-12.7(±7.9)**
summer	**-24.0 (±7.3)**	**- 23.3(±6.5)**	**-9.1 (±8.8)**	**-11.2(±8.2)**
autumn	-20.5 (±5.8)	- 20.5(±6.2)	-6.4 (±6.1)	-9.4(±7.2)

5.3.4 Dust direct effects on DNI

The peak of DNI attenuation due to dust was found over North Africa and the Middle East, with values ranging from 9% to 37% for MIDAS and from 9% to 28% for CAMS (Fig. 5.10). In summer, over northwestern Africa, the reductions reached values up to 40% and 38% for MIDAS and CAMS (Figures B13-14), respectively. The contribution of dust to the overall DNI attenuation by aerosols is ~45- 90%. For the regionally averaged values (Table 5.4), a larger DNI attenuation due to MIDAS DOD (10.7%) was found relative to CAMS DOD attenuation (7.5%). The difference can be attributed to the strong underestimation of CAMS DOD, especially over northeastern Africa, and the Middle East.

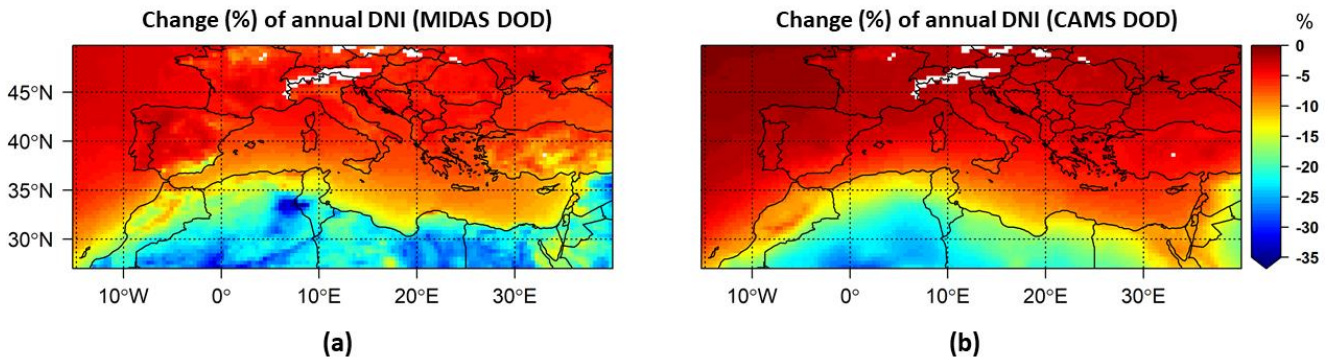

Figure 5.10 Change (in %) of the mean annual integral of DNI due to the presence of dust under **(a)** MIDAS DOD and **(b)** CAMS DOD. Blank grid points are those that did not fulfill the criterion of at least 20% data availability on an annual basis.

5.3.5 Daily Variability

The variability of the daily GHI attenuation due to total aerosols for all pixels (Fig. 5.11 a) is much larger than the variability in the annual and seasonal values. The underestimation of CAMS AOD is reflected in the systematically lower values of the daily GHI attenuation. There is no value of GHI reduction due to CAMS AOD above 50%, which is related to the absence of CAMS AOD above 3 (see Section 5.2). It is noteworthy that there are days when aerosols attenuated GHI by ~75% (for the MIDAS AOD). The daily values of GHI reduction due to dust using the MIDAS DOD dataset are constantly larger than those when CAMS DOD is used (Fig. 5.11b), with the only exception being the lower bin around zero. There are days when the MIDAS DOD GHI attenuation exceeded 60%, while the upper limit for CAMS was ~45%. The strong impact of the aerosol particles on the direct component of solar radiation reaching the Earth's surface is depicted in the distributions of the DNI attenuation due to both total aerosols (Fig. 5.11c) and dust (Fig. 5.11d) with values up to 100% for the MIDAS dataset.

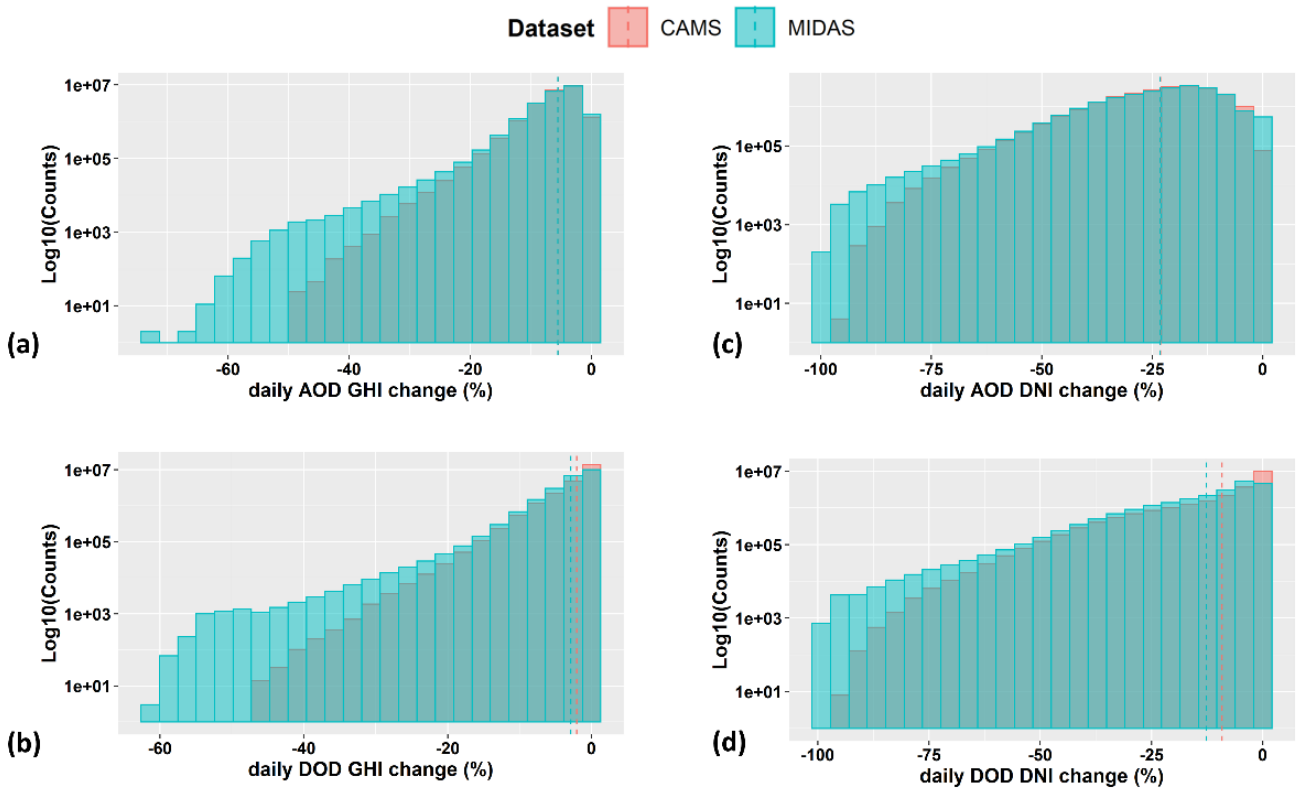

Figure 5.11 Distribution of daily GHI changes (%) due to the presence of aerosols **(a)** and dust **(b)** under MIDAS and CAMS AOD and DOD. The same for daily DNI change (%) in panels **(c,d)**.

The intercomparison between MIDAS and CAMS AOD and DOD direct effects on DSSI showed how the AOD and DOD differences between the two datasets were expressed in differences in their direct radiative effects. Underestimation of high AODs and strong DOD underestimation from CAMS were clearly depicted in the attenuation of the DSSI. Thus, the MIDAS dataset is used and discussed in the subsequent analysis. The resulting direct radiative effects on the surface indicated the important role of total aerosols and especially dust over the Middle East and North Africa (MENA) region, where DSSI attenuation by clouds is comparable or even lower than aerosols.

5.4 Extreme Dust Events

Fig. 5.12 a presents the geographical distribution of mean MIDAS DOD from the resulting 67 eDEDs. The highest values up to 0.5 of mean DOD from the extremes were found over northwestern Africa, while significantly high mean values up to 0.43 and 0.35 were found also over Egypt and the Middle East, respectively. The highest values of the associated impacts on GHI and DNI, up to 12% and 44%, respectively (Fig. 5.2 b,c), were found over northwestern Africa, specifically over southern Tunisia and central Algeria. Large values of eDED mean attenuation were also found over Libya, Egypt, and the Middle East, with values ranging from 4% to 9% for GHI and 17% to 35% for DNI for the bigger part of these areas. Cyprus is the Mediterranean island that was affected the most by the resulting extreme dust events with mean values of GHI and DNI attenuation up to 6.5% and 24%, respectively.

For the southern European countries, lower values of mean eDED attenuation were derived, up to 4% for GHI and 19% for DNI, except for very high values over southeastern Spain, up to 5% and 23%, respectively.

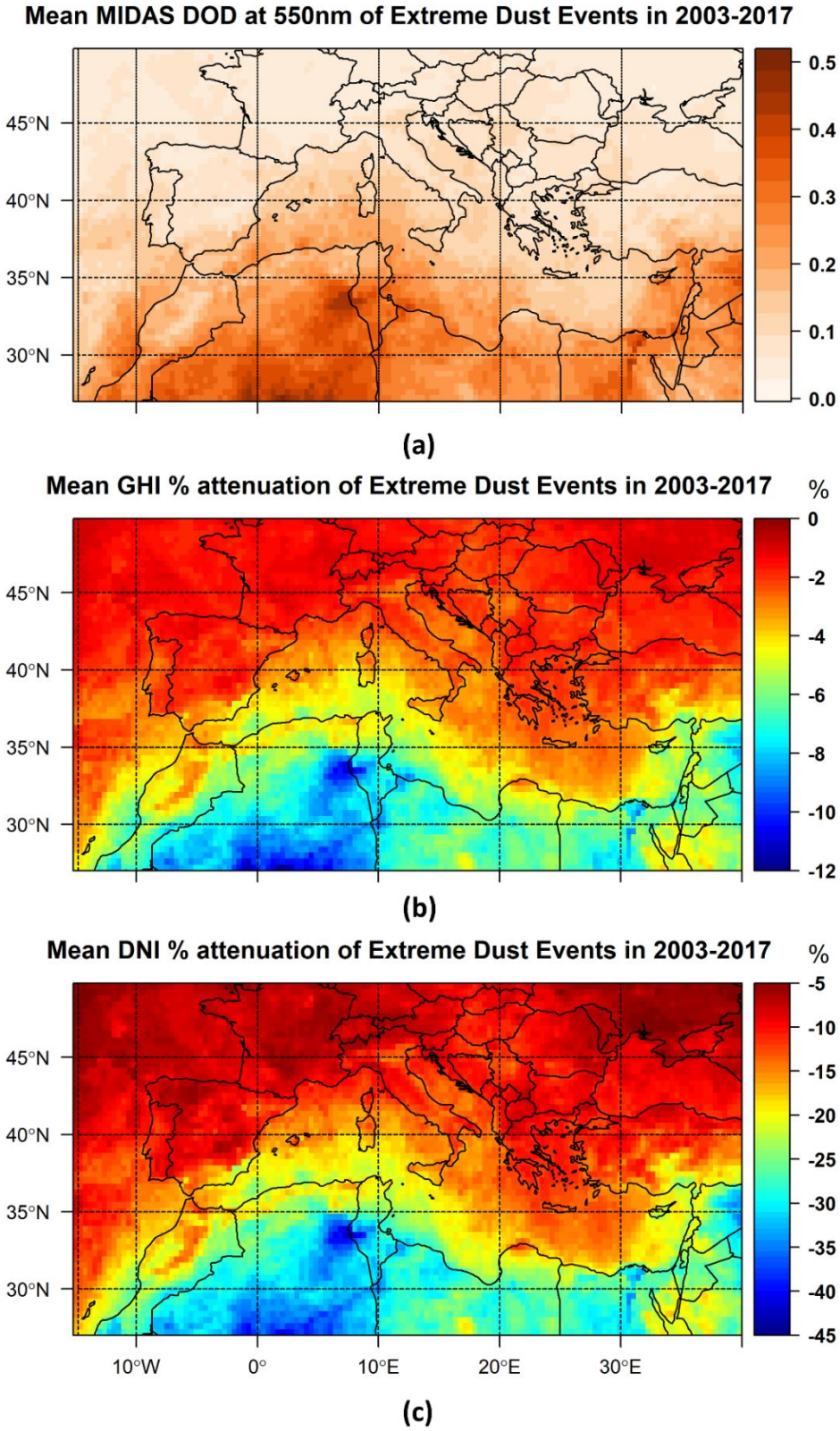

Figure 5.12 Geographical distribution of mean MIDAS DOD at 550 nm for extreme dust episode days (eDEDs) **(a)** and the corresponding GHI **(b)** and DNI **(c)** change (in %).

It should be emphasized here that these results correspond to the long-term (2003–2017) average of the eDEDs and their direct radiative effects over the region of interest (ROI). Individual dust events are associated with extremely high dust concentrations, resulting in GHI and DNI attenuations up to 50% and 90%, respectively (Kosmopoulos et al., 2017).

5.5 Interannual Variability and Trends

Using the simulated clear-sky DSSI, we investigated the interannual variability of its changes that were attributed to total aerosols and the dust and non-dust components. The non-dust optical depth (nDOD), which is considered to be the optical depth of all other aerosol components besides dust, was derived by subtracting DOD from AOD. The main assumption to derive nDOD is that the dust particles are externally mixed with the rest of the aerosol chemical species. For the nDOD RTM simulations, the same additional optical properties as those of total aerosols were assumed. By comparison with the RTM results without aerosols, the corresponding annual GHI and DNI attenuations due to all other aerosol components except dust were derived (nDOD GHI and DNI attenuation hereafter). The interannual variability of the AOD (red line), DOD (blue line) and nDOD (green line) GHI and DNI attenuation is presented (Fig. 5.13b, c) for three different domain averages. The selection of the domains for the spatial averaging was based on the south-to-north gradient of dust, and the geographical limits of those domains are illustrated in Fig. 5.13a.

The year-to-year variability of GHI attenuation by the different aerosol components is weaker (0.5% to 1%) compared to the corresponding variability of the DNI attenuation (2–4%). For the DSSI attenuation (both GHI and DNI) by total aerosols, a successive decline was found after 2008, which is more prominent for D3. This reduction in the AOD DSSI attenuation is in line with the brightening effect over the Mediterranean reported in other studies (Kazadzis, 2018a; Nastos et al., 2013). The resulting decline in the DSSI attenuation by aerosol is attributed mainly to the dust component for D1 and D2, where the variability of annual DOD DSSI attenuation is also large and highly correlated with annual attenuation by total aerosols (correlation coefficients (cc) ranging from 0.85 to 0.92). For D3, which has the sharpest decrease in DSSI attenuation by total aerosols, this is attributed to both dust (cc = 0.84) and nondust components (cc = 0.87).

The increase in GHI (DNI) in D2 and D3 represents the average of positive, statistically significant trends of the order of 1–2% (3–6%)/decade, mainly attributed to decreases in DOD, over the Mediterranean Sea and most of Europe, and negative, nonsignificant, trends over the Anatolian Peninsula. In D1, positive, significant trends in GHI (DNI) of the order of 1% (3–4%)/decade were found over Libya and northwestern Egypt, while negative significant trends of similar magnitude were found over many regions of the remaining D1 area. The overall result was a small positive trend during the whole period (2003–2017), which—as discussed earlier—mainly depicts the increase in

2008–2017. More information regarding the spatial distribution of the trends can be found in the Supplementary Materials (Fig. B17).

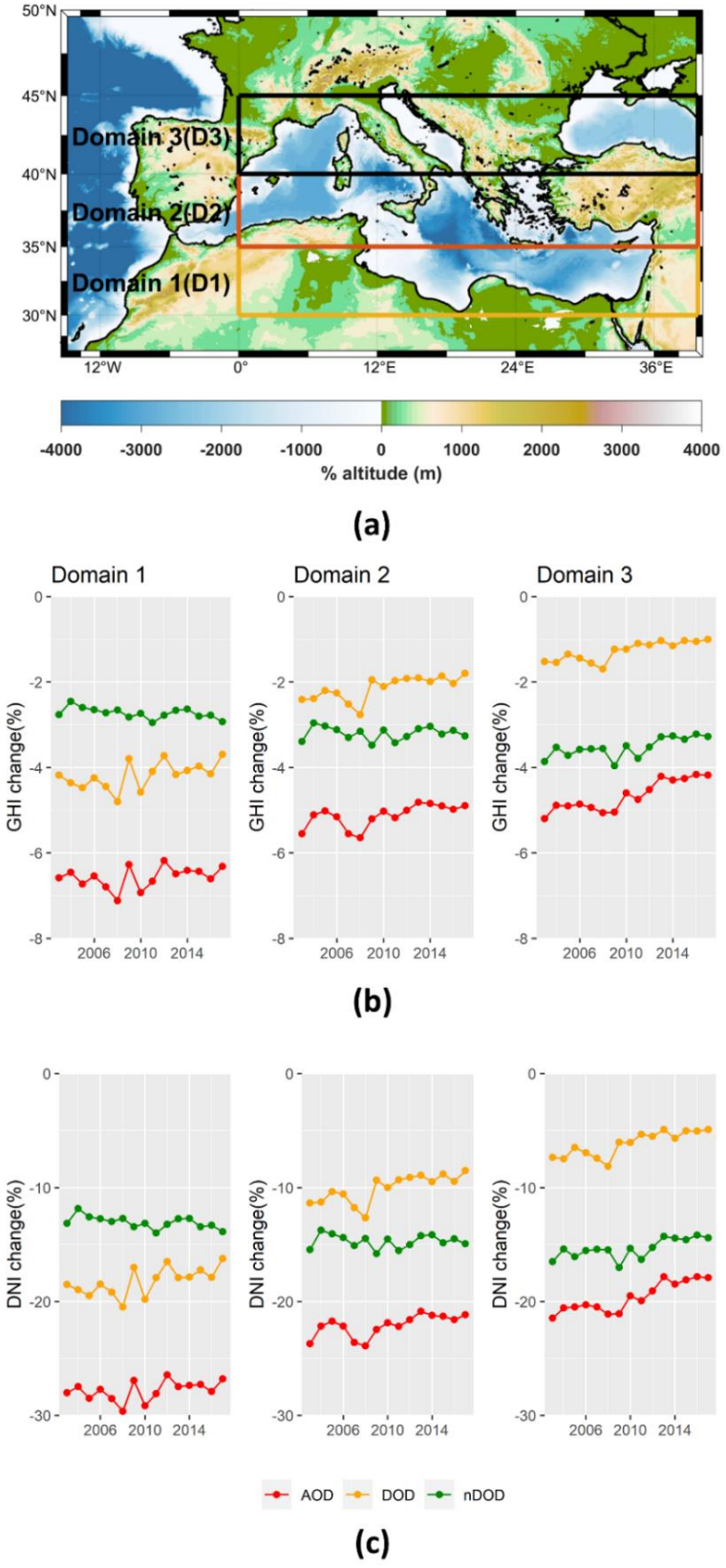

Figure 5.13 (a) The geographical limits of the domains used for the spatial averaging. Interannual variability of GHI **(b)** and DNI **(c)** annual integral change (in %) by total aerosols (AOD, red line), dust (DOD, blue line) and other aerosol components beside dust (nDOD, green line) regional averaged for domains 1, 2 and 3 for the 15-year period (2003-2017).

5.6 GHI and DNI clear -sky climatology

The availability of solar resources at the Earth's surface is essential information for the different phases of a plant's deployment and operation. Average annual solar irradiation is a primary site selection criterion (Sengupta et al., 2021), and a low seasonal variability is preferable in order to match the power demand. According to the results of previous sections, there are areas where the GHI and DNI attenuation due to aerosols can reach 13% and 50%, respectively, which are mainly areas with high solar energy potential (e.g., North Africa). So, the clear-sky GHI and DNI mean annual integrals based on high-quality AOD retrievals are of great importance for such areas with scarce cloudiness.

The clear-sky climatology of GHI and DNI was derived using the MODIS AOD as input in the RTM. Using the daily irradiations (see Section 3.8.2), annual and seasonal integrals of GHI and DNI were derived for every year, and their mean values were calculated for the entire period (2003-2017) and are presented in Fig. 5.14 and B 18-19, while their spatial averages are summarized in Table 5.5. Given the fact that the cloud effects have not been considered, the description of the results is focused on the south part of the domain, over North Africa and the Middle East, which are areas with high solar energy potential, scarce cloudiness and high aerosol loads.

The patterns of both GHI and DNI spatial variability are mainly determined by MODIS AOD (Section 5.2) and the surface altitude. For GHI, a latitudinal gradient (south-to-north) is evident as well. Over North Africa and the Middle East, the cumulative annual GHI and DNI range from 7500 to 8800 MJ/m^2 and from 7000 to 12,000 MJ/m^2, respectively (Figure 5.14). Maximum values are observed in the Atlas Mountains (Northwest Africa), in the western parts of Libya and the southeastern parts of the ROI. Regarding the spatial variability of the seasonal integrals, we focused on spring and summer, when the effect of clouds is minimal over the ROI. At this time of the year, the distribution of aerosols expands to the western parts of North Africa, and the spatial variability of DSSI components follows that pattern. While the maximum levels of DNI over the high-altitude areas are ~3300 MJ/m^2 in spring and ~3100 MJ/m^2 in summer, very low levels of ~1800 MJ/m^2 were found in the same seasons for aerosol-affected areas. These differences are less pronounced for GHI (400 MJ/m^2 difference in both seasons).

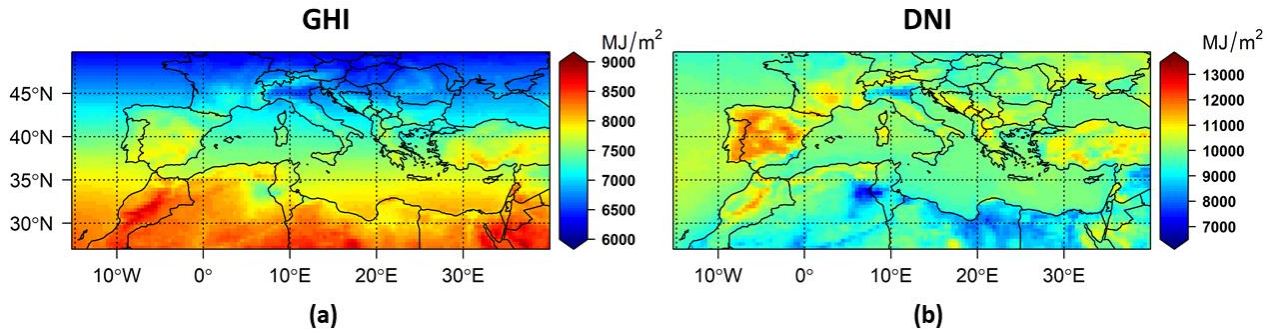

Figure 5.14 Mean (2003–2017) annual integrals for clear-sky GHI **(a)** and DNI **(b)** using MODIS AOD.

Table 5.5 Regional averages of mean annual and seasonal integrals of clear – sky GHI and DNI using MODIS AOD.

	GHI (MJ/m²)	DNI (MJ/m²)
	Annual	
	7486 (±630)	9899 (±616)
	Seasonal	
winter	1074 (±273)	1972 (±231)
spring	2287 (±116)	2747 (±247)
summer	2612 (±57)	2931 (±299)
autumn	1512 (±219)	2249 (±143)

5.7 Effects of Aerosols and Clouds on the Levels of Surface Solar Radiation and Solar Energy in Cyprus

In the analysis up to now, aerosol radiative effects were considered. To include also the effect of clouds a smaller area inside the Mediterranean domain was considered. The same methodology was applied for Cyprus including a cloud dataset, aiming to compare the relative contribution of aerosol and cloud in surface solar radiation attenuation in a Mediterranean environment. The selection of Cyprus was based on its high solar energy potential and its complex aerosol regime.

Attenuation of the monthly integrals of surface solar radiation (SSR) by clouds was calculated from CM SAF Surface Radiation Data Set-Heliosat (SARAH)-Edition 2.1 (Pfeifroth et al., 2019) retrievals of the SSR (hereon this product is referred as CM SAF-SARAH2.1) for 2004–2017. Details about the SSR retrievals of this product can be found in Posselt et al. (2012) and Pfeifroth et al. (2018). The ratio between all-sky and cloudless-sky irradiances, commonly called the cloud modification factor (CMF), was calculated for the DSSI components. Uncertainties in the retrieved monthly CMF were estimated at 3%. Then, the monthly CMF was calculated for each quantity (GHI, DNI, etc.). Monthly integrals of the cloudless-sky irradiance were multiplied with the corresponding monthly CMF for the retrieval of the all-sky irradiance. Finally, climatology of the all-skies GHI and DNI was developed

for Cyprus by averaging over the whole 14-year period, using DSSI simulations based on MODIS AOD and CMF from CM SAF-SARAH2.1.

The maps of the mean annual integrals of GHI and DNI are shown in Fig. 5.15. The mean seasonal integrals for the four seasons of the year are presented in Appendix (Fig. B20). Despite the small geographical extent of Cyprus, Troodos Mountains seem to have drastic effect on the spatial variability of solar potential, especially for DNI. The cumulative GHI is 6800–7200 MJ/m^2 (Fig. 5.15) with maximum values at the north slopes of Troodos Mountains. The cumulative DNI was 7500–8500 MJ/m^2, with maximum levels slightly shifted to the north relative to GHI.

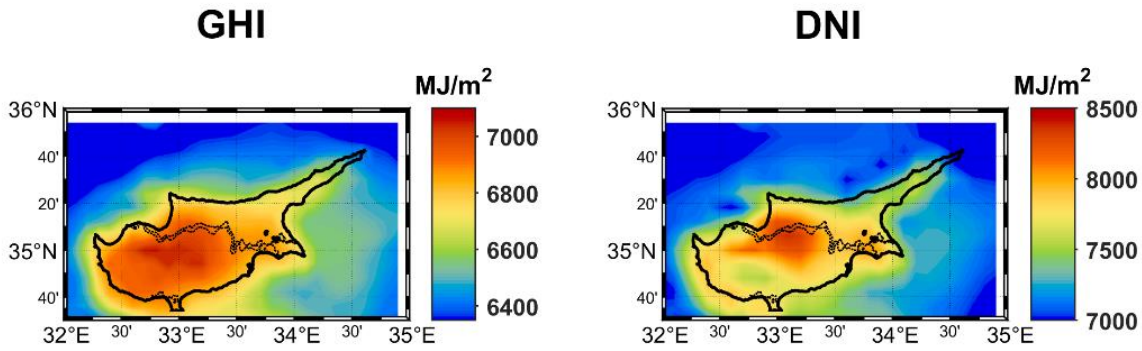

Figure 5.15 Total annual all-sky GHI and DNI.

In spring and summer, the effect of clouds was less pronounced, and the spatial variability depended mainly on the distribution of aerosols over the island (Fig. B20). Maximum levels of GHI (2100 MJ/m^2 in spring and 2700 MJ/m^2 in summer) were found at the north side of the mountains while minimum levels were found at the south (2000 MJ/m^2 in spring and 2600 MJ/m^2 in summer). Again, the differences were more pronounced for DNI. In both seasons the difference between the DNI north and south of the mountains may be up to 300 MJ/m^2.

The intra-annual variability of the effects of aerosols and clouds on GHI and DNI was investigated for five locations in Cyprus (four biggest cities of Cyprus Larnaca (34.92° N, 33.62° E); Limassol (35.17° N, 33.33° E); Nicosia (34.67° N, 33.04° E) and Paphos (34.83° N, 32.80° E) and Omodos, (34.78° N, 32.42° E) a mountainous site at 800 m altitude on Troodos Mountains) and the results are presented in Fig. 5.16. Shaded areas in the graphs represent the standard deviation of the climatological averages for the 14-year period. As expected, in Omodos, which is at a high altitude at the south side of Troodos the effects of clouds are generally the strongest among the five locations. What is interesting is that attenuation by aerosols is also strong at Troodos despite the high altitude. For all five locations there is a clear annual cycle of the attenuation by clouds. In winter, clouds decrease GHI by 25–30% and DNI by 35–50%. In spring and autumn attenuation by clouds becomes weaker. In summer, the role of clouds in the attenuation of GHI was practically the same as that of aerosols, while the

attenuation of DNI by clouds was 7–8 times weaker compared to the attenuation by aerosols. Dust blocked on average 3 times more DNI than clouds in summer.

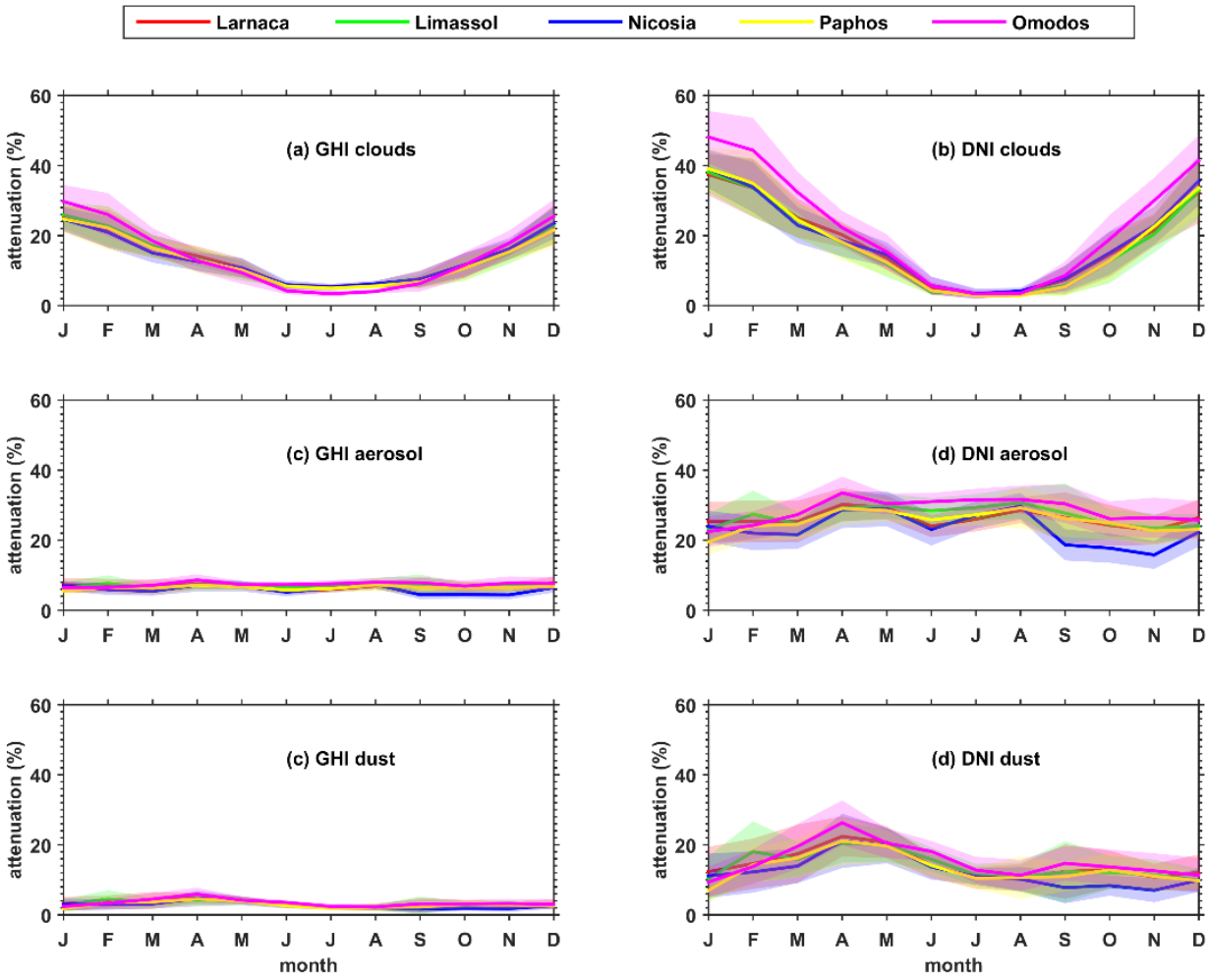

Figure 5.16 Attenuation of the monthly GHI and DNI (in %) by clouds, aerosols, and dust aerosols (climatological monthly averages for 2004–2017).

The annual cycle of the attenuation by aerosols was not as pronounced as the annual cycle of the attenuation by clouds. Attenuation by aerosols was stronger in spring and summer and weaker in winter. Maximum attenuation in April and May (8–10% for GHI and 27–32% for DNI) was mainly due to increased levels of dust. In autumn, dust and total aerosols had a noticeably weaker effect on GHI and DNI in Nicosia with respect to the four other locations.

The results presented in Fig. 5.16 show that the variability in the levels of GHI and DNI in Cyprus was strongly correlated with the variability of aerosols, and especially dust aerosols. It is noteworthy that low DOD coincided with low AOD, and high DOD coincided with high AOD for all five stations, which shows that dust was the most significant regulator of the levels of GHI and DNI.

5.8 Summary and conclusions

The broader Mediterranean Basin hosts and receives various aerosol types, which are quite variable in spatial and temporal scales. The aim of the work presented in this chapter was to provide an insight into the perturbation of the surface solar radiation, and the subsequent impacts on solar energy production, attributed to the presence of all aerosol types, but with special emphasis on dust. AOD and DOD from two different datasets (MIDAS and CAMS) were used as inputs to the libRadtran RTM (in terms of precalculated LUTs) along with other necessary aerosol and atmospheric parameters under clear-sky conditions. From the sensitivity analysis conducted, aerosol profiling has a negligible impact on the calculations of surface solar irradiances. Model outputs were the GHI and DNI, which are of particular interest for different solar power systems (PV and CSP, respectively). The study domain encloses the broader Mediterranean Basin, and the study period spans from 2003 to 2017 (15 years).

The intercomparison between MIDAS and CAMS datasets revealed that the latter slightly underestimates AOD, and this is mainly evident over areas hosting major aerosol sources, while it strongly underestimates DOD by up to 40% (-0.03) with respect to MIDAS, which agrees with the underestimation reported by Bennouna et al. (2020) when compared with ground-based retrievals. The CAMS underestimation of high AODs resulted in weaker GHI and DNI attenuations on average by 1–4% and 4–11%, respectively. Likewise, due to the pronounced CAMS DOD underestimation, weaker attenuations were found (by 0.5–4% for GHI and 1–15% for DNI). These findings reveal that using CAMS DOD to describe the radiative effects of dust would give highly uncertain results, especially over areas that are significantly affected by dust, and highlight the importance of using reliable aerosol and dust optical properties to accurately simulate DSSI.

Using the high-quality satellite-derived MIDAS AOD/DOD datasets, a 15-year climatology of total aerosols and dust was established for the broader Mediterranean Basin. The largest AODs were found over dust sources or areas affected by dust transport, with maximum long-term averaged AOD up to 0.48 over Northwest Africa (up to 0.66 for summer season). Over the same area, the peak of MIDAS DOD values was derived as well, with a mean annual value up to 0.35 (up to 0.45 for summer). Dust was found to contribute to total aerosol loads, in optical terms, from 40% to 90% over North Africa and the Middle East, making dust the most important aerosol component over these areas.

Aerosols attenuate GHI by 1–13% and DNI by 5–47%. The largest attenuation (4–13% for GHI and 15–47% for DNI) was found over North Africa and the Middle East. Over the same areas, the GHI and DNI reduction by dust ranged from 2–10% and 9–37%, respectively, contributing 45–90% to the total aerosol effects on DSSI. During the dry seasons of the year, when the cloud effects over these areas are comparable or even lower than the effects of aerosols, the maximum of aerosol and dust attenuation of the GHI (up to 14% and 11%, respectively) and DNI (up to 53% and 40%, respectively)

was found, with the dust being responsible for up to 95% of the AOD DSSI attenuation. On a daily basis, the GHI reduction due to total and dust aerosol reached substantially higher values, up to ~75% and ~60%, respectively. There were days when the DNI component was totally blocked (-100%) under high aerosol and dust loads.

The investigation of the intra-annual variability of the effects of aerosols and dust on GHI revealed, apart from their seasonal variations, the significant role of SSA in calculating the radiative effects of aerosols. The combination of low SSA values with considerable AODs/DODs resulted in peak of regional averaged AOD GHI attenuation in winter, which is reversed compared to the seasonal cycle of MIDAS AOD (maximum in summer and minimum in winter). The same reasons explain the sharp peak of regional averaged DOD GHI attenuation in spring.

The interannual variability of the DSSI attenuation by total aerosol, dust and total aerosol excluding dust was assessed for three subdomains covering the Mediterranean Basin. After 2008, a successive decline in aerosol effects on DSSI was found for all domains, which was attributed mainly to the reduction in dust.

Since it is well documented that the Mediterranean Basin is frequently affected by dust intrusions, an assessment of the GHI and DNI attenuation was conducted for extreme dust events over the area. Using the MIDAS DOD dataset and by adopting the methodology proposed by (Gkikas et al., 2009, 2012), 67 eDEDs (4.5 eDEDs $year^{-1}$) were identified over the study area for the period 2003–2017. The average DOD during these events reached values up to 0.50 (over North Africa) and the corresponding GHI and DNI attenuations were 12% and 44%, respectively. South Europe was also found to be affected by eDEDs, with the largest GHI and DNI attenuations taking place in southeastern Spain, reaching 5% and 25%, respectively.

Taking advantage of the 15 years of high-quality daily satellite retrievals of AOD from the MIDAS dataset, a clear-sky GHI and DNI climatology for the broader Mediterranean Basin was derived. An added value of this new, clear-sky climatology is that the DSSI values were simulated using, apart from satellite-derived AOD, a climatology of additional aerosol optical properties (SSA, AE), as well as model and satellite products for key atmospheric factors (TCWV and TOC). The Cyprus case study shows that for this area in summer the GHI attenuation by aerosol is comparable to the attenuation by clouds, while solely dust attenuates more DNI than clouds. Thus, of particular interest are North Africa and the Middle East in summer, where high spatial variability of GHI and DNI was found, of 14% and 42%, respectively.

The basic limitations of the study are linked with the RTM inputs and their uncertainties. The main parameter to consider is the optical depth (total aerosol or dust). The uncertainties (MODIS-AOD, MIDAS-DOD, CAMS) have been documented based on the corresponding literature. In addition, SSA

and AE data were used as monthly values for a 1° x 1° grid through MACv2 climatology. Day-to-day variability of such parameters can affect the calculated DSSI on a daily basis. However, it has an almost negligible effect when using monthly GHI and DNI for describing the basic climatology of the region under study, especially when optical depth data are relatively accurate. Finally, cloud contamination for satellite-based data is a factor that can affect such DSSI results. However, basic comparison of such data with CAMS modeled data showed no significant systematic optical depth overestimation from the satellite-based data. The same results were documented when MODIS and MIDAS optical depth comparisons with AERONET were initiated.

In conclusion, this study aims to contribute towards a better understanding of the role of aerosols and especially of dust on surface solar radiation in terms of GHI and DNI over the Mediterranean Basin. The results of this analysis, apart from their importance from the perspective of climate science, provide valuable information in terms of management and future planning of PV and CSP installations.

6 Solar radiation nowcasting and short-term forecasting

This chapter is based on the publication, under review: ***Papachristopoulou, K.****, Fountoulakis, I., Bais, A. F., Psiloglou, B. E., Papadimitriou, N., Raptis, I.-P., Kazantzidis, A., Kontoes, C., Hatzaki, M., and Kazadzis, S.: Effects of clouds and aerosols on downwelling surface solar irradiance nowcasting and sort-term forecasting, Atmos. Meas. Tech. Discuss. [preprint], https://doi.org/10.5194/amt-2023-110, in review, 2023.*

In the previous chapter, the important effect of aerosols on solar radiation attenuation was quantified, which under certain conditions can be larger than the effect of clouds. In addition, the importance of the use of accurate aerosol optical properties dataset was revealed. While the world's energy demand (e.g., electricity, heating, transportation) is growing, renewable/carbon free sources are the only way to avoid cardon emissions. As the sun is the most abundant source of energy on earth, harnessing solar energy is one of the most promising ways to achieve carbon neutrality of energy supply in the future to mitigate climate change and its effects.

For a successful deployment of renewable technologies exploiting solar energy solar resources availability and its fluctuations with time is important information provided by nowcasting and short-term forecasting tools of global horizontal irradiance (GHI). In this chapter the role of clouds and aerosols in such tools is investigated, using ground-based measurements by:

- introducing the SENSE2 and NextSENSE2 upgrades of SENSE and NextSENSE systems, respectively.
- validating the improved nowcasted GHI using ground-based pyranometer measurements for 1 year (2017).
- investigating the cloud and aerosol effects on GHI estimates.
- proposing a possible correction for GHI estimation based on MSG COT real time information.
- validating CMV-forecasted GHI and benchmarking the results with those obtained by the persistence method.

6.1 SENSE and NextSENSE improvements

SENSE2 is an operational system that produces fast estimates of GHI in real time every 15 min for a wide area including Europe and the Middle East–North Africa (MENA) region at high spatial resolution (~5 km). These estimates are calculated from earth observation (EO) data and look-up tables (LUTs) derived from radiative transfer model (RTM) simulations. The SENSE2 presented in this thesis (Fig. 6.1) is an improved system, compared to the previous SENSE version, in terms of the

parameterizations for radiative transfer calculations and, mainly, the improvement of the aerosol and cloud representation in the model using a more detailed LUT and multi-parametric equations for different aerosol and cloud scenes, respectively. The new version of the SENSE2 system is available as a web service via https: //solar.beyond-eocenter.eu/#solar_short.

The first improvements of the SENSE2 system are as follows:

- The computations of clear-sky GHI are performed during the previous day for the whole domain (1.5 million pixels) every 15 min; for the current day, the real-time cloud information is applied to provide all-skies GHI in real time (no NN is used).
- The computations of clear-sky GHI are based on a new, more-detailed LUT of ~16 million combinations of simulated GHI at the earth's surface that was generated using the National Infrastructures for Research and Technology (GRNET) High Performance Computing Services and the computational resources of the ARIS/GRNET infrastructure (see Section 3.6.2).

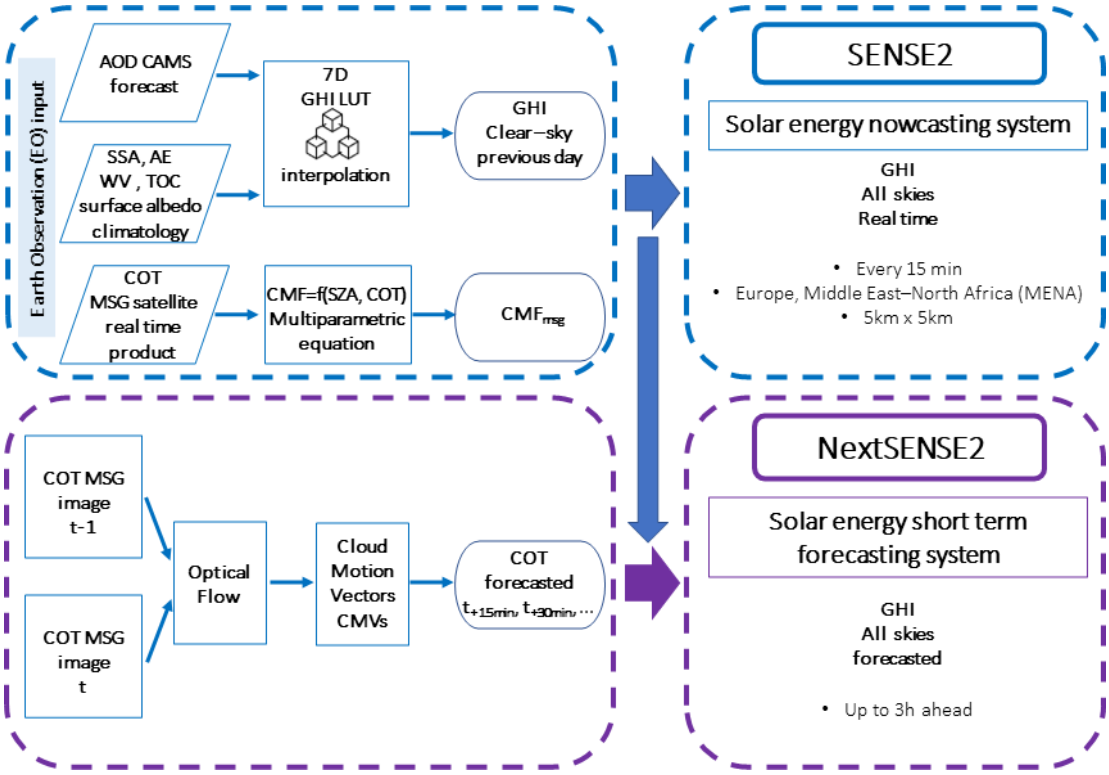

Figure 6.1 Schematic overview of the solar energy nowcasting system (SENSE2) and system for short-term forecasting up to 3h ahead (NextSENSE2).

The clear-sky GHI estimates from SENSE2 (Fig. 6.1) are calculated on the previous day by linear interpolation in the seven dimensions (7D) of the precalculated GHI LUT using the corresponding inputs. Specifically, the solar zenith angle (SZA) values are precalculated for every grid cell of the domain (1.5 million in total) for 15 min time steps. The main input parameter for the clear-sky computations is the forecasted AOD at 550 nm from CAMS ("CAMS AOD" hereafter). The forecasts

for the day of interest are values from the CAMS run initialized at 00:00 UTC on the previous day (e.g., the AOD used to simulate the GHI for the 24th of a month is derived from the CAMS run that started on the 23rd at 00:00 UTC). Climatological values are used for the interpolation in the 7D LUT for the additional aerosol optical properties SSA and AE (MACv2 climatology; Kinne, 2019), the water vapor (WV) (CAMS reanalysis; Inness et al., 2019)), the total ozone column (TOC) (climatological values based on ozone-monitoring instrument (OMI) TOC data; Bhartia, 2012) and the surface albedo (GOME-2 database of directionally dependent Lambertian-equivalent reflectivity; Tilstra et al., 2017, 2021). It should be mentioned that the interpolation procedure in the 7D LUT was added to the new SENSE2 to further improve the accuracy of the GHI estimations. Finally, since the results of the RTM runs are for sea level and the mean Earth-Sun distance, a post-correction of the clear-sky GHI values from the LUT is performed for the surface elevation using the methodology described in Fountoulakis et al., (2021) and the actual Earth-Sun distance for the particular day of the year (DOY). Based on simulations for various atmospheric and surface albedo conditions, Fountoulakis et al. (2021) estimated an average increase of the GHI of 2% per km, which has also been applied to the model output to correct the surface GHI for sites at higher altitudes than sea level.

The use of LUTs in operational surface solar radiation retrievals instead of direct RTM calculations is well established (e.g., Mueller et al., 2009; Qu et al., 2017). From a technical point of view, there are various concepts which can reduce the number of RTM simulations needed to generate a LUT by several orders of magnitude. Mueller et al. (2009) developed a flexible, fast, and accurate scheme to retrieve the broadband surface solar irradiance (CM CAF datasets) using the hybrid eigenvector approach, resulting in a combination of basis LUTs with an optimized interpolation grid and parameterizations using only almost 1000 RTM calculations. This approach was extended by Mueller et al. (2012) to wavelength bands for spectrally resolved surface solar irradiance retrievals from spaceborne data. This optimization of the computing performance is of paramount importance for the reprocessing of a large amount of satellite data (up to a few decades). In this work, the main concept behind the generation of our clear-sky LUT was to have spectral irradiance outputs (1 nm spectral resolution). The choice to calculate spectral solar data and not directly calculate total shortwave radiation is based on the fact that the SENSE2 output could be used for other applications (e.g., health and agriculture), based on the irradiance weighting of a relevant spectral range with an action spectrum (function) defined for each of the effects. So, a large number of RTM runs had to be performed (once) for the spectral surface solar irradiance that covered all possible combinations of atmospheric and surface states. Technically, since the operational setup of the SENSE2 model allows for the computation of the clear-sky GHI values from the previous day, the processing time for interpolation to the seven dimensions of the LUT has no effect on the timely production of the real-time output of the model every 15min, while the accuracy of the clear-sky output is almost identical to

direct RTM simulations, and the uncertainties of the clear-sky GHI retrievals are related only to the uncertainties of the model inputs. In addition, this LUT includes various aspects, especially for aerosols (AOD, SSA, AE), that can reduce the uncertainty under different aerosol conditions for broadband solar radiation or specific spectral regions.

Another improvement is related to the cloud representation in real time using multi-parametric equations for different cloud scenes based on the cloud modification factor (CMF) concept instead of using the COT as an input parameter in direct RTM calculations. The computation of the all-skies GHI in real time every 15 min is based on the COT product we extract operationally in real time using broadcasted MSG satellite data and the software package provided by the EUMETSAT Satellite Application Facilities of Nowcasting and Very Short Range Forecasting, NWC SAF (Derrien & Le Gléau, 2005; Meteo France, 2016). Neither the direct radiative transfer simulations nor the multi-dimensional interpolations would be sufficiently fast to provide the all-skies GHI SENSE2 product for 1.5 million pixels in a timely manner. Instead, a multi-parametric equation was constructed by fitting on libRadtran simulations for a wide range of COT values and different SZAs (see the points in Fig. 6.2a). The design of the cloud model was a trade-off between the relevance of the cloud property and the operational implementation of the model. It was shown in previous studies (Qu et al., 2017) that, in most of the cases (except for high surface albedo values >0.9), the vertical position and extent of the cloud has only a small or a negligible influence on the RTM simulations of surface solar irradiance. Under cloudy conditions, COT is the variable that has the greatest impact on the simulation of surface solar radiation (Oumbe et al., 2014; Qu et al., 2017; Taylor et al., 2016). In our simulations, spherical droplets were assumed, with typical values for the effective radius (R_{eff} =10 μm) and typical climatological mean heights (cloud's base at 2 km and its height was 3 km) (Taylor et al., 2016; Kosmopoulos et al., 2018) used given the unavailability of height descriptors in the operational mode, the negligible influence of changes in droplet effective radius with respect to COT on the simulation of surface solar radiation (Oumbe, 2009), and that this setup helps to simplify the cloud model. The COT of the cloud layer at 550 nm is additionally specified, which leads to an adjustment of the default liquid water content value of 1 g cm^{-3} using the parameterization from Hu & Stamnes (1993). Finally, homogeneous cloud layer was used for the libRadtran simulations, meaning a cloud cover fraction value of 100 %, which is one of the model's limitations, since it is not always correct to assume totally cloudy pixels for low values of COT (Mueller et al., 2009). The simulated GHI for each COT was divided by the GHI for COT=0 (clear sky) for the same SZA to derive the CMF (Eq. 6.1). The CMF ranges from zero (overcast conditions) to 1 (clear sky) and it is easy to use to provide all-skies GHI by simply multiplying clear-sky GHI by CMF (Eq. 6.3). The libRadtran-derived CMFs for each SZA were fitted against COT using the hyperbolic tangent function. The resulting fits are shown as solid lines in Fig. 6.2a and are mathematically expressed by the multi-parametric Eq. (6.2).

$$\mathrm{CMF} = \frac{\mathrm{GHI}}{\mathrm{GHI_{clr}}} \tag{6.1}$$

$$\mathrm{CMF} = 1 - \tanh^{b}(\mathrm{COT}^{\alpha}) \tag{6.2}$$

Here, α and b are polynomials of SZA:

$$\alpha = 2.24 \cdot 10^{-1} + 2.81 \cdot 10^{-4} \cdot \mathrm{SZA} - 2.18 \cdot 10^{-5} \cdot \mathrm{SZA}^2 + 3.71 \cdot 10^{-7} \cdot \mathrm{SZA}^3 - 2.65 \cdot 10^{-9} \cdot \mathrm{SZA}^4$$

$$b = 12.2 + 5.27 \cdot 10^{-3} \cdot \mathrm{SZA} - 2.24 \cdot 10^{-3} \cdot \mathrm{SZA}^2 + 8.33 \cdot 10^{-6} \cdot \mathrm{SZA}^3 + 3.94 \cdot 10^{-8} \cdot \mathrm{SZA}^4.$$

The real-time MSG COT is used, along with SZA, as an input in Eq. (6.2) every 15 min for ~1.5 million pixels to calculate the CMF ("CMFmsg" hereafter). Apart from being very fast, this formula also accurately calculates CMFmsg, as can be seen by a comparison of the CMF values derived by Eq. (6.2) against those from libRadtran runs (Fig. 6.2b). CMF differences are less than 0.015 (or 1.5%) for SZAs lower than 70°, while they are up to 0.03 (3%) for SZAs between 80 and 90°, showing the very good representation of the CMF as a function of COT achieved with Eq. (6.2). In terms of accuracy this means that using Eq. (6.2) is almost the same as running RTM simulations, but in terms of computational time, Eq. (6.2) is far more efficient in the operational mode. Finally, by multiplying CMFmsg by the clear-sky GHI, the all-skies GHI product is obtained (Eq. 6.3), in less than 1 min for 1.5 million pixels.

$$\mathrm{GHI} = \mathrm{GHI_{clr}} * \mathrm{CMFmsg} \tag{6.3}$$

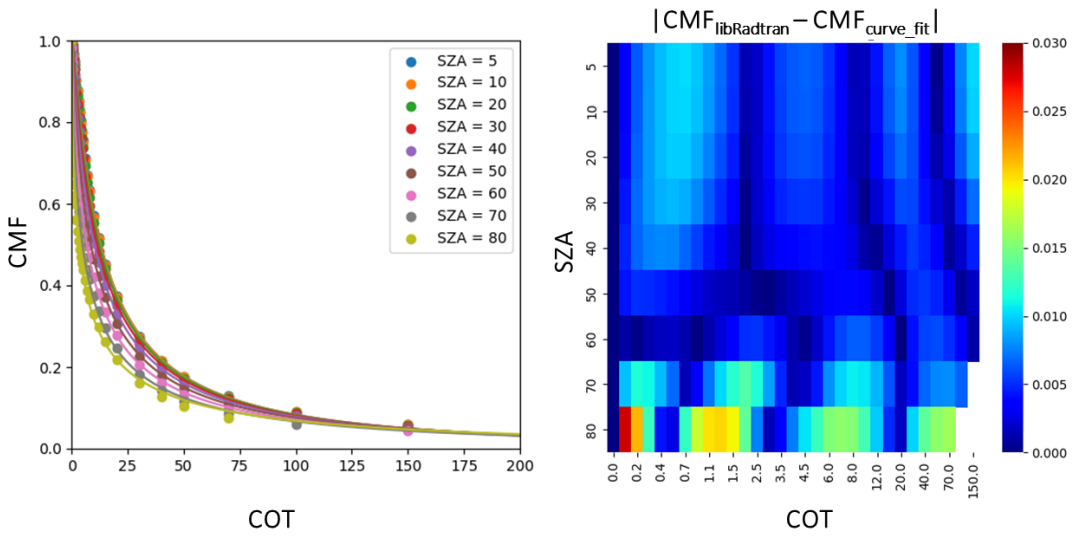

(a) **(b)**

Figure 6.2 (a) Cloud modification factor (CMF) versus cloud optical thickness (COT) and solar zenith angle (SZA) based on radiative transfer simulations of global horizontal irradiances using the libRadtran package. CMF is the ratio of global horizontal irradiance (GHI) to the GHI under cloudless conditions (COT=0). **(b)** Differences between the CMF derived directly from libRadtran simulations and that derived from Eq. (6.2), as a function of COT and SZA.

The new SENSE2 configuration was built to improve GHI nowcasting at the 15 min timescale. Additionally, it allows the system greater flexibility:

- It can include reanalysis or measured data of AOD and other optical properties e.g., CAMS reanalysis or AERONET measurements.
- It can be extended to other output products. Apart from GHI, direct normal irradiance (DNI) or total irradiance on a tilted surface could be also produced. By introducing spectral information and making the appropriate modifications, products related to specific spectral regions could be also derived (e.g., the UV Index (using real-time TOC data as input) and the photosynthetically active radiation (PAR)).
- It can run a past time series of one or few locations autonomously using actual measurements as input. In this case, if there is no time constrain, model runs could be performed without the parametrizations (LUT and multi-parametric functions).

NextSENSE2 is the operational system that provides forecasts of GHI up to 3 hours ahead with a 15 min time step by applying a CMV technique to the MSG COT product (Fig. 6.1). In Section 3.9, the method employed to produce forecasted COT is described, which is the main input to derive the operational forecasts of GHI. All the other EO inputs and the radiative transfer parameterizations for fast estimates of forecasted GHI are the same as those described in this section for the SENSE2 model.

6.2 SENSE2 and NextSENSE2 evaluation

To validate the GHI estimates, 1 year (2017) ground-based measurements from 8 BSRN stations, and from two additional stations at Athens (ASNOA: NOA's Actinometric Station) and Thessaloniki (see Section 3.4 for details and Table 3.1 and Fig. 3.1) were used.

The results are discussed separately for the evaluation of nowcasted GHI (Section 6.2.1) based on SENSE2 outputs ("modeled GHI" hereafter) and the evaluation of the short-term forecasted GHI (Section 6.2.2), namely the NextSENSE2 product ("forecasted GHI" hereafter). The comparisons between ground-based and estimated GHI were restricted to SZAs below 75° (i.e., for solar height above 15° from the local horizon) because the accuracy of satellite cloud retrievals is degraded for higher SZAs.

The CMF derived from the ground-based measurements of GHI was used in our analysis to evaluate CMFmsg and to categorize the cloudiness conditions. Specifically, the CMF was calculated as the ratio (Eq. 6.4) of measured GHI to the clear-sky irradiance calculated by the Ineichen-Perez clear-sky model (Ineichen & Perez, 2002) (see Section 3.4).

$$\mathrm{CMF} = \frac{\mathrm{GHI}_{\mathrm{measured}}}{\mathrm{GHI}_{\mathrm{clr}}} \qquad (6.4)$$

Three categories according of CMF are considered in the following: CMF≥0.9 for clear sky conditions, 0.4<CMF<0.9 for partially cloudy conditions and CMF≤0.4 for overcast conditions.

6.2.1 Nowcasting (SENSE2)

6.2.1.1 Overall performance

Figure 6.3 presents the overall performance of the SENSE2 system at the (instantaneous) 15 min timescale by comparing the modeled GHI values against ground-based measurements from all stations for a whole year (2017). We can see that most of the points (Fig. 6.3a; number of cases N>600) fall on the 1:1 line (blue line), which indicates that the system shows good performance overall, with a correlation coefficient of 0.93. For 58 % of the cases, the absolute differences between modeled and ground-based measurements of GHI are within ±50 W m^{-2} or ±10% (Fig. 6.3b). The SENSE2 system mostly overestimates the GHI, leading to points above the identity line (Fig. 6.3a; MBE is 23.8 W m^{-2} (4.9%)); this overestimation is more pronounced for low irradiances (lower-left corner of Fig. 6.3a where GHI<250 W m^{-2}). Lerwick is the most northern station and also the station with the greatest MBE (Fig. 6.3b and Figs. C1, C2 in Appendix C).

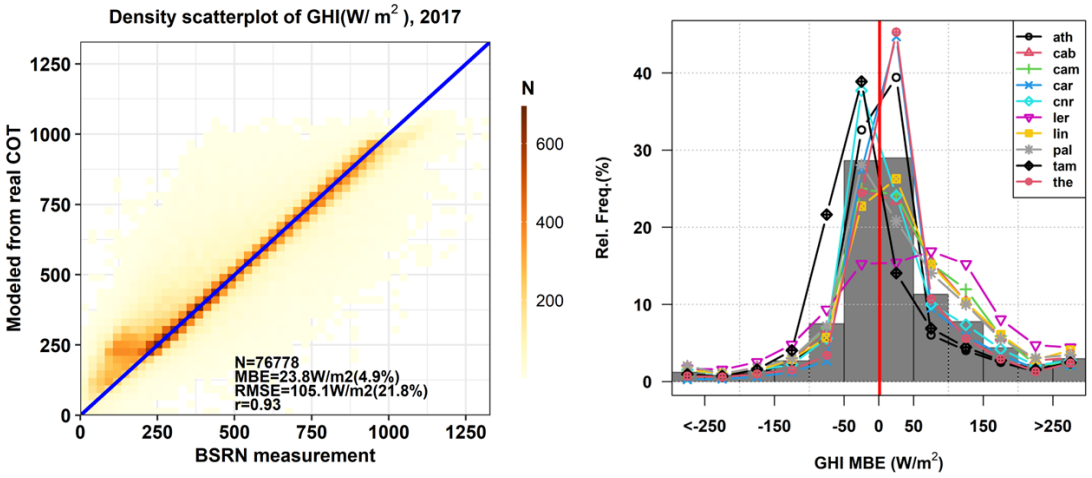

Figure 6.3 (a) Comparison of the modeled versus measured global horizontal irradiance (GHI) for all ground-based stations, for 2017. **(b)** Relative frequency of GHI MBE for all stations (grey bars) and for each station (lines with different symbols and colors).

We investigated how the mean cloudiness (CMF) of every station, the station's latitude, and the mean measured GHI influenced the GHI MBE; the results are presented in Fig. 6.4. The GHI MBE increases with an increase in cloudiness (a decrease in mean CMF). At the same time, the cloudiness increases and lower values of mean measured GHI are observed with increasing latitude. Those results are in line with previous studies (Qu et al., 2014, 2017). According to Qu et al. (2014), the error of the

satellite estimates of surface solar radiation increases with an increase in the distance from the subsatellite point (lat=0°, long=0° for Meteosat) and an increase in the occurrence of fragmented cloud cover. Qu et al. (2017) found that their retrievals for the northernmost stations were less accurate, which was attributed to the more frequent cloud occurrence over those stations and the more erroneous satellite retrievals of cloud properties for large SZAs and satellite viewing angles. One of those stations was Lerwick, which is close to the edge of the field of view of the Meteosat satellite, where errors due to parallax become important (Marie-Joseph et al., 2013; Schroedter-Homscheidt et al., 2022). The effect of clouds on GHI estimates is investigated in more detail in Section 6.2.1.3.

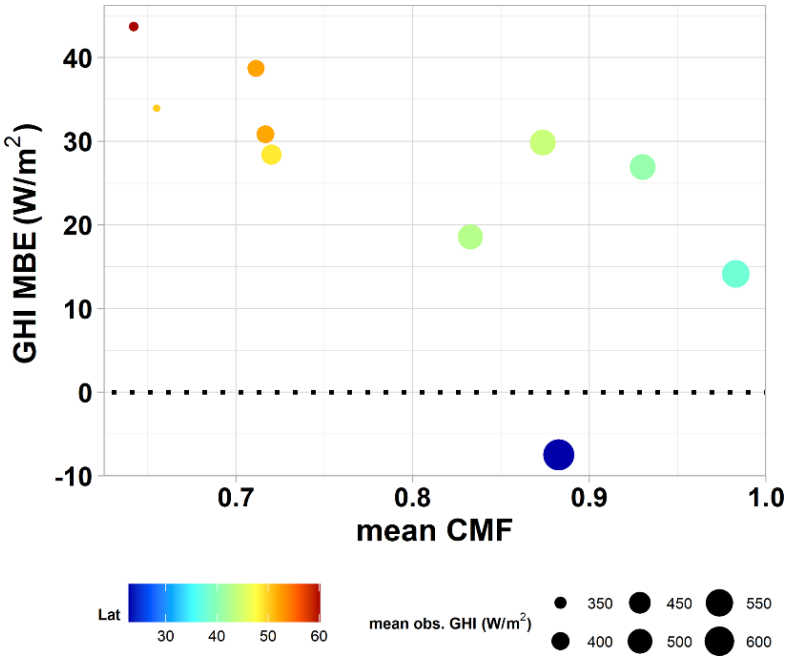

Figure 6.4 Dependence of the GHI MBE on the mean CMF for all stations. The color of each point indicates the latitude of the station, and its size indicates the magnitude of the mean GHI observed at the ground-based station.

All the statistical metrics are drastically improved by increasing timescale for all stations (Fig. 6.5). The northernmost stations (CAB, CAM, LER, LIN, and PAL) show similar results. At the 15 min timescale, the MBE, RMSE and correlation coefficient ranges of 29-43 W m^{-2}, 104-131 W m^{-2}, and 0.82-0.90, respectively. Those statistics are improved for the monthly means to 5-10 W m^{-2} for MBE, 7-13 W m^{-2} for RMSE and R~1. Similar results were found for the rest of the stations (which are the southernmost ones): the MBE, RMSE, and correlation coefficient range from -7 to 30 W m^{-2}, from 84 to 104 W m^{-2}, and from 0.93 to 0.95, respectively, for 15 min timescale, whereas the MBE ranges from -4 to 8 W m^{-2}, the RMSE ranges from 6 to 10 W m^{-2}, and R~1 for monthly means. The overall MBE and RMSE are reduced to 6.6 W m^{-2} (3.3%) and 15.4 W m^{-2} (7.7%) for the daily mean GHI and to 5.7 W m^{-2} (3.2%) and 9.2 W m^{-2} (5.2%) for the monthly means, while the correlation coefficient shows values that almost reach 1, which was anticipated since the cloud effect is smoothed out for larger timescales.

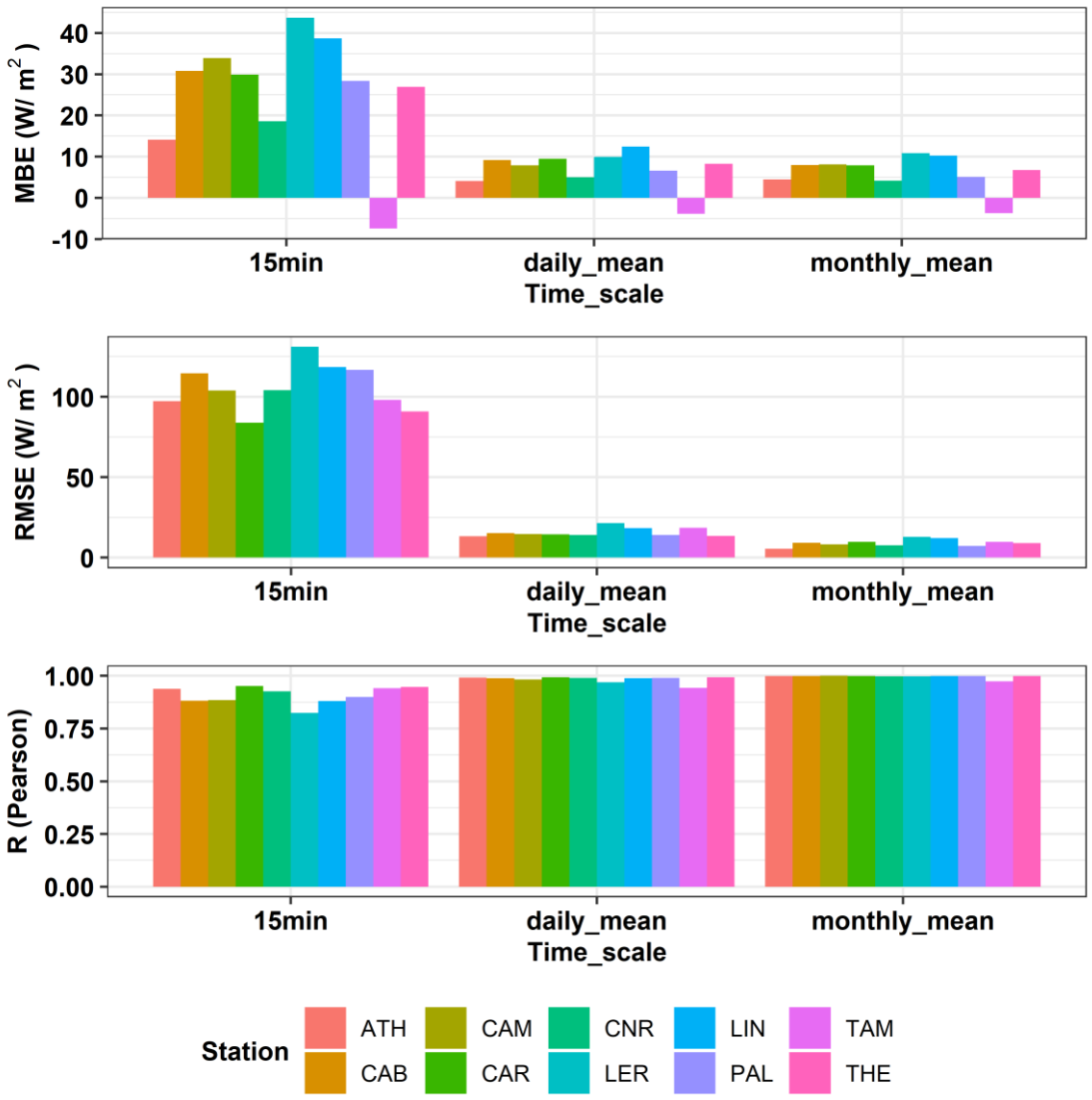

Figure 6.5 Comparison of the modeled versus measured global horizontal irradiance (GHI) per ground-based station in 2017 for different timescales (15 min, daily mean, and monthly mean).

6.2.1.2 Aerosol effect on retrieved solar irradiance

The CAMS AOD forecasts used as input to the operational model were assessed against ground-based measurements from the AERONET network (Holben et al., 1998), and the related uncertainty introduced into the modeled GHI was calculated. Each of the ground-based stations with pyranometer data (BSRN, Athens and Thessaloniki) has a collocated AERONET station (see Table 3.1). The level 2, version 3 direct sun (Giles et al., 2019) AOD data at 500nm were collected and the AOD values at 550nm were derived using the Ångström exponent for 440-675nm. However, measurements of AOD at 500 nm were not available for Cabauw, so the AOD at 440 nm was used instead and converted to 550 nm using the Ångström exponent for 440-675 nm.

The AERONET AOD direct sun measurements were matched with CAMS AOD forecasts (1 h time resolution) interpolated to the 15 min time steps of the model. The closest AERONET measurement ±10 minutes around each 15 min time step was matched (or the mean value was used if more than one measurement was available). To estimate the model uncertainties due to the forecasted AOD, the

clear-sky GHI was calculated using the forecasted CAMS AOD and the synchronized AERONET AOD measurements as input. The MBE for AOD (CAMS against AERONET) and clear-sky GHI (modeled using CAMS AOD against those using AERONET AOD) per station is presented in Fig. 6.6. CAMS forecasts mostly overestimate AOD, with an MBE of 0.015 (10%) for all stations, which results in an underestimation of the modeled clear-sky GHI of -2.7 W m^{-2} (-0.4%). The greatest overestimation, 0.05 (~50%), was found for CAM and CNR; this resulted in the greatest underestimation of modeled clear-sky irradiances: -8.5 W m^{-2} (-1.4%). An underestimation of AOD was found for CAB and THE, with an MBE of <0.01 (<3%), resulting in negligible overestimation of the modeled irradiance (MBE < 1 W m^{-2} or 1%).

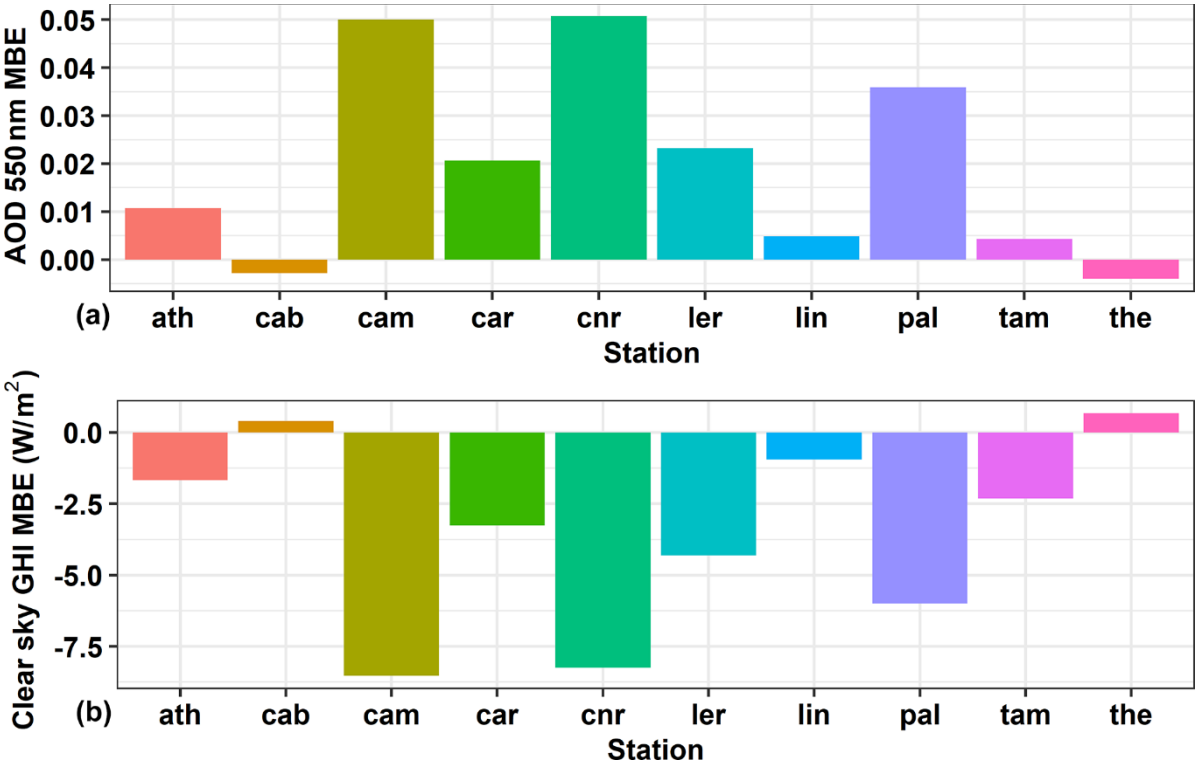

Figure 6.6 (a) Mean bias error (MBE) of the aerosol optical depth (AOD) at 550nm forecasted by CAMS (1 d ahead forecast) compared to the AOD measured by ground-based sun photometers of the AERONET network. **(b)** MBE of global horizontal irradiance (GHI) modeled under clear-sky conditions using the CAMS-forecasted AOD at 550nm as input versus measured values (AERONET).

An overestimation of the CAMS-forecasted AOD at 550 nm for 2017 over Europe is also reported (the average modified normalized mean bias ranges from ~10% to 30 %), which is based on the continuous quarterly evaluation of the AOD forecasts against daily AERONET cloud screened (i.e., version 3, level 1.5) sun photometer data (Basart et al., 2023; Eskes et al., 2021). While this is the case on average, in contrast, the CAMS-forecasted AOD is underestimated during high aerosol loads, especially in desert regions and during dust events (Basart et al., 2023), which might explain the almost zero bias for Tamanrasset station (the overestimation of small AODs is masked by the frequent underestimation of large AODs) compared to the greater values of bias (>0.01) found for most of the other stations. Qu et al. (2017) analyzed case studies at Tamanrasset and found that the CAMS

(MACC) AOD at 550 nm is frequently found to be underestimated when compared against AERONET data during summer dust events, explaining the strong positive bias they found for their modeled direct irradiance (using the Heliosat-4 method and the McClear clear-sky model). In the same study (Qu et al., 2017), in contrast to the CAMS AOD underestimation that occurred during dust events, a systematic overestimation of AOD during periods free of those events was found for the two desert stations examined (Sede Boqer and Tamanrasset) which the study linked to an underestimation of the modeled direct irradiance at those stations. The updated McClear v3 clear-sky model was used in the study by Schroedter-Homscheidt et al. (2022), and a negative bias was found for their GHI estimates under clear-sky conditions for most of the stations, especially those located in dust-affected regions, which is in line with our results –although the results are not directly comparable since they performed a direct comparison with the BRSN-measured irradiances. Those results demonstrate that the clear-sky model using CAMS forecasts shows good performance, highlighting that the AOD product forecasted by CAMS is suitable for GHI-nowcasting applications.

6.2.1.3 Cloud effects on retrieved solar irradiance

Overall, the model overestimates GHI, as we saw in Section 6.2.1.1. which can be attributed to the underestimation of cloud information from satellite (MSG COT). The improvement of the statistics upon going from an instantaneous comparison to integrated timescales (e.g., daily) indicates that this overestimation can be attributed to the uncertainties related to the cloud information from satellite retrievals but also to satellite/ground-based evaluation representativity issues. In order to understand this more closely, we investigated the effect of different conditions in cloudiness on the error in the modeled GHI.

Initially, we classified the cloudiness conditions using the ground-based CMF (Fig. 6.7a, b, c). According to the results, GHI is overestimated by the model under cloudy conditions (CMF<0.9), while for clear-sky conditions (CMF≥0.9, Fig. 6.7a), the model closely resembles the measured GHI. For partially cloudy conditions (0.4<CMF<0.9, Fig. 6.7b), the MBE is 81.6 W m^{-2} (22.8%), and the greatest error in GHI occurs for low CMF values (CMF≤0.4, Fig. 6.7c) (MBE = 100.1 W m^{-2} or 73.1%). High deviations at low measured GHI values (<250 W m^{-2}) are most commonly found in the latter category.

We also compared the modeled and measured GHI values for clear-sky conditions according to the satellite data, namely for COT=0 (Fig. 6.7d). In this case, the model overestimates GHI, with an MBE of 13.6 W m^{-2} (2.3%). Most of the cases are on the 1 : 1 line, with a few being higher, especially for measured GHI<250 W m^{-2}, meaning that there are clouds over the ground-based station that have not been resolved by the satellite pixel (COT=0). A positive bias was also found at all stations examined by Qu et al. (2017) for clear-sky pixels as defined by the APOLLO/SEV cloud properties retrieval

scheme, which contributed to the overall overestimation for all skies. This was attributed to small broken clouds that cause large variability in surface GHI and to false detections by the cloud retrieval algorithm being treated as clear-sky cases.

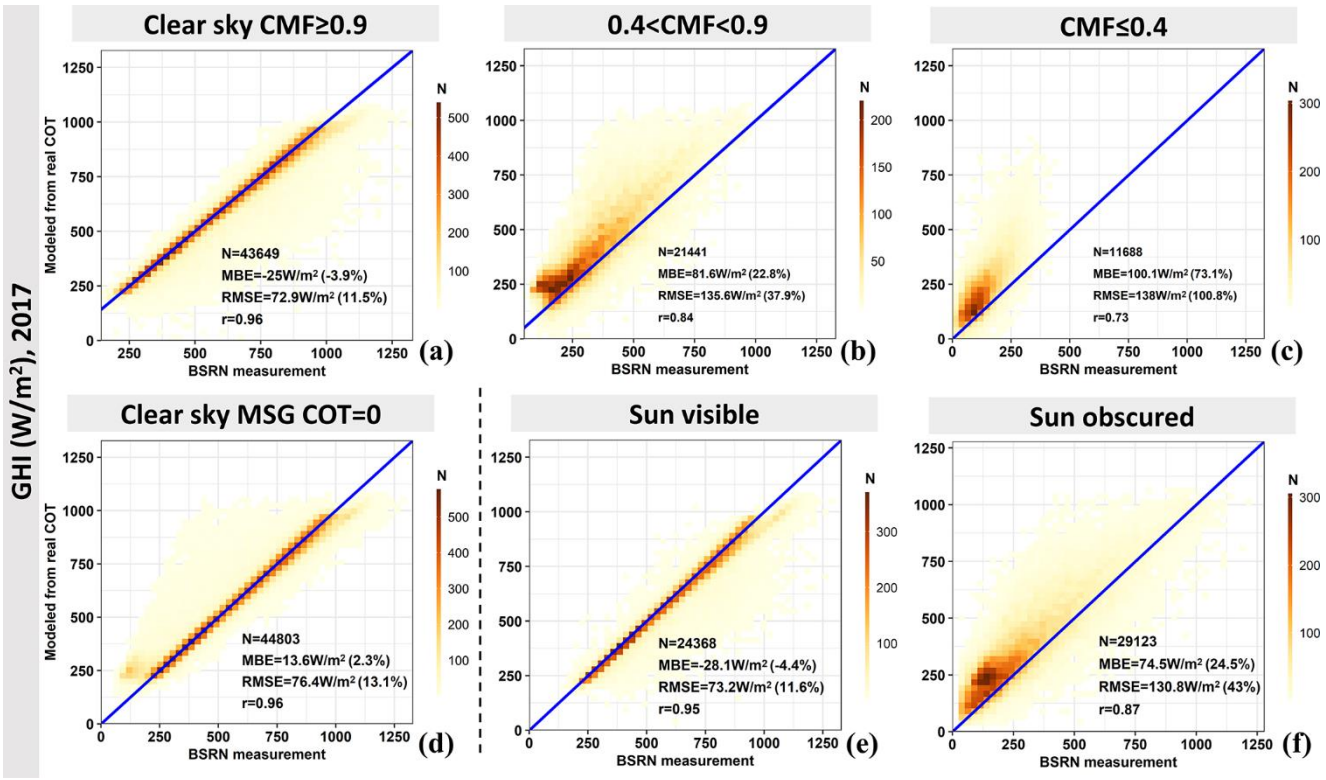

Figure 6.7 Comparisons of the modeled versus the measured global horizontal irradiance (GHI) at all ground-based stations **(a-c)** for different cloudiness conditions based on the cloud modification factor (CMF; the ratio of ground-based GHI measurements to clear-sky GHI (clear-sky model)), **(d)** for clear-sky conditions as determined by the MSG satellite product for zero cloud optical thickness (COT=0), and **(e,f)** for conditions characterized as "sun visible" or "sun obscured" over the ground-based station.

To demonstrate the effect of sun visibility over the ground-based stations on the GHI error, those instances were separated out by using the pyrheliometer measurements of direct irradiance (DNI – direct normal irradiance) available from the BSRN network. The DNI measurements (1 min) were divided by the clear-sky DNI, which was again obtained from the Ineichen-Perez clear-sky model (Ineichen & Perez, 2002). Cases with a ratio of actual to clear-sky model DNI of >0.8 were classified as "sun visible". This threshold was selected to account for the strong effect of aerosols in DNI, given that a monthly mean climatological value for the aerosol attenuation factor is used by the DNI clear-sky model (Ineichen & Perez, 2002). Cases with a ratio of <0.6 were classified as "sun obscured", and cases with ratio values between 0.6 and 0.8 were omitted ("unclassified cases") so that we could be confident by more than 40% that direct irradiance was blocked by clouds. The results of the comparison between modeled and measured GHI values were grouped based on the sun visibility classification and are presented in Fig. 6.7e and f. We can see that the sun-visible situations give quite good results (points close to the 1:1 line, with an MBE of -28.1 W m^{-2} or -4.4 %).

In contrast, the model overestimates GHI (MBE is 74.5 W m^{-2} or 24.5%) when the sun is obscured over the ground-based station. Comparing Fig. 6.7b and c with Fig. 6.7f, we can see that most of the cases that are above the 1 : 1 line happened when the sun was obscured. This is caused by the fact that the satellite-based cloud retrieval is representative of the whole pixel, while the information on whether the sun is obscured over the ground-based station is representative of the (point) station and cannot be inferred from the satellite cloud retrievals. This – combined with the facts that the direct irradiance attenuation from clouds is completely different from GHI, it does not linearly decrease with cloudiness or cloud optical thickness, and, finally, its contribution to GHI depends on various parameters (mainly the solar elevation) – introduces an issue into any instantaneous comparison between a satellite-based GHI retrieval representing a whole pixel and a GHI value measured at a single point. So, the main result of this analysis of sun visibility over a station is to discuss possible systematic biases due to the satellite pixel versus station evaluation representativeness issue. This issue makes instantaneous model output evaluation difficult, especially in partly cloudy situations.

Since the main source of errors in this analysis is associated with clouds, we further assessed the satellite-derived cloud input in the model. The MSG COT is transformed into CMFmsg using Eq. (6.2), and this is the cloud-related input in the SENSE2 model. Since this cannot be evaluated directly with ground-based measurements, we indirectly evaluated CMFmsg with the CMF derived from GHI measurements (Eq. 6.4). The results are presented in Fig. 6.8 as relative frequency distributions of CMFmsg, CMF, and the difference between them (CMFmsg – CMF) for all cases and different cloudiness conditions. Overall, the CMFmsg is overestimated (0.02; Fig. 6.8a and b), which is the reason for the overestimation of SENSE2-modeled GHI overall. This CMFmsg overestimation occurs mainly when there are cloudy conditions (Fig. 6.8g, h, i, and j) and where the sun is obscured over the ground-based station (Fig. 6.8m and n).

There are also cases of CMFmsg underestimation (CMF differences<0 in Fig. 6.8b), which come mostly from situations characterized as cloudless (CMF≥0.9, Fig. 6.8e and f) and explain the points below the 1 : 1 line in Figs. 6.3a and 6.7 (i.e., those for which the measured GHI is greater than the modeled one). The first reason for this is a cloudy satellite pixel (corresponding to CFMmsg<1 in Fig. 6.8e) but a ground-based CMF=1 (which indicates that no clouds are present over the station). There are also many cases where CMF>1 (Fig. 6.8e) that is attributed to irradiance enhancement by clouds, which often occurs when the sky above the ground station is partially cloudy but the sun is visible (see also Figs. 6.8k and l and 6.7e). In this case, the reflection of solar radiation by clouds increases the diffuse component from directions relatively close to the sun, hence the measured GHI on the ground. This is a three-dimensional effect of clouds that cannot be reproduced using the one-dimensional radiative transfer modeling used in this study. This is a limitation of the SENSE2 model – it does not include three-dimensional cloud effects (enhancement of the GHI or parallax) which can be

reproduced using 3D RT simulations (e.g., Mayer, 2009). However, three-dimensional cloud structure information is not available for an operational solar energy nowcasting model from geostationary satellites (Qu et al., 2017; Schroedter-Homscheidt et al., 2022); besides, the introduction of parameterizations and techniques to improve the computational time (Tijhuis et al., 2023) is essential.

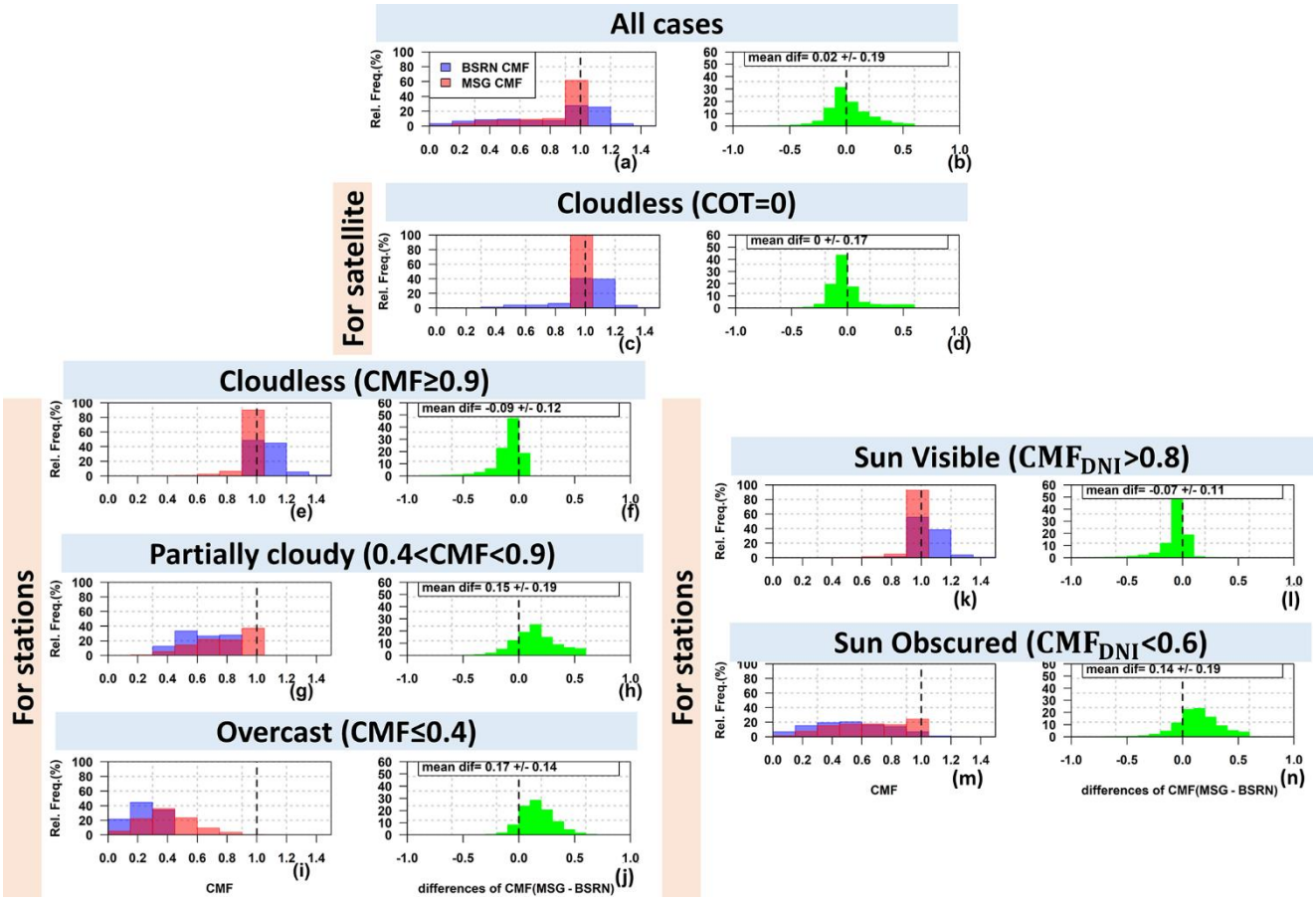

Figure 6.8 Left panels **(a, c, e, g, i, k, m)**: distributions of the cloud modification factors (CMFs) from measurements of global horizontal irradiance (GHI) (blue bars) and from the MSG cloud optical thickness (COT) (red bars) for all cases and under different cloudiness conditions. Right panels **(b, d, f, h, j, l, n)**: distributions of the differences between the CMF derived from MSG satellite COT against the CMF derived from measurements of GHI.

Summarizing, to explain the overestimation of SENSE2 GHI retrievals, we have to recognize that a direct comparison between point measurements of solar radiation at the ground and satellite estimates representative of a pixel introduces deviations (e.g., Carpentieri et al., 2023; Kazadzis et al., 2009; Schenzinger et al., 2023) that are linked with the cloud features within the pixel and the limitations of cloud monitoring using satellite data (e.g., spatial resolution). The distributions of both CMFs and the differences between the CMFs were investigated separately for, again, clear-sky conditions according to the satellite (namely COT=0; Fig. 6.8c and d). Regardless of the fact that CMFmsg can only be one, meaning that no clouds are resolved by the satellite, there are cloudy cases with CMF<1 for the ground-based station (Fig. 6.8c). Due to the satellite's spatial resolution, small-scale broken clouds cannot be resolved in some cases (e.g., Schenzinger et al., 2023; Marie-Joseph et al., 2013; Qu et al., 2017), but those clouds may have a significant impact on the ground-based measured irradiance if

they are obscuring the sun (almost total attenuation of the direct irradiance). If they do not obscure the sun, this also corresponds to the clear-sky case for the ground-based station, although the effect of cloud enhancement of the measured GHI cannot be excluded (CMF=1 and CMF>1 in Fig. 6.8c, respectively). In a recent study by Schenzinger et al. (2023) using sky camera images, the limitation of MSG satellite-based modeled CMF was demonstrated for small-scale clouds. Different results were obtained for two different stations inside the same satellite pixel, which was characterized as cloud free. For one station that was cloud free, the model agreed with the measurements; however, for the station that was covered by localized cumulus clouds that could not be resolved by the satellite, there were discrepancies between the ground-based and satellite-based modeled values. Nevertheless, even for the cases where the satellite imager can resolve clouds within a partially cloudy pixel, the COT product for this pixel is a constant value, namely a spatially homogeneous cloud optical property for the corresponding area. In this atmospheric scene with a high spatial variability of clouds, the results of the comparison will depend dramatically on whether the GHI is measured at ground level with the sun obscured or unobscured.

6.2.1.4 Bias correction based on cloud input

Overall, the model overestimates GHI, which is attributed to the CMFmsg overestimation. Based on the main conclusions from the investigation of CMF differences in the previous section, we tried to find out if there is a pattern for CMF differences (modeled against measured) as a function of CMFmsg that is common to all stations, since it is the only operationally available input every 15 min. Additionally, we found that those differences hardly change with SZA (Fig. C3), so we only investigated their relationship with CMFmsg.

The mean CMF difference was calculated and its standard deviation per CMFmsg bin for every station, and the results are presented in Fig. 6.9. A pattern of mean CMF differences in which the CFMmsg overestimation reached almost 0.1 starting at CMFmsg bin 0.3 and continuing up to bin 0.8 was found for almost all stations (apart from TAM, ATH, and THE), which was also related to the low standard deviations in those bins.

As it was discussed in the previous section, this CFMmsg overestimation (up to ~0.1) is mostly related to partial cloudiness and sun-obscured conditions over the station. Nevertheless, the sun's visibility above a station is an information that cannot be provided by satellites. Consequently, we tried to correct CMFmsg (the operational input) with the CMF differences (modeled against measured values). We used the mean of the CMF differences per CMFmsg bin from 7 out of 10 stations (excluding TAM, ATH, and THE) to derive the correction factor ("the correction" hereafter), which is depicted as a dashed thick black line in Fig. 6.9. The correction was only applied to CMFmsg values in bins 0.3-0.8. The correction was applied to all stations, including TAM, ATH, and THE, which acted as a test

bed (with a low frequency of cloudy cases) for the general correction derived from the other seven stations.

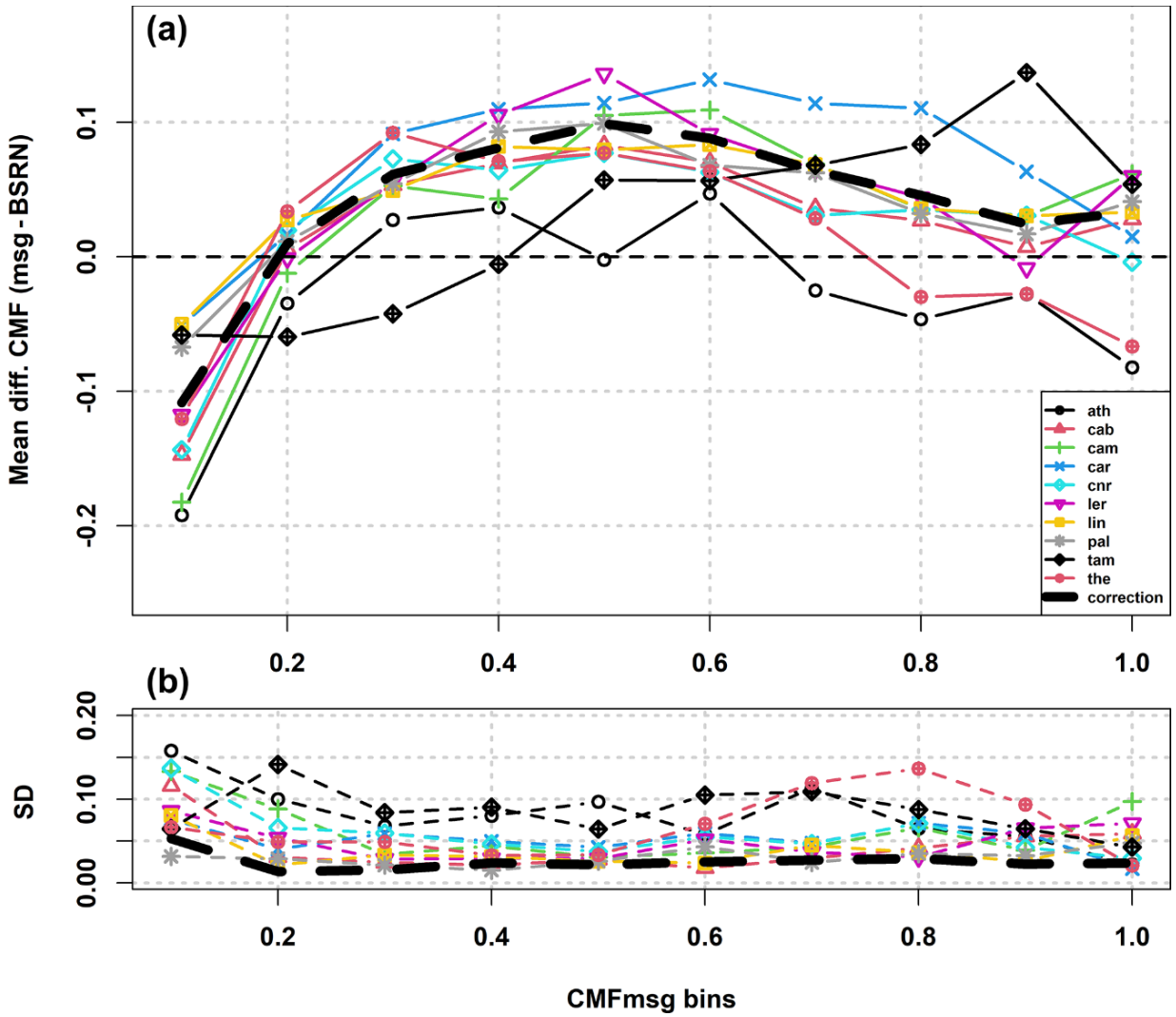

Figure 6.9 (a) Mean differences between cloud modification factor (CMF) modeled from MSG satellite cloud optical thickness values (CMFmsg) and CMF derived from global horizontal irradiance (GHI) measurements per modeled CMFmsg bin. **(b)** The corresponding standard deviations (SDs) of the CMF differences per modeled CMFmsg bin. Lines with different colors and different symbols correspond to different stations.

Table 6.1 summarizes the statistics of corrected modeled GHI against ground-based measurements. The MBE and RMSE are improved after the correction. LER and CAM are the two stations with the greatest improvement in their statistics, followed by CAB and LIN, which was anticipated since those stations are at higher latitudes (associated with high cloudiness). Even stations ATH and THE, which were not used in the correction factor derivation, exhibit better results after applying the correction. TAM is the only station for which statistics were not improved. Because cloudiness was rare at that station, its statistics were already good, indicating that a hybrid approach to the correction based on the area's cloudiness would probably be better. Overall, after the correction the GHI differences (modeled against measured values) were within ±50 W m^{-2} (or ±10%) for 61% of the cases. The MBE for all stations was also improved to 11.3 W m^{-2} (2.3%) compared to the uncorrected value (23.8 W m^{-}

^{2} or 4.9%). For the daily mean GHI, the overall MBE and RMSE were improved to 3.3 W m^{-2} (1.7 %) and 13.1 W m^{-2} (6.6 %) compared to the uncorrected values of 6.6 W m^{-2} (3.3 %) and 15.4 W m^{-2} (7.7 %), respectively. For monthly means, the MBE improved to 2.7 W m^{-2} (1.6 %) compared to 5.7 W m^{-2} (3.2 %) before correction, and the RMSE improved to 6.3 W m^{-2} or 3.6% (it was 9.2 W m^{-2} or 5.2% before correction).

Table 6.1 Performance of nowcasted irradiances before and after correction with CMFmsg. "cor." indicates corrected values; those that were improved after the correction are shown in bold.

15 min

		MBE W m^{-2} (%)		RMSE W m^{-2} (%)		R	
Station	**N**		**cor.**		**cor.**		**cor.**
ATH	9472	14 (2.5)	**8 (1.4)**	97 (17.5)	97 (17.5)	0.94	0.94
CAB	7749	31 (7.8)	**11 (2.9)**	115 (29.0)	**110 (28.0)**	0.88	0.88
CAM	2376	34 (10.1)	**13 (3.7)**	104 (30.8)	**98 (29.0)**	0.89	0.89
CAR	8985	30 (5.8)	**23 (4.5)**	84 (16.2)	**80 (15.4)**	0.95	**0.96**
CNR	8806	19 (3.7)	**6 (1.2)**	104 (20.6)	**102 (20.1)**	0.93	0.93
LER	5191	44 (12.9)	**21 (6.1)**	131 (38.6)	**124 (36.5)**	0.82	**0.83**
LIN	7989	39 (10.0)	**21 (5.3)**	119 (30.8)	**114 (29.6)**	0.88	0.88
PAL	8011	28 (6.7)	**11 (2.5)**	117 (27.4)	**113 (26.5)**	0.90	**0.91**
TAM	9011	-8 (-1.2)	-12 (-2.0)	98 (15.4)	98 (15.4)	0.94	0.94
THE	9188	27 (5.2)	**18 (3.6)**	91 (17.6)	**88 (16.9)**	0.95	0.95

Daily

		MBE W m^{-2} (%)		RMSE W m^{-2} (%)		R	
Station	**N**		**cor.**		**cor.**		**cor.**
ATH	9472	4.1 (1.9)	**2.1 (0.9)**	13.2 (5.9)	**12.3 (5.5)**	0.99	0.99
CAB	7749	9.2 (5.5)	**3.3 (2.0)**	15.2 (9.2)	**11.4 (6.9)**	0.99	0.99
CAM	2376	7.9 (5.8)	**3.6 (3.2)**	14.7 (10.8)	**11.5 (10.0)**	0.98	**0.99**
CAR	8985	9.5 (4.5)	**8.0 (3.8)**	14.5 (7.0)	**12.5 (6.0)**	0.99	0.99
CNR	8806	5.0 (2.5)	**2.1 (1.1)**	14.0 (6.9)	**11.1 (5.7)**	0.99	0.99
LER	5191	9.9 (7.0)	**3.6 (2.6)**	21.6 (15.3)	**17.9 (12.7)**	0.97	0.97
LIN	7989	12.4 (7.3)	**7.1 (4.2)**	18.4 (10.8)	**13.7 (8.1)**	0.99	0.99
PAL	8011	6.6 (3.5)	**1.9 (1.0)**	14.1 (7.4)	**11.6 (6.1)**	0.99	0.99
TAM	9011	-3.9 (-1.5)	-4.1 (-1.6)	18.5 (7.2)	**18.2 (7.2)**	0.94	0.94
THE	9188	8.2 (3.8)	**6.0 (2.8)**	13.6 (6.3)	**11.2 (5.2)**	0.99	0.99

Monthly

		MBE W m^{-2} (%)		RMSE W m^{-2} (%)		R	
Station	**N**		**cor.**		**cor.**		**cor.**
ATH	9472	4.5 (2.3)	**1.8 (0.9)**	5.6 (2.8)	**3.3 (1.7)**	~1	~1
CAB	7749	8.0 (6.0)	**3.2 (2.4)**	9.3 (7.0)	**4.2 (3.2)**	~1	~1
CAM	2376	8.1 (6.6)	**3.7 (3.4)**	8.2 (6.7)	**4.5 (4.1)**	~1	~1
CAR	8985	7.9 (4.2)	**6.6 (3.5)**	9.9 (5.3)	**8.5 (4.5)**	~1	~1
CNR	8806	4.2 (2.3)	**1.8 (1.0)**	7.6 (4.2)	**4.7 (2.7)**	~1	~1
LER	5191	10.9 (7.6)	**4.1 (2.9)**	12.9 (9.0)	**5.4 (3.8)**	~1	~1
LIN	7989	10.3 (7.6)	**6.0 (4.5)**	12.2 (9.0)	**7.5 (5.5)**	~1	~1
PAL	8011	5.1 (3.4)	**1.4 (1.0)**	7.4 (5.0)	**4.9 (3.3)**	~1	~1
TAM	9011	-3.7 (-1.5)	-4.5 (-1.8)	9.8 (3.8)	**8.8 (3.5)**	0.97	0.97
THE	9188	6.7 (3.5)	**4.8 (2.5)**	9.1 (4.7)	**7.2 (3.7)**	~1	~1

After improving the configuration of the SENSE2 model and correcting the bias in CMFmsg for partially cloudy conditions (the "bell-shaped curve" between CMFmsg bins 0.3 and 0.8, which has been also reported in other studies, e.g., Marie-Joseph et al., 2013), more accurate estimates of GHI were produced, in line with the results from similar models (Qu et al., 2014; Thomas et al., 2016; Qu et al., 2017). These SENSE2 GHI estimates will be the basis for the new forecasting system NextSENSE2 evaluated in the next section (Section 6.2.2).

Comparing our results with other studies, for the HC3v3 database of surface solar irradiation (Qu et al., 2014), correlation coefficient values greater than 0.92 and relative RMSEs between 14–38% were found for the 15 min timescale. In the same study, for daily irradiation, correlation coefficient values greater than 0.97 were found, along with relative RMSEs between 6% and 20%. For the latest version (5) of HelioClim-3 database (HC3v5), validation against 14 BSRN stations (Thomas et al., 2016) resulted in relative biases between –4% and 5% and rRMSEs between 14.1% and 37.2% for GHI. Both studies highlight the good performance of the clear-sky irradiation values from the McClear clear-sky model (which uses advanced inputs for aerosol, water vapor, and ozone instead of climatological values). A comparison of the 15 min means of global irradiance estimated by the fully physical Heliosat-4 method (a combination of the McClear and McCloud models) against ground-based measurements from 13 stations of the BSRN network (Qu et al., 2017) showed large correlation coefficients for all stations (0.91–0.97) and biases and RMSEs of GHI that ranged between 2–32 and between 74–94 W m^{-2}, respectively. In the same study, the greatest values of the relative RMSE of the mean irradiance were found for stations with rainy climates and mild winters (26% to 43%, with the greatest value found for the northernmost station), while values for stations in desert and Mediterranean climates ranged between 15% and 20%, which are in line with the findings for the northernmost and southernmost stations, respectively, in this thesis. The positive biases previously observed when using the APOLLO cloud retrieval in Heliosat-4 (Qu et al., 2017) for the CAMS Radiation Service were significantly reduced and balanced after applying the new cloud retrieval scheme APOLLO_NG (a new cloud mask with a cloud probability threshold of 1%, among other improvements; for more details, see Schroedter-Homscheidt et al., 2022). After the improvements, relative RMSE values of hourly GHI of between 10.3% and 25.5%, along with a mean value of 13.7%, were reported for 2015 (Schroedter-Homscheidt et al., 2022). An extensive validation (Urraca et al., 2017) of the operational radiation product (ICDR) of the CM SAF over Europe for the 2008–2015 period gave an MBE of 4.5 W m^{-2} (4%) and an RMSE of 18.1 W m^{-2} (15.1%) for daily means of the product, and it was reported that it was overestimated at high latitudes, in contrast to the climate data records (CDRs). For the new SARAH-3 CDR SIS (Surface Incoming Shortwave Radiation) product for the period 1983–2020, validation (Pfeifroth et al., 2023b) showed biases of 4.2, 2.18, and 2.25 W m^{-2} for the 30 min instantaneous data, daily mean, and monthly mean, respectively. The

validation of the operational product (ICDR) with respect to the SARAH-3 CDR for the year 2020 showed that the ICDR product consistently temporally extends the SARAH-3 CDR data records. The reasons for the differences between these two products were differences in the auxiliary data (water vapor, etc.) and the time range used for deriving the effective cloud albedo and daily snow cover.

6.2.2 Short-term forecasting

6.2.2.1 Overall performance – benchmarking with the persistence method

Figure 6.10 summarizes the performance of the CMV-method-predicted GHI (green points) as a function of the forecasting horizon by providing the main statistics after comparison with ground-based GHI measurements from all 10 stations for a whole year (2017). Detailed results per station for representative statistics and selected time steps (+60, +120, +180 min) can be found in Table 6.2. As a benchmark, the results from the commonly used persistence forecasting method are also presented in Fig. 6.10 (black points). We can see that the CMV model systematically outperforms persistence for all time steps. It is interesting that the first time step (+15 min) is not the one with the maximum difference between the CMV and persistence statistics (or the maximum CMV FS%), indicating that the probability of changing cloudiness is low for such a short time interval, which favors the persistence method. The second time step is the one with the maximum CMV FS% (best performance) compared to persistence (up to ~10%). As the forecasting horizon increases, all the metrics deteriorate for both methods and persistence is systematically worse than CMV.

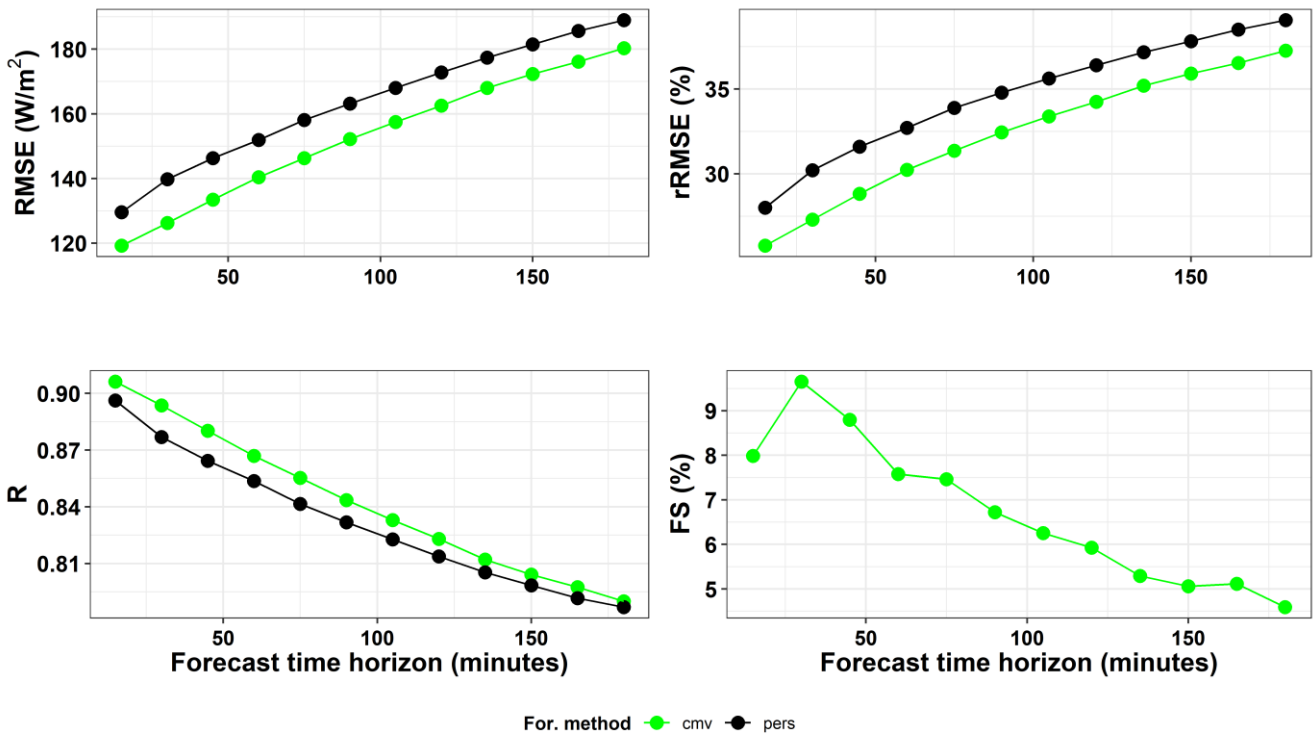

Figure 6.10 Performance statistics for forecasted global horizontal irradiance (GHI) by the CMV model (green points) and by the persistence method (black points) for every 15 min time step up to 3 h ahead.

Table 6.2 Performance statistics for CMV-forecasted global horizontal irradiance (GHI) for the 60, 120, and 180 min time steps.

Station	Mean CMF	rRSME (%) Time step (min)			R time step (min)			FS (%) time step (min)		
		+60	+120	+180	+60	+120	+180	+60	+120	+180
ATH	0.97	22.0	24.5	25.3	0.90	0.87	0.86	0	1.7	3.2
CAB	0.68	39.7	45.6	49.6	0.80	0.73	0.68	10.5	7.5	5.8
CAM	0.63	54.1	62.0	68.9	0.66	0.58	0.50	2.7	3.4	1.5
CAR	0.85	22.8	26.3	29.6	0.90	0.86	0.82	8.1	5.6	3.1
CNR	0.81	31.0	34.8	37.4	0.85	0.79	0.75	2.4	2.9	2.6
LER	0.61	50.8	56.0	59.6	0.73	0.67	0.62	10.4	9.5	9.4
LIN	0.68	39.7	45.9	51.2	0.81	0.74	0.69	13.9	10.9	8.8
PAL	0.68	38.9	44.9	48.8	0.82	0.75	0.71	11.6	7.6	6.0
TAM	0.87	21.4	23.1	24.7	0.89	0.86	0.82	2.2	1.0	-1.3
THE	0.91	23.9	27.2	29.2	0.89	0.86	0.84	6.8	5.1	2.4

An interesting grouping of stations was obtained by comparing the main statistics (rRMSE and FS) for both forecasting methods with the mean CMF (representing its mean cloudiness) for each station (Fig. 6.11). Three time steps were selected: +60, +120, +180 min (in order of increasingly transparent symbols in the plot). Two groups of stations are evident: those with high mean cloudiness (LER, CAM, PAL, LIN, and CAB), which show worse rRMSEs than those with lower cloudiness (ATH, THE, TAM, CAR and CNR), independently of the method used. Again, the CMV model (green symbols) outperforms the persistence method (black symbols) for all stations for these time steps (except +240 min for TAM). The interesting finding is that the FS (%) of the CMV method increases with decreasing CMF; in other words, the forecasting skill of the CMV model is higher compared to persistence for stations with higher cloudiness, demonstrating the applicability of the CMV method of forecasting GHI under cloudy conditions.

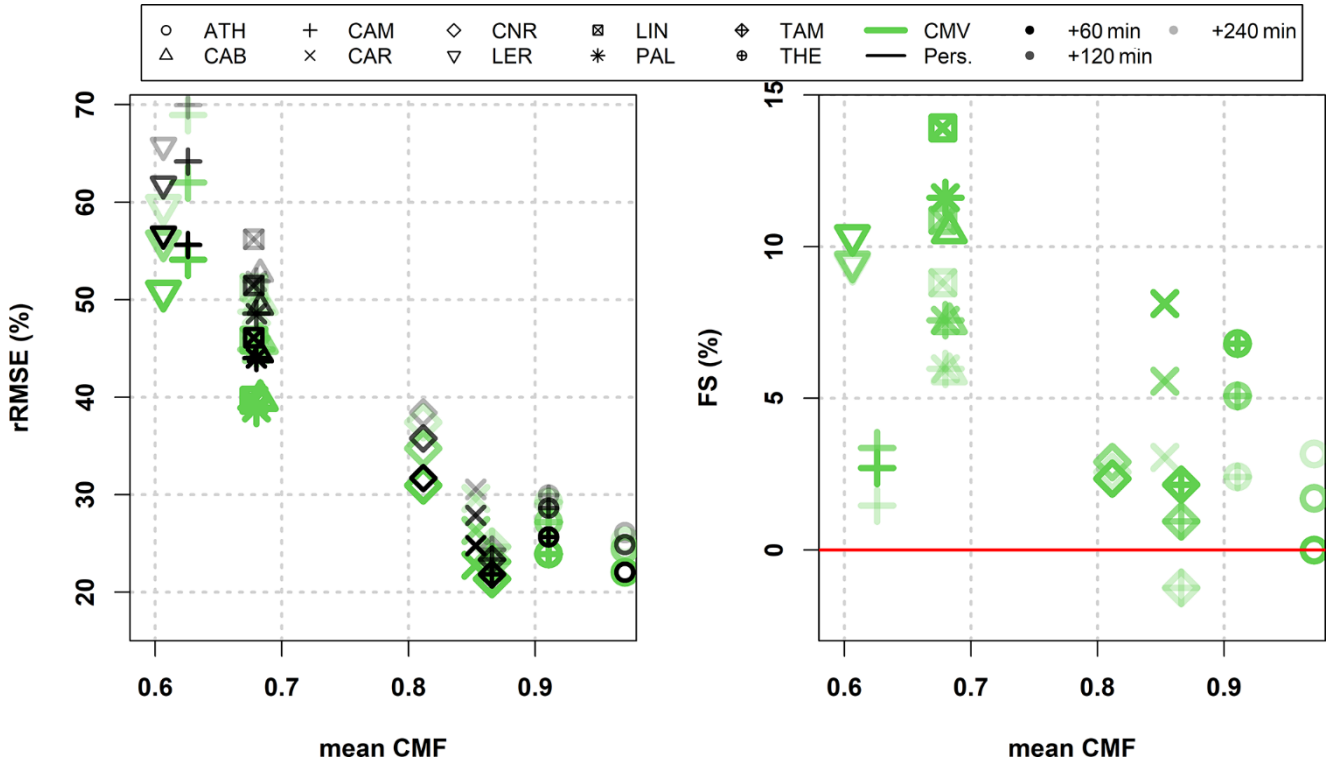

Figure 6.11 Relative root mean square error (rRMSE%) and forecasting skill expressed as a percentage (FS%) for the CMV model (green symbols) and the persistence method (black symbols) when they were used to forecast global horizontal irradiance (GHI) versus the average cloudiness of stations (mean CMF) for the time steps (in order of increasingly transparent symbols) +60, +120 and +240 min.

6.2.2.2 Performance for different cloudy conditions

To demonstrate the value of the CMV model compared to the persistence method, which assumes the same cloudy conditions for all future time steps, their performance was compared under different cloudy conditions and transitions in cloudiness. Figure 6.12 presents the RMSEs for both models (green points for CMV and black points for persistence) and the CMV model FS% as a function of CMF, for three time steps (+60, +120, and +180 min). Persistence performs better than the CMV model under clear-sky conditions, namely when CMF=1, for all times steps (as expected, as there is no change in cloudiness). This is also true for CMF bin 0.9 for the +180 min time step only and for CMF bin > 1 (a bin which mainly contains clear-sky cases) for all time steps. For cloudy conditions, namely when CMF<0.9, the CMV model outperforms persistence for all time steps (apart from +180 min when considering CMF bin 0.9). The cloudier the conditions (the smaller the CMF), the better the performance of the CMV model and the greater the CMV FS% (which is up to ~ 20% for the +60 min time step). The FS of CMV model decreases slightly with forecasting horizon; however, for the maximum forecasting horizon (+180 min), it remains quite high (~+10%) for CMF bins <0.7.

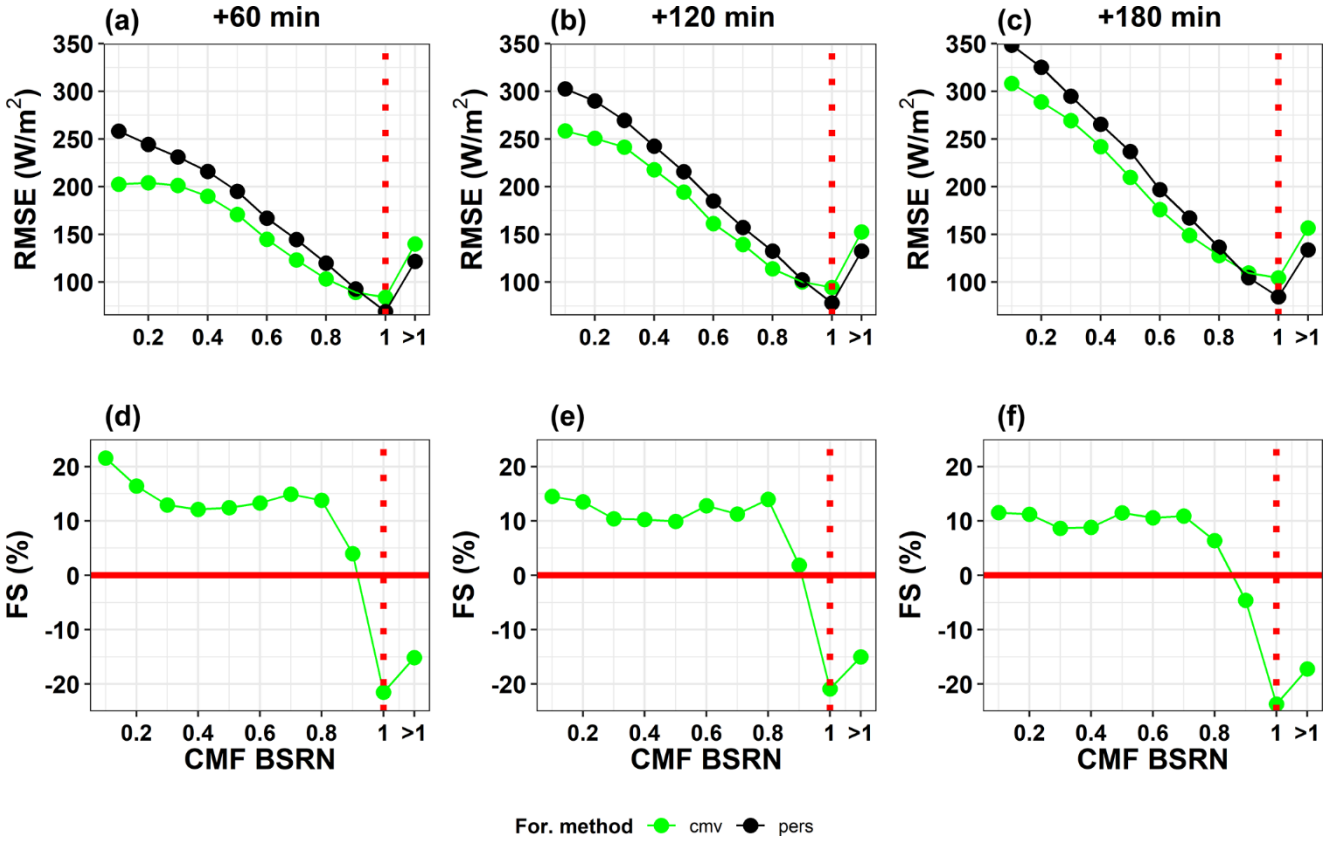

Figure 6.12 (a-c) Root mean square error (RMSE) of the global horizontal irradiance (GHI) for all stations forecasted with the CMV model (green symbols) and with the persistence method (black symbols) versus the cloud modification factor (CMF) derived from GHI measurements for three time steps (+60, +120, and +180 min). **(d-f)** The CMV model's forecasting skill plotted against CMF class for the same time steps as used for the panels **(a)-(c)**, respectively.

To demonstrate the better performance of the CMV method compared to the persistence method for all time steps under cloudy conditions, we calculated CMV FS% for partially cloudy conditions ($0.4 < CMF < 0.9$) and overcast conditions ($CMF \leq 0.4$), and the results are presented in Fig. 6.13. We can see again that the FS of CMV model decreases with time; however, the minimum value is ~10% for both categories. The maximum of FS occurs at the +15 min time step for both categories (at ~16% and ~22% for $0.4<CMF<0.9$ (cross symbols) and $CMF \leq 0.4$ (triangle symbols), respectively).

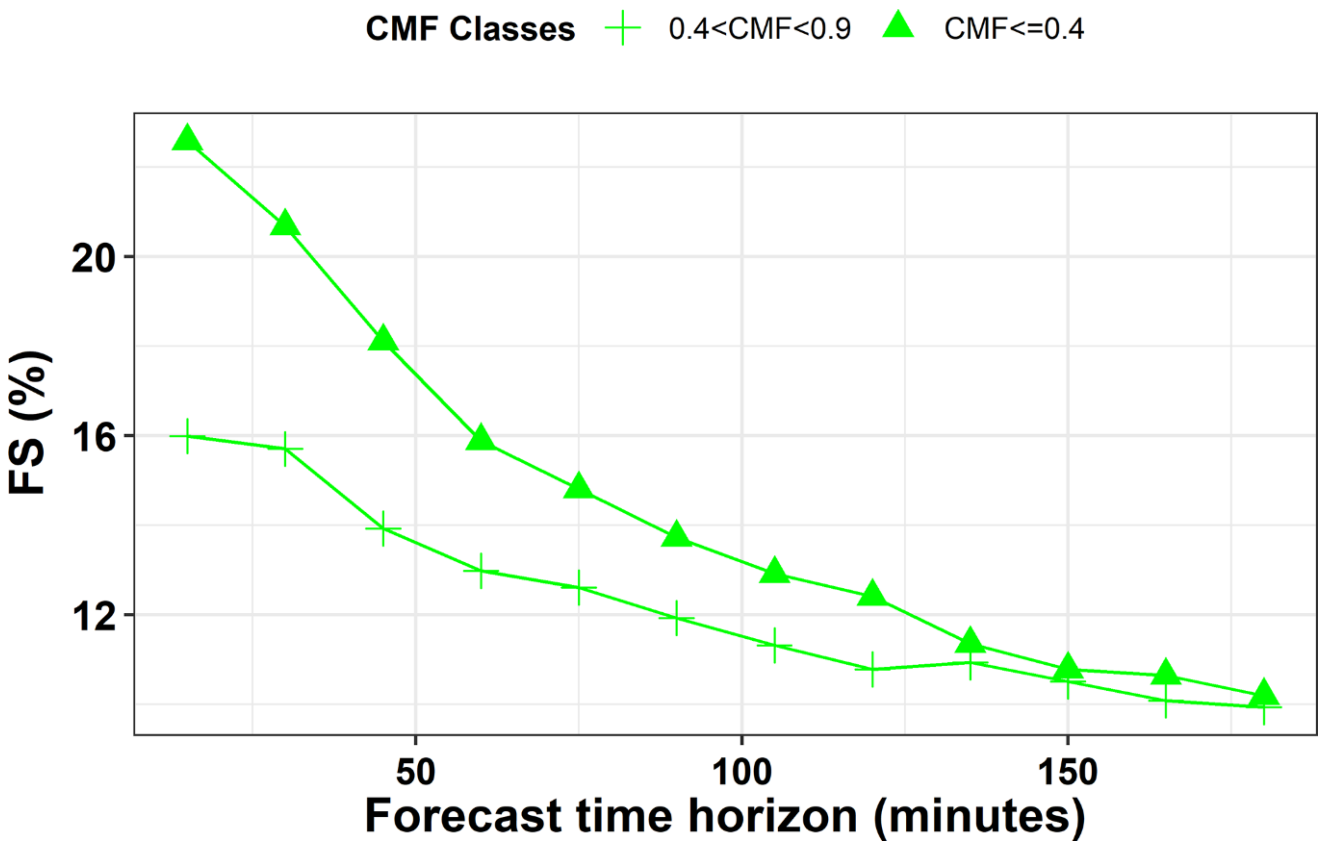

Figure 6.13 Forecasting skill (FS, expressed as a percentage) of CMV model against the persistence method for all stations as a function of time horizon for two different cloudiness conditions: 0.4<CMF<0.9 (crosses) and CMF≤0.4 (triangles).

The performance of the CMV model against the persistence method was also assessed under changing cloudiness, evaluated as the CMF changes based on ground-based measurements. The CMF changes were calculated for a time interval of 60 min (as $\Delta CMF = CMF_{t+60} - CMF_t$), and the results for the CMV model FS (%) are presented for the +60min time step as a function of CMF changes in Fig. 6.14. The high negative value of FS for the zero CMF change bin indicates that the persistence method is better for that bin, which was anticipated since there is zero or almost zero change in CMF, which is practically the definition of the persistence method. Persistence is still better than CMV for CMF changes from cloudy to clearer conditions up to the +0.3 CMF change bin, but the FS is less negative than for the zero bin. For CMF changes from cloudy to clearer conditions with higher magnitudes (bins > 0.4), CMV is better that persistence, with an FS value of 15% for the +0.6 CMF change bin. Consistent results were found for the opposite situation, namely changes from clearer to cloudy conditions, with the CMV model always giving better FS values (up to ~20%) than persistence.

Our analysis for different cloudiness conditions highlights the limited ability of the persistence method compared to the CMV-based NextSENSE2 to accurately forecast GHI under cloudy conditions (CMF values <0.9) and to follow transitions in cloudiness (especially from clearer to cloudy conditions).

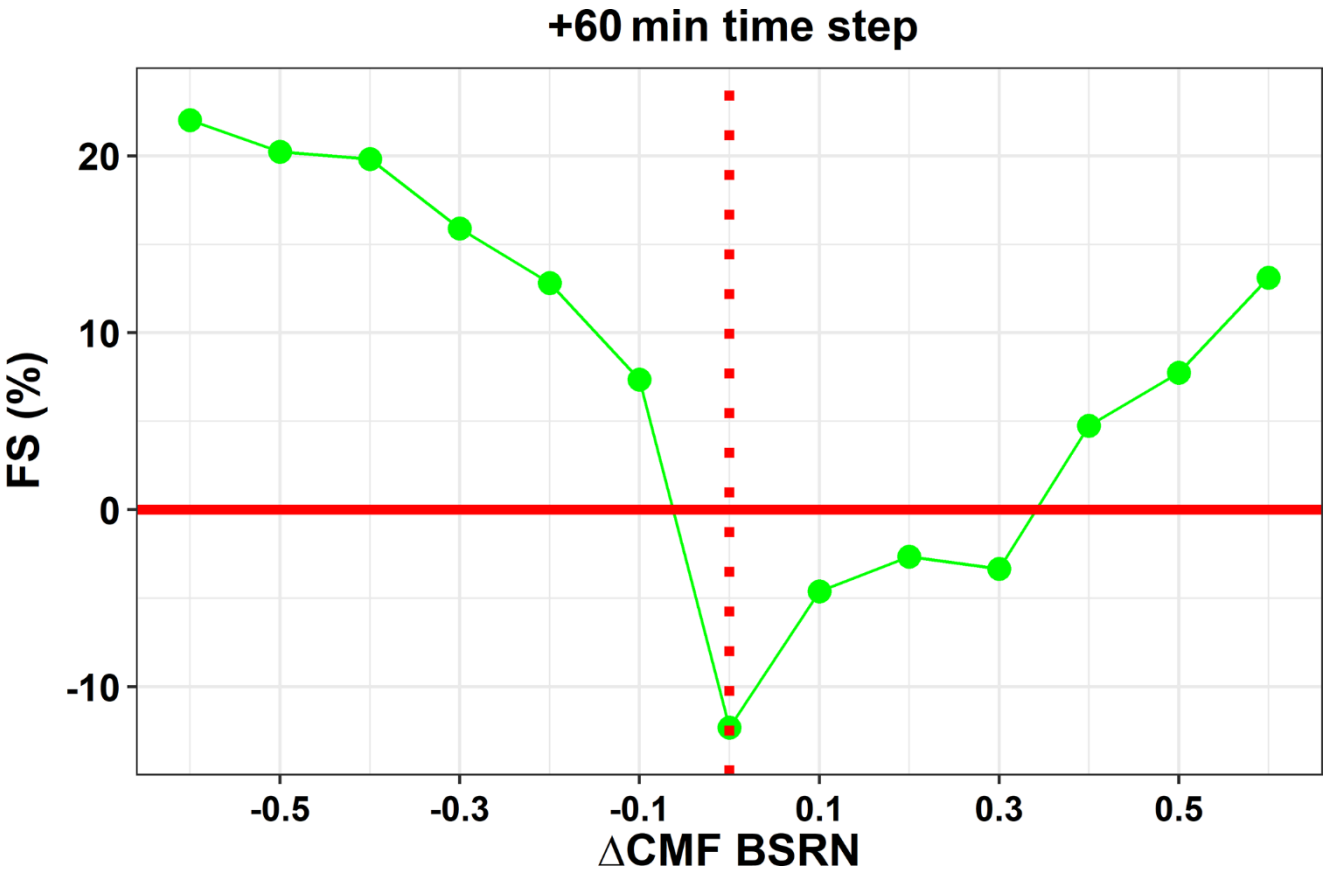

Figure 6.14 Forecasting skill (FS, expressed as a percentage) of the CMV model against the persistence method for all stations as a function of CMF change within a 60 min time interval (from time 0 to +60 min time step).

A direct comparison of the results of the present study for the NextSENSE2 short-term forecasting model with other studies is not straightforward, as the study period, the geographical area, and the validation methods used are different. Kallio-Myers et al. (2020) validated their Solis–Heliosat satellite-based GHI forecast modeled over southern Finland, and they found that the rRMSE reached 50% at the 4 h time step. Urbich et al. (2019) validated SESORA short-term forecasts of solar surface irradiance over Germany and parts of Europe for 17 different cases with different weather patterns for the period August to October 2017, with all forecasts initiated at 09:15 UTC. For validation against the SARAH-2 data by CM SAF, they reported an RMSE of 59 W m^{-2} after 15 min and a maximum RMSE of 142 W m^{-2}, reached after 165 min.

One of the limitations and sources of error for NextSENSE2 is related to the satellite-based optical flow method used for short-term forecasting: this method cannot reproduce cloud formation or dissipation. One example of this is convective clouds that form very fast, violating the optical flow criterion, i.e., that there should be constant intensity of the pixels between two consecutive images (e.g., Urbich et al., 2018, 2019). Urbich et al. (2018) applied the common approach of separation into subscales for the optimization process, which ultimately did not improve the forecast and increased the complexity of the implementation. As has already been discussed in the "Introduction" of this thesis, satellite-based short-term forecasting is the best choice for a time horizon of up to 6 h ahead,

since it is available in real time and at high spatial resolution. However, merging it with NWP models is a solution for increasing the time horizon and the quality of forecasts (Lorenz et al., 2012; Wolff et al., 2016), as it compensates for the effect of changes in intensities (during convection or cloud dissipation) that cannot be captured by CMV models (Müller and Pfeifroth, 2022). A comparison of a short-term forecasting model of surface solar radiation (the SESORA model) with different NWP models (apart with the persistence model) has been presented by Urbich et al. (2019), and they found that the intersection point where the NWP model delivers better results depends on the model and is beyond 3–4 h, which is also in line with the findings of other studies (e.g., Lorenz et al., 2012; Wolff et al., 2016). The merge of our short-term forecasting model with an NWP model is out of the scope of the present study. The elaborative benchmark analysis of the NextSENSE2 system against the persistence approach has demonstrated its applicability as an operational tool for a time horizon of up to 3 h ahead.

6.3 Summary and conclusions

The motivation of the work presented in this chapter is the continuous improvement of EO-based estimates and the accuracy of short-term forecasts of available solar resources to support solar energy exploitation systems on a regional scale (in Europe and the MENA region). The improvements in SENSE nowcasting and NextSENSE short-term forecasting operational systems were presented in this chapter and the cloud related uncertainties were analyzed in detail, using ground-based measurements to discriminate between different sun visibility conditions.

In terms of the aerosol-related inputs, a slight overestimation of CAMS AOD against the AERONET retrievals (<10%) was found, which resulted in a SENSE2 clear-sky GHI underestimation of less than 1%, highlighting the applicability of CAMS forecasts as EO inputs for operational solar resource nowcasting. In terms of modeled all-skies GHI, it was found that SENSE2 mostly overestimates GHI, with an MBE of 23.8 W m^{-2} (4.9%) for instantaneous comparisons, which was attributed to the uncertainties related to satellite cloud retrievals (overestimation of CMFmsg by ~0.02) and also to the spatial representativeness of satellite-based retrievals compared to ground-based measurements. We demonstrated that the most difficult situations to model are those with high spatial variability of solar radiation within the satellite pixel due to clouds (e.g., small broken clouds and the sun is obscured over the ground station, which is information that cannot be derived from satellite data). Based on our cloud-related analysis using ground-based data, a correction for the modeled GHI was used, resulting in an overall improvement in the SENSE2-modeled GHI such that 61% of the cases were within ±50 W m^{-2} (±10%) of the measured GHI and the final MBE of SENSE2 was 11.3 W m^{-2} (2.3%). Our main analysis was based on the 15 min timescale; however, depending on the application, hourly, daily, or monthly data could be used. The daily and monthly SENSE2 GHI showed much better statistics

(MBEs of 3.3 and 2.7 W m^{-2}, respectively). The validation results for SENSE2 demonstrate highly accurate nowcasted values of GHI which are in line with similar models. The recorded positive bias could be reduced by applying improvements in the NWC SAF cloud retrieval input to SENSE2 regarding partially cloudy pixels. NextSENSE2 was also improved due to the SENSE2 improvements. We also showed that, compared to the persistence method, the model works much better (as expected) at locations with increased cloudiness and for frequent cloudiness changes.

The data and methods involved in the estimation and prediction of the GHI in this study also revealed their limitations. As mentioned, the pixel-based approach for the model inputs (satellite and models) could not always reflect the reality above a (point) ground-based station. However, the model inputs are the state of the art for EO data and are readily available at a regional or global scale and at high spatial and temporal resolution; hence, the GHI product is representative of an area (~5 km x 5 km in this model), which is useful for photovoltaic parks covering a wide area. In general, performance evaluations of such EO-based GHI models with ground-based measurements must account for these spatial representativity issues when performing comparisons. The optical flow algorithm for calculating CMVs is also based on assumptions like 2D clouds and brightness constancy. However, it is a method based on cloud inputs from satellite data in real time, and the applicability of such methods compared with the persistence approach was demonstrated in this chapter.

Since satellite cloud information is the only real-time input, a new straightforward configuration for estimating GHI was applied (SENSE2). The advantage of calculating clear-sky GHI from the previous day, is what increases the accuracy of this product, since it is based on a detailed LUT of ~16 million combinations of seven different inputs; apart from AOD, these include additional aerosol optical properties and atmosphere/surface state inputs. Thus, the uncertainties in the estimated clear-sky GHI practically only result from uncertainties in the inputs. The new scheme for calculating the all-skies GHI by multiplying the clear-sky GHI by CMFmsg (derived in real time by multi-parametric function of MSG COT and SZA) was improved by applying a suitable CMFmsg correction. The correction was successful and improved the model performance, especially for areas with high cloudiness. Additionally, the new configuration of SENSE2 is more flexible, and it is easy to adapt so that it can provide more products (like DNI, the UV index or PAR). Finally, running the model in a retrospective way using reanalysis data or in situ observational data for certain locations is one of the prospects for the new model.

According to the results, high-resolution (every 15 min at ~5 km x 5 km) and quite accurate real-time GHI estimates and forecasts are produced from the upgraded SENSE2 and NextSENSE2 operational systems, respectively, which can contribute to solar energy systems management and planning.

7 General conclusions

The main goal of this dissertation was to investigate solar radiation interactions with aerosols and clouds to improve solar radiation forecasting capabilities and related applications. This was achieved through the synergistic use of long-term earth observation data (satellite and model based) of aerosols and clouds, ground-based measurements of surface solar radiation and state of the art algorithms. In this frame, upgrades were introduced to existing surface solar radiation nowcasting and short-term forecasting systems. The surface solar radiation attenuation by aerosols and, especially by dust, was quantified for the broader Mediterranean basin. Additionally, a study focusing on the state of the anthropogenic aerosol component over the greatest cities of the world has been conducted.

In the first part of this thesis, the anthropogenic aerosol component and its changes over time were investigated, focusing on the 81 greatest cities of the world with population more than 5 million. The analysis of long-term (2003-2020) high-resolution spaceborne aerosol retrievals revealed that the aerosol loads were increased the last two decades at the greatest cities of the planet with poor emission control measures. A population growth was also found for these cities for the same period. This is the case for megacities at the southern Asia, and especially India, Africa, and south America. This increase in aerosols is of particular concern for the health of the cities' inhabitants, as well as for the performance of solar energy exploitation systems (rooftop or large scale). Future work related to this direction is to quantify the attenuation of surface solar radiation related to this increase of aerosol loads in megacity scales.

To quantify the aerosol effects on surface solar radiation, the second part of this thesis was expanded to the regional scale and especially to the broader Mediterranean basin; an area with increasing capacity in solar energy installations and high levels of aerosol loads (both natural and anthropogenic). For the south part of the area (especially in Cyprus) during summer when the levels of DSSI are maximum, aerosols are the main attenuators of GHI and DNI. For the whole basin, using 15-year spaceborne data, it was found that aerosols attenuate GHI (important for PV installations) by 1–13 % and DNI by 5–47 %, where the maximum values were found over North Africa and the Middle East with dust contributing to 40-90 % to this attenuation. The daily values of aerosol attenuation reached substantially higher values up to 75% for GHI and 100% (totally blocked) for DNI. The use of additional aerosol optical properties for calculating aerosol direct radiative effects revealed the essential role of SSA. It was also found that CAMS underestimates slight AOD and strongly DOD compared to the satellite retrievals, resulting in underestimation of the radiative effects calculated with this dataset, highlighting the importance of selected dataset for accurately simulate DSSI. Those results, although for cloudless conditions, are important for the assessment of solar energy potential regarding the planning of solar installations.

Solar energy nowcasting and short-term forecasting have an important role in management of solar installations for the optimization of solar energy production and integration of produced energy into the grid and solar energy trading. The optimum performance of those forecasting systems is directly linked to the accuracy of their inputs, namely accurate forecasting of the cloud and aerosol related input. The upgraded version of a regional (Europe and the MENA region) solar energy nowcasting system, the SENSE2, was built and validated with ground-based measurements in the third part of this thesis. It was found that 61% of the modeled GHI cases were within ±50 W m^{-2} (±10%) of the measured GHI, with an MBE of 11.3 W m^{-2} (2.3%) for instantaneous (15 min) comparisons. Concerning the system inputs, CAMS AOD forecasts were proved quite accurate, resulting in negligible deviations. The SENSE2 system mostly overestimates GHI due to uncertainties related to satellite cloud retrievals and the spatial representativeness of satellite-based retrievals compared to ground-based measurements. It was demonstrated that the most difficult conditions to model are those with high spatial variability of solar radiation within the satellite pixel due to clouds (e.g., small broken clouds with the sun obscured over the ground station, an information that cannot be derived from satellite data). The results from SENSE2 validation demonstrate highly accurate nowcasted values of GHI which are in line with similar models. Future steps to reduce this positive bias could be to improve the NWC SAF cloud retrieval input to SENSE2 regarding the partially cloudy pixels. NextSENSE2 short-term solar forecasting system (up to 3 hours ahead), based on a state-of-the-art cloud motion vector (CMV) approach, was also validated, and benchmarked with the persistence approach. NextSENSE2 outperforms persistence forecasting method at locations with increased cloudiness and for frequent cloudiness changes.

Appendix

A. Aerosol optical depth regime over megacities

Table A1. Analytical table of 81 cities with the highest population up to 2018 (adopted by UN (2018a, 2019a)). The abreviations of the statistical concept column stand for city proper (CP), urban agglomeration (UA) and Metropolitan Area (MA). Major metropolitan areas (MMAs) are shown in bold, and the cities located in the Guangdong–Hong Kong–Macau Greater Bay Area are shown in italics.

Urban Agglomerations	Short name	Country or area	2018 Population (thousands)	Statistical concept
Tokyo	TOKY	Japan	37468	MA
Delhi	DELH	India	28514	MA
Shanghai	SHAN	China	25582	CP
Sao Paulo	SAOP	Brazil	21650	MA
Mexico City	MEXC	Mexico	21581	MA
Cairo	CAIR	Egypt	20076	MA
Bombay	BOMB	India	19980	MA
Beijing	BEIJ	China	19618	UA
Dhaka	DHAK	Bangladesh	19578	MA
Kinki M.M.A. (Osaka)	**OSAK**	**Japan**	**19281**	**MA**
New York	NEWY	United States of America	18819	UA
Karachi	KARA	Pakistan	15400	UA
Buenos Aires	BUEA	Argentina	14967	UA
Chongqing	CHON	China	14838	UA
Istanbul	ISTA	Turkey	14751	UA
Kolkata	KOLK	India	14681	MA
Manila	MANI	Philippines	13482	MA
Lagos	LAGO	Nigeria	13463	UA
Rio de Janeiro	RIOD	Brazil	13293	MA
Tianjin	TIAN	China	13215	UA
Kinshasa	KINS	Democratic Republic of the Congo	13171	UA
Guangzhou, Guangdong	*GUAN*	*China*	*12638*	*UA*
Los Angeles-Long Beach-Santa Ana	**LOSA**	**United States of America**	**12458**	**UA**
Moscow	MOSC	Russian Federation	12410	CP
Shenzhen	*SHNZ*	*China*	*11908*	*UA*
Lahore	LAHO	Pakistan	11738	UA
Bangalore	BALO	India	11440	UA
Paris	PARI	France	10901	UA
Bogota	BOGO	Colombia	10574	UA
Jakarta	JAKA	Indonesia	10517	MA
Chennai	CHNA	India	10456	UA
Lima	LIMA	Peru	10391	MA

Bangkok	BANG	Thailand	10156	UA
Seoul	SEOU	Republic of Korea	9963	UA
Chukyo M.M.A. (Nagoya)	**NAGO**	**Japan**	**9507**	**MA**
Hyderabad	HYDE	India	9482	UA
London	LOND	United Kingdom	9046	UA
Tehran	TEHR	Iran (Islamic Republic of)	8896	CP
Chicago	CHIC	United States of America	8864	UA
Chengdu	CHGD	China	8813	UA
Nanjing, Jiangsu	NANJ	China	8245	UA
Wuhan	WUHA	China	8176	UA
Ho Chi Minh City	HCMC	Viet Nam	8145	UA
Luanda	LUAN	Angola	7774	UA
Ahmadabad	AHMA	India	7681	UA
Kuala Lumpur	KUAL	Malaysia	7564	MA
Xian, Shaanxi	XIAN	China	7444	UA
Hong Kong	*HONG*	*China, Hong Kong SAR*	*7429*	*UA*
Dongguan	*DONG*	*China*	*7360*	*UA*
Hangzhou	HANG	China	7236	UA
Foshan	*FOSH*	*China*	*7196*	*UA*
Shenyang	SHYA	China	6921	UA
Riyadh	RIYA	Saudi Arabia	6907	CP
Baghdad	BAGH	Iraq	6812	MA
Santiago	SANT	Chile	6680	UA
Surat	SURA	India	6564	UA
Madrid	MADR	Spain	6497	CP
Suzhou, Jiangsu	SUZH	China	6339	UA
Pune	PUNE	India	6276	UA
Haerbin	HAER	China	6115	UA
Houston	HOUS	United States of America	6115	UA
Dallas-Fort Worth	**DALL**	**United States of America**	**6099**	**UA**
Toronto	TORO	Canada	6082	MA
Dar es Salaam	DARE	United Republic of Tanzania	6048	UA
Miami	MIAM	United States of America	6036	UA
Belo Horizonte	BELO	Brazil	5972	MA
Singapore	SING	Singapore	5792	UA
Philadelphia	PHIL	United States of America	5695	UA
Atlanta	ATLA	United States of America	5572	UA
Kitakyushu-Fukuoka M.M.A.	**FUKU**	**Japan**	**5551**	**MA**
Khartoum	KHAR	Sudan	5534	UA
Barcelona	BARC	Spain	5494	CP
Johannesburg	JOHA	South Africa	5486	UA
Saint Petersburg	STPE	Russian Federation	5383	CP

Qingdao	QING	China	5381	UA
Dalian	DALI	China	5300	UA
Washington, D.C.	WASH	United States of America	5207	UA
Yangon	YANG	Myanmar	5157	UA
Alexandria	ALEX	Egypt	5086	CP
Jinan, Shandong	JINA	China	5052	UA
Guadalajara	GUAD	Mexico	5023	MA

Table A2. AERONET stations that have been used in the analysis and the corresponding urban agglomerations.

AERONET station	Period	Urban Agglomerations	Short name	Country or area
Sao_Paulo	2003-2019	Sao Paulo	SAOP	Brazil
Mexico_City	2003-2018	Mexico City	MEXC	Mexico
Cairo_EMA_2	2010-2019	Cairo	CAIR	Egypt
Beijing	2003-2019	Beijing	CHN	China
Dhaka_University	2012-2020	Dhaka	BGD	Bangladesh
Osaka	2004-2020	Osaka	JPN	Japan
CCNY	2003-2020	New York	USA	United States of America
Karachi	2006-2020	Karachi	PAK	Pakistan
CEILAP-BA	2003-2019	Buenos Aires	ARG	Argentina
Manila_Observatory	2009-2020	Manila	MANI	Philippines
Santa_Monica_Colg	2013-2020	Los Angeles	LOSA	United States of America
Moscow_MSU_MO	2003-2020	Moscow	MOSC	Russian Federation
Lahore	2007-2020	Lahore	LAHO	Pakistan
Paris	2005-2020	Paris	PARI	France
Yonsei_University	2011-2020	Seoul	SEOU	Republic of Korea
Hong_Kong_PolyU	2006-2020	Hong Kong	HONG	China, Hong Kong SAR
Solar_Village	2003-2013	Riyadh	RIYA	Saudi Arabia
Madrid	2012-2020	Madrid	MADR	Spain
Taihu	2005-2016	Suzhou	SUZH	China
Pune	2005-2019	Pune	PUNE	India
Univ_of_Houston	2006-2020	Houston	HOUS	United States of America
Toronto	2004-2020	Toronto	TORO	Canada
Key_Biscayne	2007-2018	Miami	MIAM	United States of America
Singapore	2007-2020	Singapore	SING	Singapore
Fukuoka	2012-2020	Fukuoka	FUKU	Japan
Barcelona	2005-2020	Barcelona	BARC	Spain
GSFC	2003-2020	Washington, D.C.	WASH	United States of America

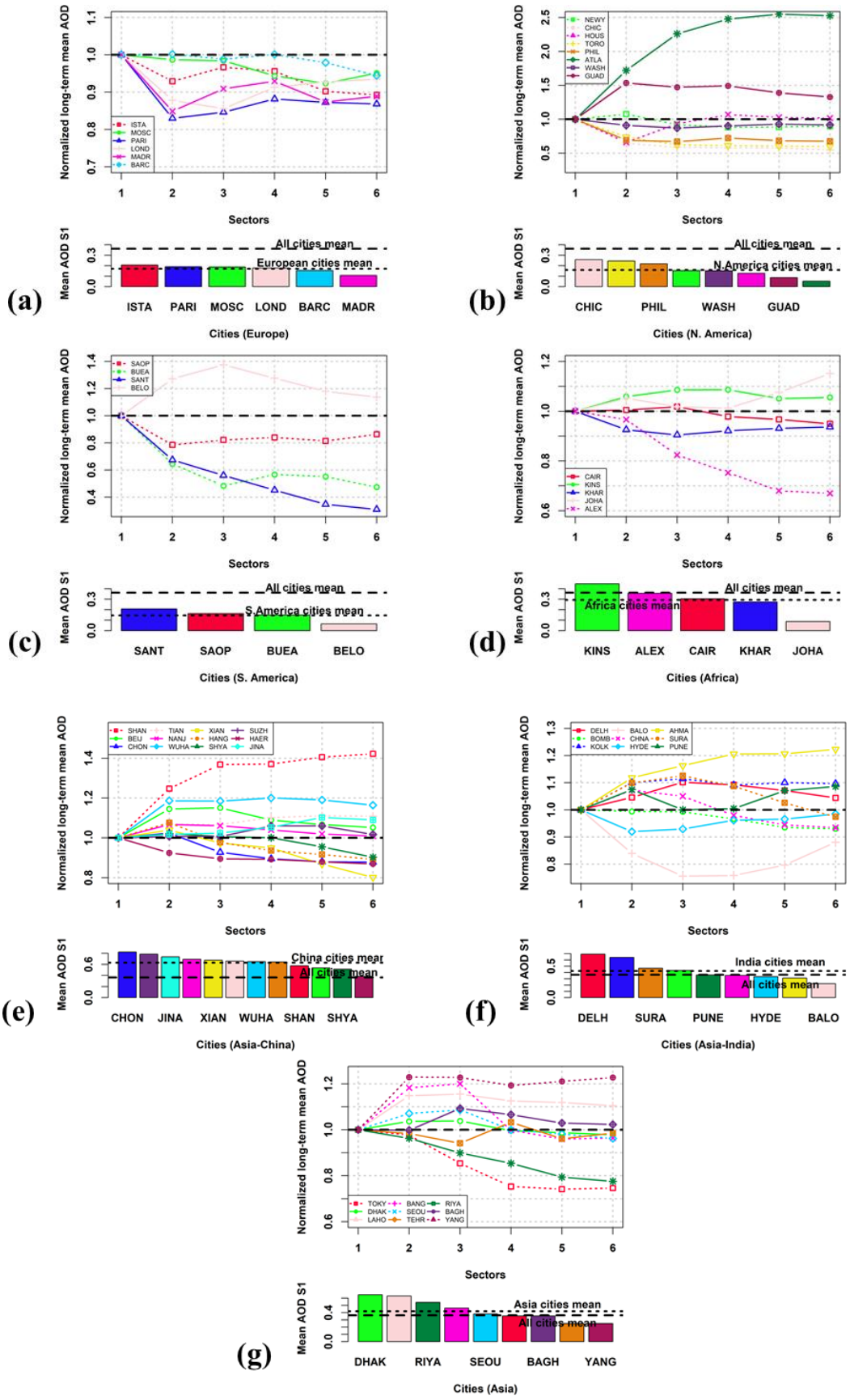

Figure A1. Panels **(a)–(g)** correspond to different geographical domains. For every panel, the long-term mean AOD for the six different sectors normalized with the mean value of sector 1 (S1) is given with different colors, and symbols correspond to different cities. Solid/dashed lines denote inland/coastal cities, respectively. The bar plot shows the long-term mean AOD of S1 for every city in the geographical domain, denoted with the same color used in the upper plot. The dashed line corresponds to the mean from all cities, while the dotted line gives the mean AOD for the cities of the corresponding geographical domain.

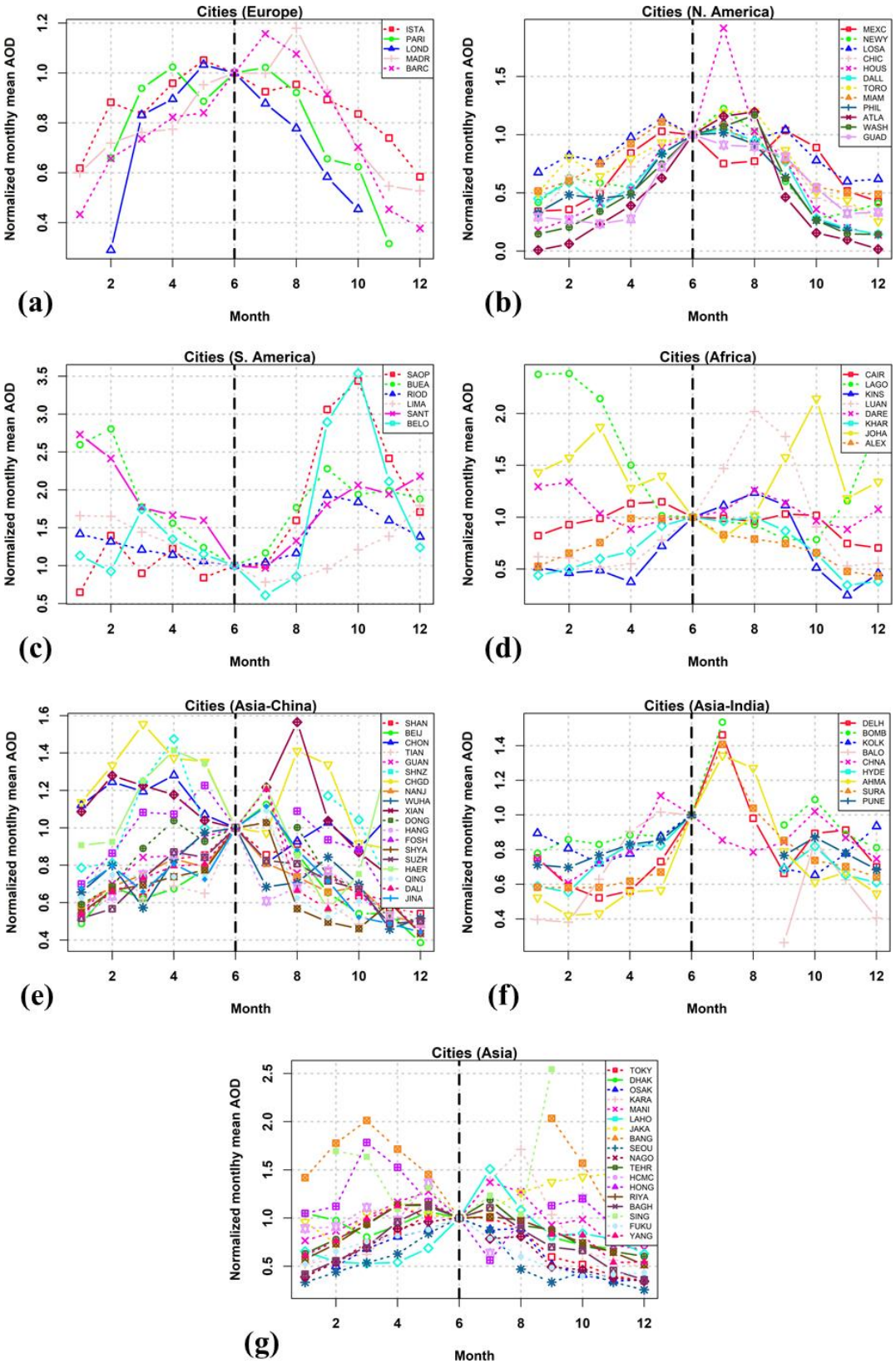

Figure A2. Long-term monthly mean AOD values (intraannual variability) normalized against the mean value of month June. The different colors and symbols correspond to different cities. Solid/dashed lines denote inland/coastal cities, respectively. Long-term monthly mean AOD values (intraannual variability) normalized against the mean value of month June. The different colors and symbols correspond to different cities. Solid/dashed lines denote inland/coastal cities, respectively.

B. 15-Year Analysis of Direct Effects of Total and Dust Aerosols in Solar Radiation/Energy over the Mediterranean Basin

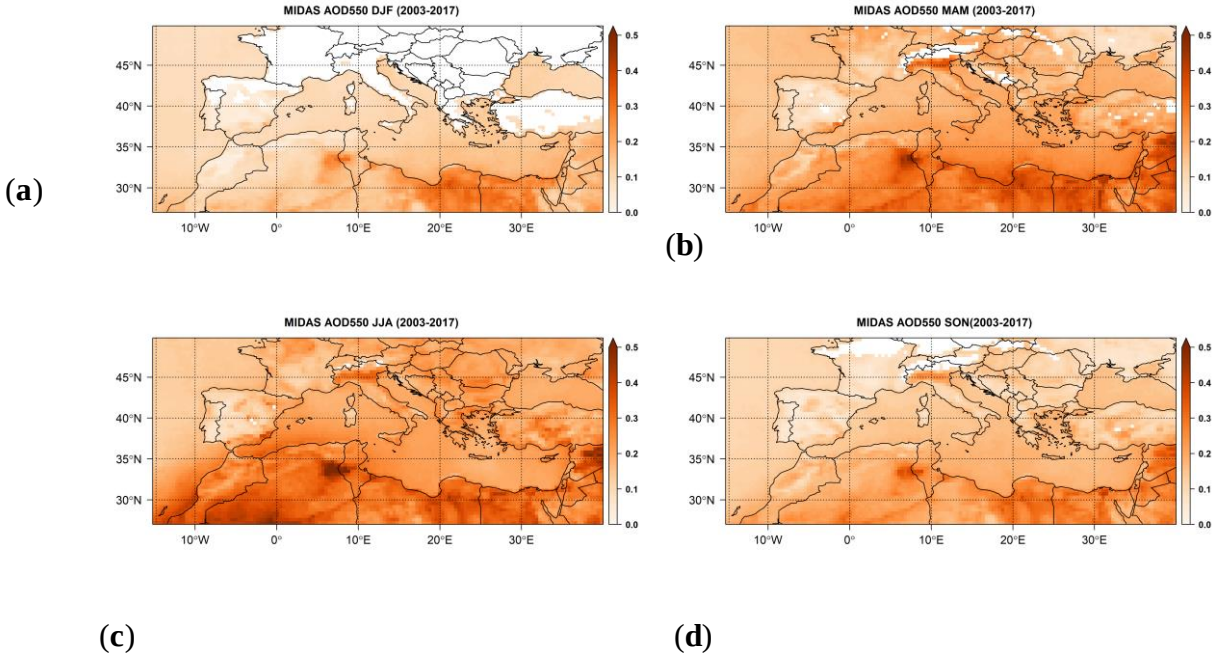

(**a**) (**b**)

(**c**) (**d**)

Figure B1 Geographical distribution of long-term average of seasonal mean AOD at 550 nm from MODIS. Blank grid points are those that did not fulfill the criterion of at least 20% data availability on an annual basis.

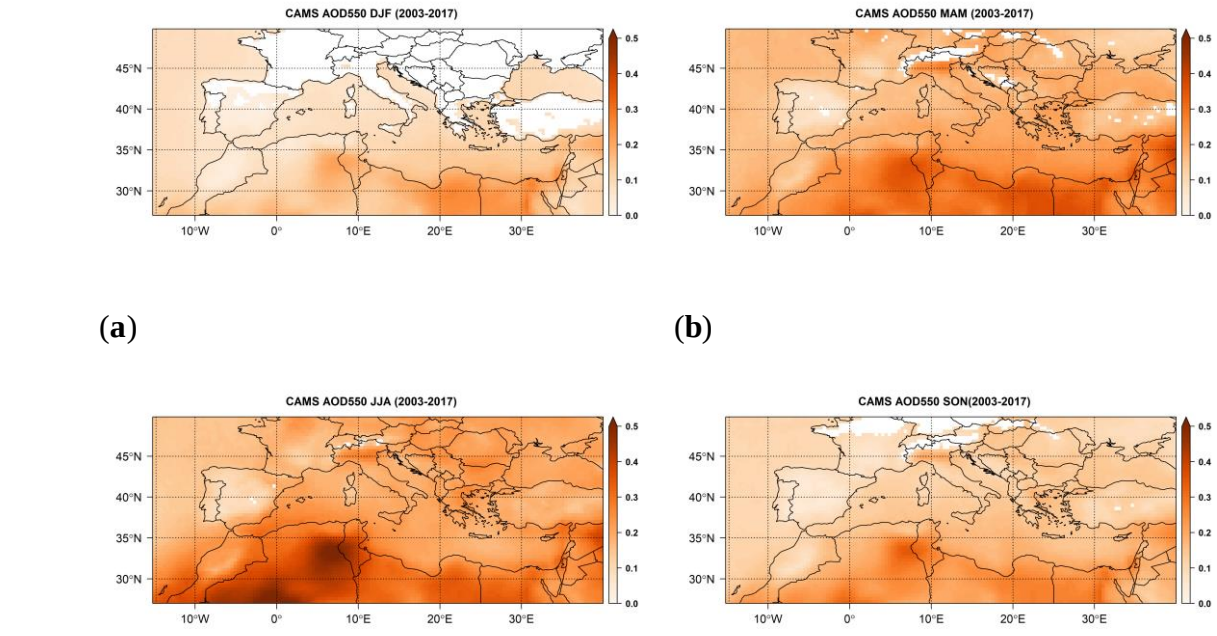

(**a**) (**b**)

(**c**) (**d**)

Figure B2 Geographical distribution of long-term average of seasonal mean AOD at 550 nm from CAMS. Blank grid points are those that did not fulfill the criterion of at least 20% data availability on an annual basis.

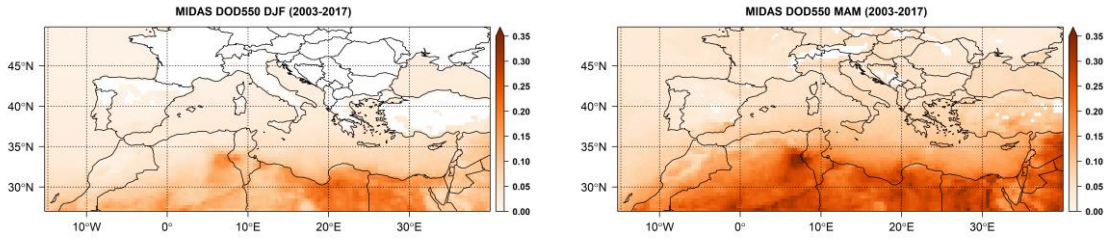

(**a**) (**b**)

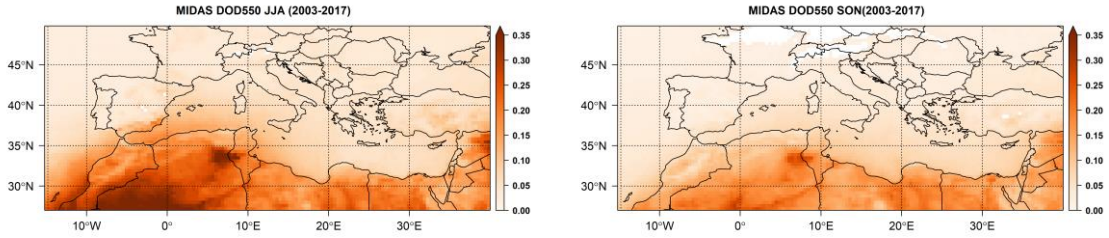

(**c**) (**d**)

Figure B3 Geographical distribution of long-term average of seasonal mean DOD at 550 nm from MIDAS. Blank grid points are those that did not fulfill the criterion of at least 20% data availability on an annual basis.

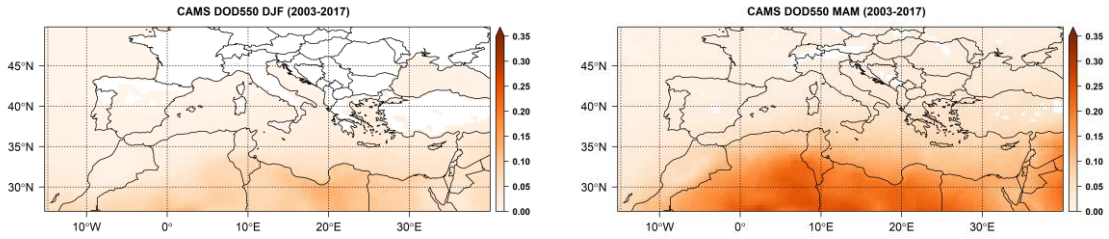

(**a**) (**b**)

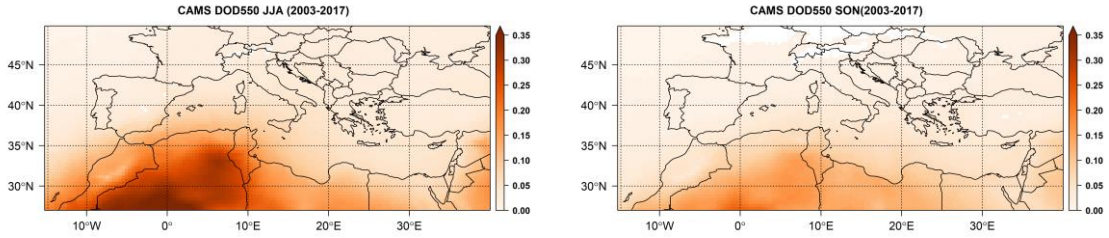

(**c**) (**d**)

Figure B4 Geographical distribution of long-term average of seasonal mean DOD at 550 nm from CAMS. Blank grid points are those that did not fulfill the criterion of at least 20% data availability on an annual basis.

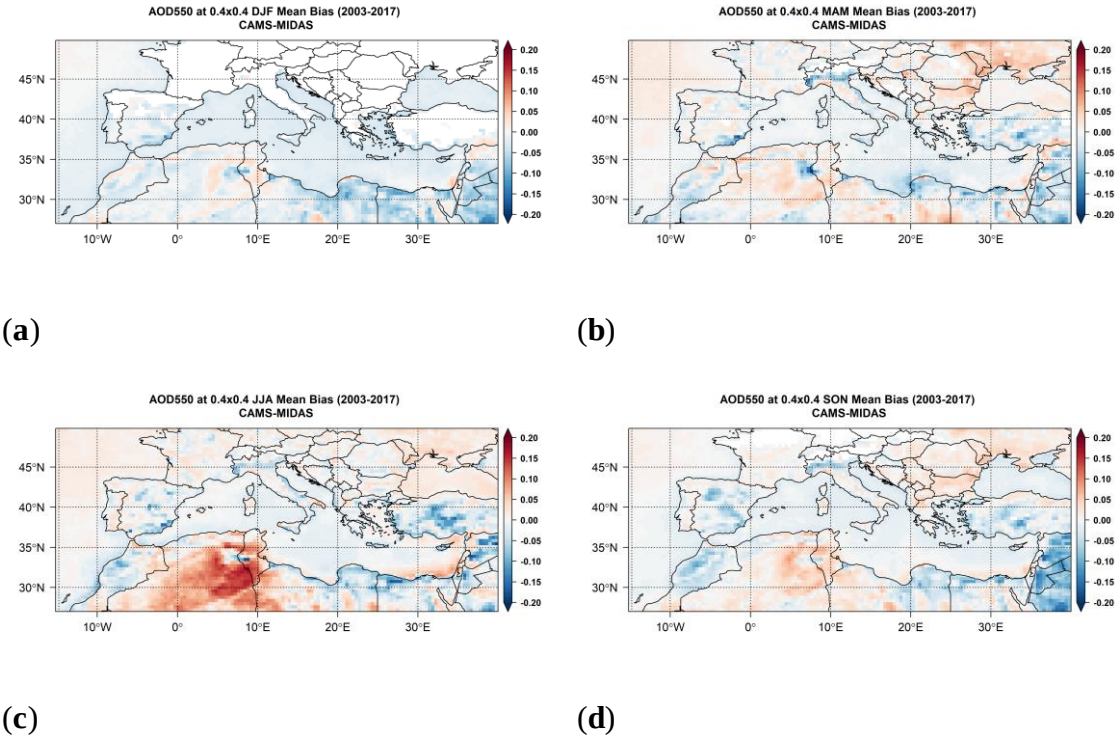

(**a**) (**b**)

(**c**) (**d**)

Figure B5 Geographical distribution of annual mean CAMS–MIDAS AOD biases. Blank grid points are those that did not fulfill the criterion of at least 20% data availability on an annual basis.

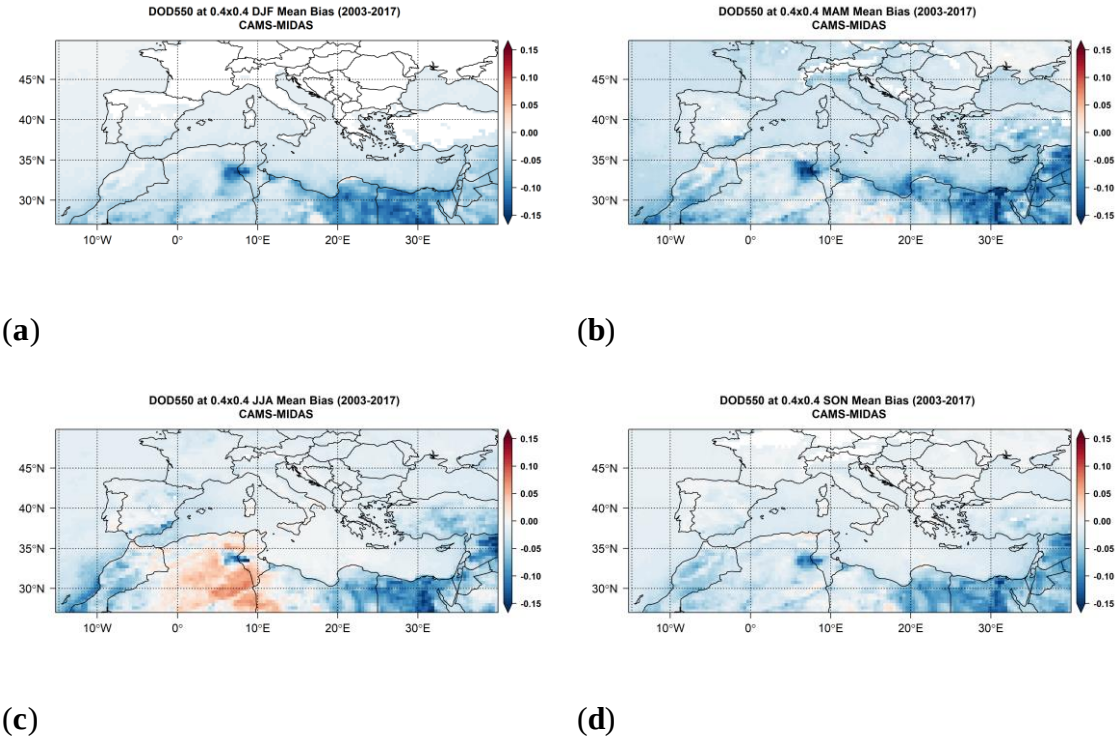

(**a**) (**b**)

(**c**) (**d**)

Figure B6 Geographical distribution of annual mean CAMS–MIDAS DOD biases. Blank grid points are those that did not fulfill the criterion of at least 20% data availability on an annual basis.

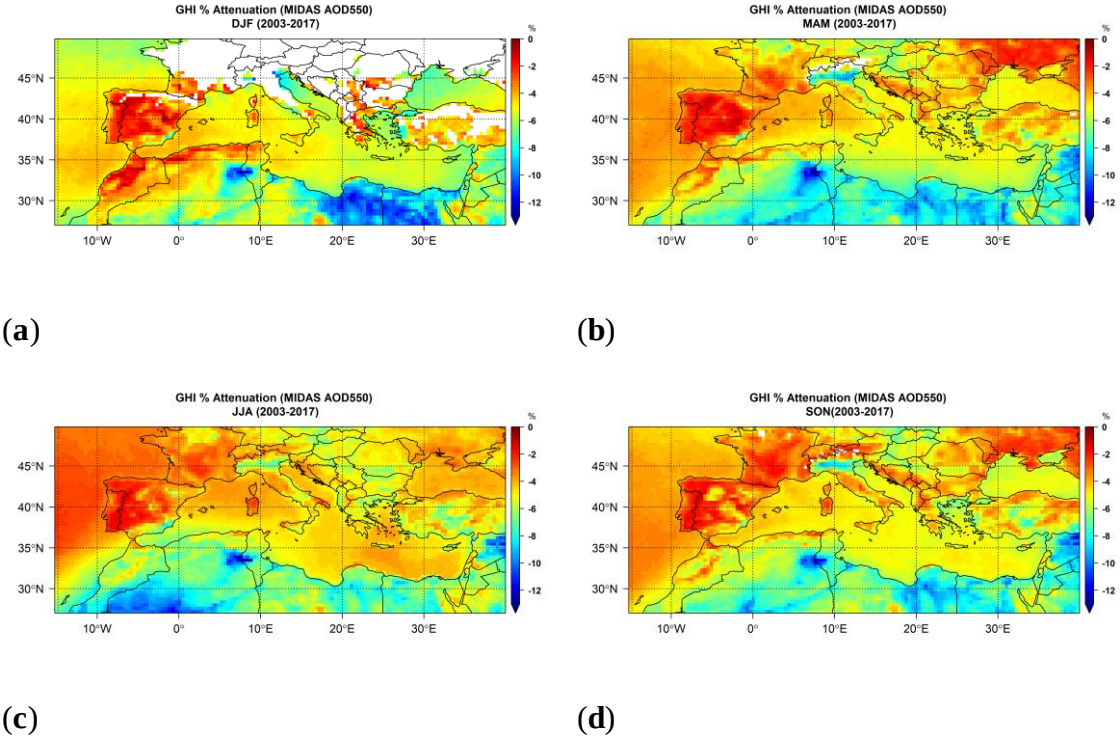

(**a**) (**b**)

(**c**) (**d**)

Figure B7 Change (in %) of the mean seasonal integral of GHI due to the presence of aerosols under MODIS AOD. Blank grid points are those that did not fulfill the criterion of at least 20% data availability on an annual basis.

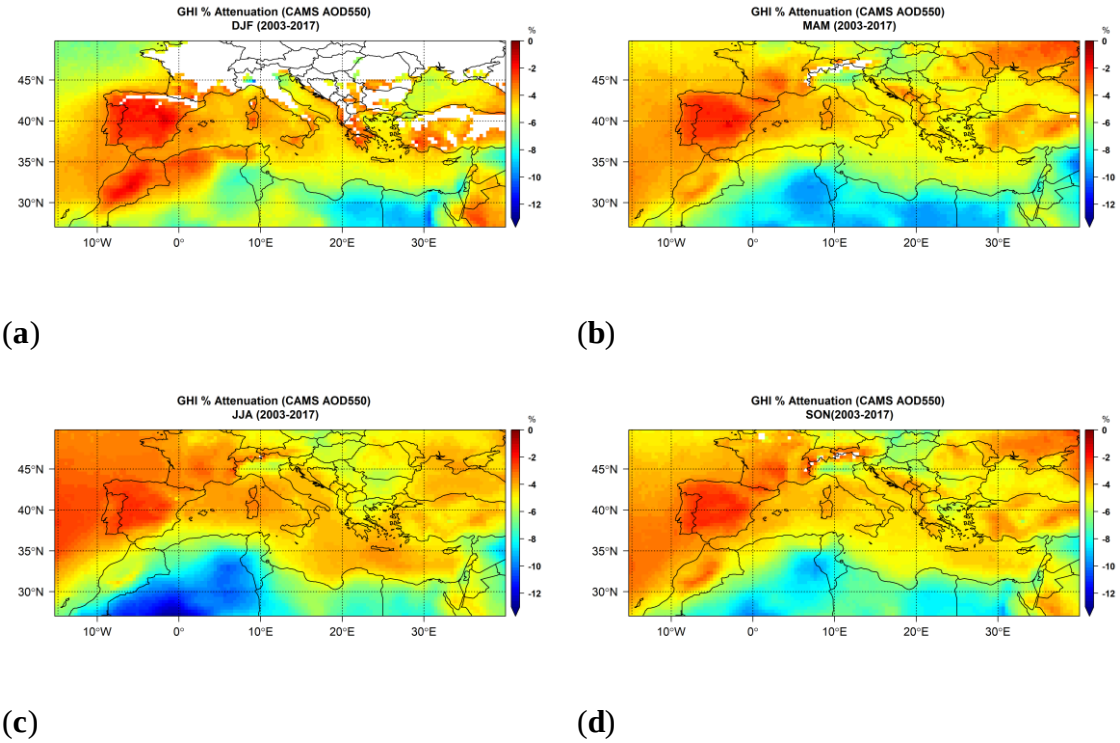

(**a**) (**b**)

(**c**) (**d**)

Figure B8 Change (in %) of the mean seasonal integral of GHI due to the presence of aerosols under CAMS AOD. Blank grid points are those that did not fulfill the criterion of at least 20% data availability on an annual basis.

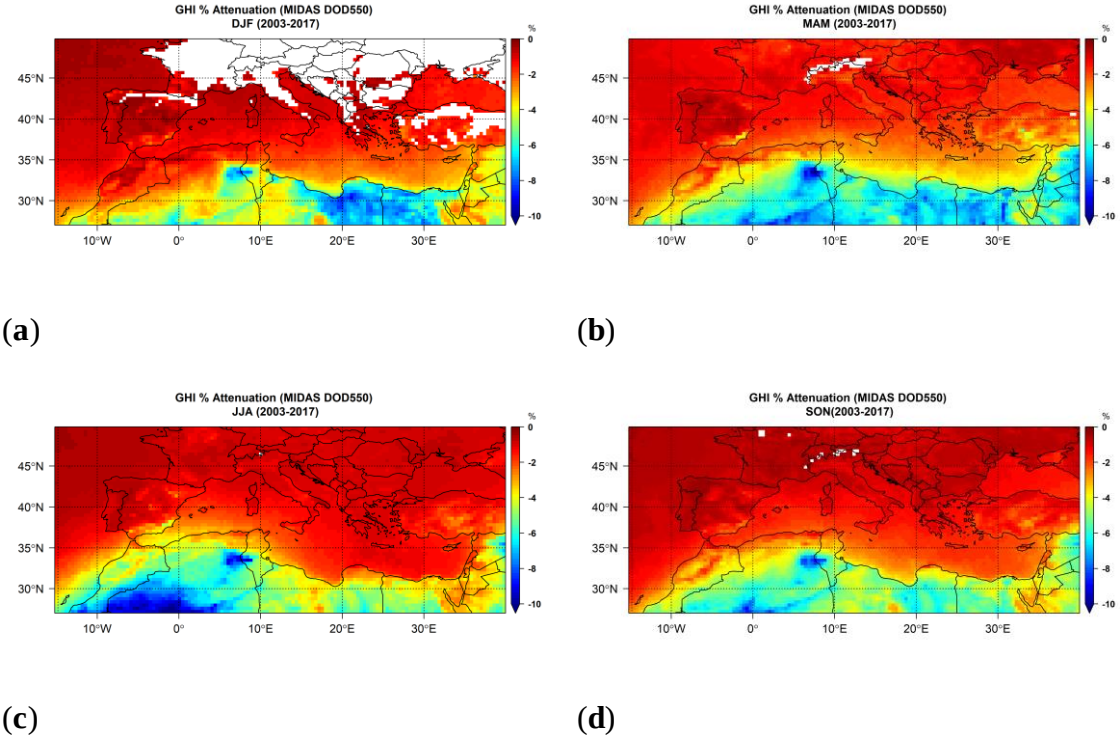

(**a**) (**b**)

(**c**) (**d**)

Figure B9 Change (in %) of the mean annual integral of GHI due to the presence of dust under MIDAS DOD. Blank grid points are those that did not fulfill the criterion of at least 20% data availability on an annual basis.

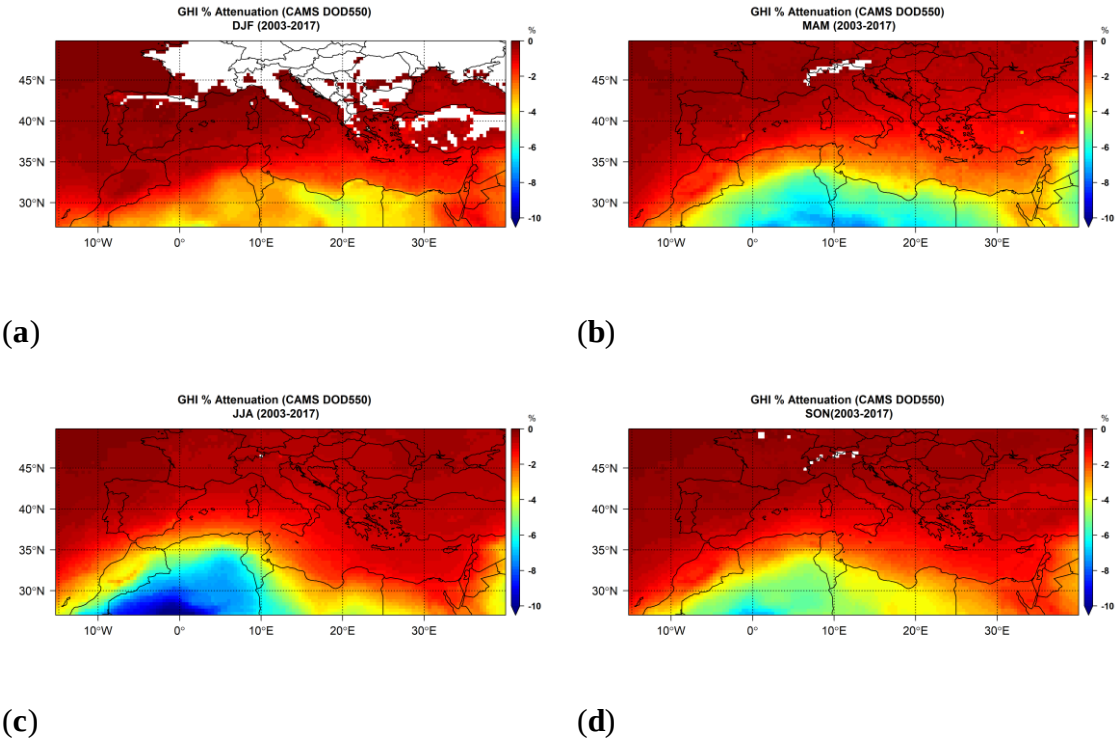

(**a**) (**b**)

(**c**) (**d**)

Figure B10 Change (in %) of the mean annual integral of GHI due to the presence of dust under CAMS DOD. Blank grid points are those that did not fulfill the criterion of at least 20% data availability on an annual basis.

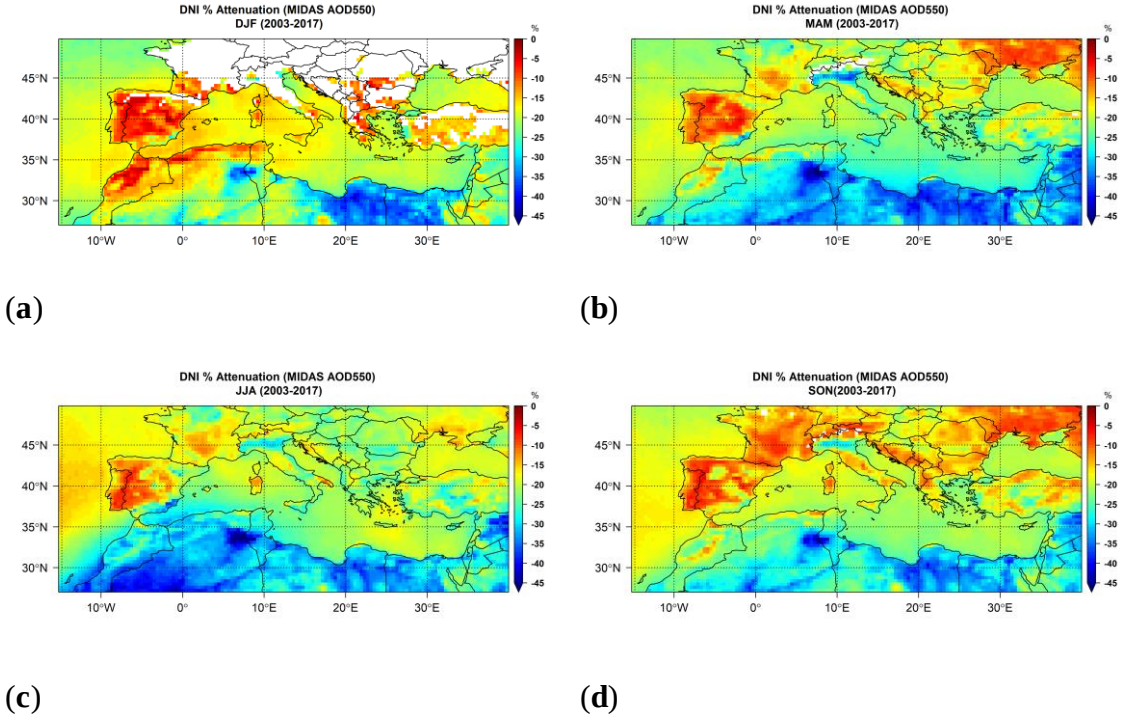

(**a**) (**b**)

(**c**) (**d**)

Figure B11 Change (in %) of the mean annual integral of DNI due to the presence of aerosols under MODIS AOD. Blank grid points are those that did not fulfill the criterion of at least 20% data availability on an annual basis.

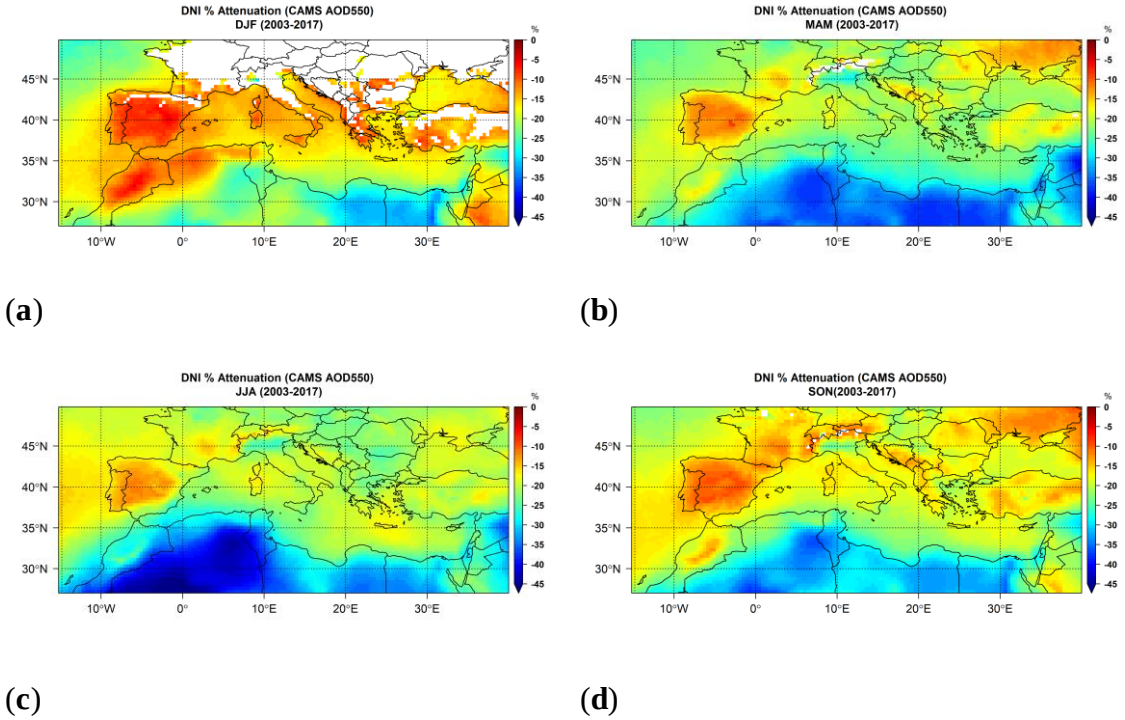

(**a**) (**b**)

(**c**) (**d**)

Figure B12 Change (in %) of the mean annual integral of DNI due to the presence of aerosols under CAMS AOD. Blank grid points are those that did not fulfill the criterion of at least 20% data availability on an annual basis.

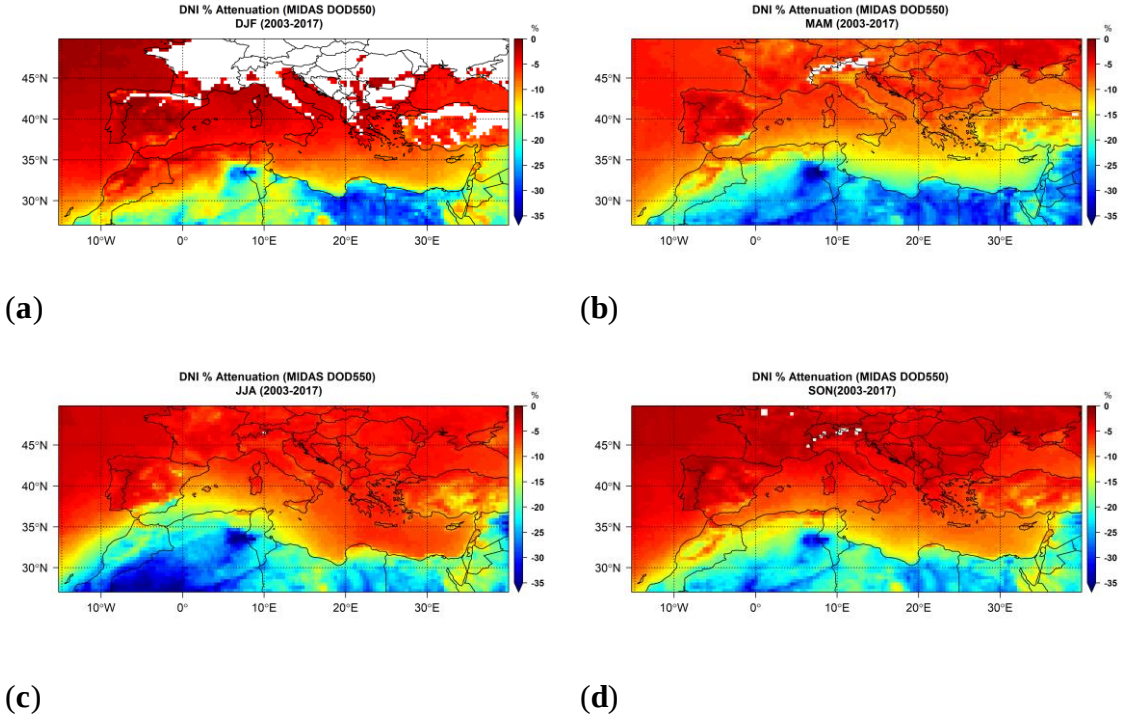

(**a**) (**b**)

(**c**) (**d**)

Figure B13 Change (in %) of the mean annual integral of DNI due to the presence of dust under MIDAS DOD. Blank grid points are those that did not fulfill the criterion of at least 20% data availability on an annual basis.

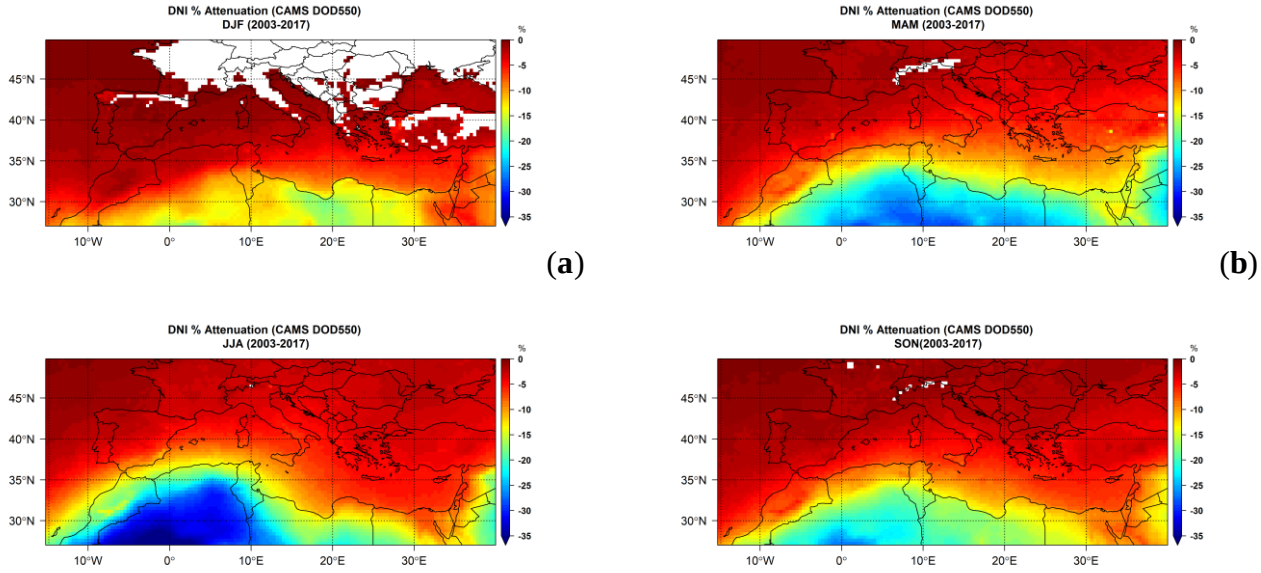

(**a**) (**b**)

(**c**) (**d**)

Figure B14 Change (in %) of the mean annual integral of DNI due to the presence of dust under CAMS DOD. Blank grid points are those that did not fulfill the criterion of at least 20% data availability on an annual basis.

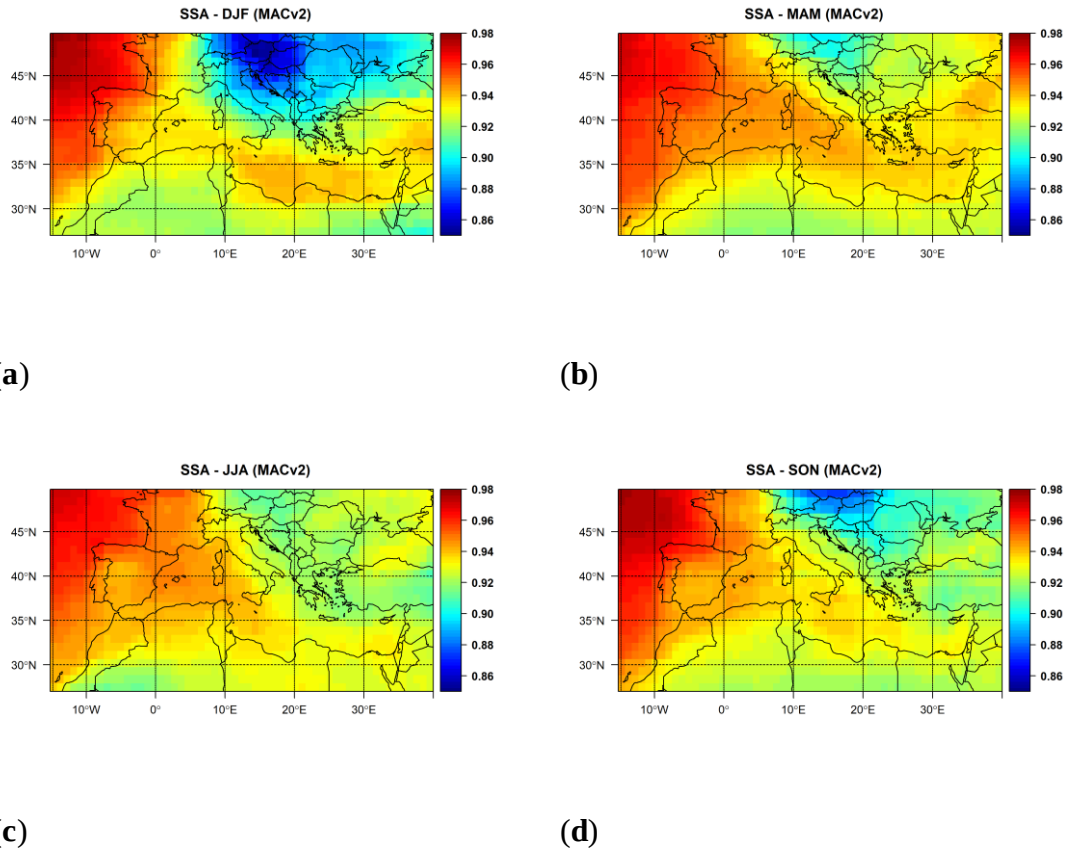

(**a**) (**b**)

(**c**) (**d**)

Figure B15 Geographical distribution of seasonal mean SSA (MACv2 (Kinne, 2019)).

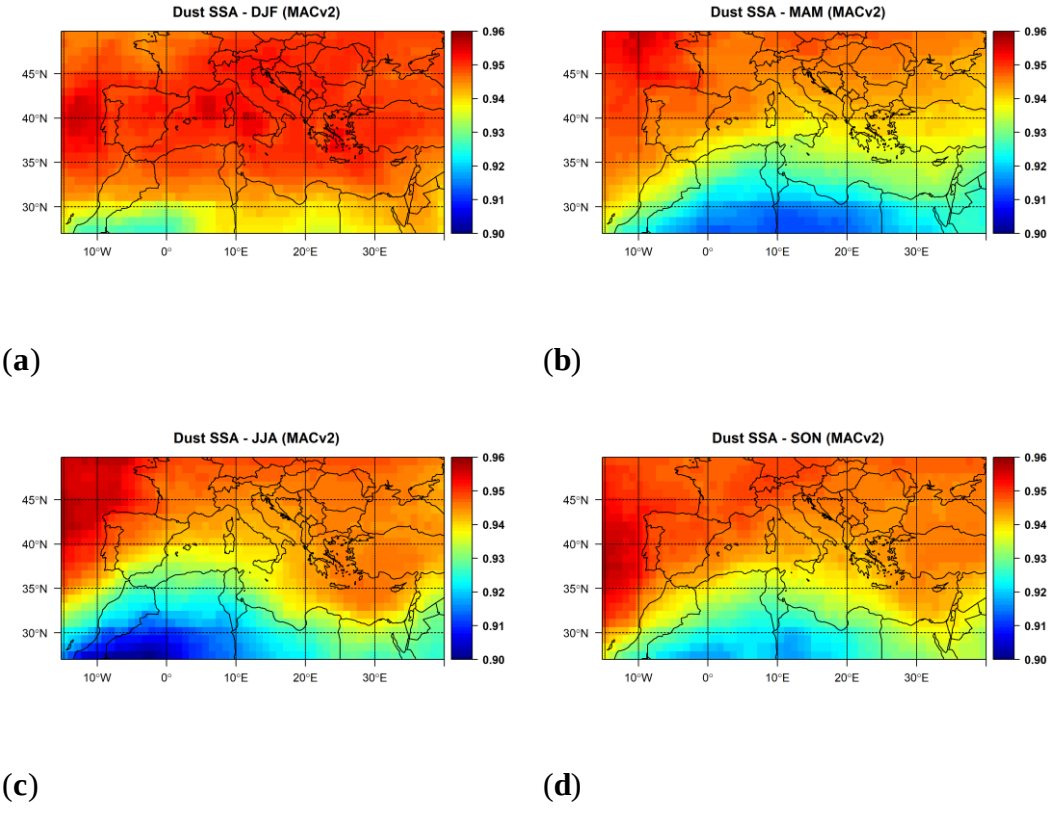

(**a**) (**b**)

(**c**) (**d**)

Figure B16 Geographical distribution of seasonal mean DU SSA (MACv2 (Kinne, 2019)).

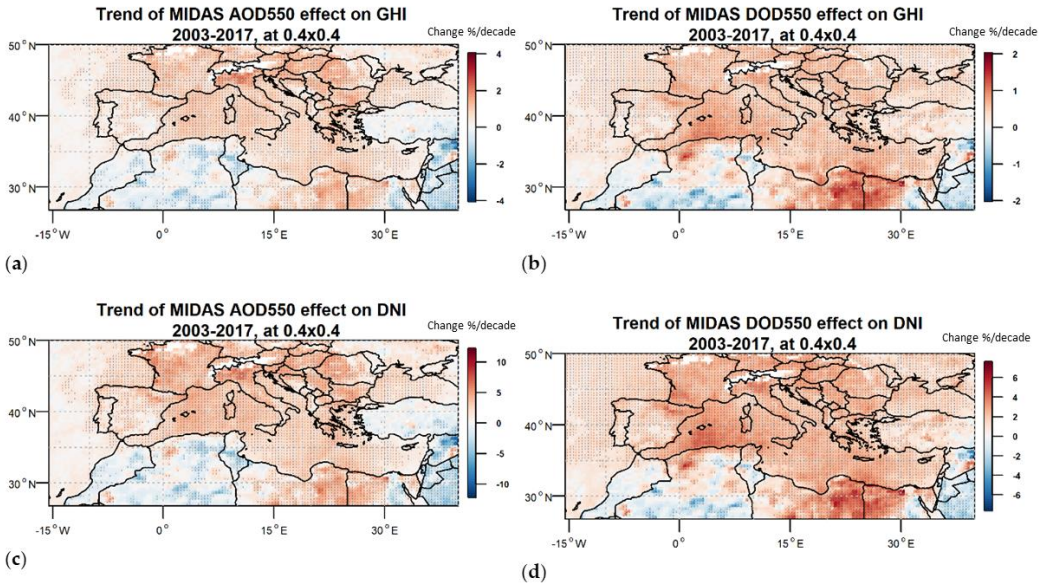

Figure B17 Trends in % per decade for GHI (panels (**a**), (**b**)) and DNI (panels (**c**), (**d**)) due to the changes in AOD (panels (**a**), (**c**)) and DOD (panels (**b**), (**d**)).

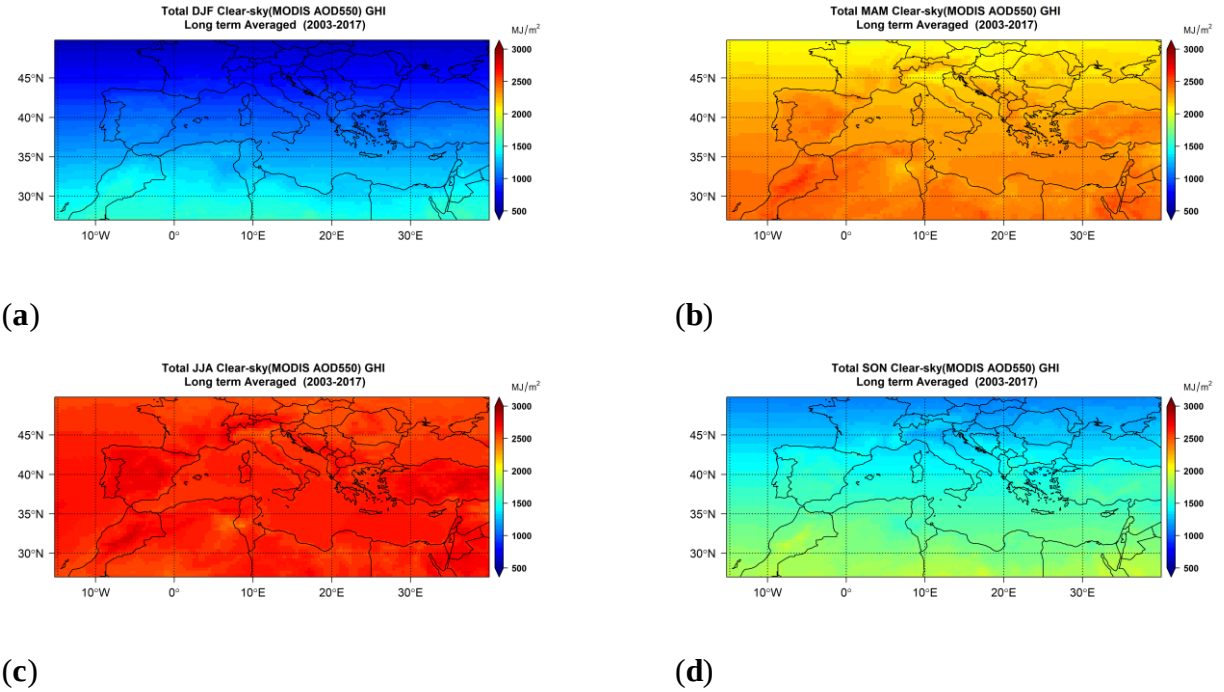

Figure B18 Mean seasonal integrals for clear-sky GHI using MODIS AOD.

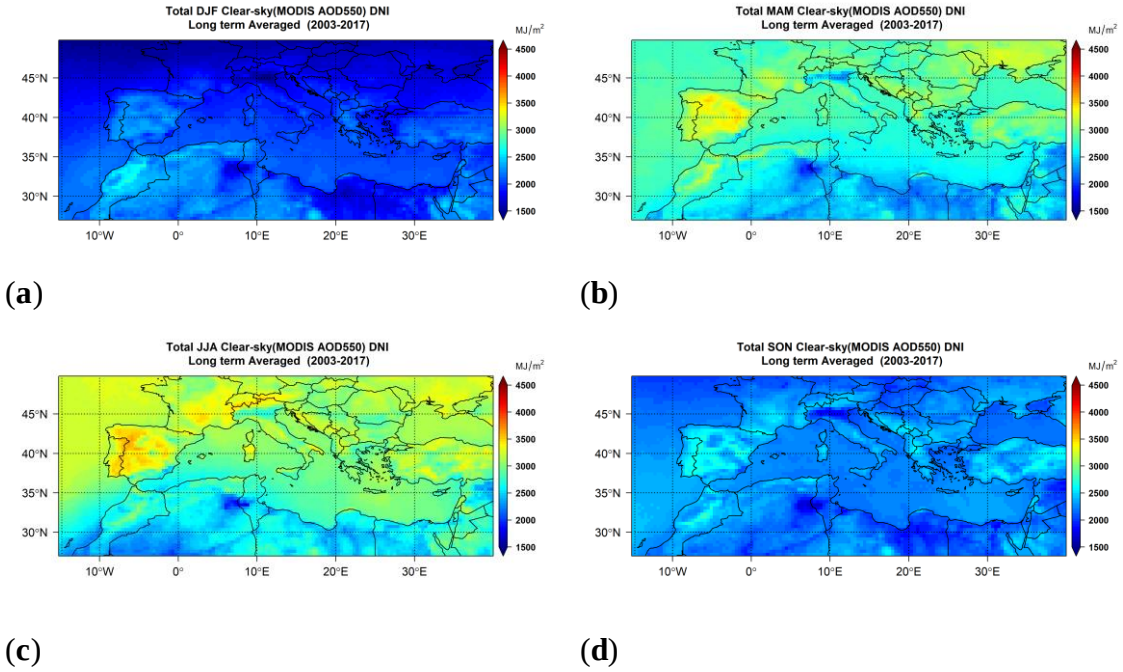

Figure B19 Mean seasonal integrals for clear-sky DNI using MODIS AOD.

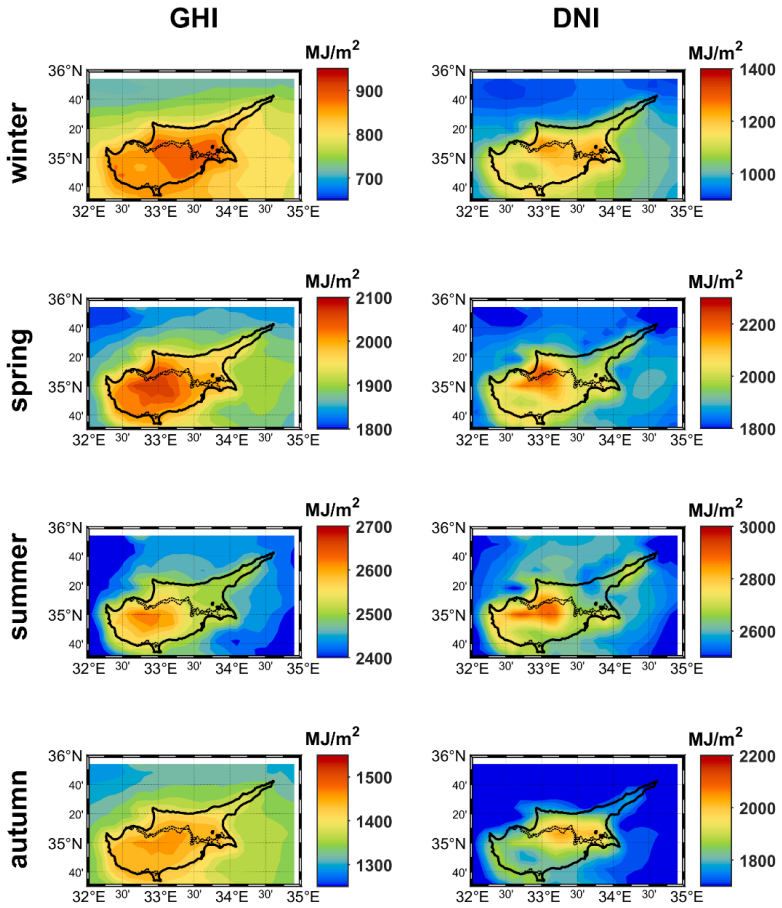

Figure B20 Total seasonal all-sky GHI and DNI.

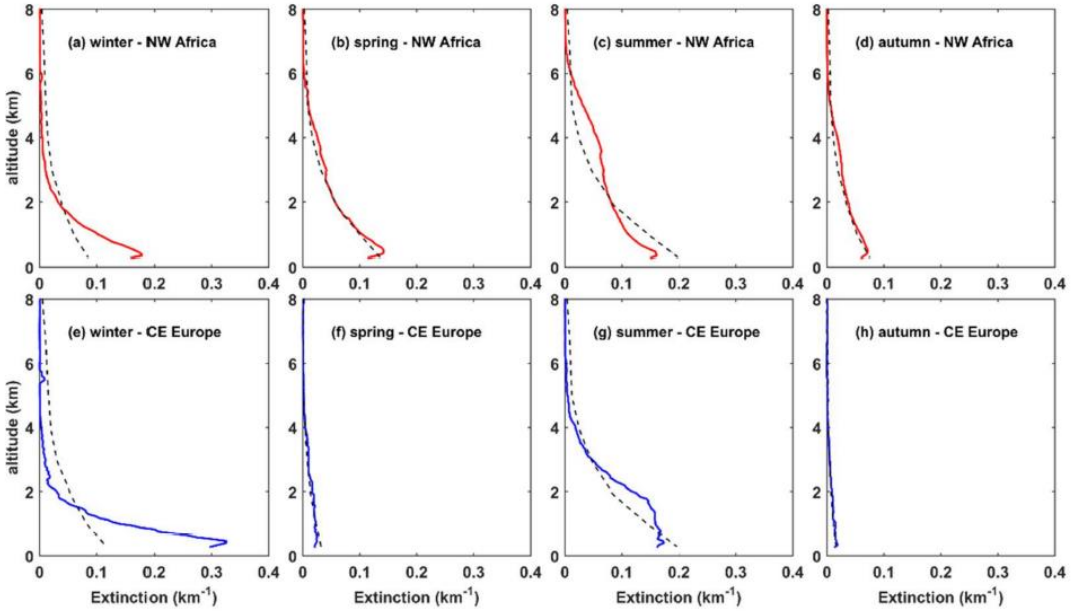

Figure B21 LIVAS (red line for NW Africa, blue line for CE Europe) and libRadtran (black dashed line) default extinction coefficient profiles for AOD at 350 nm. The results are shown for the four seasons of the year.

C. Solar radiation nowcasting and short-term forecasting

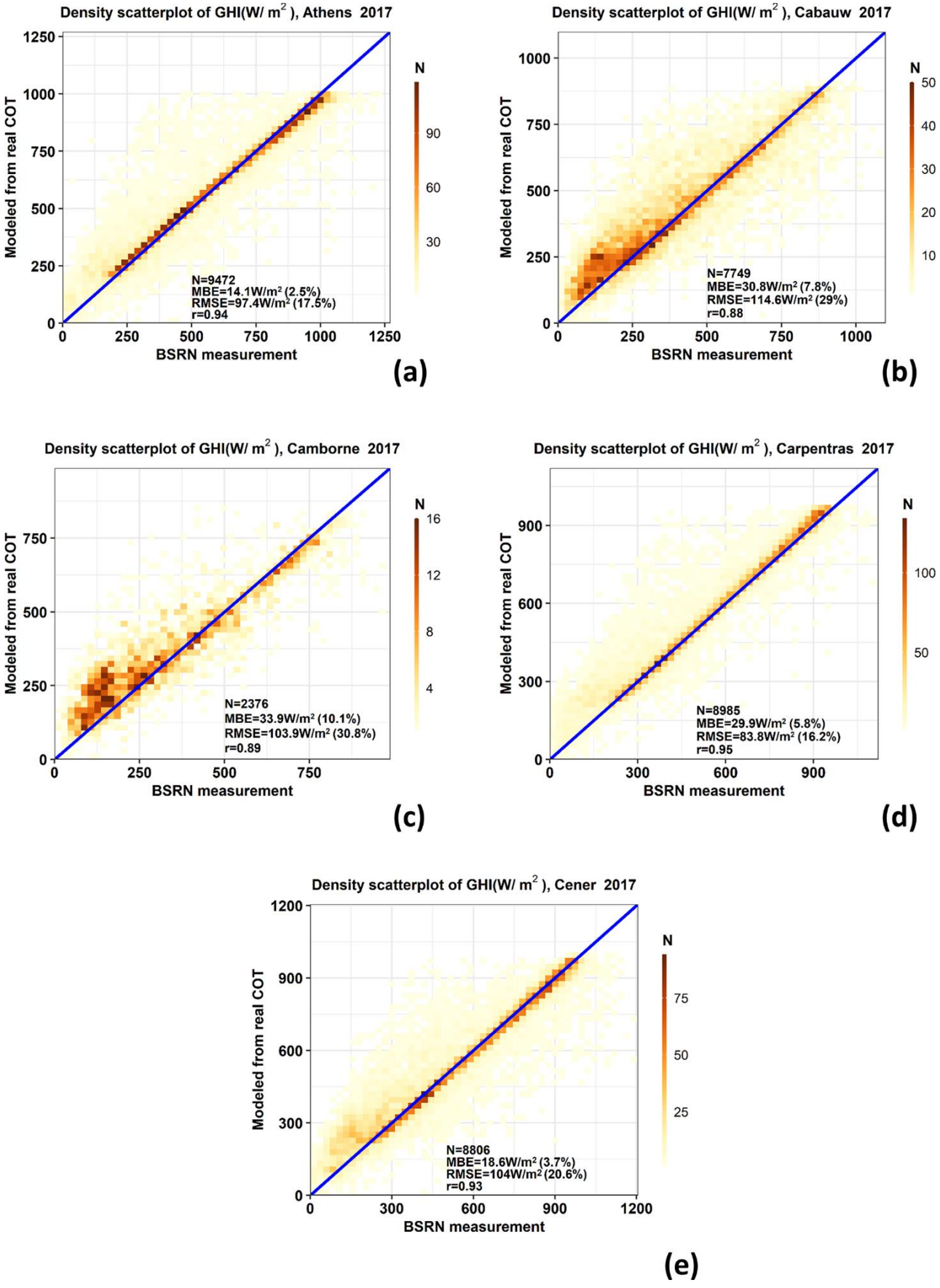

Figure C1 Comparison of the modeled versus measured global horizontal irradiance (GHI) for **(a)** Athens, **(b)** Cabauw, **(c)** Camborne, **(d)** Carpentras, and **(e)** Cener for 2017.

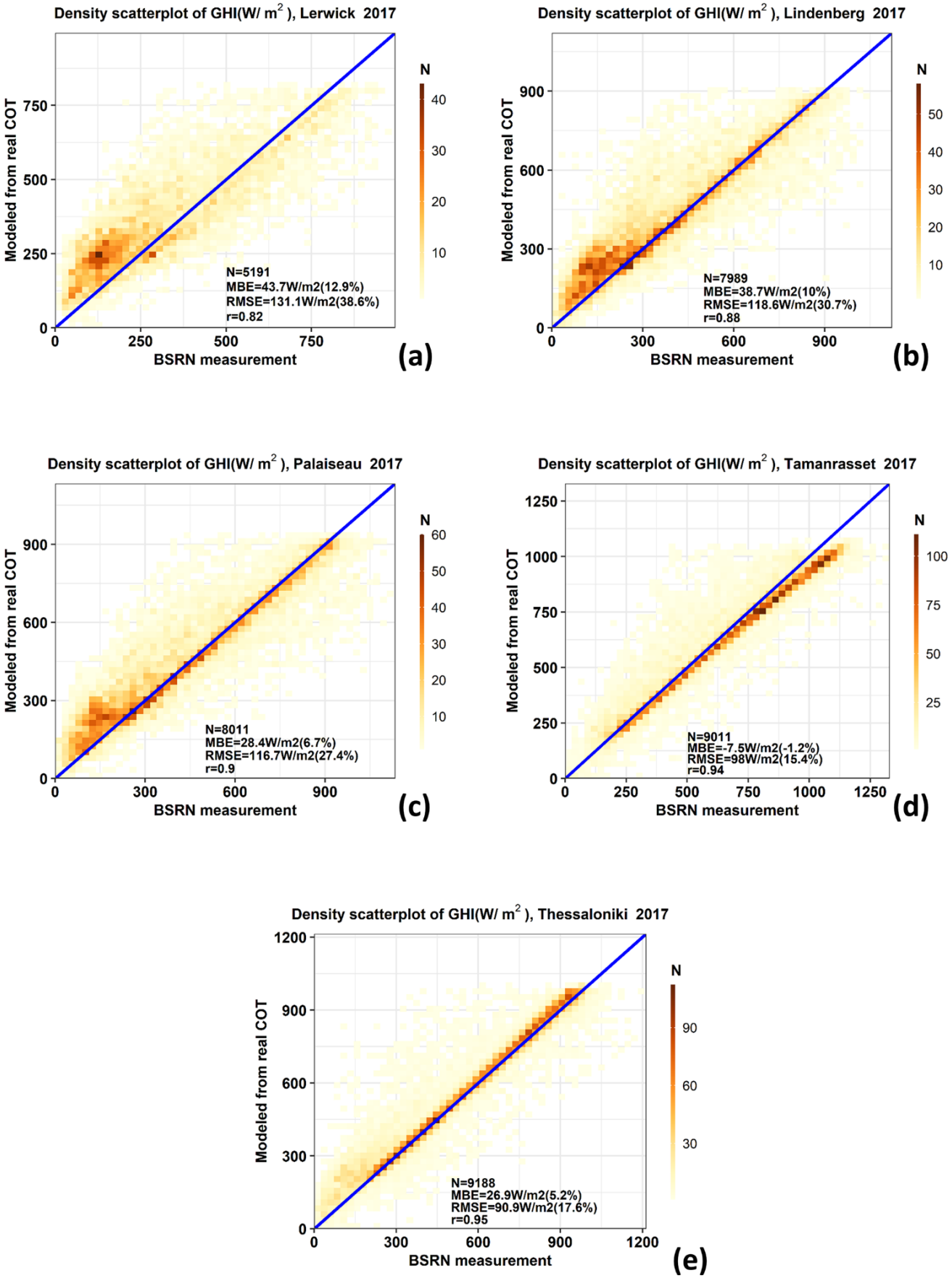

Figure C2 Comparison of the modeled versus measured global horizontal irradiance (GHI) for **(a)** Lerwick, **(b)** Lindenberg, **(c)** Palaiseau, **(d)** Tamanrasset, and **(e)** Thessaloniki for 2017.

To see if the CMF differences (modeled against measured) changed with SZA, the MBE of CMF was calculated for 10° bins of SZA. The measured CMF was considered to be the one derived from GHI measurements (Eq. 6.4) and the modeled one was derived using Eq. (6.2). The results are presented in Fig. C3 for all cases and under different cloudiness conditions, along with the relative values of CMF MBE expressed as percentages. We can again see that most of the overestimation of CMF values by MSG COT occurs for cloudy conditions (CMF < 0.9). Specifically, for partially cloudy conditions (0.4 < CMF <0.9), the MBE reaches values of up to ~ 0.20, and for overcast skies (CMF ≤ 0.4), there are SZA bins (0°) for which the MBE reaches values of up to 0.25. However, the MBE hardly changes with SZA for those two categories.

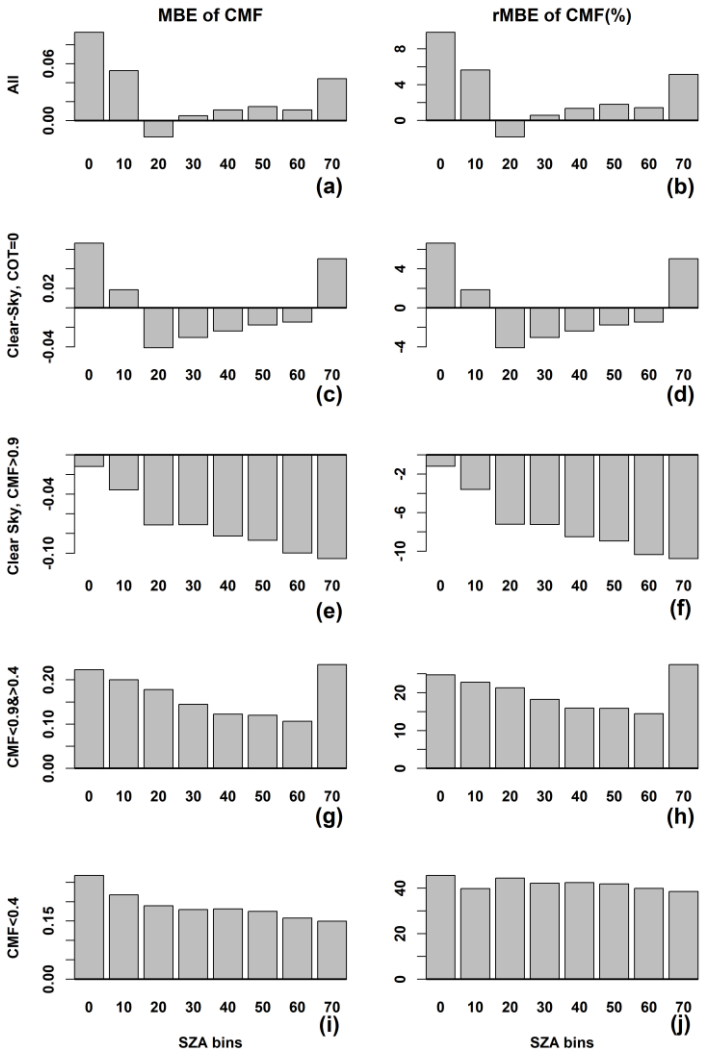

Figure C3 Cloud modification factor (CMF) mean bias error (MBE – left column) and relative MBE (% - right column) as functions of solar zenith angle (SZA) for all cases and different cloudiness conditions.

Table of Figures

List of tables

References

1. Abera, A., Friberg, J., Isaxon, C., Jerrett, M., Malmqvist, E., Sjöström, C., Taj, T., & Vargas, A. M. (2020). Air Quality in Africa: Public Health Implications. *Annual Review of Public Health*, *42*(January), 193–210. https://doi.org/10.1146/annurev-publhealth-100119-113802
2. Alpert, P., Shvainshtein, O., & Kishcha, P. (2012). AOD Trends over Megacities Based on Space Monitoring Using MODIS and MISR. *American Journal of Climate Change*, *01*(03), 117–131. https://doi.org/10.4236/ajcc.2012.13010
3. Amiridis, V., Marinou, E., Tsekeri, A., Wandinger, U., Schwarz, A., Giannakaki, E., Mamouri, R., Kokkalis, P., Binietoglou, I., Solomos, S., Herekakis, T., Kazadzis, S., Gerasopoulos, E., Proestakis, E., Kottas, M., Balis, D., Papayannis, A., Kontoes, C., Kourtidis, K., … Ansmann, A. (2015). LIVAS: A 3-D multi-wavelength aerosol/cloud database based on CALIPSO and EARLINET. *Atmospheric Chemistry and Physics*, *15*(13), 7127–7153. https://doi.org/10.5194/acp-15-7127-2015
4. Anderson, G. P., Clough, S. A., Kneizys, F. X., Chetwynd, J. H., & Shettle, E. P. (1986). *AFGL atmospheric constituent profiles (0.120 km)*. AIR FORCE GEOPHYSICS LAB HANSCOM AFB MA.
5. Ångström, A. (1929). On the atmospheric transmission of sun radiation and on dust in the air. *Geografiska Annaler*, *11*(2), 156–166.
6. Arvizu, D., Balaya, P., Cabeza, L., Hollands, T., Kondo, M., Konseibo, C., Meleshko, V., Stein, W. H., Tamaura, Y., & Xu, H. (2011). *Direct solar energy*.
7. Bais, A. F., Drosoglou, T., Meleti, C., Tourpali, K., & Kouremeti, N. (2013). Changes in surface shortwave solar irradiance from 1993 to 2011 at Thessaloniki (Greece). *International Journal of Climatology*, *33*(13), 2871–2876. https://doi.org/10.1002/joc.3636
8. Basart, S., Langerock, B., Arola, A., Benedictow, A., Bennouna, Y., Bouarar, I., Cuevas, E., Errera, Q., Eskes, H. J., Griesfeller, J., Kapsomenakis, J., Mortier, A., P+ison, I., Pitkänen, M., Ramonet, M., Richter, A., Schoenhardt, A., Schulz, M., Tarniewicz, J., … Zerefos, C. (2023). *Validation report of the CAMS near-real-time global atmospheric composition service: June–August 2022*.
9. Basart, S., Pay, M. T., Jorba, O., Pérez, C., Jiḿnez-Guerrero, P., Schulz, M., & Baldasano, J. M. (2012). Aerosols in the CALIOPE air quality modelling system: Evaluation and analysis of PM levels, optical depths and chemical composition over Europe. *Atmospheric Chemistry and Physics*, *12*(7), 3363–3392. https://doi.org/10.5194/acp-12-3363-2012
10. Bégue, N., Tulet, P., Chaboureau, J. P., Roberts, G., Gomes, L., & Mallet, M. (2012). Long-range transport of Saharan dust over northwestern Europe during EUCAARI 2008 campaign: Evolution of dust optical properties by scavenging. *Journal of Geophysical Research Atmospheres*, *117*(17), D17201. https://doi.org/10.1029/2012JD017611
11. Benedetti, A., Morcrette, J. J., Boucher, O., Dethof, A., Engelen, R. J., Fisher, M., Flentje, H., Huneeus, N., Jones, L., Kaiser, J. W., Kinne, S., Mangold, A., Razinger, M., Simmons, A. J., & Suttie, M. (2009). Aerosol analysis and forecast in the European Centre for Medium-Range Weather Forecasts integrated forecast system: 2. data assimilation. *Journal of Geophysical Research Atmospheres*, *114*(13), D13205. https://doi.org/10.1029/2008JD011115
12. Bennouna, Y., Schulz, M., Christophe, Y., Eskes, H. J., Basart, S., Benedictow, A., Blechschmidt, A. M., Chabrillat, S., Clark, H., Cuevas, E., Flentje, H., Hansen, K. M., Im, U., Kapsomenakis, J., Langerock, B., Petersen, K., Richter, A., Sudarchikova, N., Thouret, V., … Zerefos, C. (2020). Validation report of the CAMS global Reanalysis of aerosols and reactive gases, years 2003–2019. In *Copernicus Atmosphere Monitoring Service (CAMS) report. CAMS84_2018SC2_D5*. https://doi.org/10.24380/2v3p-ab79
13. Bhartia, P. K. (2012). OMI/Aura TOMS-Like Ozone, Aerosol Index, Cloud Radiance Fraction L3 1 day 1 degree x 1 degree V3, NASA Goddard Space Flight Center, Goddard Earth Sciences Data and Information Services Center (GES DISC), 10, [data set], https://doi.org/10.5067/Aura/OMI/DATA3001.
14. Boucher, O., Randall, D., Artaxo, P., Bretherton, C., Feingold, G., Forster, P., Kerminen, V.-M., Kondo, Y., Liao, H., & Lohmann, U. (2013). Clouds and aerosols. In *Climate change 2013: the physical science basis. Contribution of Working Group I to the Fifth Assessment Report of the Intergovernmental Panel on Climate Change* (pp. 571–657). Cambridge University Press.

15. Buchholz, R. R., Worden, H. M., Park, M., Francis, G., Deeter, M. N., Edwards, D. P., Emmons, L. K., Gaubert, B., Gille, J., Martínez-Alonso, S., Tang, W., Kumar, R., Drummond, J. R., Clerbaux, C., George, M., Coheur, P. F., Hurtmans, D., Bowman, K. W., Luo, M., … Kulawik, S. S. (2021). Air pollution trends measured from Terra: CO and AOD over industrial, fire-prone, and background regions. *Remote Sensing of Environment*, *256*. https://doi.org/10.1016/j.rse.2020.112275
16. Buras, R., Dowling, T., & Emde, C. (2011). New secondary-scattering correction in DISORT with increased efficiency for forward scattering. *Journal of Quantitative Spectroscopy and Radiative Transfer*, *112*(12), 2028–2034. https://doi.org/10.1016/j.jqsrt.2011.03.019
17. Burrows, J. P., Platt, U., & Borrell, P. (2011). *The remote sensing of tropospheric composition from space*. Springer Science & Business Media.
18. Cano, D., Monget, J. M., Albuisson, M., Guillard~, H., Regas, N., & Wald, L. (1986). *A METHOD FOR THE DETERMINATION OF THE GLOBAL SOLAR RADIATION FROM METEOROLOGICAL SATELLITE DATA* (Vol. 37, Issue 1).
19. Carpentieri, A., Folini, D., Wild, M., Vuilleumier, L., & Meyer, A. (2023). Satellite-derived solar radiation for intra-hour and intra-day applications: Biases and uncertainties by season and altitude. *Solar Energy*, *255*, 274–284. https://doi.org/10.1016/j.solener.2023.03.027
20. Che, H., Gui, K., Xia, X., Wang, Y., Holben, B. N., Goloub, P., Cuevas-Agulló, E., Wang, H., Zheng, Y., Zhao, H., & Zhang, X. (2019). Large contribution of meteorological factors to inter-decadal changes in regional aerosol optical depth. *Atmospheric Chemistry and Physics*, *19*(16), 10497–10523. https://doi.org/10.5194/acp-19-10497-2019
21. Chen, L. (2021). Uncertainties in solar radiation assessment in the United States using climate models. *Climate Dynamics*, *56*(1), 665–678. https://doi.org/10.1007/s00382-020-05498-7
22. Cherian, R., & Quaas, J. (2020). Trends in AOD, Clouds, and Cloud Radiative Effects in Satellite Data and CMIP5 and CMIP6 Model Simulations Over Aerosol Source Regions. *Geophysical Research Letters*, *47*(9). https://doi.org/10.1029/2020GL087132
23. Crosier, J., Allan, J. D., Coe, H., Bower, K. N., Formenti, P., & Williams, P. I. (2007). Chemical composition of summertime aerosol in the Po Valley (Italy), northern Adriatic and Black Sea. *Quarterly Journal of the Royal Meteorological Society*, *133*(S1), 61–75. https://doi.org/10.1002/qj.88
24. DeMocker, M. J. (2003). Benefits and Costs of the Clean Air Act 1990–2020: Revised Analytical Plan For EPA's Second Prospective Analysis. *Industrial Economics Incorporated, Cambridge, MA*.
25. Derrien, M., & Le Gléau, H. (2005). MSG/SEVIRI cloud mask and type from SAFNWC. *International Journal of Remote Sensing*, *26*(21), 4707–4732. https://doi.org/10.1080/01431160500166128
26. Di Biagio, C., Formenti, P., Balkanski, Y., Caponi, L., Cazaunau, M., Pangui, E., Journet, E., Nowak, S., Andreae, M. O., Kandler, K., Saeed, T., Piketh, S., Seibert, D., Williams, E., & Doussin, J.-F. (2019). Complex refractive indices and single-scattering albedo of global dust aerosols in the shortwave spectrum and relationship to size and iron content. *Atmos. Chem. Phys.*, *19*(24), 15503–15531. https://doi.org/10.5194/acp-19-15503-2019
27. Diémoz, H., Barnaba, F., Magri, T., Pession, G., Dionisi, D., Pittavino, S., Tombolato, I. K. F., Campanelli, M., Ceca, L. S. Della, Hervo, M., Di Liberto, L., Ferrero, L., & Gobbi, G. P. (2019). Transport of Po Valley aerosol pollution to the northwestern Alps-Part 1: Phenomenology. *Atmospheric Chemistry and Physics*, *19*(5), 3065–3095. https://doi.org/10.5194/acp-19-3065-2019
28. Driemel, A., Augustine, J., Behrens, K., Colle, S., Cox, C., Cuevas-Agulló, E., Denn, F. M., Duprat, T., Fukuda, M., Grobe, H., Haeffelin, M., Hodges, G., Hyett, N., Ijima, O., Kallis, A., Knap, W., Kustov, V., Long, C. N., Longenecker, D., … König-Langlo, G. (2018). Baseline Surface Radiation Network (BSRN): Structure and data description (1992-2017). *Earth System Science Data*, *10*(3), 1491–1501. https://doi.org/10.5194/essd-10-1491-2018
29. Dumka, U. C., Kosmopoulos, P. G., Ningombam, S. S., & Masoom, A. (2021). Impact of aerosol and cloud on the solar energy potential over the central gangetic himalayan region. *Remote Sensing*, *13*(16). https://doi.org/10.3390/rs13163248
30. Eck, T. F., Holben, B. N., Reid, J. S., Dubovik, O., Smirnov, A., O'neill, N. T., Slutsker, I., & Kinne, S. (1999). Wavelength dependence of the optical depth of biomass burning, urban, and desert dust aerosols. *Journal of Geophysical Research: Atmospheres*, *104*(D24), 31333–31349.
31. Edenhofer, O., Pichs-Madruga, R., Sokona, Y., Seyboth, K., Matschoss, P., Kadner, S., Zwickel, T., Eickemeier, P., Hansen, G., & Schlömer, S. (2011). IPCC special report on renewable energy sources and

climate change mitigation. *Prepared By Working Group III of the Intergovernmental Panel on Climate Change, Cambridge University Press, Cambridge, UK*.
32. El Alani, O., Hajjaj, C., Ghennioui, H., Ghennioui, A., Blanc, P., Saint-Drenan, Y. M., & El Monady, M. (2023). Performance assessment of SARIMA, MLP and LSTM models for short-term solar irradiance prediction under different climates in Morocco. *International Journal of Ambient Energy*, *44*(1), 334–350. https://doi.org/10.1080/01430750.2022.2127889
33. El-Metwally, M., Alfaro, S. C., Abdel Wahab, M., & Chatenet, B. (2008). Aerosol characteristics over urban Cairo: Seasonal variations as retrieved from Sun photometer measurements. *Journal of Geophysical Research Atmospheres*, *113*(14), D14219. https://doi.org/10.1029/2008JD009834
34. Emde, C., Buras-Schnell, R., Kylling, A., Mayer, B., Gasteiger, J., Hamann, U., Kylling, J., Richter, B., Pause, C., Dowling, T., & Bugliaro, L. (2016). The libRadtran software package for radiative transfer calculations (version 2.0.1). *Geoscientific Model Development*, *9*(5), 1647–1672. https://doi.org/10.5194/gmd-9-1647-2016
35. Engelstaedter, S., Tegen, I., & Washington, R. (2006). North African dust emissions and transport. *Earth-Science Reviews*, *79*(1–2), 73–100. https://doi.org/10.1016/j.earscirev.2006.06.004
36. Eskes, H. J., Basart, S., Benedictow, A., Bennouna, Y., Blechschmidt, A.-M., Chabrillat, S., Cuevas, E., Errera, Q., Flentje, H., Hansen, K. M., Kapsomenakis, J., Langerock, B., Ramonet, M., Richter, A., Schulz, M., Sudarchikova, N., Wagner, A., Warneke, T., & Zerefos, C. (2021). *Observation characterisation and validation methods document*.
37. Farnebäck, G. (2003). Two-Frame Motion Estimation Based on Polynomial Expansion. In *Lecture Notes in Computer Science* (Vol. 2749, Issue 1, pp. 363–370). https://doi.org/10.1007/3-540-45103-X_50
38. Feister, U., & Grewe, R. (1995). SPECTRAL ALBEDO MEASUREMENTS IN THE UV and VISIBLE REGION OVER DIFFERENT TYPES OF SURFACES. *Photochemistry and Photobiology*, *62*(4), 736–744. https://doi.org/10.1111/j.1751-1097.1995.tb08723.x
39. Floutsi, A. A., Korras-Carraca, M. B., Matsoukas, C., Hatzianastassiou, N., & Biskos, G. (2016). Climatology and trends of aerosol optical depth over the Mediterranean basin during the last 12years (2002–2014) based on Collection 006 MODIS-Aqua data. *Science of The Total Environment*, *551–552*, 292–303. https://doi.org/https://doi.org/10.1016/j.scitotenv.2016.01.192
40. Fountoulakis, I., Kosmopoulos, P., Papachristopoulou, K., Raptis, I. P., Mamouri, R. E., Nisantzi, A., Gkikas, A., Witthuhn, J., Bley, S., Moustaka, A., Buehl, J., Seifert, P., Hadjimitsis, D. G., Kontoes, C., & Kazadzis, S. (2021). Effects of aerosols and clouds on the levels of surface solar radiation and solar energy in cyprus. *Remote Sensing*, *13*(12), 1–26. https://doi.org/10.3390/rs13122319
41. Fussell, J. C., & Kelly, F. J. (2021). Mechanisms underlying the health effects of desert sand dust. *Environment International*, *157*, 106790. https://doi.org/https://doi.org/10.1016/j.envint.2021.106790
42. Ganguly, T., Selvaraj, K. L., & Guttikunda, S. K. (2020). National Clean Air Programme (NCAP) for Indian cities: Review and outlook of clean air action plans. *Atmospheric Environment: X*, *8*. https://doi.org/10.1016/j.aeaoa.2020.100096
43. Gao, H., Yang, W., Wang, J., & Zheng, X. (2021). Analysis of the effectiveness of air pollution control policies based on historical evaluation and deep learning forecast: A case study of chengdu-chongqing region in china. *Sustainability (Switzerland)*, *13*(1), 1–28. https://doi.org/10.3390/su13010206
44. Garniwa, P. M. P., Rajagukguk, R. A., Kamil, R., & Lee, H. J. (2023). Intraday forecast of global horizontal irradiance using optical flow method and long short-term memory model. *Solar Energy*, *252*, 234–251. https://doi.org/10.1016/j.solener.2023.01.037
45. Gasteiger, J., Emde, C., Mayer, B., Buras, R., Buehler, S. A., & Lemke, O. (2014). Representative wavelengths absorption parameterization applied to satellite channels and spectral bands. *Journal of Quantitative Spectroscopy and Radiative Transfer*, *148*, 99–115. https://doi.org/10.1016/j.jqsrt.2014.06.024
46. Gelaro, R., McCarty, W., Suárez, M. J., Todling, R., Molod, A., Takacs, L., Randles, C. A., Darmenov, A., Bosilovich, M. G., Reichle, R., Wargan, K., Coy, L., Cullather, R., Draper, C., Akella, S., Buchard, V., Conaty, A., da Silva, A. M., Gu, W., … Zhao, B. (2017). The modern-era retrospective analysis for research and applications, version 2 (MERRA-2). *Journal of Climate*, *30*(14), 5419–5454. https://doi.org/10.1175/JCLI-D-16-0758.1
47. Georgoulias, A. K., Alexandri, G., Kourtidis, K. A., Lelieveld, J., Zanis, P., Pöschl, U., Levy, R., Amiridis, V., Marinou, E., & Tsikerdekis, A. (2016). Spatiotemporal variability and contribution of different aerosol

types to the aerosol optical depth over the Eastern Mediterranean. *Atmospheric Chemistry and Physics*, *16*(21), 13853–13884. https://doi.org/10.5194/acp-16-13853-2016
48. Giles, D. M., Sinyuk, A., Sorokin, M. G., Schafer, J. S., Smirnov, A., Slutsker, I., Eck, T. F., Holben, B. N., Lewis, J. R., Campbell, J. R., Welton, E. J., Korkin, S. V., & Lyapustin, A. I. (2019). Advancements in the Aerosol Robotic Network (AERONET) Version 3 database – automated near-real-time quality control algorithm with improved cloud screening for Sun photometer aerosol optical depth (AOD) measurements. *Atmospheric Measurement Techniques*, *12*(1), 169–209. https://doi.org/10.5194/amt-12-169-2019
49. Ginoux, P., Chin, M., Tegen, I., Prospero, J. M., Holben, B., Dubovik, O., & Lin, S.-J. (2001). Sources and distributions of dust aerosols simulated with the GOCART model. *Journal of Geophysical Research: Atmospheres*, *106*(D17), 20255–20273. https://doi.org/10.1029/2000JD000053
50. Ginoux, P., Prospero, J. M., Gill, T. E., Hsu, N. C., & Zhao, M. (2012). Global-scale attribution of anthropogenic and natural dust sources and their emission rates based on MODIS Deep Blue aerosol products. *Reviews of Geophysics*, *50*(3), RG3005. https://doi.org/10.1029/2012RG000388
51. Gkikas, A., Basart, S., Hatzianastassiou, N., Marinou, E., Amiridis, V., Kazadzis, S., Pey, J., Querol, X., Jorba, O., Gassó, S., & Baldasano, J. M. (2016). Mediterranean intense desert dust outbreaks and their vertical structure based on remote sensing data. *Atmospheric Chemistry and Physics*, *16*(13), 8609–8642. https://doi.org/10.5194/acp-16-8609-2016
52. Gkikas, A., Hatzianastassiou, N., & Mihalopoulos, N. (2009). Aerosol events in the broader Mediterranean basin based on 7-year (2000-2007) MODIS C005 data. *Annales Geophysicae*, *27*(9), 3509–3522. https://doi.org/10.5194/angeo-27-3509-2009
53. Gkikas, A., Hatzianastassiou, N., Mihalopoulos, N., Katsoulis, V., Kazadzis, S., Pey, J., Querol, X., & Torres, O. (2013). The regime of intense desert dust episodes in the Mediterranean based on contemporary satellite observations and ground measurements. *Atmospheric Chemistry and Physics*, *13*(23), 12135–12154. https://doi.org/10.5194/acp-13-12135-2013
54. Gkikas, A., Houssos, E. E., Hatzianastassiou, N., Papadimas, C. D., & Bartzokas, A. (2012). Synoptic conditions favouring the occurrence of aerosol episodes over the broader Mediterranean basin. *Quarterly Journal of the Royal Meteorological Society*, *138*(665), 932–949. https://doi.org/10.1002/qj.978
55. Gkikas, A., Houssos, E. E., Lolis, C. J., Bartzokas, A., Mihalopoulos, N., & Hatzianastassiou, N. (2015). Atmospheric circulation evolution related to desert-dust episodes over the Mediterranean. *Quarterly Journal of the Royal Meteorological Society*, *141*(690), 1634–1645. https://doi.org/10.1002/qj.2466
56. Gkikas, A., Proestakis, E., Amiridis, V., Kazadzis, S., Di Tomaso, E., Marinou, E., Hatzianastassiou, N., Kok, J. F., & García-Pando, C. P. (2022). Quantification of the dust optical depth across spatiotemporal scales with the MIDAS global dataset (2003-2017). *Atmospheric Chemistry and Physics*, *22*(5), 3553–3578. https://doi.org/10.5194/acp-22-3553-2022
57. Gkikas, A., Proestakis, E., Amiridis, V., Kazadzis, S., Di Tomaso, E., Tsekeri, A., Marinou, E., Hatzianastassiou, N., & Pérez Garciá-Pando, C. (2021). ModIs Dust AeroSol (MIDAS): A global fine-resolution dust optical depth data set. *Atmospheric Measurement Techniques*, *14*(1), 309–334. https://doi.org/10.5194/amt-14-309-2021
58. Gkikas, A., Proestakis, E., Amiridis, V., Kazadzis, S., Di Tomaso, E., Tsekeri, A., Proestakis, E., Marinou, E., Hatzianastassiou, N., & Pérez García-Pando, C. (2020). *ModIs Dust AeroSol (MIDAS): A global fine resolution dust optical depth dataset [data set]*. Zenodo. https://doi.org/10.5281/zenodo.4244106
59. *Global Modeling and Assimilation Office (GMAO) (2015), MERRA-2 tavgM_2d_ocn_Nx: 2d,Monthly mean,Time-Averaged,Single-Level,Assimilation,Ocean Surface Diagnostics V5.12.4, Greenbelt, MD, USA, Goddard Earth Sciences Data and Information Services Center (GES DISC), 10.5067/4IASLIDL8EEC*. (n.d.).
60. Goldstein, A. H., Koven, C. D., Heald, C. L., Fung, I. Y., Designed, I. Y. F., & Performed, C. L. H. (2009). Biogenic carbon and anthropogenic pollutants combine to form a cooling haze over the southeastern United States. In *PNAS* (Vol. 106). www.pnas.orgcgidoi10.1073pnas.0904128106
61. Gschwind, B., Wald, L., Blanc, P., Lefèvre, M., Schroedter-Homscheidt, M., & Arola, A. (2019). Improving the McClear model estimating the downwelling solar radiation at ground level in cloud-free conditions - McClear-v3. *Meteorologische Zeitschrift*, *28*(2), 147–163. https://doi.org/10.1127/metz/2019/0946

62. Gueymard, C. A., & Yang, D. (2020). Worldwide validation of CAMS and MERRA-2 reanalysis aerosol optical depth products using 15 years of AERONET observations. *Atmospheric Environment*, *225*(December 2019), 117216. https://doi.org/10.1016/j.atmosenv.2019.117216
63. Gulev, S. K., Thorne, P. W., Ahn, J., Dentener, F. J., Domingues, C. M., Gerland, S., Gong, D., Kaufman, D. S., Nnamchi, H. C., & Quaas, J. et al. (2021). *Changing state of the climate system In Climate Change 2021: The Physical Science Basis. Contribution of Working Group I to the Sixth Assessment Report of the Intergovernmental Panel on Climate Change [Masson-Delmotte, V., P. Zhai, A. Pirani, S.L. C.* https://doi.org/10.1017/9781009157896.004
64. Gupta, G., Venkat Ratnam, M., Madhavan, B. L., & Narayanamurthy, C. S. (2022). Long-term trends in Aerosol Optical Depth obtained across the globe using multi-satellite measurements. *Atmospheric Environment*, *273*(October 2021). https://doi.org/10.1016/j.atmosenv.2022.118953
65. Gupta, P., Levy, R. C., Mattoo, S., Remer, L. A., & Munchak, L. A. (2016). A surface reflectance scheme for retrieving aerosol optical depth over urban surfaces in MODIS Dark Target retrieval algorithm. *Atmospheric Measurement Techniques*, *9*(7), 3293–3308. https://doi.org/10.5194/amt-9-3293-2016
66. Habte, A., Sengupta, M., & Lopez, A. (2017). *Evaluation of the national solar radiation database (NSRDB): 1998-2015*. National Renewable Energy Lab.(NREL), Golden, CO (United States).
67. Hammer, A., Heinemann, D., Hoyer, C., Kuhlemann, R., Lorenz, E., Müller, R., & Beyer, H. G. (2003). Solar energy assessment using remote sensing technologies. *Remote Sensing of Environment*, *86*(3), 423–432. https://doi.org/10.1016/S0034-4257(03)00083-X
68. Hammer, A., Heinemann, D., Lorenz, E., & Lückehe, B. (1999). Short-term forecasting of solar radiation: A statistical approach using satellite data. *Solar Energy*, *67*(1–3), 139–150. https://doi.org/10.1016/s0038-092x(00)00038-4
69. Hatzianastassiou, N., Gkikas, A., Mihalopoulos, N., Torres, O., & Katsoulis, B. D. (2009). Natural versus anthropogenic aerosols in the eastern Mediterranean basin derived from multiyear TOMS and MODIS satellite data. *Journal of Geophysical Research Atmospheres*, *114*(24), D24202. https://doi.org/10.1029/2009JD011982
70. Health Effects Institute. (2020). *State of Global Air 2020. Special Report. Boston, MA:Health Effects Institute.* http://www.stateofglobalair.org/sites/default/files/soga_2019_report.pdf
71. Holben, B. N., Eck, T. F., Slutsker, I., Tanré, D., Buis, J. P., Setzer, A., Vermote, E., Reagan, J. A., Kaufman, Y. J., Nakajima, T., Lavenu, F., Jankowiak, I., & Smirnov, A. (1998). AERONET - A federated instrument network and data archive for aerosol characterization. *Remote Sensing of Environment*, *66*(1), 1–16. https://doi.org/10.1016/S0034-4257(98)00031-5
72. Hou, X., Papachristopoulou, K., Saint-Drenan, Y. M., & Kazadzis, S. (2022). Solar Radiation Nowcasting Using a Markov Chain Multi-Model Approach. *Energies*, *15*(9). https://doi.org/10.3390/en15092996
73. Hsu, N. C., Gautam, R., Sayer, A. M., Bettenhausen, C., Li, C., Jeong, M. J., Tsay, S. C., & Holben, B. N. (2012). Global and regional trends of aerosol optical depth over land and ocean using SeaWiFS measurements from 1997 to 2010. *Atmospheric Chemistry and Physics*, *12*(17), 8037–8053. https://doi.org/10.5194/acp-12-8037-2012
74. Hu, Y. X., & Stamnes, K. (1993). An accurate parameterization of the radiative properties of water clouds suitable for use in climate models. *Journal of Climate*, *6*(4), 728–742.
75. IEA. (2022). *Renewables 2022*. https://www.iea.org/reports/renewables-2022, License: CC BY 4.0
76. Ineichen, P., & Perez, R. (2002). *A NEW AIRMASS INDEPENDENT FORMULATION FOR THE LINKE TURBIDITY COEFFICIENT* (Vol. 73, Issue 3). www.elsevier.com/locate/solener
77. Inman, R. H., Pedro, H. T. C., & Coimbra, C. F. M. (2013). Solar forecasting methods for renewable energy integration. In *Progress in Energy and Combustion Science* (Vol. 39, Issue 6, pp. 535–576). https://doi.org/10.1016/j.pecs.2013.06.002
78. Inness, A., Ades, M., Agustí-Panareda, A., Barr, J., Benedictow, A., Blechschmidt, A. M., Jose Dominguez, J., Engelen, R., Eskes, H., Flemming, J., Huijnen, V., Jones, L., Kipling, Z., Massart, S., Parrington, M., Peuch, V. H., Razinger, M., Remy, S., Schulz, M., & Suttie, M. (2019). The CAMS reanalysis of atmospheric composition. *Atmospheric Chemistry and Physics*, *19*(6), 3515–3556. https://doi.org/10.5194/acp-19-3515-2019
79. International Energy Agency. (2020). *Renewables 2020—Analysis and Forecast to 2025*. IEA Paris, France.

80. IPCC. (2013). *Climate Change 2013: The Physical Science Basis. Contribution of Working Group I to the Fifth Assessment Report of the Intergovernmental Panel on Climate Change* (T. F. Stocker, D. Qin, G.-K. Plattner, M. Tignor, S. K. Allen, J. Boschung, A. Nauels, Y. Xia, V. Bex, & P. M. Midgley, Eds.). Cambridge University Press.
81. IPCC. (2022). Summary for Policymakers, edited by: Pörtner, H.-O., Roberts, D. C., Poloczanska, E. S., Mintenbeck, K., Tignor, M., Alegría, A., Craig, M., Langsdorf, S., Löschke, S., Möller, V.,and Okem, A., in: Climate Change 2022: Impacts, Adaptation and Vulnerability, Contribution of Working Group II to the Sixth Assessment Report of the Intergovernmental Panel on Climate Change, edited by: Pörtner, H.-O., Roberts, D. C., Tignor, M., Poloczanska, E. S., Mintenbeck, K., Alegría, A., Craig, M., Langsdorf, S., Löschke, S., Möller, V., Okem, A., and Rama, B., Cambridge University Press, Cambridge, UK and New York, NY, USA, 3–33, https://doi.org/10.1017/9781009325844.001.
82. Jickells, T. D., An, Z. S., Andersen, K. K., Baker, A. R., Bergametti, G., Brooks, N., Cao, J. J., Boyd, P. W., Duce, R. A., Hunter, K. A., Kawahata, H., Kubilay, N., laRoche, J., Liss, P. S., Mahowald, N., Prospero, J. M., Ridgwell, A. J., Tegen, I., & Torres, R. (2005). Global Iron Connections Between Desert Dust, Ocean Biogeochemistry, and Climate. *Science*, *308*(5718), 67–71. https://doi.org/10.1126/science.1105959
83. Jin, Y., Andersson, H., & Zhang, S. (2016). Air pollution control policies in China: A retrospective and prospects. *International Journal of Environmental Research and Public Health*, *13*(12). https://doi.org/10.3390/ijerph13121219
84. Juliano, T. W., Jiménez, P. A., Kosović, B., Eidhammer, T., Thompson, G., Berg, L. K., Fast, J., Motley, A., & Polidori, A. (2022). Smoke from 2020 United States wildfires responsible for substantial solar energy forecast errors. *Environmental Research Letters*, *17*(3), 34010. https://doi.org/10.1088/1748-9326/ac5143
85. Kallio-Myers, V., Riihelä, A., Lahtinen, P., & Lindfors, A. (2020). Global horizontal irradiance forecast for Finland based on geostationary weather satellite data. *Solar Energy*, *198*, 68–80. https://doi.org/10.1016/j.solener.2020.01.008
86. Kallos, G., Papadopoulos, A., Katsafados, P., & Nickovic, S. (2006). Transatlantic Saharan dust transport: Model simulation and results. *Journal of Geophysical Research: Atmospheres*, *111*(D9). https://doi.org/https://doi.org/10.1029/2005JD006207
87. Kato, S., Ackerman, T. P., Mather, J. H., & Clothiaux, E. E. (1999). The k-distribution method and correlated-k approximation for a shortwave radiative transfer model. In *Journal of Quantitative Spectroscopy & Radiative Transfer* (Vol. 62).
88. Kato, T. (2016). Prediction of photovoltaic power generation output and network operation. In *Integration of Distributed Energy Resources in Power Systems* (pp. 77–108). Elsevier. https://doi.org/10.1016/B978-0-12-803212-1.00004-0
89. Kaufman, Y. J., Tanré, D., & Boucher, O. (2002). A satellite view of aerosols in the climate system. *Nature*, *419*(6903), 215–223. https://doi.org/10.1038/nature01091
90. Kazadzis, S., Bais, A., Balis, D., Kouremeti, N., Zempila, M., Arola, A., Giannakaki, E., Amiridis, V., & Kazantzidis, A. (2009). Spatial and temporal UV irradiance and aerosol variability within the area of an OMI satellite pixel. *Atmos. Chem. Phys.*, *9*(14), 4593–4601. https://doi.org/10.5194/acp-9-4593-2009
91. Kazadzis, S., Founda, D., Psiloglou, B. E., Kambezidis, H., Mihalopoulos, N., Sanchez-Lorenzo, A., Meleti, C., Raptis, P. I., Pierros, F., & Nabat, P. (2018a). Long-term series and trends in surface solar radiation in Athens, Greece. *Atmospheric Chemistry and Physics*, *18*(4), 2395–2411. https://doi.org/10.5194/acp-18-2395-2018
92. Kazadzis, S., Kouremeti, N., Nyeki, S., Gröbner, J., & Wehrli, C. (2018b). The World Optical Depth Research and Calibration Center (WORCC) quality assurance and quality control of GAW-PFR AOD measurements. *Geoscientific Instrumentation, Methods and Data Systems*, *7*(1), 39–53. https://doi.org/10.5194/gi-7-39-2018
93. Kim, M. H., Omar, A. H., Tackett, J. L., Vaughan, M. A., Winker, D. M., Trepte, C. R., Hu, Y., Liu, Z., Poole, L. R., Pitts, M. C., Kar, J., & Magill, B. E. (2018). The CALIPSO version 4 automated aerosol classification and lidar ratio selection algorithm. *Atmospheric Measurement Techniques*, *11*(11), 6107–6135. https://doi.org/10.5194/amt-11-6107-2018
94. Kinne, S. (2019). The MACv2 aerosol climatology. *Tellus, Series B: Chemical and Physical Meteorology*, *71*(1), 1–21. https://doi.org/10.1080/16000889.2019.1623639

95. Kosmopoulos, P. G., Kazadzis, S., El-Askary, H., Taylor, M., Gkikas, A., Proestakis, E., Kontoes, C., & El-Khayat, M. M. (2018b). Earth-observation-based estimation and forecasting of particulate matter impact on solar energy in Egypt. *Remote Sensing*, *10*(12), 1–23. https://doi.org/10.3390/rs10121870
96. Kosmopoulos, P. G., Kazadzis, S., Schmalwieser, A. W., Raptis, P. I., Papachristopoulou, K., Fountoulakis, I., Masoom, A., Bais, A. F., Bilbao, J., Blumthaler, M., Kreuter, A., Siani, A. M., Eleftheratos, K., Topaloglou, C., Gröbner, J., Johnsen, B., Svendby, T. M., Vilaplana, J. M., Doppler, L., … Kontoes, C. (2021). Real-time UV index retrieval in Europe using Earth observation-based techniques: System description and quality assessment. *Atmospheric Measurement Techniques*, *14*(8), 5657–5699. https://doi.org/10.5194/amt-14-5657-2021
97. Kosmopoulos, P. G., Kazadzis, S., Taylor, M., Athanasopoulou, E., Speyer, O., Raptis, P. I., Marinou, E., Proestakis, E., Solomos, S., Gerasopoulos, E., Amiridis, V., Bais, A., & Kontoes, C. (2017). Dust impact on surface solar irradiance assessed with model simulations, satellite observations and ground-based measurements. *Atmospheric Measurement Techniques*, *10*(7), 2435–2453. https://doi.org/10.5194/amt-10-2435-2017
98. Kosmopoulos, P. G., Kazadzis, S., Taylor, M., Raptis, P. I., Keramitsoglou, I., Kiranoudis, C., & Bais, A. F. (2018a). Assessment of surface solar irradiance derived from real-time modelling techniques and verification with ground-based measurements. *Atmospheric Measurement Techniques*, *11*(2), 907–924. https://doi.org/10.5194/amt-11-907-2018
99. Kosmopoulos, P., Kouroutsidis, D., Papachristopoulou, K., Raptis, P. I., Masoom, A., Saint-Drenan, Y. M., Blanc, P., Kontoes, C., & Kazadzis, S. (2020). Short-term forecasting of large-scale clouds impact on downwelling surface solar irradiation. *Energies*, *13*(24). https://doi.org/10.3390/en13246555
100. Kurucz, R. L. (1994). Synthetic Infrared Spectra. *Symposium - International Astronomical Union*, *154*(13), 523–531. https://doi.org/10.1017/S0074180900124805
101. Landi, T. C., Bonasoni, P., Brunetti, M., Campbell, J. R., Marquis, J. W., Di Girolamo, P., & Lolli, S. (2021). Aerosol Direct Radiative Effects under Cloud-Free Conditions over Highly-Polluted Areas in Europe and Mediterranean: A Ten-Years Analysis (2007–2016). In *Remote Sensing* (Vol. 13, Issue 15). https://doi.org/10.3390/rs13152933
102. Lefèvre, M., Oumbe, A., Blanc, P., Espinar, B., Gschwind, B., Qu, Z., Wald, L., Schroedter-Homscheidt, M., Hoyer-Klick, C., Arola, A., Benedetti, A., Kaiser, J. W., & Morcrette, J. J. (2013). McClear: A new model estimating downwelling solar radiation at ground level in clear-sky conditions. *Atmospheric Measurement Techniques*, *6*(9), 2403–2418. https://doi.org/10.5194/amt-6-2403-2013
103. Lelieveld, J., Berresheim, H., Borrmann, S., Crutzen, P. J., Dentener, F. J., Fischer, H., Feichter, J., Flatau, P. J., Heland, J., Holzinger, R., Korrmann, R., Lawrence, M. G., Levin, Z., Markowicz, K. M., Mihalopoulos, N., Minikin, A., Ramanathan, V., De Reus, M., Roelofs, G. J., … Ziereis, H. (2002). Global air pollution crossroads over the Mediterranean. *Science*, *298*(5594), 794–799. https://doi.org/10.1126/science.1075457
104. Levy, R. C., Mattoo, S., Munchak, L. A., Remer, L. A., Sayer, A. M., Patadia, F., & Hsu, N. C. (2013). The Collection 6 MODIS aerosol products over land and ocean. *Atmospheric Measurement Techniques*, *6*(11), 2989–3034. https://doi.org/10.5194/amt-6-2989-2013
105. Liou, K.-N. (2002). *An introduction to atmospheric radiation* (Vol. 84). Elsevier.
106. Loeb, N. G., Su, W., Bellouin, N., & Ming, Y. (2021). Changes in Clear-Sky Shortwave Aerosol Direct Radiative Effects Since 2002. *Journal of Geophysical Research: Atmospheres*, *126*(5), e2020JD034090. https://doi.org/https://doi.org/10.1029/2020JD034090
107. Logothetis, S. A., Salamalikis, V., Gkikas, A., Kazadzis, S., Amiridis, V., & Kazantzidis, A. (2021). 15-Year Variability of Desert Dust Optical Depth on Global and Regional Scales. *Atmospheric Chemistry and Physics*, *21*(21), 16499–16529. https://doi.org/10.5194/acp-21-16499-2021
108. Lohmann, U., & Feichter, J. (2005). Global indirect aerosol effects: A review. *Atmospheric Chemistry and Physics*, *5*(3), 715–737. https://doi.org/10.5194/acp-5-715-2005
109. Long, C. N., & Dutton, E. G. (2010). *BSRN Global Network recommended QC tests, V2. x*.
110. Lorenz, E., Hammer, A., & Heienmann, D. (2004). Short term forecasting of solar radiation based on cloud motion vectors from satellite images. *EUROSUN2004 (ISES Europe Solar Congress)*, *June*, 841–848. https://www.osti.gov/etdeweb/biblio/20637868

111. Lorenz, E., Kühnert, J., & Heinemann, D. (2012). Short term forecasting of solar irradiance by combining satellite data and numerical weather predictions. *Proceedings of the 27th European PV Solar Energy Conference (EU PVSEC), Frankfurt, Germany, 2428*, 44014405.
112. Marie-Joseph, I., Linguet, L., Gobinddass, M. L., & Wald, L. (2013). On the applicability of the Heliosat-2 method to assess surface solar irradiance in the Intertropical Convergence Zone, French Guiana. *International Journal of Remote Sensing*, *34*(8), 3012–3027. https://doi.org/10.1080/01431161.2012.756598
113. Mayer, B. (2009). Radiative transfer in the cloudy atmosphere. *EPJ Web of Conferences*, *1*, 75–99. https://doi.org/10.1140/epjconf/e2009-00912-1
114. Mayer, B., & Kylling, A. (2005). Technical note: The libRadtran software package for radiative transfer calculations - description and examples of use. *Atmos. Chem. Phys.*, *5*(7), 1855–1877. https://doi.org/10.5194/acp-5-1855-2005
115. Meteo France. (2016). *Algorithm Theoretical Basis Document for the Cloud Product Processors of the NWC/GEO (GEO-CMA-v4.0, GEO-CT-v3.0, GEO-CTTH-v3.0, GEO-CMIC-v1.0), Techni30 cal Report NWC/CDOP2/GEO/MFL/SCI/ATBD/Cloud*.
116. Morcrette, J. J., Boucher, O., Jones, L., Salmond, D., Bechtold, P., Beljaars, A., Benedetti, A., Bonet, A., Kaiser, J. W., Razinger, M., Schulz, M., Serrar, S., Simmons, A. J., Sofiev, M., Suttie, M., Tompkins, A. M., & Untch, A. (2009). Aerosol analysis and forecast in the european centre for medium-range weather forecasts integrated forecast system: Forward modeling. *Journal of Geophysical Research Atmospheres*, *114*(6), D06206. https://doi.org/10.1029/2008JD011235
117. Moulin, C., Lambert, C. E., Dayan, U., Masson, V., Ramonet, M., Bousquet, P., Legrand, M., Balkanski, Y. J., Guelle, W., Marticorena, B., Bergametti, G., & Dulac, F. (1998). Satellite climatology of African dust transport in the Mediterranean atmosphere. *Journal of Geophysical Research Atmospheres*, *103*(D11), 13137–13144. https://doi.org/10.1029/98JD00171
118. Mueller, R., Behrendt, T., Hammer, A., & Kemper, A. (2012). A new algorithm for the satellite-based retrieval of solar surface irradiance in spectral bands. *Remote Sensing*, *4*(3), 622–647. https://doi.org/10.3390/rs4030622
119. Mueller, R. W., Matsoukas, C., Gratzki, A., Behr, H. D., & Hollmann, R. (2009). The CM-SAF operational scheme for the satellite based retrieval of solar surface irradiance - A LUT based eigenvector hybrid approach. *Remote Sensing of Environment*, *113*(5), 1012–1024. https://doi.org/10.1016/j.rse.2009.01.012
120. Müller, R., & Pfeifroth, U. (2022). Remote sensing of solar surface radiation-a reflection of concepts, applications and input data based on experience with the effective cloud albedo. In *Atmospheric Measurement Techniques* (Vol. 15, Issue 5, pp. 1537–1561). Copernicus GmbH. https://doi.org/10.5194/amt-15-1537-2022
121. Müller, R., Pfeifroth, U., Träger-Chatterjee, C., Trentmann, J., & Cremer, R. (2015). Digging the METEOSAT treasure-3 decades of solar surface radiation. *Remote Sensing*, *7*(6), 8067–8101. https://doi.org/10.3390/rs70608067
122. Nabat, P., Somot, S., Mallet, M., Chiapello, I., Morcrette, J. J., Solmon, F., Szopa, S., Dulac, F., Collins, W., Ghan, S., Horowitz, L. W., Lamarque, J. F., Lee, Y. H., Naik, V., Nagashima, T., Shindell, D., & Skeie, R. (2013). A 4-D climatology (1979-2009) of the monthly tropospheric aerosol optical depth distribution over the Mediterranean region from a comparative evaluation and blending of remote sensing and model products. *Atmospheric Measurement Techniques*, *6*(5), 1287–1314. https://doi.org/10.5194/amt-6-1287-2013
123. Nakajima, T., Campanelli, M., Che, H., Estellés, V., Irie, H., Kim, S.-W., Kim, J., Liu, D., Nishizawa, T., Pandithurai, G., Soni, V. K., Thana, B., Tugjsurn, N.-U., Aoki, K., Hashimoto, M., Higurashi, A., Kazadzis, S., Khatri, P., Kouremeti, N., … Uchiyama, A. (2020). An overview and issues of the sky radiometer technology and SKYNET. *Atmospheric Measurement Techniques Discussions*, *March*, 1–36. https://doi.org/10.5194/amt-2020-72
124. Nastos, P. T. (2012). Meteorological patterns associated with intense saharan dust outbreaks over greece in winter. *Advances in Meteorology*, *2012*, 12–14. https://doi.org/10.1155/2012/828301
125. Nastos, P. T., Kambeyidis, H. D., & Demetriou, D. (2013). Solar dimming/brightening within the Mediterranean. *Solar Dimming/Brightening within the Mediterranean. In Proceedings of the 13th*

International Conference on Environmental Science and Technology, Athens, Greece, 5–7 September 2013; Global NEST: Athens, Greece, 2013. ISBN 978-960-7475-51-0.
126. Neher, I., Buchmann, T., Crewell, S., Pospichal, B., & Meilinger, S. (2019). Impact of atmospheric aerosols on solar power. *Meteorologische Zeitschrift*, *28*(4), 305–321. https://doi.org/10.1127/metz/2019/0969
127. Obregón, M. A., Costa, M. J., Silva, A. M., & Serrano, A. (2020). Spatial and temporal variation of aerosol and water vapour effects on solar radiation in the mediterranean basin during the last two decades. *Remote Sensing*, *12*(8). https://doi.org/10.3390/RS12081316
128. Otto, S., Bierwirth, E., Weinzierl, B., Kandler, K., Esselborn, M., Tesche, M., Schladitz, A., Wendisch, M., & Trautmann, T. (2009). Solar radiative effects of a Saharan dust plume observed during SAMUM assuming spheroidal model particles. *Tellus B: Chemical and Physical Meteorology*, *61*(1), 270–296. https://doi.org/10.1111/j.1600-0889.2008.00389.x
129. Oumbe, A. (2009). *Exploitation des nouvelles capacités d'observation de la terre pour évaluer le rayonnement solaire incident au sol (Assessment of solar surface radiation using new earth observation capabilities)* [PhD thesis]. MINES ParisTech.
130. Oumbe, A., Qu, Z., Blanc, P., Lefèvre, M., Wald, L., & Cros, S. (2014). Decoupling the effects of clear atmosphere and clouds to simplify calculations of the broadband solar irradiance at ground level. *Geoscientific Model Development*, *7*(4), 1661–1669. https://doi.org/10.5194/gmd-7-1661-2014
131. Papadimas, C. D., Hatzianastassiou, N., Matsoukas, C., Kanakidou, M., Mihalopoulos, N., & Vardavas, I. (2012). The direct effect of aerosols on solar radiation over the broader Mediterranean basin. *Atmospheric Chemistry and Physics*, *12*(15), 7165–7185. https://doi.org/10.5194/acp-12-7165-2012
132. Papadimas, C. D., Hatzianastassiou, N., Mihalopoulos, N., Querol, X., & Vardavas, I. (2008). Spatial and temporal variability in aerosol properties over the Mediterranean basin based on 6-year (2000-2006) MODIS data. *Journal of Geophysical Research Atmospheres*, *113*(11), D11205. https://doi.org/10.1029/2007JD009189
133. Papayannis, A., Amiridis, V., Mona, L., Tsaknakis, G., Balis, D., Bösenberg, J., Chaikovski, A., De Tomasi, F., Grigorov, I., Mattis, I., Mitev, V., Müller, D., Nickovic, S., Pérez, C., Pietruczuk, A., Pisani, G., Ravetta, F., Rizi, V., Sicard, M., … Pappalardo, G. (2008). Systematic lidar observations of Saharan dust over Europe in the frame of EARLINET (2000-2002). *Journal of Geophysical Research Atmospheres*, *113*(10), D10204. https://doi.org/10.1029/2007JD009028
134. Pelland, S., Remund, J., Kleissl, J., Oozeki, T., & De Brabandere, K. (2013). Photovoltaic and Solar Forecasting : State of the Art. *IEA PVPS Task 14, Subtask 3.1. Report Iea-PVPS T14–01: 2013; International Energy Agency: Paris, France*.
135. Petržala, J. (2022). Assessment of Influence of Urban Aerosol Vertical Profile on Clear- Sky Diffuse Radiance Pattern. *Journal of Solar Energy Engineering, Transactions of the ASME*, *144*(2). https://doi.org/10.1115/1.4053259
136. Pfeifroth, U., Kothe, S., Drücke, J., Trentmann, J., Schröder, M., Selbach, N., & Hollmann, R. (2023a). *Surface Radiation Data Set - Heliosat (SARAH) - Edition 3*. Satellite Application Facility on Climate Monitoring (CM SAF) [data set]. https://doi.org/10.5676/EUM_SAF_CM/SARAH/V003
137. Pfeifroth, U., Kothe, S., Müller, R., Trentmann, J., Hollmann, R., Fuchs, P., & Werscheck, M. (2019). Surface radiation data set–heliosat (sarah)–edition 2, satellite application facility on climate monitoring. *CM-SAF*.
138. Pfeifroth, U., Sanchez-Lorenzo, A., Manara, V., Trentmann, J., & Hollmann, R. (2018). Trends and Variability of Surface Solar Radiation in Europe Based On Surface- and Satellite-Based Data Records. *Journal of Geophysical Research: Atmospheres*, *123*(3), 1735–1754. https://doi.org/10.1002/2017JD027418
139. Pfeifroth, U., & Trentmann, J. (2023). *Algorithm Theoretical Baseline Document: Meteosat Solar Surface Radiation and effective Cloud Albedo Climate Data Records – Heliosat SARAH-3 The 70 MAGICSOL method applied for the generation of SARAH- 3*. https://www.cmsaf.eu/SharedDocs/Literatur/document/2023/saf_cm_dwd_atbd_sarah_3_5_pdf.pdf?__blob=publicationFile
140. Pfeifroth U., Trentmann J., & Drücke J. (2023b). *Validation Report Meteosat Solar Surface Radiation and Effective Cloud Albedo Climate Data Records SARAH-3*. https://doi.org/https://doi.org/10.5676/EUM_SAF_CM/SARAH/V003

141. Posselt, R., Mueller, R. W., Stöckli, R., & Trentmann, J. (2012). Remote sensing of solar surface radiation for climate monitoring - the CM-SAF retrieval in international comparison. *Remote Sensing of Environment*, *118*, 186–198. https://doi.org/10.1016/j.rse.2011.11.016
142. Proestakis, E., Amiridis, V., Marinou, E., Georgoulias, A. K., Solomos, S., Kazadzis, S., Chimot, J., Che, H., Alexandri, G., Binietoglou, I., Daskalopoulou, V., Kourtidis, K. A., De Leeuw, G., & Van Der A, R. J. (2018). Nine-year spatial and temporal evolution of desert dust aerosols over South and East Asia as revealed by CALIOP. *Atmospheric Chemistry and Physics*, *18*(2), 1337–1362. https://doi.org/10.5194/acp-18-1337-2018
143. Prospero, J. M. (1996). *Saharan Dust Transport Over the North Atlantic Ocean and Mediterranean: An Overview BT - The Impact of Desert Dust Across the Mediterranean* (S. Guerzoni & R. Chester, Eds.; pp. 133–151). Springer Netherlands. https://doi.org/10.1007/978-94-017-3354-0_13
144. Prospero, J. M., Ginoux, P., Torres, O., Nicholson, S. E., & Gill, T. E. (2002). Environmental characterization of global sources of atmospheric soil dust identified with the Nimbus 7 Total Ozone Mapping Spectrometer (TOMS) absorbing aerosol product. *Reviews of Geophysics*, *40*(1), 2-1-2–31. https://doi.org/10.1029/2000RG000095
145. Qu, Z., Gschwind, B., Lefevre, M., & Wald, L. (2014). Improving HelioClim-3 estimates of surface solar irradiance using the McClear clear-sky model and recent advances in atmosphere composition. *Atmospheric Measurement Techniques*, *7*(11), 3927–3933. https://doi.org/10.5194/amt-7-3927-2014
146. Qu, Z., Oumbe, A., Blanc, P., Espinar, B., Gesell, G., Gschwind, B., Klüser, L., Lefèvre, M., Saboret, L., Schroedter-Homscheidt, M., & Wald, L. (2017). Fast radiative transfer parameterisation for assessing the surface solar irradiance: The Heliosat-4 method. *Meteorologische Zeitschrift*, *26*(1), 33–57. https://doi.org/10.1127/metz/2016/0781
147. Querol, X., Tobías, A., Pérez, N., Karanasiou, A., Amato, F., Stafoggia, M., Pérez García-Pando, C., Ginoux, P., Forastiere, F., Gumy, S., Mudu, P., & Alastuey, A. (2019). Monitoring the impact of desert dust outbreaks for air quality for health studies. *Environment International*, *130*, 104867. https://doi.org/https://doi.org/10.1016/j.envint.2019.05.061
148. Randles, C. A., da Silva, A. M., Buchard, V., Colarco, P. R., Darmenov, A., Govindaraju, R., Smirnov, A., Holben, B., Ferrare, R., Hair, J., Shinozuka, Y., & Flynn, C. J. (2017). The MERRA-2 aerosol reanalysis, 1980 onward. Part I: System description and data assimilation evaluation. *Journal of Climate*, *30*(17), 6823–6850. https://doi.org/10.1175/JCLI-D-16-0609.1
149. Raptis, I. P., Kazadzis, S., Amiridis, V., Gkikas, A., Gerasopoulos, E., & Mihalopoulos, N. (2020). A decade of aerosol optical properties measurements over athens, Greece. *Atmosphere*, *11*(2), 1–21. https://doi.org/10.3390/atmos11020154
150. Rigollier, C., Lefèvre, M., & Wald, L. (2004). The method Heliosat-2 for deriving shortwave solar radiation from satellite images. *Solar Energy*, *77*(2), 159–169.
151. Samset, B. H., Lund, M. T., Bollasina, M., Myhre, G., & Wilcox, L. (2019). Emerging Asian aerosol patterns. *Nature Geoscience*, *12*(8), 582–584. https://doi.org/10.1038/s41561-019-0424-5
152. Sayer, A. M., Govaerts, Y., Kolmonen, P., Lipponen, A., Luffarelli, M., Mielonen, T., Patadia, F., Popp, T., Povey, A. C., Stebel, K., & Witek, M. L. (2020). A review and framework for the evaluation of pixel-level uncertainty estimates in satellite aerosol remote sensing. *Atmos. Meas. Tech.*, *13*(2), 373–404. https://doi.org/10.5194/amt-13-373-2020
153. Sayer, A. M., Hsu, N. C., Bettenhausen, C., & Jeong, M.-J. (2013). Validation and uncertainty estimates for MODIS Collection 6 "Deep Blue" aerosol data. *Journal of Geophysical Research: Atmospheres*, *118*(14), 7864–7872. https://doi.org/https://doi.org/10.1002/jgrd.50600
154. Sayer, A. M., & Knobelspiesse, K. D. (2019). How should we aggregate data? Methods accounting for the numerical distributions, with an assessment of aerosol optical depth. *Atmospheric Chemistry and Physics*, *19*(23), 15023–15048. https://doi.org/10.5194/acp-19-15023-2019
155. Sayer, A. M., Munchak, L. A., Hsu, N. C., Levy, R. C., Bettenhausen, C., & Jeong, M. J. (2014). Modis collection 6 aerosol products: Comparison between aqua's e-deep blue, dark target, and "merged" data sets, and usage recommendations. *Journal of Geophysical Research*, *119*(22), 13,965-13,989. https://doi.org/10.1002/2014JD022453
156. Schenzinger, V., Kreuter, A., Klotz, B., Schwarzmann, M., & Gröbner, J. (2023). *On the production and validation of satellite based UV index maps*. Atmos. Meas. Tech. Discuss. [preprint], https://doi.org/10.5194/amt-2023-188

157. Schroedter-Homscheidt, M., Azam, F., Betcke, J., Hanrieder, N., Lefèvre, M., Saboret, L., & Saint-Drenan, Y. M. (2022). Surface solar irradiation retrieval from MSG/SEVIRI based on APOLLO Next Generation and HELIOSAT-4 methods. *Meteorologische Zeitschrift*, *31*(6), 455–476. https://doi.org/10.1127/metz/2022/1132
158. Seinfeld, J. H., & Pandis, S. N. (2006). Atmospheric Chemistry and Physics, A Wiley-Inter Science Publication. In *John Wiley & Sons Inc*.
159. Sengupta, M., Habte, A., Wilbert, S., Gueymard, C., & Remund, J. (2021). *Best practices handbook for the collection and use of solar resource data for solar energy applications*. National Renewable Energy Lab.(NREL), Golden, CO (United States).
160. Sengupta, M., Xie, Y., Lopez, A., Habte, A., Maclaurin, G., & Shelby, J. (2018). The National Solar Radiation Data Base (NSRDB). In *Renewable and Sustainable Energy Reviews* (Vol. 89, pp. 51–60). Elsevier Ltd. https://doi.org/10.1016/j.rser.2018.03.003
161. Shettle, E. P. (1989). Models of aerosols, clouds and precipitation for atmospheric propagation studies, paper presented at Conference on Atmospheric Propagation in the UV, Visible, IR and MM-Region and Related System Aspects, NATO Adv. Group for Aerosp. *Res. and Dev., Copenhagen*.
162. Shin, S.-K., Tesche, M., Noh, Y., & Müller, D. (2019). Aerosol-type classification based on AERONET version 3 inversion products. *Atmos. Meas. Tech.*, *12*(7), 3789–3803. https://doi.org/10.5194/amt-12-3789-2019
163. Sicard, M., Bertolín, S., Mallet, M., Dubuisson, P., & Comerón, A. (2014). Estimation of mineral dust long-wave radiative forcing: sensitivity study to particle properties and application to real cases in the region of Barcelona. *Atmos. Chem. Phys.*, *14*(17), 9213–9231. https://doi.org/10.5194/acp-14-9213-2014
164. Smirnov, A., Holben, B. N., Eck, T. F., Slutsker, I., Chatenet, B., & Pinker, R. T. (2002). Diurnal variability of aerosol optical depth observed at AERONET (Aerosol Robotic Network) sites. *Geophysical Research Letters*, *29*(23), 28–31. https://doi.org/10.1029/2002GL016305
165. Sogacheva, L., Rodriguez, E., Kolmonen, P., Virtanen, T. H., Saponaro, G., De Leeuw, G., Georgoulias, A. K., Alexandri, G., Kourtidis, K., & Van Der, R. J. A. (2018). Spatial and seasonal variations of aerosols over China from two decades of multi-satellite observations - Part 2: AOD time series for 1995-2017 combined from ATSR ADV and MODIS C6.1 and AOD tendency estimations. *Atmospheric Chemistry and Physics*, *18*(22), 16631–16652. https://doi.org/10.5194/acp-18-16631-2018
166. Soleimani, Z., Teymouri, P., Darvishi Boloorani, A., Mesdaghinia, A., Middleton, N., & Griffin, D. W. (2020). An overview of bioaerosol load and health impacts associated with dust storms: A focus on the Middle East. *Atmospheric Environment*, *223*, 117187. https://doi.org/https://doi.org/10.1016/j.atmosenv.2019.117187
167. Tackett, J. L., Winker, D. M., Getzewich, B. J., Vaughan, M. A., Young, S. A., & Kar, J. (2018). CALIPSO lidar level 3 aerosol profile product: Version 3 algorithm design. *Atmospheric Measurement Techniques*, *11*(7), 4129–4152. https://doi.org/10.5194/amt-11-4129-2018
168. Taylor, M., Kazadzis, S., Amiridis, V., & Kahn, R. A. (2015). Global aerosol mixtures and their multiyear and seasonal characteristics. *Atmospheric Environment*, *116*, 112–129. https://doi.org/https://doi.org/10.1016/j.atmosenv.2015.06.029
169. Taylor, M., Kosmopoulos, P. G., Kazadzis, S., Keramitsoglou, I., & Kiranoudis, C. T. (2016). Neural network radiative transfer solvers for the generation of high resolution solar irradiance spectra parameterized by cloud and aerosol parameters. *Journal of Quantitative Spectroscopy and Radiative Transfer*, *168*, 176–192. https://doi.org/10.1016/j.jqsrt.2015.08.018
170. Tegen, I., & Schepanski, K. (2009). The global distribution of mineral dust. *IOP Conference Series: Earth and Environmental Science*, *7*, 012001. https://doi.org/10.1088/1755-1307/7/1/012001
171. Textor, C., Schulz, M., Guibert, S., Kinne, S., Balkanski, Y., Bauer, S., Berntsen, T., Berglen, T., Boucher, O., Chin, M., Dentener, F., Diehl, T., Easter, R., Feichter, H., Fillmore, D., Ghan, S., Ginoux, P., Gong, S., Grini, A., … Tie, X. (2006). Analysis and quantification of the diversities of aerosol life cycles within AeroCom. *Atmospheric Chemistry and Physics*, *6*(7), 1777–1813. https://doi.org/10.5194/acp-6-1777-2006
172. Thomas, C., Wey, E., Blanc, P., Wald, L., & Lefèvre, M. (2016). Validation of HelioClim-3 version 4, HelioClim-3 version 5 and MACC-RAD using 14 BSRN stations. *Energy Procedia*, *91*, 1059–1069. https://doi.org/10.1016/j.egypro.2016.06.275ï

173. Tijhuis, M., van Stratum, B. J. H., Veerman, M. A., & van Heerwaarden, C. C. (2023). An Efficient Parameterization for Surface Shortwave 3D Radiative Effects in Large-Eddy Simulations of Shallow Cumulus Clouds. *Journal of Advances in Modeling Earth Systems*, *15*(1). https://doi.org/10.1029/2022MS003262
174. Tilstra, L. G., Tuinder, O. N. E., Wang, P., & Stammes, P. (2017). Surface reflectivity climatologies from UV to NIR determined fromEarth observations by GOME-2 and SCIAMACHY. *Journal of Geophysical Research*, *122*(7), 4084–4111. https://doi.org/10.1002/2016JD025940
175. Tilstra, L. G., Tuinder, O. N. E., Wang, P., & Stammes, P. (2021). Directionally dependent Lambertian-equivalent reflectivity (DLER) of the Earth's surface measured by the GOME-2 satellite instruments. *Atmospheric Measurement Techniques*, *14*(6), 4219–4238. https://doi.org/10.5194/amt-14-4219-2021
176. Turnock, S. T., Butt, E. W., Richardson, T. B., Mann, G. W., Reddington, C. L., Forster, P. M., Haywood, J., Crippa, M., Janssens-Maenhout, G., Johnson, C. E., Bellouin, N., Carslaw, K. S., & Spracklen, D. V. (2016). The impact of European legislative and technology measures to reduce air pollutants on air quality, human health and climate. *Environmental Research Letters*, *11*(2). https://doi.org/10.1088/1748-9326/11/2/024010
177. United Nations, Department of Economic and Social Affairs, P. D. (2018a). The World 's Cities in 2018 - Data Booklet. In *(ST/ESA/ SER.A/417)*.
178. United Nations, Department of Economic and Social Affairs, P. D. (2018b). *World Urbanization Prospects: The 2018 Revision, Online Edition.* https://population.un.org/wup/Download/
179. United Nations, Department of Economic and Social Affairs, P. D. (2019a). World Urbanization Prospects 2018: Highlights. In *(ST/ESA/SER.A/421)*. https://population.un.org/wup/
180. United Nations, Department of Economic and Social Affairs, P. D. (2019b). World Urbanization Prospects 2018: The 2018 Revision. In *(ST/ESA/SER.A/420)*. https://population.un.org/wup/Publications/Files/WUP2018-Report.pdf
181. United Nations Environment Programme. (2016). *Integrated assessment of short-lived climate pollutants in Latin America and the Caribbean: Summary for decision makers*. United Nations Environment Programme. https://wedocs.unep.org/20.500.11822/8972
182. Urbich, I., Bendix, J., & Müller, R. (2018). A novel approach for the short-term forecast of the effective cloud albedo. *Remote Sensing*, *10*(6), 1–16. https://doi.org/10.3390/rs10060955
183. Urbich, I., Bendix, J., & Müller, R. (2019). The seamless solar radiation (SESORA) forecast for solar surface irradiance-method and validation. *Remote Sensing*, *11*(21), 1–23. https://doi.org/10.3390/rs11212576
184. Urraca, R., Gracia-Amillo, A. M., Koubli, E., Huld, T., Trentmann, J., Riihelä, A., Lindfors, A. V., Palmer, D., Gottschalg, R., & Antonanzas-Torres, F. (2017). Extensive validation of CM SAF surface radiation products over Europe. *Remote Sensing of Environment*, *199*, 171–186. https://doi.org/10.1016/j.rse.2017.07.013
185. Varga, G., Dagsson-Waldhauserová, P., Gresina, F., & Helgadottir, A. (2021). Saharan dust and giant quartz particle transport towards Iceland. *Scientific Reports*, *11*(1), 11891. https://doi.org/10.1038/s41598-021-91481-z
186. Varotsos, C. A., Melnikova, I. N., Cracknell, A. P., Tzanis, C., & Vasilyev, A. V. (2014). New spectral functions of the near-ground albedo derived from aircraft diffraction spectrometer observations. *Atmospheric Chemistry and Physics*, *14*(13), 6953–6965. https://doi.org/10.5194/acp-14-6953-2014
187. Vohra, K., Marais, E. A., Suckra, S., Kramer, L., Bloss, W. J., Sahu, R., Gaur, A., Tripathi, S. N., Van Damme, M., Clarisse, L., & Coheur, P. F. (2021). Long-Term trends in air quality in major cities in the UK and India: A view from space. *Atmospheric Chemistry and Physics*, *21*(8), 6275–6296. https://doi.org/10.5194/acp-21-6275-2021
188. Wald, L. (2021). *Fundamentals of solar radiation*. CRC Press.
189. Wandji Nyamsi, W., Arola, A., Blanc, P., Lindfors, A. V., Cesnulyte, V., Pitkänen, M. R. A., & Wald, L. (2015). Technical Note: A novel parameterization of the transmissivity due to ozone absorption in the <i>k</i>-distribution method and correlated-<i>k</i> approximation of Kato et al. (1999) over the UV band. *Atmospheric Chemistry and Physics*, *15*(13), 7449–7456. https://doi.org/10.5194/acp-15-7449-2015

190. Wang, Z., Liu, C., Hu, Q., Dong, Y., Liu, H., Xing, C., & Tan, W. (2021). Quantify the Contribution of Dust and Anthropogenic Sources to Aerosols in North China by Lidar and Validated with CALIPSO. In *Remote Sensing* (Vol. 13, Issue 9). https://doi.org/10.3390/rs13091811
191. Wei, J., Li, Z., Peng, Y., & Sun, L. (2019b). MODIS Collection 6.1 aerosol optical depth products over land and ocean: validation and comparison. *Atmospheric Environment*, *201*(December 2018), 428–440. https://doi.org/10.1016/j.atmosenv.2018.12.004
192. Wei, J., Peng, Y., Guo, J., & Sun, L. (2019c). Performance of MODIS Collection 6.1 Level 3 aerosol products in spatial-temporal variations over land. *Atmospheric Environment*, *206*(September 2018), 30–44. https://doi.org/10.1016/j.atmosenv.2019.03.001
193. Wei, J., Peng, Y., Mahmood, R., Sun, L., & Guo, J. (2019a). Intercomparison in spatial distributions and temporal trends derived from multi-source satellite aerosol products. *Atmospheric Chemistry and Physics*, *19*(10), 7183–7207. https://doi.org/10.5194/acp-19-7183-2019
194. Wei, X., Chang, N.-B., Bai, K., & Gao, W. (2020). Satellite remote sensing of aerosol optical depth: advances, challenges, and perspectives. *Critical Reviews in Environmental Science and Technology*, *50*(16), 1640–1725. https://doi.org/10.1080/10643389.2019.1665944
195. WHO. (2016). Health and Environment: Draft road map for an enhanced global response to the adverse health effects of air pollution A69/18. World Health Organization. In *Who* (Issue 69th world health assembly).
196. Winker, D. M., Pelon, J., Coakley, J. A., Ackerman, S. A., Charlson, R. J., Colarco, P. R., Flamant, P., Fu, Q., Hoff, R. M., Kittaka, C., Kubar, T. L., Le Treut, H., Mccormick, M. P., Mégie, G., Poole, L., Powell, K., Trepte, C., Vaughan, M. A., & Wielicki, B. A. (2010). The CALIPSO Mission. *Bulletin of the American Meteorological Society*, *91*(9), 1211–1230. https://doi.org/10.1175/2010BAMS3009.1
197. Wolff, B., Kühnert, J., Lorenz, E., Kramer, O., & Heinemann, D. (2016). Comparing support vector regression for PV power forecasting to a physical modeling approach using measurement, numerical weather prediction, and cloud motion data. *Solar Energy*, *135*, 197–208. https://doi.org/10.1016/j.solener.2016.05.051
198. World Health Organization. (2021). *WHO global air quality guidelines: particulate matter (PM2.5 and PM10), ozone, nitrogen dioxide, sulfur dioxide and carbon monoxide*. World Health Organization. https://apps.who.int/iris/handle/10665/345329
199. Yang, D. (2019). SolarData package update v1.1: R functions for easy access of Baseline Surface Radiation Network (BSRN). *Solar Energy*, *188*, 970–975. https://doi.org/10.1016/j.solener.2019.05.068
200. Yang, D., Wang, W., Gueymard, C. A., Hong, T., Kleissl, J., Huang, J., Perez, M. J., Perez, R., Bright, J. M., Xia, X., van der Meer, D., & Peters, I. M. (2022). A review of solar forecasting, its dependence on atmospheric sciences and implications for grid integration: Towards carbon neutrality. In *Renewable and Sustainable Energy Reviews* (Vol. 161). Elsevier Ltd. https://doi.org/10.1016/j.rser.2022.112348
201. Yu, H., Kaufman, Y. J., Chin, M., Feingold, G., Remer, L. A., Anderson, T. L., Balkanski, Y., Bellouin, N., Boucher, O., Christopher, S., DeCola, P., Kahn, R., Koch, D., Loeb, N., Reddy, M. S., Schulz, M., Takemura, T., & Zhou, M. (2006). A review of measurement-based assessments of the aerosol direct radiative effect and forcing. *Atmospheric Chemistry and Physics*, *6*(3), 613–666. https://doi.org/10.5194/acp-6-613-2006
202. Yu, L., Zhang, M., Wang, L., Lu, Y., & Li, J. (2021). Effects of aerosols and water vapour on spatial-temporal variations of the clear-sky surface solar radiation in China. *Atmospheric Research*, *248*. https://doi.org/10.1016/j.atmosres.2020.105162
203. Zhang, G., Yang, D., Galanis, G., & Androulakis, E. (2022). Solar forecasting with hourly updated numerical weather prediction. *Renewable and Sustainable Energy Reviews*, *154*. https://doi.org/10.1016/j.rser.2021.111768
204. Zhao, B., Jiang, J. H., Diner, D. J., Su, H., Gu, Y., Liou, K. N., Jiang, Z., Huang, L., Takano, Y., Fan, X., & Omar, A. H. (2018). Intra-annual variations of regional aerosol optical depth, vertical distribution, and particle types from multiple satellite and ground-based observational datasets. *Atmospheric Chemistry and Physics*, *18*(15), 11247–11260. https://doi.org/10.5194/acp-18-11247-2018
205. Zhao, B., Jiang, J. H., Gu, Y., Diner, D., Worden, J., Liou, K. N., Su, H., Xing, J., Garay, M., & Huang, L. (2017). Decadal-scale trends in regional aerosol particle properties and their linkage to emission changes. *Environmental Research Letters*, *12*(5). https://doi.org/10.1088/1748-9326/aa6cb2

206. Zheng, B., Tong, D., Li, M., Liu, F., Hong, C., Geng, G., Li, H., Li, X., Peng, L., Qi, J., Yan, L., Zhang, Y., Zhao, H., Zheng, Y., He, K., & Zhang, Q. (2018). Trends in China's anthropogenic emissions since 2010 as the consequence of clean air actions. *Atmospheric Chemistry and Physics*, *18*(19), 14095–14111. https://doi.org/10.5194/acp-18-14095-2018